The Pennsylvania State University

The Graduate School

College of Engineering

THREE-DIMENSIONAL COMPUTATIONAL FLUID DYNAMICS SIMULATIONS OF OZONE UPTAKE IN THE RESPIRATORY TRACT

A Thesis in

Chemical Engineering

by

Adekemi B. Taylor

© 2006 Adekemi B. Taylor

Submitted in Partial Fulfillment
of the Requirements
for the Degree of

Doctor of Philosophy

December 2006

The thesis of Adekemi B. Taylor was reviewed and approved* by the following:

James S. Ultman
Professor Emeritus of Chemical Engineering
Thesis Advisor
Co-Chair of Committee

Ali Borhan
Professor of Chemical Engineering
Co-Chair of Committee

Abdellaziz Ben-Jebria
Professor of Chemical Engineering

John Cimbala
Professor of Mechanical Engineering

Andrew L. Zydney
Professor of Chemical Engineering
Head of the Department of Chemical Engineering

*Signatures are on file in the Graduate School

ABSTRACT

Ozone (O_3), a highly reactive gas, is the major component of photochemical smog and causes a reproducible heterogeneous pattern of lung injury. We hypothesize that this spatial distribution of lung injury mirrors an analogous distribution of O_3 dose delivered to different tissue sites in the respiratory tract. The purposes of this study were: 1) to predict the local uptake of O_3 using three-dimensional computational fluid dynamics (CFD); and 2) to investigate the effects of flow rate, airway structure and chemical reaction in the respiratory tract lining fluid (RTLF) on O_3 uptake. These objectives were achieved by using the commercial CFD package FLUENT (ANSYS Inc., Lebanon, NH) to numerically solve the three-dimensional continuity, Navier-Stokes, and convection-diffusion equations in single idealized airway bifurcations as well as an anatomically accurate airway geometry.

To investigate the effect of flow rate on O_3 uptake, steady inspiratory and expiratory flow simulations in an idealized symmetric bifurcation with a branching angle of 90° were performed at Reynolds numbers based on the parent branch radius (Re) ranging from 100 to 500. The reaction of O_3 in the RTLF was assumed to be so rapid that O_3 concentration was negligible along the entire surface of the bifurcation wall. The total rate of O_3 uptake was found to increase with increasing flow rate during both inspiration and expiration. Hot spots of O_3 flux appeared at the carina of the bifurcation for virtually all inspiratory and expiratory Re considered in the simulations. At the lowest expiratory Re, however, the location of the maximum flux was shifted to the

outer wall of the daughter branch. For expiratory flow, additional hot spots of flux were found on the parent branch wall just downstream of the branching region.

To investigate the effects of airway structure, steady inspiratory and expiratory flow simulations were conducted in single idealized airway bifurcations at $Re = 300$, also assuming an infinitely fast reaction in the RTLF. The effect of branching angle was studied in three idealized symmetric single airway bifurcations with branching angles of 45°, 90°, and 135°. The average dimensionless flux $\langle N \rangle$ (dimensionless uptake rate normalized by dimensionless surface area) increased with increasing branching angle during both inspiratory and expiratory flows. The effect of the mode of branching was studied by comparing simulations in an idealized symmetric 90° bifurcation to those conducted in an idealized monopodial 90° bifurcation. The overall $\langle N \rangle$ in the symmetric 90° bifurcation was higher than in the monopodial bifurcation during inspiratory and expiratory flow. During inspiratory flow, the minor daughter branch of the monopodial bifurcation had the highest $\langle N \rangle$ of all the regions in both geometries.

Before incorporating a finite RTLF reaction into the CFD model, two RTLF reaction models were compared, both modeling the interaction between O_3 and endogenous substrates in the RTLF as quasi-steady lateral diffusion with homogeneous chemical reaction. The first reaction model assumed a reaction rate that was pseudo-first order with respect to O_3 concentration, while the second assumed a reaction rate that was first order with respect to both the O_3 and substrate concentrations and second order overall. The O_3 concentration profiles within the RTLF as well as the flux of O_3 into the RTLF and tissue were virtually identical in the two models. Because of its greater simplicity, the pseudo-first order reaction model was selected for incorporation into the CFD simulations investigating the effects of RTLF reaction-diffusion parameters on O_3 uptake distribution.

To study the effect of RTLF thickness on O_3 uptake into the RTLF and underlying tissue, the pseudo-first order reaction rate constant was characterized by defining a dimensionless Damkohler number, based on the parent branch radius (Da_R). Steady inspiratory flow simulations at $Re = 300$ were carried out at $Da_R = 1.7\times 10^7$ and $Da_R = 1.7\times 10^{10}$ on idealized symmetric 90° bifurcations with RTLF thicknesses ranging from 0.014% to 0.282% of the parent branch radius. The rate of uptake in the RTLF was generally insensitive to the thickness of the RTLF layer, except at the lower Da_R at which the RTLF uptake rate increased markedly as the ELF thickness was reduced below about 0.07% of the airway radius. At the lower Da_R, the tissue uptake rates were more sensitive to RTLF thickness than were the RTLF uptake rates, but at the higher Da_R, no O_3 reached the tissue, regardless of RTLF thickness.

The effect of the reaction rate constant, characterized by the Damkohler number based on the RTLF thickness (Da), was investigated by simulating flow and O_3 uptake in the idealized 90° symmetric and 90° monopodial bifurcations at Re of 10, 100, and also at Re 1000 in the symmetric bifurcation, for Da ranging from 1 to 10^6. An increase in Da led to an increased rate of O_3 uptake into the RTLF but a reduced uptake rate in the underlying tissue. The sensitivity of both uptake rates to flow rate became more pronounced as the reaction rate constant was increased.

In the final study, two steady inspiratory flow simulations at $Re = 152$ in an anatomically accurate geometry representative of the first three generations of the airways of a rhesus monkey beginning at the trachea was constructed. Steady inspiratory flow simulations were conducted, one assuming an instantaneous reaction at the bifurcation walls and the other assuming a pseudo first order RTLF reaction at an intermediate Da of 1000. In both simulations, hot spots of flux were located at all three carinas of the geometry, similar to what was found in the idealized single airway bifurcations.

TABLE OF CONTENTS

LIST OF FIGURES x

LIST OF TABLES xviii

ACKNOWLEDGEMENTS xix

Chapter 1 INTRODUCTION 1

Chapter 2 BACKGROUND 6

- 2.1 THE RESPIRATORY TRACT 7
- 2.2 RESPIRATORY TRACT LINING FLUID (RTLF) 9
- 2.3 FACTORS INFULUENCING O_3 UPTAKE 13
  - 2.3.1 Respiratory Tract Structure 13
  - 2.3.2 Ventilation 13
  - 2.3.3 Physical Properties of the RTLF 14
  - 2.3.4 Chemical Composition of the RTLF 15
- 2.4 MATHEMATICAL DOSIMETRY MODELS 16

Chapter 3 CONSTRUCTION OF IDEALIZED AIRWAYS AND PROBLEM FORMULATION 22

- 3.1 BIFURCATION GEOMETRIES 22
- 3.2 GOVERNING EQUATIONS 27
- 3.3 IMPLEMENTATION IN FLUENT 31
- 3.4 DISCUSSION 33

Chapter 4 EFFECT OF FLOW RATE ON OZONE UPTAKE IN A SINGLE IDEALIZED BIFURCATION 41

- 4.1 CFD Simulations 41
  - 4.1.1 Resolution and Accuracy 42
- 4.2 RESULTS 45
  - 4.2.1 Flow Field 46
  - 4.2.2 Concentration and Flux Distributions 48
  - 4.2.3 Overall Rate of Uptake 54
- 4.3 DISCUSSION 57
  - 4.3.1 Model Assumptions 57
  - 4.3.2 Flux Distribution and Uptake 59

4.3.3 Implications for O_3-induced Injury ... 61
4.4 SUMMARY AND CONCLUSIONS ... 63

Chapter 5 EFFECT OF AIRWAY GEOMETRY ON OZONE UPTAKE ... 78

5.1 RESULTS – EFFECT OF BRANCHING ANGLE ... 78
5.1.1 Flow Fields ... 79
5.1.2 Concentration Distributions ... 81
5.1.3 Flux Distributions ... 82
5.1.4 Rate of Uptake/Average Fluxes ... 86
5.2 RESULTS – EFFECT OF MODE OF BRANCHING ... 87
5.2.1 Flow Fields ... 88
5.2.2 Concentration Distributions ... 90
5.2.3 Flux Distributions ... 91
5.2.4 Average Fluxes ... 93
5.3 DISCUSSION ... 95
5.3.1 Effect of Branching Angle ... 95
5.3.2 Effect of Mode of Branching ... 96

Chapter 6 SELECTION OF AN RTLF REACTION MODEL ... 116

6.1 GENERAL RTLF SPECIES CONSERVATION EQUATION ... 117
6.2 PSEUDO-FIRST ORDER REACTION MODEL ... 122
6.2.1 Model Description ... 122
6.2.2 Sensitivity of O_3 Concentration and Uptake to Damkohler Number ... 124
6.3 SECOND ORDER REACTION MODEL ... 126
6.3.1 Model Description ... 126
6.3.2 Sensitivity of O_3 Concentration and Uptake Rate to Reaction Model Parameters ... 129
6.4 COMPARISON OF REACTION MODELS ... 132
6.5 DISCUSSION ... 133

Chapter 7 SENSITIVITY OF OZONE UPTAKE TO RTLF DIFFUSION-REACTION PARAMETERS IN SINGLE AIRWAY BIFURCATIONS ... 149

7.1 IMPLEMENTATION OF RTLF REACTION IN FLUENT ... 149
7.2 RESULTS – SYMMETRIC BIFURCATIONS ... 152
7.2.1 Sensitivity of Uptake Rate to RTLF Thickness ... 152
7.2.2 Sensitivity to Da ... 154
7.2.2.1 RTLF and Tissue Uptake Rates ... 155
7.2.2.2 Flux Distributions ... 157
7.2.2.3 Flow and Concentration Fields ... 157
7.3 RESULTS – MONOPODIAL BIFURCATION ... 160
7.3.1 Sensitivity to Da ... 161
7.3.1.1 Total Uptake Rates ... 161
7.3.1.2 Flux Distributions ... 161

        7.3.1.3 Flow Fields and Concentration Distributions 162
    7.4 COMPARISON OF SYMMETRIC AND MONOPODIAL BIFURCATIONS 163
    7.5 DISCUSSION 164

Chapter 8 OZONE UPTAKE IN AN ANATOMICALLY ACCURATE AIRWAY MODEL 186

    8.1 CONSTRUCTION AND MESHING OF AN ANATOMICALLY ACCURATE GEOMETRY 186
        8.1.1 Surface Generation 186
        8.1.2 Construction and Meshing of Airway Volume 189
    8.2 CFD SIMULATIONS 191
        8.2.1 Governing Equations and Boundary Conditions 191
        8.2.2 Grid Resolution 193
    8.3 RESULTS – INFINITELY FAST REACTION IN RTLF 194
    8.4 RESULTS – FINITE REACTION IN RTLF 196
    8.5 DISCUSSION 198

Chapter 9 SUMMARY AND RECOMMENDATIONS FOR FUTURE WORK 214

Bibliography 221

Appendix A NOMENCLATURE 230

Appendix B NUMERICAL SOLUTION OF GOVERNING EQUATIONS WITH FLUENT 235

Appendix C USER-DEFINED PROGRAMS FOR CALCULATING O_3 FLUX 239

    C.1 USER-DEFINED FUNCTION FOR CALCULATING FLUX FOR THE CASE OF AN INFINITE WALL REACTION 240
    C.2 USER-DEFINED FUNCTION FOR THE CASE OF A FINITE PSUEDO-FIRST ORDER REACTION IN THE RTLF 244

Appendix D SOLUTION OF 2ND ORDER REACTION MODEL 246

D.1 MATHEMATICA CODE USED TO IMPLEMENT THE SHOOTING METHOD 246

    D.2 SOLUTION OF GOVERNING EQUATIONS USING ASYMPTOTIC EXPANSIONS 250

Appendix E GRID CONVERGENCE RESULTS FOR Re 1000 252

LIST OF FIGURES

Figure **1-1**: The exposure-dose-response paradigm. 5

Figure **2-1**: (a) The human respiratory system. Source: Silverthorn, 2001. (b) Airway branching. Source: West, 1999. 19

Figure **2-2**: A schematic of the respiratory tract lining fluid. Source: Miller *et al.*, 1993. 20

Figure **2-3**: Airflow patterns in bifurcations during inspiration and expiration. IW: inner wall; OW: outer wall, u: velocity. Source: Overton, 1984. 21

Figure **3-1**: Idealized dichotomous bifurcations. T: transition region 37

Figure **3-2**: Idealized monopodial bifurcation. T: transition region, Minor D: minor daughter branch. 38

Figure **3-3**: Schematic definition of (a) azimuthal angles ϕ_p and ϕ_d in the parent and daughter branches, respectively, and (b) wall coordinate s in the symmetric bifurcations. 39

Figure **3-4**: Schematic definition of (a) azimuthal angles ϕ_p and ϕ_d in the parent and daughter branches, respectively, and (b) wall coordinate s in the monopodial bifurcation. 40

Figure **4-1**: Mesh in the bifurcation region of the 90° symmetric bifurcation. (a) Mesh 1 (b) Mesh 2 (c) Mesh 3 64

Figure **4-2**: Results of mesh independence study (inspiratory flow). The inset shows the locations used in testing mesh independence. Both lines are in the bifurcation plane. 65

Figure **4-3**: Schematic definition of various cross-sections along the wall coordinate s on which flux distributions are reported. 66

Figure **4-4**: Isocontours of the magnitude of dimensionless velocity in the bifurcation plane for inspiratory and expiratory flows. 67

Figure **4-5**: Dimensionless velocity vectors (colored by dimensionless velocity magnitude) in the plane of the outflow boundary of the daughter branch during steady inspiratory flow at $Re = 300$ showing pair of counter-rotating vortices. The line denotes the location of the bifurcation plane. 68

Figure **4-6**: Dimensionless velocity magnitude (top panel) and dimensionless concentration (bottom panel) profiles along the intersections of various cross sections (H, I, J, K, L) and the bifurcation plane for steady expiratory flow in the daughter branch at $Re = 300$. Radial coordinate = -0.7 is intersects the inner wall and radial coordinate = 0.7 intersects the outer wall. 69

Figure **4-7**: Isocontours of (A) magnitude of dimensionless velocity and (B) dimensionless O_3 concentration on cross-sections *A*, *C*, *D*, and *G* (top to bottom) along the parent branch axis for expiratory flow at $Re = 500$. The lines denote the intersections of the bifurcation plane with the parent branch wall. (C) Dimensionless velocity vectors (colored by dimensionless velocity magnitude) in the plane of the outflow boundary of the parent branch for steady expiratory flow at $Re = 300$ showing the quadruple vortex pattern. The line denotes the location of the bifurcation plane. 70

Figure **4-8**: Isocontours of dimensionless O_3 concentration in the bifurcation plane for inspiratory and expiratory flows. 71

Figure **4-9**: Distribution of the circumferentially-averaged dimensionless flux $\left(\overline{N}\right)$ along the bifurcation wall for inspiratory flow (top panel) and expiratory flow (bottom panel) at three different Reynolds numbers. The arrows indicate the flow direction. 72

Figure **4-10**: Isocontours of the dimensionless flux (N) along the bifurcation wall for (A) inspiratory flow and (B) expiratory flow ($Re = 300$). 73

Figure **4-11**: Circumferential variation of the local dimensionless wall flux, N, at various cross-sections in the parent and daughter branches for inspiratory flow at (A) $Re = 100$ and (B) $Re = 500$. 74

Figure **4-12**: Circumferential variation of the local dimensionless wall flux, N, at various cross-sections in the parent and daughter branches for expiratory flow at (A) $Re = 100$ and (B) $Re = 500$ 75

Figure **4-13**: Dependence of the dimensionless rate of O_3 uptake ($\dot{M}$) on Reynolds number for (A) inspiratory flow and (B) expiratory flow. The total rate of uptake for the entire bifurcation, as well as those in the parent branch and in a single daughter branch are shown. Also shown for comparison is the simulated rate of uptake in a straight tube with the same diameter as that of the parent branch and wall surface area equivalent to that of the entire bifurcation. (**NOTE:** The uptake rate reported for the daughter branch includes the uptake rate in half of the transition region.) 76

Figure **4-14**: Circumferential variation of the scaled local wall flux, $x^{1/2} Sh/Re^{1/2}$, at various cross-sections in (A) the parent branch for inspiratory flow at $Re = 300$ and (B) the daughter branch for expiratory flow at $Re = 300$. In the top panel, the lines corresponding to the parent branch cross-sections *B*, *C*, and *D* are not labeled because they are virtually indistinguishable, as are the unlabeled lines in the lower panel representing daughter branch cross-sections *J* and *K*. 77

Figure **5-1**: Isocontours of the magnitude of dimensionless velocity in the bifurcation plane for inspiratory and expiratory flows and for three symmetric branching angles ($Re = 300$). 99

Figure **5-2**: Dimensionless velocity vectors during inspiratory flow in the plane of the bifurcation of the 135° symmetric bifurcation showing the region of backflow along the outer wall of the daughter branch ($Re = 300$). Vectors are colored by dimensionless velocity magnitude. 100

Figure **5-3**: Dimensionless velocity profiles in the bifurcation plane at the outflow boundaries of the daughter branches of the three symmetric bifurcations during inspiratory flow ($Re = 300$). 101

Figure **5-4**: Dimensionless velocity vectors in the bifurcation plane of the 135° symmetric bifurcation during expiratory flow ($Re = 300$) showing (A) the pair of counter-rotating vortices surrounding the carina and (B) the backflow regions along the parent branch walls. Vectors are colored by dimensionless velocity magnitude. 102

Figure **5-5**: Isocontours of (A) dimensionless velocity magnitude and (B) dimensionless concentration in the plane normal to the bifurcation plane for expiratory flow for three symmetric branching angles ($Re = 300$). The bottom of the cross-section corresponds to the carina. 103

Figure **5-6**: Isocontours of dimensionless concentration in the bifurcation plane for inspiratory and expiratory flows and for three symmetric branching angles ($Re = 300$). 104

Figure **5-7**: Dimensionless concentration distributions at the outflow boundaries of the daughter branches of the idealized symmetric bifurcations during inspiratory flow ($Re = 300$). The lines denote the location of the bifurcation plane. I.W.: inner wall; O.W.: outer wall. 105

Figure **5-8**: Isocontours of the dimensionless flux N along the bifurcation walls for inspiratory and expiratory flows and for three symmetric branching angles ($Re = 300$). 106

Figure **5-9**: Distribution of the circumferentially-averaged dimensionless flux $\overline{N}$ along the bifurcation walls for inspiratory flow (top panel) and expiratory flow (bottom panel) and for three different branching angles. The arrows indicate the flow direction. 107

Figure **5-10**: (A) The enclosed area shows one-fourth of the area A_Φ, which is symmetric about both the bifurcation plane and the normal plane. (B) Average dimensionless flux $\langle N \rangle_\Phi$ through area A_Φ as a function of angle $\boldsymbol{\Phi}$ (all defined in Section **5.1.3**) in the three idealized symmetric bifurcations during steady inspiratory flow. 108

Figure **5-11**: Average dimensionless flux $\langle N \rangle$ in each bifurcation region and in the entire bifurcation for (A) inspiratory flow and (B) expiratory flow for three branching angles. 109

Figure **5-12**: Isocontours of the magnitude of dimensionless velocity in the bifurcation plane for inspiratory and expiratory flows in the symmetric and monopodial bifurcations ($Re = 300$). Also shown are dimensionless velocity vectors (colored by dimensionless velocity magnitude) showing regions of backflow during inspiratory flow in both daughter branches of the monopodial bifurcation. 110

Figure **5-13**: In-plane velocity vectors on the outflow boundary of the parent branch in the symmetric (top panel) and monopodial (bottom panel) bifurcations during steady expiratory flow. Vectors are colored by dimensionless velocity magnitude. O.W.: outer wall, and I.W.: inner wall of monopodial parent branch. The line across each outflow plane marks the location of the bifurcation plane. 111

Figure **5-14**: Isocontours of dimensionless O_3 concentration in the bifurcation plane for inspiratory and expiratory flows in the symmetric and monopodial bifurcations ($Re = 300$). 112

Figure **5-15**: Isocontours of the dimensionless flux N along the bifurcation walls for inspiratory and expiratory flows in the symmetric and monopodial bifurcations ($Re = 300$). Regions with fluxes higher the maximums indicated on the scales are not displayed. 113

Figure **5-16**: Distribution of the circumferentially-averaged dimensionless flux $\left(\overline{N}\right)$ along the bifurcation wall for inspiratory flow (top panel) and expiratory flow (bottom panel) at three different branching angles. The arrows indicate the flow direction. The monopodial minor daughter branch extends from $6 \le s \le 9.2$ and the major daughter from $6 \le s \le 12$ 114

Figure **5-17**: Average dimensionless fluxes $\langle N \rangle$ in each bifurcation region and in the entire bifurcation for (A) inspiratory flow and (B) expiratory flow for three branching angles. 115

Figure **6-1**: Schematic of half of the cross-section along the length L of an airway with ELF thickness Δ and radius R_0. The x^* direction is perpendicular to both the y^* and z^* directions and parallel to the circumference of the tube. 138

Figure **6-2**: Pseudo-first order reaction model for the consumption of O_3 in the RTLF. Symbols are defined in the text. 139

Figure **6-3**: Sensitivity of the Damkohler number Da to the reaction rate constant at different RTLF thicknesses. $D_l = 2.66 \times 10^{-5}\ \text{cm}^2/\text{s}$ 140

Figure **6-4**: Sensitivity of the Damkohler number to RTLF thickness at different reaction rates. $D_l = 2.66 \times 10^{-5}\ \text{cm}^2/\text{s}$ 141

Figure **6-5**: Effect of the Damkohler number Da on the O_3 concentration profile in the RTLF. $y = 0$ corresponds to the gas-RTLF interface, and $y = 1$ corresponds to the RTLF-tissue interface. 142

Figure **6-6**: Dependence on the Damkohler number Da of (top panel) the dimensionless flux of O_3 into the RTLF (N_{RTLF}) and tissue (N_{tissue}) and (bottom panel) the amount of O_3 that reaches the tissue. 143

Figure **6-7**: Second order reaction model for the consumption of O_3 reaction and diffusion in the RTLF. Symbols are defined in the text. 144

Figure **6-8**: Comparison of numerical and asymptotic solutions of O_3 concentration for $Da = 0.001$ and $Da = 0.01$, $\beta = 1$. $y = 0$ corresponds to the gas-RTLF interface, and $y = 1$ corresponds to the RTLF-tissue interface. 145

Figure **6-9**: Comparison of numerical and asymptotic solutions of substrate concentration for $Da = 0.001$ and $Da = 0.01$, $\beta = 1$. $y = 0$ corresponds to the gas-RTLF interface, and $y = 1$ corresponds to the RTLF-tissue interface. 146

Figure **6-10**: Sensitivity of (A) O_3 and (B) substrate concentration profiles to β. For the substrate concentration, only the results for $\text{Da}_2 = 250$ are shown. For $\text{Da}_2 = 0.01$, c_S maintained a value of 1.00 throughout the RTLF for both values of β, as was the case when $\text{Da}_2 = 250$ and $\beta = 6.2 \times 10^{-9}$. $y = 0$ corresponds to the gas-RTLF interface, and $y = 1$ corresponds to the RTLF-tissue interface. 147

Figure **6-11**: Comparison between O_3 concentration profiles from the pseudo-first order and second order reaction models. The solid lines represent the pseudo-first order model and the dashed lines the second order model. 148

Figure **7-1**: Sensitivity to Δ/R_0 of the dimensionless RTLF (top panel) and tissue (middle panel) uptake rates and the fraction of ozone absorbed that penetrates to the tissue (bottom panel)...172

Figure **7-2**: Sensitivity of the dimensionless RTLF and tissue uptake rates to Da and Re in a symmetric bifurcation. The dimensionless RTLF uptake rates for an infinitely fast reaction at the gas-RTLF interface ($Da \to \infty$) are shown for comparison. 173

Figure **7-3**: Isocontours of the dimensionless flux into the RTLF (N) for various Re and Da in a symmetric bifurcation...174

Figure **7-4**: Side views of isocontours of dimensionless flux into the RTLF (N) for three Re when $Da = 10^4$ in a symmetric bifurcation. The views in this figure are rotated 90° about the parent branch axes from those in Figure **7-3**. 175

Figure **7-5**: Isocontours of the dimensionless flux into tissue for various Da at $Re = 1000$ in a symmetric bifurcation. 176

Figure **7-6**: Isocontours of dimensionless velocity magnitude for Re = 10, 100, and 1000 in the bifurcation plane for inspiratory flow in a symmetric bifurcation...177

Figure **7-7**: Velocity vector plot in the bifurcation plane (colored by dimensionless velocity magnitude) for inspiratory flow at $Re = 1000$. The magnified regions show the two areas of backflow along the daughter branch walls...178

Figure **7-8**: Dimensionless velocity profiles in the plane of the bifurcation at the outflow boundaries of the daughter branch at Re = 10, 100, and 1000. 179

Figure **7-9**: Isocontours of dimensionless O_3 concentration in the bifurcation plane at various Re and Da for inspiratory flow in a symmetric bifurcation.....180

Figure **7-10**: Sensitivity of the dimensionless RTLF uptake rate to Da and Re in a monopodial bifurcation. The dimensionless RTLF uptake rates for an infinitely fast reaction at the gas-RTLF interface ($Da \to \infty$) are shown for comparison...181

Figure **7-11**: Isocontours of dimensionless RTLF flux for $Re = 10$ and $Re = 100$ at various Da in a monopodial bifurcation...182

Figure **7-12**: Isocontours of dimensionless velocity magnitude in the bifurcation plane at Re = 10 and 100 for inspiratory flow in a monopodial bifurcation........183

Figure **7-13**: Isocontours of the dimensionless O_3 concentration in a monopodial bifurcation for $Re = 10$ and $Re = 100$ at various Da in the bifurcation plane for inspiratory flow. 184

Figure **7-14**: Comparison of average fluxes $\langle N \rangle$ in the symmetric and monopodial bifurcations for different Da and at Re of 10 and 100...................185

Figure **8-1**: (A) A slice of MRI data. The dark holes that are surrounded by the gray region represent airway lumina. (B) Segmentation of the MRI data slice. The segmented airways are colored red. (C) Isosurface of tracheobronchial tree of the rhesus monkey. The red loop identifies the airways that were used in the simulations. 203

Figure **8-2**: (A) Surface imported from AMIRA™. The artificial airway wall is marked. (B) Truncated airway geometry. The pink outlines identify the perimeters of the inflow and outflow boundaries. (C) Meshed airway volume. (D) Cross-section through meshed volume showing *hexcore* mesh....204

Figure **8-3**: Isocontours of velocity magnitude at three cross-sections through the anatomically accurate airway model. (a) y = 0.01 cm, (b) y = 0.29 cm, (c) y = 0.33 cm. The y coordinate increases in the direction pointing out of the page and the airway spans y = -0.271 (anterior–behind the page) to y = 0.503 cm (posterior–in front of the page). The terminal airway segments are labeled in (a) and the Reynolds numbers (based on the inlet radius R_0 or outlet radius R^*, where the radius is defined as half the hydraulic diameter) in the trachea and each of the terminal airways are labeled in (c). 205

Figure **8-4**: Isocontours of velocity magnitude at each of the outlets of the anatomically accurate airway model. O.W.: outer wall, I.W.: inner wall, P: posterior, A: anterior. Outlets are not all represented at the same scale. The posterior and anterior of the geometry are defined in the caption of Figure **8-3**. 206

Figure **8-5**: Isocontours of scaled concentration for an infinitely fast RTLF reaction at three cross-sections through the anatomically accurate airway. (a) y = 0.01 cm, (b) y = 0.29 cm, (c) y = 0.33 cm. The y coordinate increases in the direction pointing out of the page and the airway spans y = -0.271 (anterior–behind page) to y = 0.503 cm (posterior–in front of page). The terminal airway segments are labeled in (a) and the average concentration $\bar{c}$ in (c)..207

Figure **8-6**: Isocontours of scaled concentration for an infinitely fast RTLF reaction at each of the outlets of the anatomically accurate airway model. O.W.: outer wall, I.W.: inner wall, P: posterior, A: anterior. Outlets are not all represented at the same scale. The posterior and anterior of the geometry are defined in the caption of Figure **8-3**..208

Figure **8-7**: Isocontours of scaled flux (N^*/c_0) for an infinitely fast RTLF reaction in the anatomically accurate airway model..209

Figure **8-8**: Scaled flux distributions in branching regions for an infinitely fast RTLF reaction. (a) First generation branching (b) Minor second generation branching (c) Major second generation branching. Airway segments are labeled. The dark lines mark the perimeters of the outflow boundaries.............210

Figure **8-9**: Isocontours of scaled concentration for $Da = 1000$ at three cross-sections through the anatomically accurate airway. (a) y = 0.01 cm, (b) y = 0.29 cm, (c) y = 0.33 cm. The terminal airway segments are labeled in (a)........211

Figure **8-10**: Isocontours of scaled flux for $Da = 1000$ in the anatomically accurate airway model. 212

Figure **8-11**: Scaled flux distributions in branching regions for for $Da = 1000$. (a) First generation branching (b) Minor second generation branching (c) Major second generation branching. Airway segments are labeled. The dark lines mark the perimeters of the outflow boundaries..213

Figure **C-1**: Vectors used to calculate the flux through the gas-RTLF interface. The triangle represents a cell/control volume adjacent to the gas-RTLF interface, a portion of which is spanned by face *f*. The dark circles represent a cell or face centroid..240

Figure **C-2**: Comparison of the circumferentially averaged dimensionless fluxes along the parent branch of an idealized symmetric bifurcation (90° branching angle, Re = 100) calculated using equation **C.2** (wall_flux1) and an approximation of equation **3.8** (wall_flux2)...243

LIST OF TABLES

Table **2-1**: RTLF substrate concentrations (μM) along the respiratory tract. 11

Table **2-2**: Reported reaction rate constants of selected RTLF constituents with O_3. UA: uric acid; AH_2: ascorbic acid; GSH: reduced glutathione. 12

Table **3-1**: Dimensionless surface areas of different regions of the bifurcation geometries 25

Table **3-2**: Dimensional and dimensionless forms of the boundary conditions on the continuity and Navier-Stokes equations. $\mathbf{n}$ is the unit vector normal to the boundary; A^* and A are the dimensional and dimensionless surface areas, respectively, of the boundaries. All other variables are defined in the text. 28

Table **3-3**: Dimensional and dimensionless forms of the boundary conditions on the convection-diffusion equation. $\mathbf{n}$ is the unit vector normal to the boundary. All other variables are defined in the text. 30

Table **6-1**: Ratio of RTLF thickness to Airway Radius and Length in the Respiratory Tract 121

Table **7-1**: Re and Da (assuming $k_{r1} = 10^5$ s^{-1}) at different levels of exertion in selected lower conducting airway generations along the respiratory tract. Reynolds numbers in generations roughly corresponding to the Re simulated in this chapter are highlighted in boldface. Weibel's model A (Weibel, 1963) was used to define airway diameters, and thickness scheme A of Miller *et al.* (1985) was used to define RTLF thicknesses. 167

Table **8-1**: Rhesus monkey airway dimensions. The radius is defined as half the hydraulic diameter, which is defined in equation **8.3**. The airway segment length measurements are very approximate. The radii and cross-sectional areas of only the inflow and outflow boundaries are given. 190

Table **8-2**: Boundary conditions for steady inspiratory flow and O_3 transport in the anatomically-accurate airway geometry. 192

Table **8-3**: Comparison of the flow splits predicted by the simulation (zero pressure at outflow boundaries) and flow splits based on Poiseuille flow. 199

Table **8-4**: Comparisons of the dimensionless uptake rate $\dot{M}$, overall average dimensionless flux, and fractional uptake in the idealized 90° symmetric bifurcation and the anatomically accurate airway model. 202

ACKNOWLEDGEMENTS

First of all, I would like to express my deep gratitude to my advisor, Dr. James Ultman, for teaching me so much during my stay at Penn State. Thank you for always making yourself available, even if that caused you inconvenience, and for being so understanding and supportive. Words cannot express how much I appreciate you. I will forever be grateful to you.

I would also like to express my heartfelt appreciation to Dr. Ali Borhan for packing the three years we have worked together with so much knowledge. Thank you for guiding me from total ignorance about CFD to being able to complete this thesis, all in a relatively short time. Thank you for always being available to meet with me when I was confused or when I just needed to make sure I was doing the right thing. I have learnt so much from you.

I also wish to thank the other members of my committee, Dr. Aziz Ben-Jebria, whom I worked closely with during my first two years at Penn State, and Dr. John Cimbala, for their constructive criticism and insightful suggestions.

I would not be where I am today without the love, prayers, support, and encouragement of my family – my parents, Mr. Victor Taylor and Dr. Victoria Ezeokoli, my siblings, Nike, Gbenga, and Ayo, my dearest Aunty Charity, and my favorite nephew Timi. I dedicate this thesis to them.

I also want to thank my church family at State College Assembly of God, especially my fellow choir members, for their love and fellowship. I am especially indebted to Dr. Anthony and Mrs. Moradeyo Olorunnisola not only for giving me a home

to live in during my last few months at Penn State, but also for their friendship and advice. Aunty Deyo, thank you for being there for me during some very hard times. Another member of my church family I deeply appreciate is Dr. Justina Osa. Thank you, ma, for being such a wonderful friend and for being my mom in State College.

I want to thank my lab mates – Sanaz, Banafsheh, Ali, Amit, Melissa, and Tim – for their encouragement and just plain fun times during my time at Penn State. Sanaz, your friendship throughout my entire stay at Penn State has been very dear to me and will remain so. I will always remember our long conversations. Banafsheh, I've only known you for a short time, but I have enjoyed being your friend.

I would be remiss if I did not acknowledge the help of the technical support staff at ANSYS Inc.

Chapter 1

INTRODUCTION

Ozone (O_3) is a major component of photochemical smog that is commonly present in urban areas. It is a well-established fact that this highly reactive air pollutant causes adverse health effects. Not only does O_3 inhalation result in lung irritation and impaired lung function (Blomberg *et al.*, 2001; McDonnell *et al.*, 1983) but it has also been shown to lead to a reproducible heterogeneous pattern of tissue injury in laboratory animals (Castleman *et al.*, 1977; Plopper *et al.*, 1998).

We hypothesize that the process by which O_3 inhalation leads to tissue injury can be explained by the exposure-dose-response paradigm (Figure **1-1**). The local dose of O_3 or its reaction products to lung tissue after inhalation of the pollutant is determined by airflow patterns in the gas phase, which are affected by airway anatomy and ventilation rates, and by diffusion and reaction between O_3 and reactive substances in the respiratory tract lining fluids (RTLF) that coat the respiratory tract epithelial cells and in the lung tissue. It is the dose of O_3 or the toxic byproducts of its reaction with RTLF constituents and/or lung epithelial cell components that is responsible for O_3 induced tissue damage. The tissue response may also modify the local tissue dose. This hypothesis is consistent with studies that demonstrate an O_3 exposure concentration dependence of tissue injury (Plopper *et al.*, 1998; Postlethwait *et al.*, 2000). Hence, it can be inferred that the observed heterogeneous pattern of O_3-induced injury is at least partly a result of differences in tissue dose at various sites along the respiratory tract.

A secondary hypothesis is that the local dose of O_3 can be predicted by mathematical models that account for airway anatomy, gas phase convection and diffusion, and diffusion and reaction in the RTLF and tissue. This hypothesis is important for at least two reasons. Firstly, the use of O_3 exposure concentration is inadequate as a surrogate for O_3 dose, and it is difficult to experimentally determine the local dose of O_3 along the respiratory tract. Secondly, most O_3 exposure studies are carried out in a variety of species of laboratory animals and under a variety of exposure conditions; consequently, it is necessary to extrapolate exposure-response data from these animal studies to humans.

To test the dose-response hypothesis, several investigators have simulated gas transport throughout the lung using one dimensional, single-path models that predict the longitudinal distribution of O_3 uptake into mucus and underlying epithelium (Miller *et al.*, 1978; Miller *et al.*, 1985; Overton *et al.*, 1987; Grotberg *et al.*, 1990; Grotberg, 1990; Hu *et al.*, 1992; Overton and Graham, 1995). Consistent with observed patterns of tissue injury, these simulations predicted that the maximum O_3 uptake by epithelial cells does occur in the proximal alveolar region. The strength of these simulations is that they include the convection-diffusion processes occurring in the respired air as well as the diffusion-reaction occurring in the underlying mucus and tissue layers. Their major weakness is that they cannot account for three-dimensional flow and diffusion effects that can have an important influence on local patterns of O_3 uptake. These limitations can be overcome by using solving the three-dimensional forms of the governing equations using computational fluid dynamics (CFD).

The primary goal of this thesis was to study the dose distribution of O_3 in idealized single airway bifurcations and anatomically-accurate airway bifurcations and examine the effects of various factors on O_3 uptake. The specific aims of this work were to use three-dimensional CFD and other mathematical tools to:

1. Investigate the effect of respiratory flow rate and airway branching structure on O_3 uptake in idealized single airway bifurcation.
2. Compare different models of O_3 reaction in the RTLF and select one to be used in further studies.
3. Investigate the sensitivity of O_3 uptake and dose distribution in a single idealized airway bifurcation to RTLF diffusion-reaction parameters, specifically, RTLF thickness and reaction rate constant.
4. Construct an anatomically accurate airway geometry, simulate O_3 uptake in this geometry, and compare the simulation predictions with those in the idealized airway bifurcations.

This thesis is structured as follows: Chapter 2 provides background information relevant to the work to be presented. Next, Chapter 3 describes the construction of the idealized airway geometries and the procedure for solving the governing equations for predicting O_3 uptake distribution. In Chapter 4, the effect of respiratory flow rate on O_3 uptake is investigated, while Chapter 5 considers the effect of branching structure, specifically, branching angle and mode of branching. In the next chapter, Chapter 6, two RTLF reaction models are compared, and one is selected for incorporation into subsequent CFD simulations. Chapter 7 examines the sensitivity of O_3 uptake and dose distribution to RTLF reaction parameters in single symmetric bifurcations, and Chapter 8 presents simulations carried out in an anatomically accurate representation of a portion of the lower respiratory tract of a rhesus monkey. Finally, a summary of the results of the various studies and general conclusions reached, as well as suggestions for future work, are given in Chapter 9.

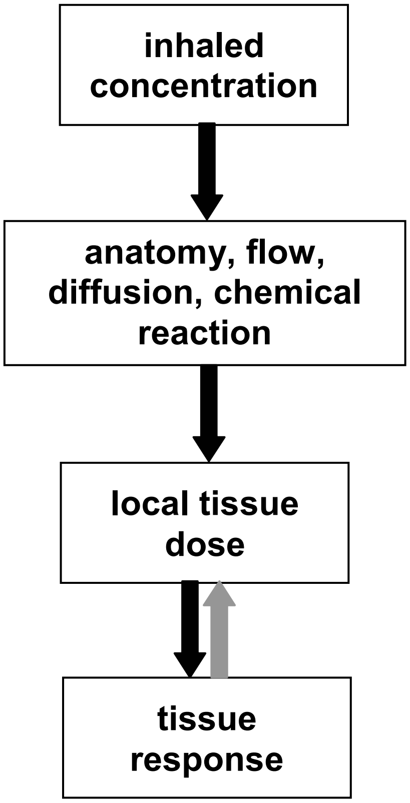
inhaled concentration
anatomy, flow, diffusion, chemical reaction
local tissue dose
tissue response

Figure **1-1**: The exposure-dose-response paradigm.

Chapter 2

BACKGROUND

Ozone (O_3, O–O=O) is a highly reactive, poorly water soluble gas and is the major oxidant present in photochemical smog. O_3 plays opposing roles in the two layers of the atmosphere where it is found. Most atmospheric O_3 is found in the stratosphere, 8 to 50 km above ground level, where it is naturally occurring (Mustafa, 1990) and prevents harmful ultraviolet rays from the sun from reaching the surface of the earth. In contrast, O_3 in the atmosphere immediately surrounding us, i.e., the troposphere, arises from photochemical reactions involving oxides of nitrogen and volatile organic compounds, which are produced from manmade emissions (Mustafa, 1990) such as those from factories and motor vehicles. Thus, O_3 is most abundant in and around areas with high levels of such emissions, for instance, in urban areas.

O_3 causes many adverse health effects, for example, impaired pulmonary function, lung inflammation, bronchial reactivity, altered membrane and vascular permeability, and various kinds of epithelial injury in the respiratory tract (Mustafa, 1990; Mudway and Kelly, 2000), and it may also exacerbate preexisting lung disease (Kelly, 2003). These deleterious effects are mainly due to the high reactivity of O_3 with all kinds of biomolecules.

2.1 THE RESPIRATORY TRACT

Because inhalation is the main route by which O_3 enters the body and O_3 is such a reactive gas, the respiratory tract is the main target of O_3 toxicity. The respiratory tract (Figure **2-1**) begins at the nasal and oral cavities, which are the first to come in contact with inhaled air. About 40% of inhaled O_3 is absorbed in the nasal passages alone (Gerrity *et al*., 1988). The convoluted anatomy of the nasal passages imparts complexity to respired air flow patterns. Air leaving the nasal and oral cavities enters the pharynx, which leads into the larynx. Airflow through this narrow aperture forms a laryngeal jet that can cause turbulence at tracheal Reynolds numbers below the transition Reynolds number for a tube. The larynx empties into the trachea, a tube supported by cartilaginous rings. The trachea then divides into two main bronchi, which in turn each divide into two secondary bronchi. Branching continues in this manner, and the amount of cartilage on the walls of the bronchi decrease moving down the bronchial tree until the final bronchi divide into bronchioles, which possess no supporting cartilage. The bronchioles continue to divide until the last non-respiratory bronchioles, or terminal bronchioles, are reached. Each level of branching in the lungs is termed a *generation*. The terminal bronchioles occur at about the 16th generation in humans (West, 1999) and constitute the most distal part of the conducting airways (CA), which begin at the nasal and oral cavities.

The terminal bronchioles divide into respiratory bronchioles, which have alveoli budding from their walls, and which form a transition to the respiratory region of the lungs. After two or three generations, the respiratory bronchioles branch into alveolar ducts, which are conduits whose walls are completely covered by alveoli. The respiratory region ends with the alveolar sacs, blind-ended airspaces that are completely composed of alveoli, which are cluster-like outcroppings that are the main site of gas exchange between the lungs and the blood. The portion of the lungs containing the respiratory bronchioles, alveolar ducts, and alveolar sacs makes up the respiratory region, which spans generations 17 to 23 in people (West, 1999).

The different regions of respiratory tract can also be grouped in another manner into the upper airways (UA), comprised of all sections between and including the nasal and oral cavities and the larynx, and the lower respiratory tract (LRT), consisting of all other regions of the respiratory tract. The LRT can also be further regarded as composed of the tracheobronchial tree (trachea to non-respiratory bronchioles) and the respiratory region.

A comparison of the respiratory tracts of various species reveals several differences, one of which is the mode of branching. Two major types of airway branching can be found in mammals – dichotomous and monopodial branching. In dichotomously branching systems, an airway segment divides into two daughter branches, whereas in monopodial branching, lateral branches are given off from a main axial stem. Airway branching in humans is essentially dichotomous (Hofmann *et al.*, 1989), while branching is monopodial in most laboratory animals used in O_3 exposure studies (Kott *et al.*, 2002; Heyder and Takenaka, 1996; Boyden, 1976). Another difference in respiratory tract anatomy among species is that although respiratory bronchioles are found in humans and dogs, they are either very short or not present at all in rodents. These and other differences in respiratory tract anatomy must be taken into account in performing animal to human exposure-response extrapolation.

2.2 RESPIRATORY TRACT LINING FLUID (RTLF)

Before inhaled O_3 can reach respiratory tract epithelial tissue, it must first pass through the respiratory tract lining fluid (RTLF), a heterogeneous thin film lining the air passages from the nasal cavity to the alveoli. As depicted in Figure **2-2**, the RTLF in the conducting airways consists of two layers – the sol or hypophase layer, which is a watery fluid bathing the cilia that protrude from the ciliated cells of the epithelium, and the gel-like epiphase, a mat-like mucous layer overlaying the hypophase (Hatch, 1992; Kimbell and Miller, 1999). The beating of the cilia transports mucus proximally in the tracheobronchial airways toward the epiglottis where the mucus is swallowed (Hatch, 1992; Kimbell and Miller, 1999; Miller *et al.*, 1993). The pulmonary airspaces, on the other hand, are lined by a surfactant layer (Miller *et al.*, 1993). The RTLF varies in thickness along the respiratory tract, with thicknesses in humans reported to range from 1 – 10 μm in the conducting airways to 0.2 – 0.5 μm in the distal bronchoalveolar region (Mudway and Kelly, 2000; Cross *et al.*, 1994), where it may occur in patches (Pryor, 1992).

Not only does the RTLF act as a diffusion barrier that protects the underlying epithelium, but paradoxically, it also contains many O_3-reactive substrates that cause it to act as a sink for O_3, further enhancing O_3 absorption from inspired air beyond that which would occur due only to dissolution in the RTLF. This process has been termed "reactive-absorption" by Postlethwait et al. (1994). In the RTLF, O_3 reacts with several classes of biomolecules, some of which are:

- **Low molecular weight antioxidants** such as uric acid (UA), ascorbic acid or vitamin C (AH_2), α-tocopherol (vitamin E), and reduced glutathione (GSH), which are thought to act as sacrificial antioxidants that detoxify O_3 (van der Vliet and Cross, 2001; Cross *et al.*, 1994). However, AH_2 and GSH have also been reported to promote O_3 injury, depending on their concentrations (Ballinger *et al.*, 2005).
- **Lipids**: O_3 reacts with unsaturated fatty acids (UFA) in the RTLF to yields lipid ozonation products which initiate a cascade of reactions and processes that lead to O_3 toxicity (Pryor *et al.*, 1995).
- **Proteins**, e.g. albumin, transferrin, cerruloplasmin, and antioxidant protein enzymes like catalase, superoxide dismutase, glutathione reductase, and glutathione peroxidase (Cross *et al.*, 1994), which are also thought to act as sacrificial antioxidants (Davis and Pacht, 1991).
- **High molecular weight glycoconjugates**, which include mucous glucoproteins such as mucins. These compounds may also act as sacrificial antioxidants, scavenging hydroxyl radicals (Hatch, 1992; Cross *et al.*, 1994).

The RTLF also varies in composition along the respiratory tract, as evident from Table **2-1**. Furthermore, RTLF thicknesses and composition vary among species (Cross *et al.*, 1994; Kimbell and Miller, 1999; Slade *et al.*, 1993). Since most estimates of RTLF constituent concentrations are obtained from nasal and bronchoalveolar lavage (NL and BAL), i.e, nasal and lung washings, the actual concentrations of RTLF constituents are uncertain because the amount of dilution from these procedures is unclear. Nevertheless, the concentrations of urea in NL and BAL and in plasma have been used to estimate dilution factors (van der Vliet et al., 1999; Santiago, 2001).

Table **2-1**: RTLF substrate concentrations (μM) along the respiratory tract.

	Nasal RTLF	Proximal RTLF	Distal RTLF
Ascorbic acid	10 – 50	20 – 45	10 – 35
Uric acid	100 – 400	100 – 300	150 – 330
Glutathione	5 – 10	50 – 200	70 - 225
a-tocopherol	< 0.005	0.05 – 0.45	0.1 – 0.5
Albumin-SH[†]	10	No data	70

Source: Mudway and Kelly, 2000, except [†]: Source: Cross *et al.*, 1994.

The reaction kinetics and reaction rates constants of RTLF constituents with O_3 are also not definitively known. Table **2-2** summarizes reaction rate constants of RTLF constituents with O_3 that have been reported in the literature. It is important to note that different researchers obtained these values using different experimental set ups. Although there is not unanimous agreement regarding the reactivity of RTLF substrates with O_3, several studies have reported the following hierarchy: $UA \approx$ or $> AH_2 >> GSH$ (Mudway and Kelly, 1998; Kelly *et al.*, 1996; Kermani *et al.*, 2006). Some other researchers also investigated additional substrates and reported the following hierarchies: $AH_2 \approx UA > BSA > GSH \approx$ egg PC (Postlethwait et. al., 1998; BSA stands for bovine serum albumin, and egg PC, used to model UFAs, stands for egg phosphatidylcholine) and $AH_2 \approx UA > \text{protein thiols} \gg \alpha\text{-tocopherol}$ (Cross and Halliwell, 1994).

Table **2-2**: Reported reaction rate constants of selected RTLF constituents with O_3. UA: uric acid; AH_2: ascorbic acid; GSH: reduced glutathione.

UA	5.8×10^4 M^{-1}s^{-1}	1.18×10^4 M^{-1}s^{-1}	—	1.4×10^6 M^{-1}s^{-1}	—
AH_2	5.5×10^4 M^{-1}s^{-1}	1.36×10^4 M^{-1}s^{-1}	4.8×10^7 M^{-1}s^{-1}	6.0×10^7 M^{-1}s^{-1}	—
GSH	57.5 M$^{-0.75}$s^{-1}	4.94 M$^{-0.75}$s^{-1}	2.5×10^6 M^{-1}s^{-1}	—	7.0×10^8 M^{-1}s^{-1}
Reference	Kermani *et al.* (2006)	Mudway and Kelly (1998)	Kanofsky and Sima (1995)	Gimalva *et al.* (1985)	Pryor *et al.* (1984)
O_3 concentration (ppm)	3	0.1 – 1.5	20 – 40	Extremely high	Extremely high
Antioxidant concentration (μM)	50 – 200	200 – 400	5000 – 100,000	Not given	Not given
Reactor Type	Stirred liquid contacted with ozonated air distributed with sintered glass diffuser	1 ml multi-well plates in a 5.6 L chamber on an orbital shaker with 3 L min^{-1} flow of ozonated air	Stagnant liquid contacted with ozonated air through an impinging jet	Liquid-liquid reaction in stopped-flow apparatus	Liquid-liquid reaction in stopped-flow apparatus

Source: Reproduced from Kermani *et al.* (2006).

2.3 FACTORS INFULUENCING O_3 UPTAKE

2.3.1 Respiratory Tract Structure

The structure of the airways varies along a single respiratory tract, between individual organisms of the same species, and among species. Differences can exist with respect to the mode of branching, branching angles, and length-to-diameter ratios of airway branches. All these features affect airflow patterns, which in turn affect the distribution of O_3 absorption. For example, using computational fluid dynamics simulations, Kimbell and colleagues (2001) demonstrated differences in airflow patterns in the rat, monkey, and human nasal passages as well as differences in local flux distributions of inhaled formaldehyde. One would also expect differences in LRT geometry to impact respiratory airflow patterns and O_3 uptake as well.

2.3.2 Ventilation

Variations in the route of breathing (nasal vs. oral) and breathing frequency can also lead to differences in O_3 uptake. Gerrity and fellow researchers (1988) and Kabel and colleagues (1994) found differences in the fraction of O_3 absorbed by the nose and the mouth. The former group observed a slight but statistically significant increase in O_3 uptake during oral breathing compared with nasal breathing, whereas the latter group determined the percentage of inhaled O_3 absorbed by the nose and mouth to be about 80% and 50%, respectively.

Several studies have also investigated the effects of respiratory flow rate on O_3 absorption. Hu and coworkers (1994) found that an increase in respiratory flow rate led to a distal shift of the longitudinal distribution of O_3 absorption along the respiratory tract. In studies carried out in isolated rat lungs, Postlethwait and fellow researchers (1994) found that at a fixed tidal volume, O_3 absorption efficiency (i.e., absorbed fraction) was reduced when the ventilation frequency was increased, a change equivalent to increasing the respiratory flow rate. Mathematical models have also predicted a large increase in the total amount of O_3 absorbed (a quantity different from absorbed fraction or absorbed efficiency) during heavy exercise conditions (higher frequency and respiratory flow rate) compared to that during resting breathing (Miller et *al.*, 1985). Turbulence generated by the laryngeal jet should also persist further into the LRT at increased breathing flow rates such as those during exercise conditions, probably enhancing O_3 uptake as a result of increased mixing.

2.3.3 Physical Properties of the RTLF

The physical properties of the RTLF include RTLF thickness and the solubility and diffusivity of O_3 in the RTLF. Increasing the RTLF thickness increases the diffusion distance O_3 travels through the RTLF to reach the tissue surface.

The solubility of any molecule in a medium can be expressed in terms of a partition coefficient $\alpha_{i,j}$, which is the ratio of the equilibrium concentration of the molecule in question in the layer constituting phase *i* to that in the layer constituting phase *j*. The solubility of O_3 will affect the amount of O_3 that can dissolve in the RTLF.

For the purposes of O_3 reaction modeling, the mucus layer can be considered to be stagnant, rendering convection negligible (Schlosser, 1999). Therefore, the flux of O_3 into the RTLF can be calculated from Fick's law, which states that the diffusive flux $J^*_{O_3}$ of O_3 into the RTLF from the gas phase is

$$J^*_{O_3} = -D_l \left(\nabla^* c_l^* \bullet \mathbf{n} \right) \Big|_{\mathrm{i}} \tag{2.1}$$

where D_l is the diffusivity of O_3 in the RTLF and $\left(\nabla^* c_l^* \bullet \mathbf{n} \right) \Big|_{\mathrm{i}}$ is the interfacial O_3 concentration gradient normal to the gas-RTLF interface. Hence, the diffusivity of O_3 in the RTLF will affect the flux of O_3 into that compartment.

2.3.4 Chemical Composition of the RTLF

The concentration of a RTLF substrate can vary considerably among individuals of the same animal species. For example, in a study conducted by Schock *et al.* (2004), the concentration of AH_2 in the NL of human subjects ranged from 0.18 to 4.66 μm. In fact, in a study conducted by Kelly *et al.* (1996), AH_2 was detected in the BAL of only 2 out of 16 subjects. The chemical composition of RTLF is also different in different species (Slade, 1993; Cross *et al.*, 1994). Differences in RTLF chemical composition will impact the reactive-absorption of O_3 in the respiratory tract by affecting the reaction rate of O_3 with reactive substrates.

2.4 MATHEMATICAL DOSIMETRY MODELS

Because experimentally determining O_3 dosimetry in the respiratory tract is difficult, researchers have frequently relied on mathematical models that predict O_3 dose distribution based on the theories of mass transport. Most models used to predict LRT dosimetry have been one-dimensional single-path models (SPMs). There are two kinds of SPMs. In the first type, each airway branch is modeled as a right circular cylinder (Miller *et al.*, 1978; Miller *et al.*, 1985; Overton *et al.*, 1987; Overton and Graham, 1995). In the second kind of SPM, each generation is modeled as a single cylindrical pathway, the cross-sectional area of which is equal to the summed cross-sectional area of all the branches in that generation, and each pathway is connected to the next by means of a short transition region to accommodate the increase in cross-sectional area. This type of SPM has been employed by Hu *et al*. (1992) and Bush *et al*. (1996) and necessarily assumes a symmetrical tracheobronchial tree such that all branches in the same generation are equivalent. One-dimensional SPMs (Miller *et al.*, 1978; Miller *et al.*, 1985; Overton *et al.*, 1987; Hu *et al.*, 1992) predict that the tissue in the distal portion of the respiratory tract receives the highest dose of molecular O_3, consistent with injury patterns observed in lab animals.

In spite of the successes of one-dimensional SPMs, they suffer from at least two main weaknesses. Firstly, being one-dimensional models, they use radially averaged velocities and concentrations. Consequently, they have to make use of dispersion coefficients to account for coupled diffusion and convection of O_3 in the gas phase and mass transfer coefficients to account for boundary layer resistance at the gas-RTLF interfaces. These coefficients are often empirically determined and depend on the geometry of the system. This problem has been overcome by two-dimensional axisymmetric SPMs (Grotberg *et al.*, 1990; Madasu *et al.*, 2006). However these models still suffer from the second limitation of SPMs, which is the reduction of the structure of the LRT to a series of cylinders, whereas the LRT is in reality a branching network. Experimental studies (Caro *et al.*, 2002; Schreck, 1972; Fresconi *et al.*, 2003; Farag *et al.*, 2000) and numerical simulations (Martonen *et al.*, 2001a, b, c; Zhang *et al.*, 2002) of flow in bifurcations reveal several flow features such as skewed velocity distributions, vortices, and flow separation, features that cannot be captured by modeling the LRT as a series of straight tubes and which are certain to affect the local flux distribution of O_3.

Both shortcomings can be overcome by using three-dimensional computational fluid dynamics (CFD) to predict the local O_3 dose distributions by solving the three-dimensional forms of the governing equations. Three-dimensional CFD has already been used extensively to study air flow (Martonen *et al.*, 2001a, b, c; Zhang *et al.*, 2002; Calay *et al.*, 2002) and particle deposition (Zhang *et al.*, 2000; Nowak *et al.*, 2003; Robinson *et al.*, 2006; Balásházy *et al.*, 2003a, Balásházy *et al.*, 2003b) in LRT airway models. However, to the author's knowledge, the only three-dimensional CFD reactive gas dosimetry studies have been carried out by Kimbell's group (Kimbell *et al.*, 1993; Hubal *et al.*, 1996; Kepler *et al.*, 1998; Kimbell *et al.*, 2001; Moulin *et al.*, 2002), who used CFD to predict the flux distributions of gaseous toxicants like hydrogen sulfide, formaldehyde, and O_3 in the nose. Using 3D CFD on anatomically accurate reconstructions of the nasal passages of rats, Moulin and colleagues (2002) were able to predict with reasonable accuracy the locations of lesions caused by hydrogen sulfide inhalation. In light of these positive results, this thesis will explore the use of three-dimensional CFD to study O_3 uptake distribution in airway models representing portions of the LRT.

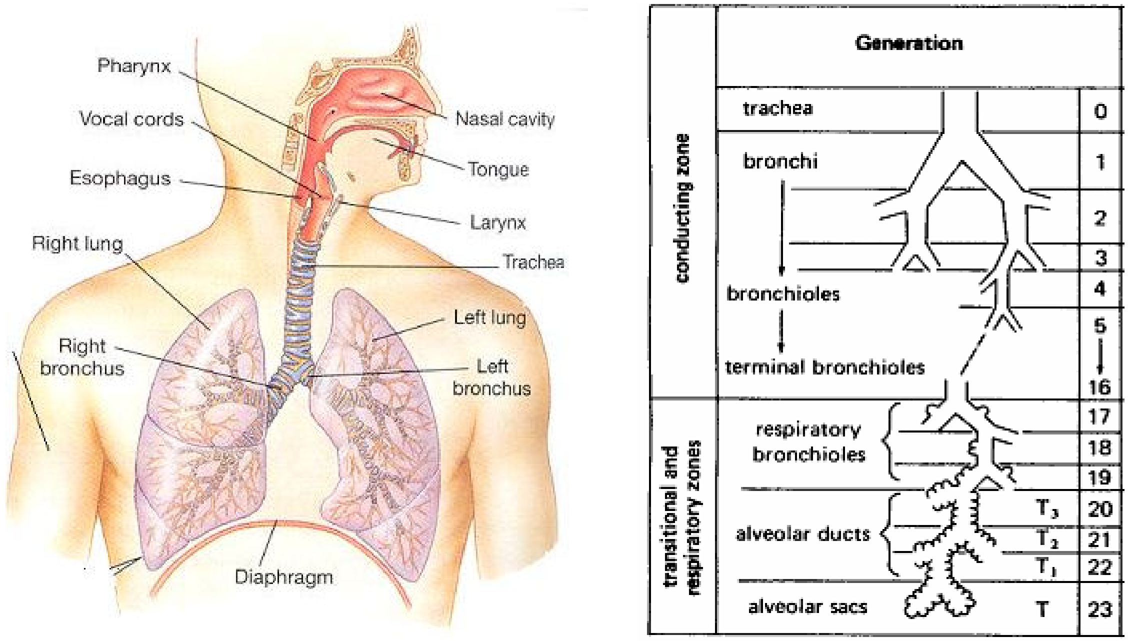
Pharynx
Vocal cords
Esophagus
Right lung
Right bronchus
Nasal cavity
Tongue
Larynx
Trachea
Left lung
Left bronchus
Diaphragm
Generation
conducting zone
trachea
bronchi
bronchioles
terminal bronchioles
transitional and respiratory zones
respiratory bronchioles
alveolar ducts
alveolar sacs
T_3
T_2
T_1
T
0
1
2
3
4
5
16
17
18
19
20
21
22
23

(a) **(b)**

Figure **2-1**: (a) The human respiratory system. Source: Silverthorn, 2001. (b) Airway branching. Source: West, 1999.

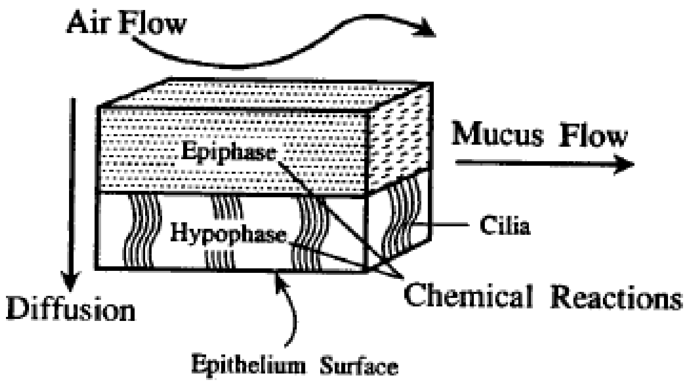
Air Flow
Mucus Flow
Epiphase
Hypophase
Cilia
Diffusion
Chemical Reactions
Epithelium Surface

Figure **2-2**: A schematic of the respiratory tract lining fluid. Source: Miller *et al*., 1993.

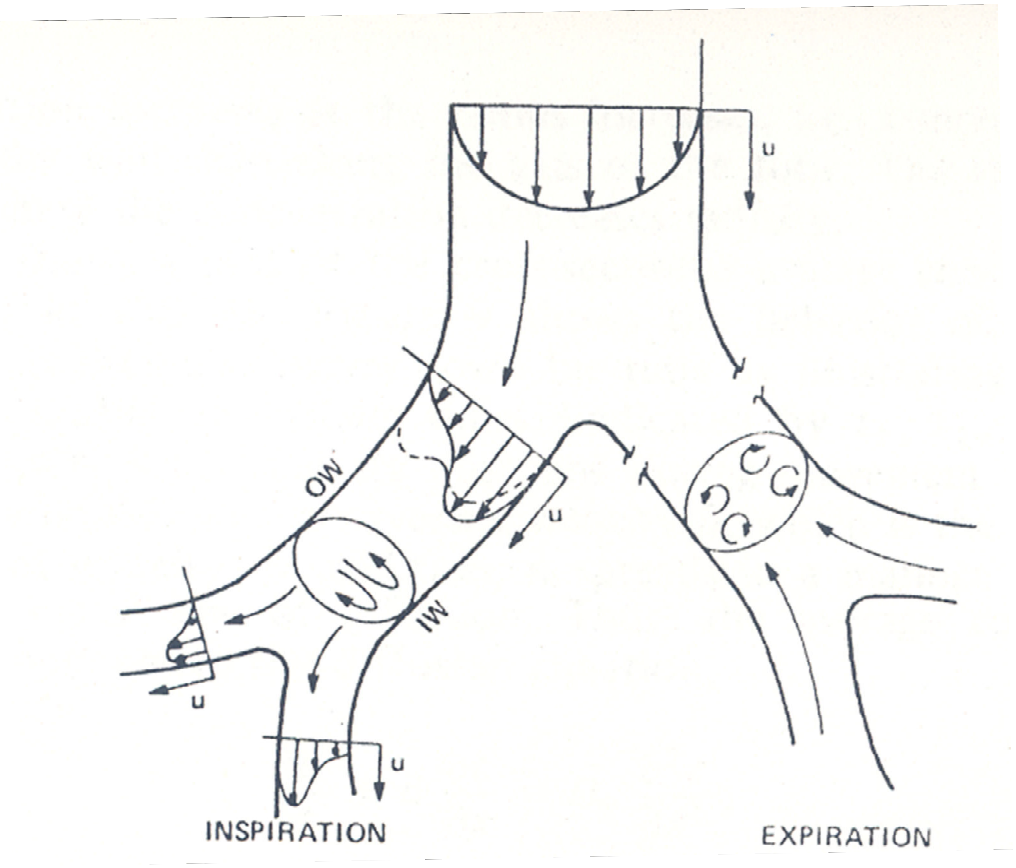
u
OW
u
IW
u
u
INSPIRATION
EXPIRATION

Figure **2-3**: Airflow patterns in bifurcations during inspiration and expiration. IW: inner wall; OW: outer wall, u: velocity. Source: Overton, 1984.

Chapter 3

CONSTRUCTION OF IDEALIZED AIRWAYS AND PROBLEM FORMULATION

The prediction of three dimensional dose distributions of O_3 using computational fluid dynamics (CFD) requires the construction of representative airway geometries and the solution of the equations governing continuity, momentum transport, and mass transport in three-dimensional form. This chapter will describe in detail the construction and meshing of the idealized single airway bifurcations used to study the effects of flow rate, airway geometry, and RTLF reaction parameters on O_3 uptake; the governing equations and boundary conditions used in the CFD simulations; and the implementation of the numerical solution in FLUENT (ANSYS Inc., Lebanon, NH), the commercial CFD package used for the simulations.

3.1 BIFURCATION GEOMETRIES

Two types of airway geometry were considered in the studies using idealized airway bifurcations – dichotomous and monopodial. The idealized dichotomous geometries used were single airway bifurcations consisting of one parent branch and two identical daughter branches with total branching angles of 45°, 90°, and 135° (Figure **3-1**). The branching angle is defined as the angle formed by the intersection of the daughter branch axes. The symmetric bifurcations can be considered to consist of three different regions: the parent branch, the daughter branches, and the transition region. The parent branch divides into two smaller daughter branches, defined as the completely tubular portions of the branched part of the geometry. The two daughter branches join at the carina, and the region containing the carina that connects the parent branch to the daughter branches is termed the transition region (Figure **3-1**). Relative to the radius of the parent branch, the lengths of the parent and daughter branches were 6.0 and 3.5, respectively, and the radii of each of the daughter branches was 0.7. This resulted in length-to-diameter ratios of 3.0 and 2.5 for the parent and daughter branches, respectively.

The idealized monopodial geometry was a single bifurcation consisting of a main stem and a smaller lateral offshoot branch, referred to as the minor daughter branch (Figure **3-2**). The parent branch is the portion of the main stem that extends from the top of the geometry to the highest point of the minor daughter branch, while the major daughter branch is considered to be that portion extending from the lowest point of the minor daughter branch to the bottom of the main stem. Connecting the three aforementioned regions is the transition zone. The parent and major daughter branches are of equal radius and length. Relative to the parent branch radius, the parent and major daughter branches both had a length of 6.0, and the length and radius of the minor daughter branch were 3.2 and 0.7, respectively. Hence, the length-to-diameter ratios of the parent, major daughter, and minor daughter branches were 3.0, 3.0, and 2.29, respectively.

The bifurcation geometries were constructed using standard operations in the commercial meshing software GAMBIT (ANSYS Inc., Lebanon, NH). Each branch was modeled as a right circular cylinder. In the symmetric bifurcation, the parent branch cylinder gave rise to two daughter branch cylinders of smaller diameter. Since direct connection of these three cylinders would lead to discontinuities in the resulting surface of the branching region, a transition region was used to connect the cylindrical portion constituting each daughter branch to the parent branch cylinder. Because of the different branching angles, the resulting transition regions in each bifurcation possessed different surface areas. Furthermore, in constructing the 45° geometry, it was necessary to attach as part of the parent branch a small tapered tubular portion that was connected to the transition region. This resulted in a parent branch with a slightly smaller surface area than those of the 90° and 135° bifurcations, both of which had identical parent branch surface areas. Similarly, the construction of the 90° and 135° bifurcations required the attachment of slightly tapering tubular portions (similar to conical frustums) to the proximal ends of the right cylinders comprising the major portions of the daughter branches. A part of each attachment lay in the transition region and the other in the daughter branch region, and these additions resulted in angles at the carina that were slightly smaller than the branching angles. The surface areas of all bifurcation geometries are summarized in Table **3-1**.

Table **3-1**: Dimensionless surface areas of different regions of the bifurcation geometries

	SYMMETRIC			**MONOPODIAL**
	45°	90°	135°	90°
Parent	37.62	37.70	37.70	37.70
Transition	5.88	2.37	5.13	7.14
Minor/Symmetric Daughter	15.39	15.47	15.47	14.67
Major Daughter	–	–	–	37.70
Total	74.28	71.01	73.75	97.21

The resulting bifurcation geometries were meshed in GAMBIT using hexahedral elements. Elements of a uniform dimensionless size of 0.04 (i.e., relative to the parent branch radius) were initially used to generate a coarse mesh. Adaptive mesh refinement was subsequently implemented to improve the mesh quality near the walls and in the branching region where large gradients were present. (See Section **4.1.1**). The meshed structures were exported to the commercial CFD solver FLUENT versions 6.1 and 6.2 (ANSYS Inc., Lebanon, NH) for simulation.

In order to facilitate the presentation of flux in the bifurcation, azimuthal angles and wall coordinates were defined. In the symmetric bifurcations, azimuthal angles ϕ_p and ϕ_d were defined over parent and daughter branch cross-sections, respectively, to allow presentation of the circumferential distributions on the wall at each cross-section. As shown in Figure **3-3**, the plane containing the axes of the parent and daughter branches was represented by $\phi_p = 0^\circ, 180^\circ$ within the parent branch, and by

$\phi_d = 90^\circ, 270^\circ$ within the daughter branches, with both azimuthal angles ϕ_p and ϕ_d increasing in the counterclockwise direction over the labeled cross-sections.

In subsequent chapters, the regions $0^\circ < \phi_d < 180^\circ$ and $180^\circ < \phi_d < 360^\circ$ on the daughter branch walls of the symmetric bifurcations are referred to as the "outer wall" and the "inner wall," respectively, the $\phi_p = 0^\circ, 180^\circ$ plane containing the axes of the parent and daughter branches is referred to as the "bifurcation plane," and the $\phi_p = 90^\circ, 270^\circ$ plane is referred to as the "symmetry plane." In addition, a dimensionless wall coordinate s is defined along the lines $\phi_p = 0^\circ$ on the parent branch wall and $\phi_d = 90^\circ$ on the outer wall of the daughter branch, with $s = 0$ located at the entrance of the parent branch. For the particular bifurcation considered in this study, the wall coordinate achieves a maximum value of $s = 9.5$ at the external end of the daughter branch, while the internal ends of the parent and daughter branches, respectively, are both characterized by $s = 6$.

The azimuthal angles in the monopodial bifurcation are also similarly defined, as shown in Figure **3-4**, with the exception that the azimuthal angles are identical in the parent branch and the major daughter branch. The regions $0^\circ < \phi_d < 180^\circ$ and $180^\circ < \phi_d < 360^\circ$ on the minor daughter branch walls are also referred to as the "outer" and "inner walls," respectively. Unlike in the symmetric bifurcation, the parent wall in the monopodial bifurcation can also be considered to consist of an inner wall and an outer wall. On the walls of the parent and major daughter branches, the half furthest away from the minor daughter branch, i.e., $90^\circ < \phi_p < 270^\circ$, is designated the "outer wall" and the other half, i.e., $0^\circ < \phi_p < 90^\circ$ and $270^\circ < \phi_d < 360^\circ$, the “inner wall.” (Note that $\phi_{p,d} = 0^\circ$ and $\phi_{p,d} = 360^\circ$ coincide.) As in the symmetric bifurcation, the plane containing all branch axes ($\phi_p = 0^\circ, 180^\circ$) is termed the “bifurcation plane.” The $\phi_p = 90^\circ, 270^\circ$ plane containing the axes of the parent and major daughter branches but not the minor daughter branch axis is called the “normal plane.”

3.2 GOVERNING EQUATIONS

In the idealized single airway bifurcations, simulations were carried out assuming steady state flow and mass transport, and separate inspiratory and expiratory flow simulations were performed. Steady incompressible flow of a binary gas mixture of density ρ and constant viscosity μ is governed by the continuity and Navier-Stokes equations given by

$$\nabla^* \bullet \mathbf{u}^* = 0 \qquad \mathbf{3.1}$$

$$\rho \mathbf{u}^* \bullet \nabla^* \mathbf{u}^* = -\nabla^* p^* + \mu \nabla^{*2} \mathbf{u}^* \qquad \mathbf{3.2}$$

where $\mathbf{u}^*$ is the velocity, p^* is the pressure, ∇^* is the gradient operator, and ∇^{*2} is the Laplace operator. For the simulations in idealized single bifurcations, $\mathbf{u}^*$ was made dimensionless by the average axial velocity $V_0 \equiv Q_0 / \pi R_0^2$ (where Q_0 is the volumetric flow rate through the parent branch of radius R_0), all lengths were made dimensionless by R_0, and the pressure was made dimensionless by ρV_0^2, yielding the following dimensionless continuity and Navier-Stokes equations:

$$\nabla \bullet \mathbf{u} = 0 \qquad \mathbf{3.3}$$

$$\mathbf{u} \bullet \nabla \mathbf{u} = -\nabla p + \frac{1}{Re} \nabla^2 \mathbf{u} \qquad \mathbf{3.4}$$

where the absence of an asterisk indicates a dimensionless variable, and $Re = V_0 \, R_0 \, \rho / \mu$ is the Reynolds number (based on the *parent branch radius* and average velocity). Table **3-2** lists the boundary conditions applied to the continuity and Navier-Stokes equations.

Table **3-2**: Dimensional and dimensionless forms of the boundary conditions on the continuity and Navier-Stokes equations. **n** is the unit vector normal to the boundary; A^* and A are the dimensional and dimensionless surface areas, respectively, of the boundaries. All other variables are defined in the text.

	INSPIRATION	**EXPIRATION**
Bifurcation walls	$\mathbf{u}^* = \mathbf{u} = \mathbf{0}$	$\mathbf{u}^* = \mathbf{u} = \mathbf{0}$
Proximal end of parent branch	$\mathbf{u}^* \bullet \mathbf{n} = V_0; \quad \mathbf{u} \bullet \mathbf{n} = 1$ $\mathbf{u}^* \times \mathbf{n} = \mathbf{u} \times \mathbf{n} = \mathbf{0}$	$\mathbf{n} \bullet \nabla \mathbf{u}^* \bullet \mathbf{n} = \mathbf{n} \bullet \nabla \mathbf{u} \bullet \mathbf{n} = 0$ $\frac{1}{A^*} \int_{A^*} \mathbf{u}^* \bullet \mathbf{n} \, dA^* = V_0; \quad \frac{1}{A} \int_A \mathbf{u} \bullet \mathbf{n} \, dA = 1$
Distal end of daughter branch	$\mathbf{n} \bullet \nabla \mathbf{u}^* \bullet \mathbf{n} = \mathbf{n} \bullet \nabla \mathbf{u} \bullet \mathbf{n} = 0$ $\frac{1}{A^*} \int_{A^*} \mathbf{u}^* \bullet \mathbf{n} \, dA^* = \frac{V_0}{2\kappa}; \frac{1}{A} \int_A \mathbf{u} \bullet \mathbf{n} \, dA = \frac{1}{2\kappa}$	$\mathbf{u}^* \bullet \mathbf{n} = \frac{V_0}{2\kappa}; \quad \mathbf{u} \bullet \mathbf{n} = \frac{1}{2\kappa}$ $\mathbf{u}^* \times \mathbf{n} = \mathbf{u} \times \mathbf{n} = \mathbf{0}$

The no-slip condition was imposed at the bifurcation walls, i.e., the gas-RTLF interface. At the proximal end of the parent branch, zero radial velocity and uniform velocity V_0 normal to the inflow plane (corresponding to a volumetric flow rate Q_0) were imposed during inspiration, and zero normal viscous stress and average normal velocity V_0 were imposed at the same boundary during expiration. At the distal ends of the daughter branches, zero viscous normal stress and average normal velocity $V_0/2\kappa^2$ at the outflow planes (corresponding to a volumetric flow rate $Q_0/2$) were imposed during inspiration, where κ is the dimensionless radius of the daughter branch, and zero radial velocity and uniform velocity $V_0/2\kappa^2$ normal to the same boundaries were imposed during expiration. This assumes an equal flow split between the two daughter branches during both inspiration and expiration.

For dilute gas mixtures with constant ρ and gas phase diffusivity D_g, the steady-state O_3 concentration in the mixture is governed by the convection-diffusion equation:

$$\mathbf{u}^* \bullet \nabla^* c^* = D_g \nabla^{*2} c^* \qquad \mathbf{3.5}$$

where c^* is the gas-phase O_3 concentration. In the idealized bifurcations, c^* was made dimensionless with the inlet concentration c_0, and the other variables were made dimensionless as previously described to yield the dimensionless convection-diffusion equation:

$$\mathbf{u} \bullet \nabla c = \frac{1}{Pe} \nabla^2 c \qquad \mathbf{3.6}$$

where c is the dimensionless gas-phase concentration, $Pe = Re\,Sc$ is the parent branch radius-based Peclet number, and $Sc \equiv \mu/\rho D_g$ is the Schmidt number. Based on values of $\rho = 1.14\times10^{-3}$ g/cm^3 (Geankoplis, 1993), $\mu = 1.9\times10^{-4}$ g cm^{-1}s^{-1} (Geankoplis, 1993) and

$D_g = 0.195$ cm^2/s (Bush et al., 1996), a value of $Sc = 0.85$ was calculated for the O_3-air mixture. The convection-diffusion equation was solved subject to the boundary conditions listed in Table **3-3**.

Table **3-3**: Dimensional and dimensionless forms of the boundary conditions on the convection-diffusion equation. **n** is the unit vector normal to the boundary. All other variables are defined in the text.

	INSPIRATION	**EXPIRATION**
Bifurcation walls	$c^* = c = 0$ OR $-(\mathbf{n} \bullet \nabla c) = K\, c_{gi}$	$c^* = c = 0$
Proximal end of parent branch	$c^* = c_0; \quad c = 1$	$\mathbf{n} \bullet \nabla c = 0$
Distal end of daughter branch	$\mathbf{n} \bullet \nabla c = 0$	$c^* = c_0; \quad c = 1$

At the walls of the bifurcation, zero O_3 concentration (corresponding to an infinitely fast reaction in the RTLF) or a specified flux Kc_{gi} at the gas-RTLF interface (corresponding to a finite pseudo-first order reaction between O_3 and O_3-reactive substrates in the RTLF) was imposed, where c_{gi} is the gas-phase concentration at the gas-RTLF interface scaled by the inlet O_3 concentration c_0, and K is a mass transfer parameter derived in Section **7.1**. At the proximal end of the parent branch, a uniform O_3 concentration c_0 was imposed during inspiration, and a zero normal concentration gradient was imposed during expiration. At the distal ends of the daughter branches, a zero normal concentration gradient was imposed during inspiration and a uniform O_3 concentration c_0 during expiration.

One of the aims of the research presented in this thesis is to determine the local distribution of O_3 absorption in the respiratory tract. This necessitates the calculation of the flux of O_3 into the RTLF, which is given by

$$N^* = -D_g \left(\mathbf{n} \bullet \nabla^* c^*\right)_{wall} \qquad \textbf{3.7}$$

or in dimensionless form as

$$N = -\left(\mathbf{n} \bullet \nabla c\right)_{wall} \qquad \textbf{3.8}$$

where $\mathbf{n}$ is the outward normal unit vector, and the dimensionless flux N is related to the dimensional flux N^* by the equation

$$N^* = \frac{D_g\, c_0}{R_0} N\,. \qquad \textbf{3.9}$$

3.3 IMPLEMENTATION IN FLUENT

The commercial CFD solver FLUENT (versions 6.1 and 6.2, ANSYS Inc., Lebanon, NH) was used to solve the three-dimensional form of the governing equations. FLUENT uses the finite volume method to solve the integral forms of the conservation equations. In the finite volume method, the flow domain is partitioned into a set of control volumes or elements, and the transport equations are integrated about each control volume, yielding a set of algebraic equations. The resulting discretized equations are then solved numerically using a matrix solution algorithm. For a more detailed description of the numerical solution procedure, see Appendix B.

In order to implement a non-dimensionalized solution of the governing equations, the following substitutions were made for the dimensional parameters required by FLUENT: the FLUENT density was set equal to 1, the FLUENT viscosity to $1/Re$, the FLUENT diffusivity to $1/Pe$, the FLUENT inlet velocity to 1, and the FLUENT inlet concentration to 1. The rationale for these substitutions can be understood by comparing equation **3.2** to equation **3.4** and equation **3.5** to equation **3.6**.

FLUENT solves the following transport equation for steady laminar flow of a binary mixture with constant properties and no chemical reaction (FLUENT 6.2 User's Guide):

$$\mathbf{u}^* \bullet \nabla^* Y_i = D_i \nabla^{*2} Y_i \qquad \textbf{3.10}$$

where Y_i and D_i are the mass fraction and diffusivity, respectively, of species *i*. A comparison between equation **3.10** and equation **3.6** shows a one to one correspondence between Y_i and c. Therefore, upon substituting $1/Pe$ for FLUENT's D_i, and $\mathbf{u}$ for FLUENT's $\mathbf{u}^*$, the mass fraction Y_i in FLUENT is equivalent to the scaled concentration c.

The three-dimensional forms of the governing equations and their corresponding boundary conditions were solved using FLUENT's segregated implicit solver, which solves the governing equations sequentially, in conjunction with the SIMPLE algorithm

(Patankar, 1981), used for pressure-velocity coupling. The flow and species conservation equations could be solved sequentially rather than simultaneously because changes in gas composition due to O_3 transport lead to negligible changes in the density and viscosity of the gas mixture. A second-order accurate flux-limiting upwind scheme was implemented in FLUENT to reduce numerical diffusion while avoiding numerical instabilities in these convection-dominated simulations.

The computations were started by initializing the flow and concentration fields throughout the domain to their respective values at the inflow boundary. Convergence to steady state was achieved when the successive changes in the dimensionless average velocity and O_3 molar flow rate at the outflow boundary did not exceed 5×10^{-5} for at least 50 iterations. At that point, the residuals for the continuity, Navier-Stokes, and convection-diffusion equations were all reduced to less than 10^{-5}. (See Appendix B for the definition of the residuals.) At steady state, the overall mass balance on the entire bifurcation was always satisfied to within a maximum error of 10^{-7}.

User-defined functions written in C were used to compute the flux of O_3 into the RTLF and into lung epithelial tissue, where applicable (see Appendix C).

3.4 DISCUSSION

The symmetric dichotomous bifurcation geometries used in this study had length-to-diameter ratios of 3.0 and 2.5 in the parent and daughter branches, respectively, total branching angles ranging from 45° to 135°, and a sharp carinal ridge. These length-to-diameter ratios are similar to the average value of 3.1 calculated from Weibel's model

(1963) for the conducting airways (excluding the trachea). Horsfield and Cumming (1968) defined the airway segments lengths in a different manner, as the distance between the respective intersections of the axis of the segment in question with its parent branch axis and the axes of its daughter branches. Using this definition leads to the length-to-diameter ratio of 3.0 in both the parent and daughter branches of the 90° symmetric bifurcation and similar ratios in the others. A length-to-diameter ratio of 2.8 for the human conducting airways, excluding the trachea, was inferred from Horsfield and Cumming (1968). Thus the length-to-diameter ratios in our idealized models are comparable to those of both Weibel (1963) and Horsfield and Cumming (1968).

Horsefield *et al*. (1971) have reported the deviation of the daughter branch axis from the parent branch axis in a human respiratory tract to range from 32° to 50° in smaller airways. These angles can be considered to be approximately equivalent to half the branching angle as defined in this study. Raabe *et al*. (1976) compiled respiratory tract data from four mammalian species, and reported total branching angles as small as 30° and as large as 160° in the airways of a human male. Thus the total branching angles of the idealized symmetric bifurcations fall well within these reported ranges. Horsfield *et al*. (1971) have also stated that, in general, the carinal radius of curvature is at most on the order of 10% of the corresponding daughter branch diameter, indicative of a relatively sharp carinal ridge. Therefore, the symmetric dichotomous models described in this chapter are representative of a human conducting airway bifurcation, albeit an idealized one.

While airway branching in humans is essentially dichotomous and relatively symmetric (Hofmann *et al*., 1989), it tends to be monopodial in other mammals such as rodents (Hofmann *et al*., 1989; Kott *et al*., 2002), canines (Heyder and Takenaka, 1996), and non-human primates (Boyden, 1976; Tyler *et al*., 1988), animals often used as human surrogates in inhalation toxicology studies. Raabe *et al*. (1976) obtained respiratory tract data from a female hooded rat specimen. The author's analysis of the major pathway of the right diaphragmatic lobe revealed mainly monopodial branching similar to that of the idealized monopodial bifurcation. The majority of the axes of the major daughter branches in the rat deviated minimally from the axes of their parent branches, and the minor daughter branches exhibited an average deviation of about 73° from the parent branch axis. (Deviations ranged from 20° to 100°.) Raabe *et al*. (1976) defined the length of an airway segment similarly to Horsfield and Cumming (1968), and using their data, an average length-to-diameter ratio of 2.0 was determined for monopodial minor branches along this pathway, close to that of the idealized monopodial minor daughter, which had a ratio of 2.6, based on the definition of airway segment length of Raabe *et al*. (1976). Just as in the idealized geometry, the lengths of parent and major daughter branches in the hooded rat were also comparable, as evidenced by an average parent-to-major daughter length ratio of 1.16.

There were, however, some differences between the idealized monopodial bifurcation and the airway structures reported by Raabe's group. First, whereas the major daughter branch of the idealized bifurcation had a length-to-diameter ratio of 3.0, the length-to-diameter ratios along the major pathway of the hooded rat were generally less than 1, signifying short distances between consecutive branchings. Furthermore, about a third of the time, the rat's major daughter branches were shorter than the minor daughter segments. In spite of these differences, and in light of the many similarities between the idealized monopodial bifurcation and the airways described in Raabe *et al*. (1976), the idealized monopodial geometry can be considered representative of a mammalian monopodial airway, specifically that of a hooded rat, and the airway segment lengths chosen for the idealized monopodial geometry enable a direct comparison of uptake in the dichotomous and monopodial geometries.

Even though it is possible to obtain anatomically-accurate geometries for performing CFD studies, there is great variability in airway branching geometry from generation to generation and from lung to lung, and the use of idealized airway model will enable the elucidation of mechanisms responsible for the dose distribution of O_3.

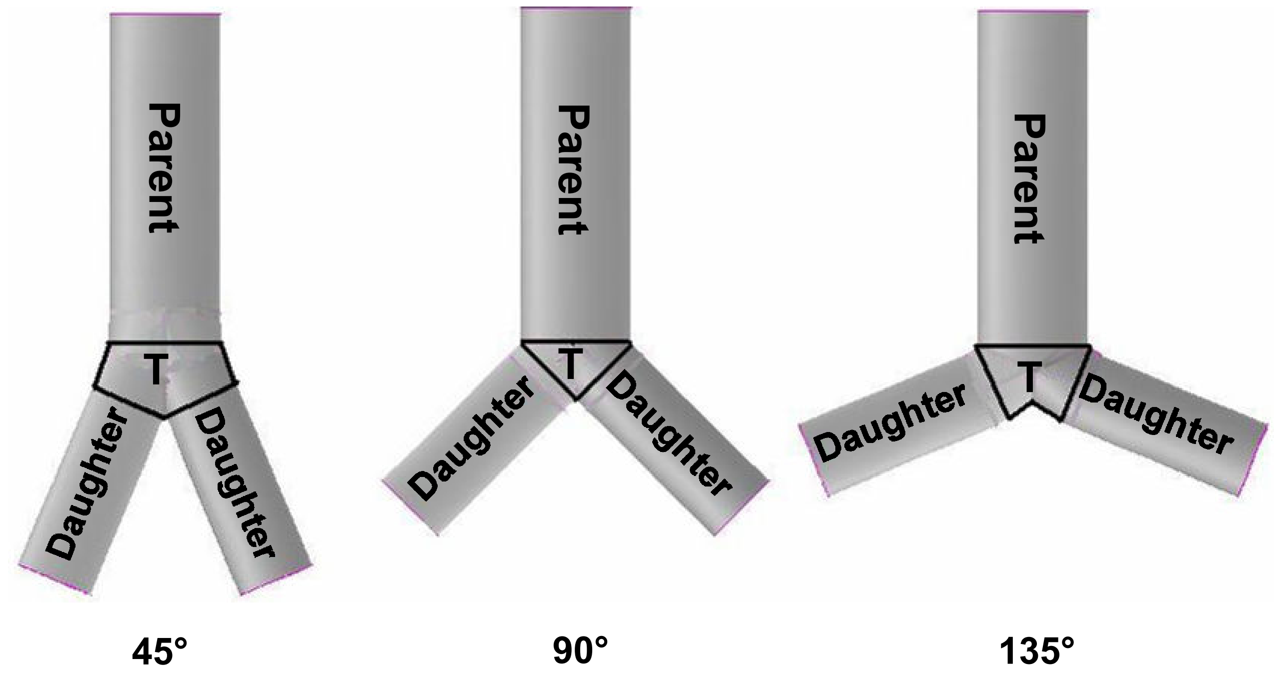
Parent
T
Daughter
Daughter
45°
Parent
T
Daughter
Daughter
90°
Parent
T
Daughter
Daughter
135°

Figure **3-1**: Idealized dichotomous bifurcations. T: transition region

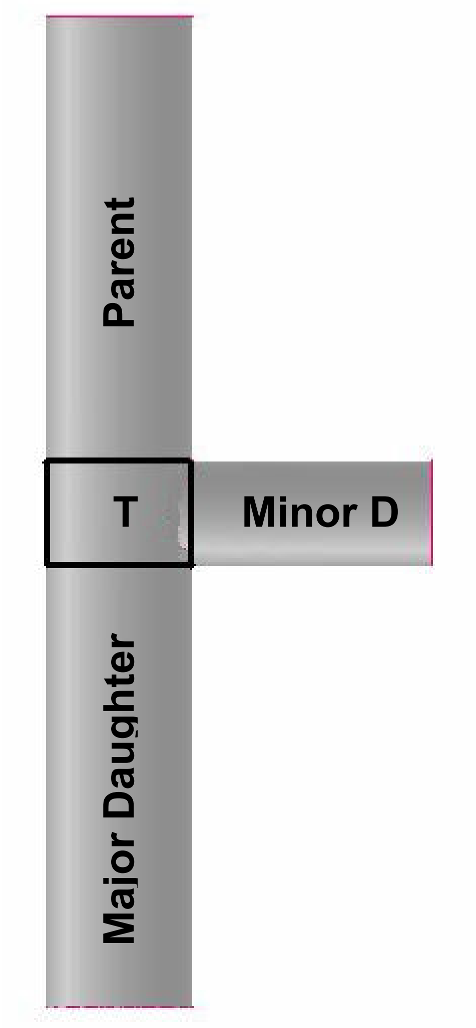
Parent
T
Minor D
Major Daughter

Figure **3-2**: Idealized monopodial bifurcation. T: transition region, Minor D: minor daughter branch.

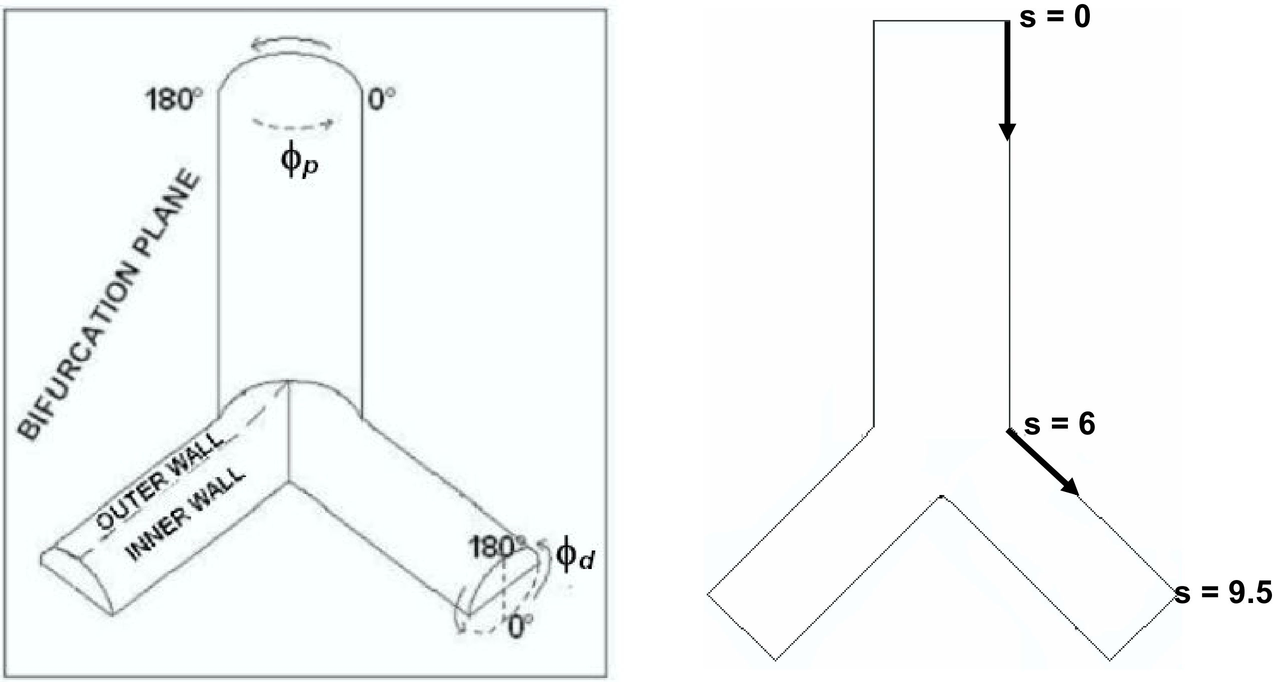
180°
0°
ϕ_p
BIFURCATION PLANE
OUTER WALL
INNER WALL
180°
ϕ_d
0°
s = 0
s = 6
s = 9.5

(a) **(b)**

Figure **3-3**: Schematic definition of (a) azimuthal angles ϕ_p and ϕ_d in the parent and daughter branches, respectively, and (b) wall coordinate s in the symmetric bifurcations.

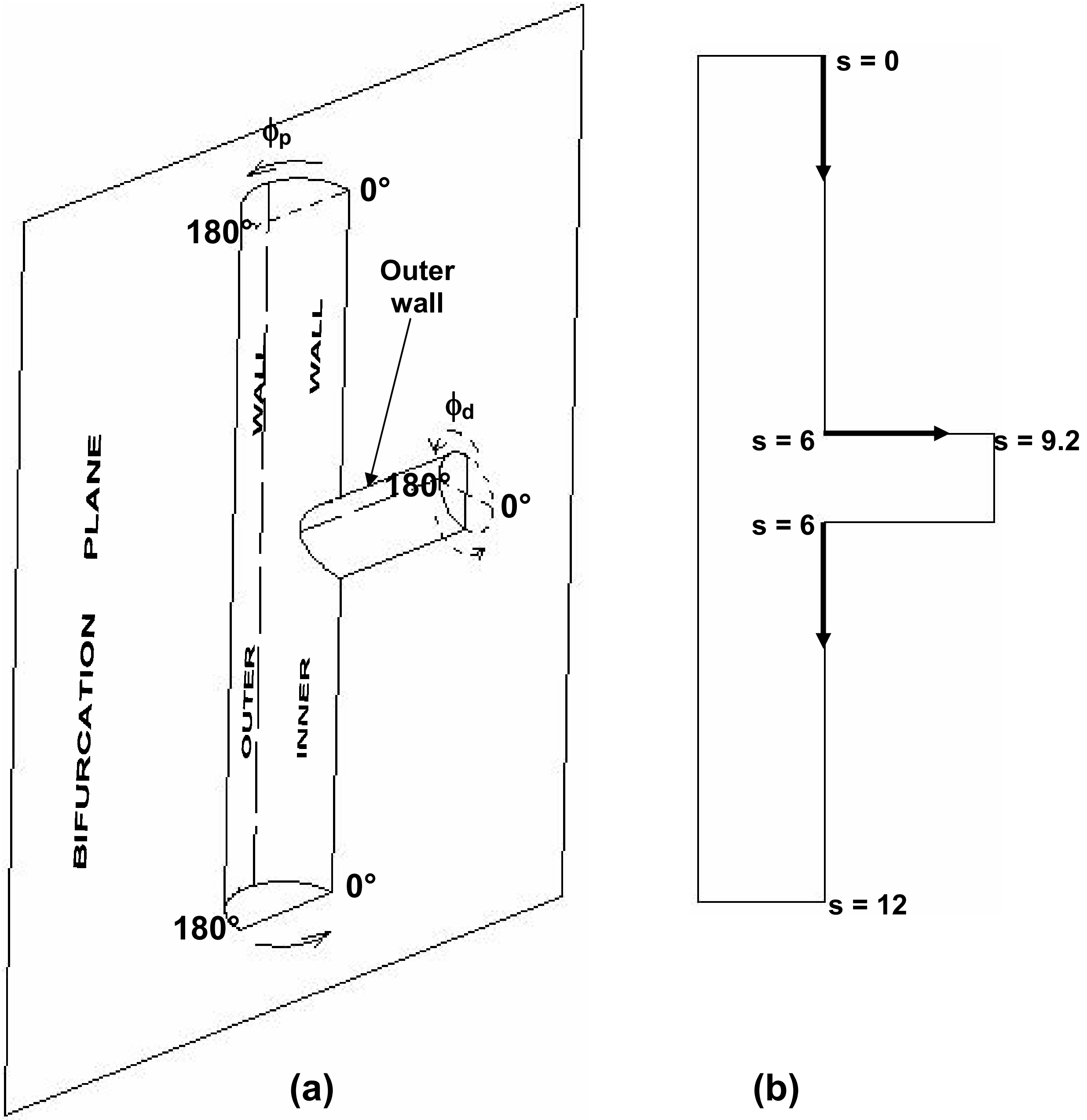
ϕp
0°
180°
Outer
wall
WALL
WALL
ϕd
180°
0°
BIFURCATION PLANE
OUTER
INNER
0°
180°
(a)
s = 0
s = 6
s = 9.2
s = 6
s = 12
(b)

Figure **3-4**: Schematic definition of (a) azimuthal angles ϕ_p and ϕ_d in the parent and daughter branches, respectively, and (b) wall coordinate s in the monopodial bifurcation.

Chapter 4

EFFECT OF FLOW RATE ON OZONE UPTAKE IN A SINGLE IDEALIZED BIFURCATION

Both the dose of O_3 to the respiratory tract and injury caused by exposure to the pollutant have been shown to be dependent on flow conditions as evidenced by experimental studies of O_3 uptake and O_3-induced injury (Alfaro *et al.*, 2004; Joad *et al.*, 2000). The purpose of the current chapter is two-fold: to predict local O_3 flux distributions in the respiratory tract and to determine the effect of flow rate on local uptake and flux distributions. These objectives were accomplished by simulating inspiratory and expiratory flow and O_3 uptake in a single idealized symmetric bifurcation at different flow conditions, assuming O_3 reacts very rapidly when it comes in contact with the respiratory tract lining fluid (RTLF).

4.1 CFD Simulations

Separate simulations for inspiratory and expiratory flows applying the boundary conditions listed in Section **3.2** were conducted in the 90° symmetric bifurcation at Reynolds numbers ranging from 100 to 500 (in increments of 100), all corresponding to laminar flow conditions. Zero O_3 concentration was specified at the bifurcation walls, corresponding to an infinitely fast chemical reaction in the RTLF.

4.1.1 Resolution and Accuracy

In order to ensure that simulation results were independent of mesh size, an adaptive mesh refinement study was carried out. Using the original mesh of $735,296$ uniformly-sized hexahedral elements (Mesh 1), computations were performed for $Re = 500$ which is the highest Reynolds number considered in this study. (Note that this is equivalent to a Reynolds number of 1000 based on the parent branch diameter.) Once a converged steady-state solution was obtained, a curvature-based adaptive grid refinement scheme was implemented in FLUENT (ANSYS Inc., Lebanon, NH) to improve the mesh quality in regions of high velocity gradient. An element was refined if $\left(V_{cell}\right)^{1/3}\left|\nabla^2 u\right| \geq 3$, where V_{cell} is the element volume, and u is the velocity magnitude in the element. The refined mesh (Mesh 2) was composed of $1,093,668$ nonuniform elements. A second level of mesh refinement was then implemented to yield a final mesh (Mesh 3) consisting of $1,397,790$ non-uniform elements. As expected, most of the grid refinement occurred in the vicinity of the walls and in the branching region (Figure **4-1**).

The sensitivity of the numerical predictions to mesh size was examined by comparing the computed O_3 concentration distributions along selected axial and radial paths in a daughter branch for the three levels of mesh refinement (Figure **4-2**). The maximum observed variation between the simulations performed with Mesh 1 and Mesh 2 was about 4%, while the corresponding variation after a second level of refinement from Mesh 2 to Mesh 3 was less than 2%. Hence, a single level of refinement was found to provide adequate resolution, and Mesh 2 was used in subsequent simulations for all values of Reynolds number. Separate but similar adaption procedures were performed for expiratory flow simulations and simulations in the other geometries.

The accuracy of the numerical method was tested by performing computations for steady laminar flow of a reactive gas through a straight tube with the same boundary conditions as those used for the single bifurcation, a problem for which an analytical solution is available. The comparison between numerical predictions and analytical results was made in terms of the local O_3 flux (i.e., the rate of mass transfer per unit area) at the wall, which is the main quantity of interest in this study. In particular, the dimensionless flux determined in the simulations is equivalent to a local Sherwood number Sh:

$$Sh \equiv \left(\frac{N^*}{c_0}\right)\left(\frac{R_0}{D_g}\right) = N \qquad \textbf{4.1}$$

where Sh can be viewed as a local mass transfer coefficient. The analytical expression for Sh for laminar flow of a Newtonian fluid in the entrance region of a tube is given by (Goddard and Acrivos, 1966):

$$Sh = 0.339\, x^{-1/2}\, Re^{1/2}\, Sc^{1/3} \qquad \textbf{4.2}$$

where x is the dimensionless axial position along the tube. This result, based on a thin developing concentration boundary layer and a linearized velocity profile within that boundary layer, is restricted to small values of Sc. Alternatively, an average Sherwood number, $\overline{Sh}$, can be obtained by averaging over a dimensionless length λ of the tube, namely,

$$\overline{Sh} \equiv \frac{1}{\lambda}\int_0^\lambda Sh\,dx = 0.678\lambda^{-1/2}\,Re^{1/2}\,Sc^{1/3}\,. \qquad \textbf{4.3}$$

Numerical simulations were performed to compute the overall dimensionless mass transfer coefficient, $\overline{Sh}$, for flow in a straight tube of dimensionless length $\lambda = 5.5$ at Reynolds numbers ranging from 100 to 500. Numerical predictions of the overall mass transfer coefficient were then regressed with Reynolds number to obtain the following correlation:

$$\overline{Sh} \simeq 0.30\,Re^{0.495}; \quad R^2 = 0.999\,. \qquad \textbf{4.4}$$

This result compares well with the analytical expression given by equation **4.3**, which for $Sc = 0.85$ reduces to equation **4.5:**

$$\overline{Sh} = 0.27\,Re^{0.5}\,. \qquad \textbf{4.5}$$

The maximum error in the computed values of the overall mass transfer coefficient occurred for the largest Reynolds number considered in this study, and was about 5.8%. This error was primarily due to the presence of a singularity in the local mass transfer coefficient at the tube entrance where the thickness of the concentration boundary layer tends to zero. This singularity at $x = 0$ is evident in the analytical expression given by equation **4.2** for the local Sherwood number. The lack of a sufficiently refined mesh to resolve the thin concentration boundary layer near the tube entrance eventually led to errors in the computed fluxes as $x \to 0$. The same source of error was present in numerical simulations of flow through a bifurcation since boundary layer development in the immediate vicinity of the flow inlet in a bifurcation is identical to that in a straight tube.

The size of the entrance region over which the computed fluxes were in error was determined by comparing numerical predictions of the scaled local Sherwood number, $x^{1/2} Sh$, to the analytical prediction given by equation **4.2**. The latter reduced to a value of $0.339\, Re^{1/2}\, Sc^{1/3} = 0.32\, Re^{1/2}$ for all values of x. For the resolution provided by Mesh 2, computed values of the local Sherwood number for all values of Re were in excellent agreement with the analytical results everywhere except in the region $x < 0.35$. The same region of inaccuracy persisted in simulations of flow within a bifurcation since boundary layer development in the entrance region of a bifurcation was independent of downstream branching details. In principle, the size of this region could be reduced by further refining the mesh near the entrance. However, this was not a practical approach because the computational costs of resolving the concentration boundary layer near the entrance became prohibitive as the Reynolds number increased. Instead, we used analytical continuation of the numerical solution into the singular region to obtain a uniformly accurate solution over the entire length of the tube. Namely, we combined the analytical solution for $x \leq 0.35$ with the numerical solution for $x \geq 0.35$ to obtain a composite solution. This composite solution was smooth in the transition region near $x = 0.35$, giving us additional confidence in this approach.

4.2 RESULTS

In order to facilitate the presentation of three-dimensional distributions of concentration and flux in the bifurcation, various cross-sections at different axial locations along the parent and daughter branches were labeled as shown in Figure **4-3**. Note that cross-sections *G* and *H* at the internal ends of the parent and daughter branches, respectively, are both characterized by $s = 6$ since they share the junction between the parent and daughter branch walls.

4.2.1 Flow Field

Contour maps of the magnitude of velocity in the bifurcation plane are presented in Figure **4-4** for both inspiratory and expiratory flow at Reynolds numbers of 100, 300 and 500. For the particular bifurcation considered in this study, neither the parent branch nor the daughter branch was sufficiently long for the flow to become fully developed in the upstream branch at the aforementioned Reynolds numbers. During inspiration, the velocity distribution remained axisymmetric throughout most of the parent branch, but was skewed towards the inner wall within the daughter branches. This is a well-established feature of flow in symmetric bifurcations that has been observed in both experiments (Caro *et al*., 2002; Farag *et al*., 2000) and previous CFD studies (Lui *et al*., 2002; Zhang *et al*., 2002). The maximum velocity in the daughter branches decreased with increasing Reynolds number. This occurred because the velocity profile exiting the parent branch more closely resembled a fully-developed parabolic profile at lower Reynolds numbers for which the momentum boundary layer on the parent branch wall grew faster with axial distance from the inlet. As the flow leaving the parent branch through cross-section *G* impinged on the carina in the branching region, a new boundary layer was formed along the inner wall of each daughter branch. At high Reynolds numbers, flow separation along the outer walls of the daughter branches resulted in areas of backflow. Moreover, at all Reynolds numbers a pair of counter-rotating vortices positioned symmetrically with respect to the bifurcation plane was observed at the outflow boundary of each of the daughter branches (Figure **4-5**). These qualitative features of the flow field are consistent with the observations of Martonen *et al*. (2001a, b) and Zhang *et al*. (2002).

For expiratory flow, the velocity distribution was slightly skewed towards the outer walls of the daughter branches through which flow entered the bifurcation and became more skewed downstream (Figure **4-6**). In contrast to the results obtained for inspiratory flow, the velocity distribution in the parent branch was not axisymmetric during expiration. Fluid elements leaving the daughter branches merged near the upstream end of the parent branch to form a sheet of high-velocity fluid normal to the bifurcation plane in the parent branch. This is evident from the contour maps of the magnitude of velocity shown in Figure **4-7A** for cross-sections *A*-*G* of the parent branch at an expiratory Reynolds number of 500. The maximum dimensionless velocity of the sheet of fast-moving fluid increased as the Reynolds number was reduced, because the flow leaving the daughter branch was more developed at lower Reynolds numbers. Figure **4-7A** also shows that the velocity distribution in the parent branch maintained its symmetry with respect to the two symmetry planes of the bifurcation characterized by $\phi_p = 0^\circ, 180^\circ$ and $\phi_p = 90^\circ, 270^\circ$. Stagnation flows were observed at the carina, near the junction of the daughter and parent branch walls, and on the parent branch wall downstream of the branching region. These stagnation regions were most prominent at the highest Reynolds number considered in the simulations. A quadruple vortex pattern was observed at the outflow boundary of the parent branch (Figure **4-7C**), consistent with the experimental findings of Fresconi *et al*. (2003).

4.2.2 Concentration and Flux Distributions

Contour maps of O_3 concentration in the bifurcation plane are shown in Figure **4-8** for both inspiratory and expiratory flow at Reynolds numbers of 100, 300, and 500. The computed O_3 concentration distributions were qualitatively similar to the corresponding distributions of the magnitude of velocity, as can be seen from a comparison of Figure **4-4** and Figure **4-8**. During inspiration, the concentration distribution was axisymmetric in the parent branch, and skewed towards the inner walls in the daughter branches. The average O_3 concentration in the fluid leaving the bifurcation increased with increasing Reynolds number, as the concentration boundary layer on the parent branch wall became thinner everywhere. The formation and development of new concentration boundary layers on the inner walls of the daughter branches immediately downstream of the carina were also observed (see Figure **4-8**), with the boundary layer thickness decreasing everywhere as the Reynolds number increased.

For expiratory flow, the O_3 concentration distributions in the daughter branches were somewhat skewed towards the outer walls and became more skewed downstream (Figure **4-6**). The convergence of flows from the daughter branches led to the development of a high concentration sheet of fluid in the parent branch normal to the bifurcation plane and symmetric about the $\phi_p = 90^\circ, 270^\circ$ plane. This effect is clearly shown by the contour maps of O_3 concentration in cross-sections *A*-*G* of the parent branch shown in Figure **4-7B** for an expiratory Reynolds number of 500. Comparison of the contour maps in Figure **4-7A** and **4-7**B reveals that the concentration distribution within the parent branch displayed a pattern that was quite similar to the distribution of the magnitude of velocity.

The dimensionless flux of O_3 at the bifurcation wall was computed by implementing a user-defined function in FLUENT based on equation **3.8** (Appendix C). The resulting flux distribution on the bifurcation wall was subsequently integrated over the perimeter of an airway cross-section (at fixed *s*) to compute the circumferentially-averaged dimensionless flux $\overline{N}$:

$$\overline{N}(s) = \frac{1}{2\pi}\int_0^{2\pi} N(s,\ \phi_i)\,d\phi\,; \quad i = p, d\,. \qquad \textbf{4.6}$$

The resulting distribution of the circumferentially-averaged flux along the parent branch and an individual daughter branch is presented in Figure **4-9**. The appearance of large fluxes near the inflow plane (i.e., $s = 0$ during inspiration and $s = 9.5$ during expiration) was due to the singularity described earlier, that is, the O_3 concentration became double-valued at the leading edge of the airway wall as fluid with a uniform concentration profile entered an airway with a zero-concentration wall condition. Since the concentration distribution of the fluid entering a bifurcation in an intact lung will not be uniform, the large fluxes appearing at the flow entrance can be considered to be artifacts.

Downstream of the leading edge, the unrealistically high fluxes caused by the singularity decayed continuously as the branching region was approached. During inspiration, the circumferentially-averaged flux achieved a local maximum at the daughter branch inlet (cross-section *H* with $s = 6$), and then monotonically decreased with s along the daughter branch. During expiration, on the other hand, the circumferentially-averaged flux achieved a local minimum at cross-section *H*, and then increased to reach a local maximum in the vicinity of $s = 4.5$ (between cross-sections *D* and *E*) in the parent branch before finally decaying as the outflow plane was approached. For both inspiration and expiration, increasing the Reynolds number led to a larger circumferentially-averaged flux at all cross-sections.

More detailed representations of the three-dimensional flux distribution on the bifurcation wall are provided by the surface contour maps shown in Figure **4-10** for both inspiration and expiration. Hot spots of wall flux appeared at the carina for both inspiratory and expiratory flows. For expiratory flow, a second hot spot was found just downstream of the flow entrance to the parent branch. These local maxima are more clearly shown by the circumferential distributions of the local wall flux, N, (at various cross-sections) presented in Figures **4-11** and **4-12** for inspiratory and expiratory flows, respectively. During inspiration, the wall flux distribution remained axisymmetric through most of the parent branch, as evidenced by the uniform distribution of N values along the perimeter of all cross-sections upstream of cross-section *F* (see Figure **4-11**). On cross- section *G* (at $s = 6$), corresponding to the outflow plane of the parent branch, two local maxima of equal magnitude in the wall flux occurred at the intersections with the bifurcation plane, (i.e., at $\phi_p = 0^\circ, 180^\circ$), while two local flux minima of equal magnitude were found at the intersections with the symmetry plane.

It is clear from Figure **4-11** that the flux distribution in the parent branch exhibited two-fold symmetry, as expected. In the daughter branch, on the other hand, the two-fold symmetry was broken and the flux distribution exhibited symmetry only with respect to the bifurcation plane. As such, only a single local maximum in the wall flux was found at $\phi_d = 270^\circ$ (in the bifurcation plane) over each cross-section of the daughter branch, except for cross-section *H* ($s = 6$) over which a second local maximum of much weaker intensity appeared at $\phi_d = 90^\circ$. Accordingly, the primary local maximum in wall flux over cross-section *H* at the daughter branch entrance occurred right at the carina. This maximum wall flux turned out to be a global maximum as its intensity far exceeded the magnitude of the wall flux everywhere else in the bifurcation (aside from the singular leading edge of the parent branch), as can easily be verified from inspection of Figure **4-11**. The spatial distributions of wall flux were qualitatively the same for all inspiratory Reynolds numbers considered in the simulations. In general, increasing the Reynolds number led to a larger flux everywhere on the bifurcation wall, with the local maxima and minima becoming more pronounced without changing location.

For expiratory flow, the wall flux remained uniformly distributed along the perimeter of all cross-sections upstream of cross-section *I* (at $s = 7$), as shown in Figure **4-12**. Hence, the wall flux distribution remained nearly axisymmetric through most of the daughter branches, qualitatively similar to the flux distribution found in the parent branch during inspiration. In contrast to the latter case, however, the wall flux distributions in the daughter branches did not display two-fold symmetry, as indicated by the wall flux distribution on cross-section *H* (corresponding to the outflow plane of the daughter branch at $s = 6$) in Figure **4-12**. Although the two local maxima in the wall flux on cross section *H* still occurred at the intersections with the bifurcation plane (i.e., at $\phi_d = 90^\circ, 270^\circ$, they were clearly not of the same magnitude. Furthermore, the local maxima were separated by broad minima centered about $\phi_d = 0^\circ, 180^\circ$, in contrast to the more localized minima observed in the parent branch during inspiration.

Perhaps the most interesting feature of the wall flux distribution in the daughter branch during expiration was the shift in the location of the primary local maximum in the wall flux from the outer wall to the inner wall as the Reynolds number was increased. At $Re = 100$, the largest wall flux on cross-section H occurred at $\phi_d = 90^\circ$ on the junction between the daughter and parent branches. When the Reynolds number was increased to 500, the wall flux increased everywhere on the daughter branch wall, as it did in the case of inspiratory flow. However, the increase in wall flux intensity was not uniform over cross-section *H*, and the location of the largest wall flux shifted to the carina ($\phi_d = 270^\circ$) on the inner wall of the daughter branch (see Figure **4-12**). This Reynolds number dependence of the wall flux distribution during expiration was qualitatively different from that observed for inspiratory flow.

The spatial distribution of wall flux in the parent branch during expiration was more complex than that found in the daughter branches during inspiration, particularly near the branching region. On all cross-sections more than one airway radius away from the branching region (i.e., for $s < 5$), the wall flux for $Re = 100$ exhibited two identical local maxima at the intersections with the symmetry plane, separated by two identical local minima at the intersections with the bifurcation plane. On cross-section *G* at the entrance to the parent branch, on the other hand, there were two distinct pairs of local maxima in the wall flux, one pair at the intersections with each symmetry plane. These pairs of maxima at $\phi_p = 0^\circ, 180^\circ$ and $\phi_p = 90^\circ, 270^\circ$ had different magnitudes, and their relative importance changed as the Reynolds number was increased from 100 to 500. At $Re = 100$, the primary pair of maxima with the largest wall flux on cross-section *G* occurred at the intersection with the bifurcation plane. As the Reynolds number was increased to 500, however, the wall flux over cross-section *G* increased non-uniformly, causing the location of the primary maxima in wall flux to shift by 90° to the intersections with the symmetry plane, as shown in Figure **4-12**.

Another interesting effect of Reynolds number on expiratory flow appeared in the wall flux distributions near the outflow plane of the parent branch. Inspection of the wall flux distributions over cross-sections with $s \leq 5$ in Figure **4-12** indicates a broadening of the pair of wall flux maxima located at $\phi_p = 90^\circ, 270^\circ$, as the Reynolds number was increased from 100 to 500. On cross-sections *A-C* at or near the outflow plane, this broadening at $Re = 500$ eventually caused the pair of maxima in wall flux to transform into shallow local minima at $\phi_p = 90^\circ, 270^\circ$. At the same time, each of the original flux maxima at $\phi_p = 90^\circ, 270^\circ$ evolved into a pair of identical local maxima centered about the symmetry plane, thereby maintaining the two-fold symmetry of the flux distribution in the parent branch. The development of the four symmetrically-positioned flux maxima on cross-sections *A* and *C* at an expiratory Reynolds number of 500 is consistent with the contour maps of concentration shown in Figure **4-7** for these cross-sections.

Considering the entire bifurcation (with the exception of the singular leading edge), the maximum value of wall flux at an expiratory Reynolds number of 500 occurred at the carina (i.e., $\phi_d = 270^\circ$ on cross-section *H*). At an expiratory Reynolds number of 100, on the other hand, two comparable hot spots of wall flux appeared, one at the junction of the parent and daughter branch walls (i.e., $\phi_d = 90^\circ$ on cross-section *H*) and another at the intersection of the parent branch wall with the symmetry plane about one airway radius downstream of the branching region (i.e., $\phi_p = 270^\circ$ on cross-section *E*).

4.2.3 Overall Rate of Uptake

The dimensionless rate of O_3 uptake, $\dot{M}$, was determined from an overall mass balance according to

$$\dot{M} = Pe\left\langle \int_A c\mathbf{u} \bullet \mathbf{n}\, dA \right\rangle, \qquad \textbf{4.7}$$

where the brackets denote the jump in the value of the integral from the inflow boundary to the outflow boundary, and A represents the dimensionless area of these boundaries of integration. As indicated in Figure **4-13**, the overall rate of uptake in both parent and daughter branches increased with Reynolds number for both inspiratory and expiratory flow. This figure also compares the overall rate of uptake in the bifurcation to that in a “surface-equivalent” section of the parent airway, i.e., in a straight tube with the same radius as that of the parent branch and a wall surface area equal to that of the entire bifurcation. The total rate of uptake in the bifurcation was greater than that in the surface-equivalent straight tube during both inspiration and expiration.

The rate of uptake in a straight tube of dimensionless length λ can be obtained from $\dot{M} = 2\pi\lambda\overline{Sh}$, where the average Sherwood number, $\overline{Sh}$, is given by equation **4.3**. According to this expression, the rate of uptake in a straight tube is expected to depend on Reynolds number like $Re^{1/2}$. To evaluate the sensitivity of the rate of uptake to gas flow, simulation results for the rate of uptake in the bifurcation were also regressed with the Reynolds number according to a power-law relation incorporating Re^{n} dependence. The simulated rates of uptake for the surface-equivalent straight tube and the upstream branches during inspiration and expiration were characterized by n values of 0.51, 0.48, and 0.52, respectively, close to the theoretically-predicted value of $1/2$ for a straight tube. For the downstream branches, however, the resulting values of n were 0.71 and 0.90 during inspiration and expiration, respectively. Thus, the values of n for the downstream branches were significantly larger than those for their upstream counterparts, indicating a greater sensitivity of the rate of uptake to flow in downstream branches.

The slight deviation of the n values for the upstream branches of the bifurcation from $1/2$ was caused by the departure of the wall flux distribution in the vicinity of the branching region from that predicted for a straight tube. This is clearly illustrated in Figure **4-14** where the circumferential distribution of the wall flux at various cross-sections is plotted in the form $x^{1/2}\, Sh \big/ Re^{1/2}$. For a straight tube, this quantity is predicted to have a constant value of 0.32 regardless of axial position along the tube. The flux distributions for both inspiratory flow through the parent branch and expiratory flow through the daughter branches were in excellent agreement with this prediction for all cross-sections that were at least one airway radius upstream of the branching region. Within one airway radius of the branching region, however, local maxima and minima in $x^{1/2}\,Sh\big/Re^{1/2}$ dominated the uptake behavior and led to deviations in the value of n from ½.

The overall fractional uptake, θ, defined as the ratio of the overall rate of uptake to the rate of inflow of O_3 through inlet area A_{in}, was also calculated using the expression

$$\theta = \frac{\left\langle \int_A c\mathbf{u}\bullet\mathbf{n}\,dA \right\rangle}{\int_{A_{in}} c\mathbf{u}\bullet\mathbf{n}\,dA} \qquad \mathbf{4.8}$$

The fractional uptake is a measure of the efficiency of the gas uptake process, and is related to the overall rate of uptake according to $\theta = \dot{M}\big/\pi\,Pe$. The fractional uptake was found to decrease with increasing Reynolds number due to the reduced residence time of the reactive gas in the bifurcation at higher Reynolds numbers. The value of θ during expiratory flow exceeded that for inspiratory flow by about 5% at $Re = 200$ (θ = 0.50 and 0.53 for inspiratory and expiratory flow, respectively) and by about 12% at $Re = 500$ (θ = 0.34 and 0.38 for inspiratory and expiratory flow, respectively). At $Re = 100$, on the other hand, the fractional uptake during inspiratory flow was about 2% larger than that for expiratory flow (θ = 0.66 and 0.64 for inspiratory and expiratory flow, respectively).

4.3 DISCUSSION

4.3.1 Model Assumptions

The boundary condition imposed at the bifurcation walls assumes an infinitely fast reaction of O_3 with endogenous substrates in the lung epithelial lining fluid (ELF), thereby rendering the concentration of O_3 negligible on the walls of the airways. In reality, the rate of reaction of O_3 in the ELF is finite. However, the actual values of appropriate reaction rate constants are unknown. Assuming a pseudo-first order reaction between O_3 and ELF constituents, various estimates for the reaction rate constant have been reported in the literature, spanning a wide range from $1198\ \mathrm{s}^{-1}$ (Miller *et al.*, 1985) to $8\times10^{6}\ \mathrm{s}^{-1}$ (Bush *et al.*, 2001). Although the use of an infinite reaction rate overestimates the rate of O_3 uptake, it also makes the nonuniformities in the flux distributions more pronounced, thereby facilitating the identification of hot spots of O_3 flux, which is one of the main objectives of this study.

The selection of appropriate inlet boundary conditions for velocity and concentration in this problem is an important issue that deserves special attention. Specification of velocity and concentration profiles at the inlet of an actual airway bifurcation is confounded by the development of those profiles within upstream branches and airway passages. In order to correctly determine realistic velocity and concentration profiles for an arbitrary bifurcation, one would need to simulate flow and ozone uptake in the entire respiratory tract, from the nostrils to the alveoli. The inlet boundary conditions selected for this study represent good approximations in those bifurcations for which upstream secondary vortices have flattened the inlet velocity and concentration profiles (Fresconi *et al*., 2003). To investigate the sensitivity of the predicted flux distributions to the assumed form of the inlet velocity profile, the simulation results presented in this paper were compared to their counterparts obtained using a parabolic inlet velocity profile. The resulting flux distributions in the two cases were found to be qualitatively similar in that for inspiratory flow the flux progressively decreased along the parent branch, the hot spot of flux was located at the carina, and the flux in the daughter branches was higher along the inner walls. These findings further justify the use of a flat inlet velocity profile in pursuit of possible hot spots of O_3 flux.

Although respiratory flow is oscillatory, rather than steady as we have assumed, gas transport can often be treated as a quasi-steady process under quiet breathing conditions (Fresconi *et al*., 2003). Moreover, because we have selected an idealized bifurcation geometry and performed the analysis in dimensionless form, we can apply the results to different airway generations within a single tracheobronchial tree or to the bifurcations of different lungs. The identification of the particular airway generations to which our simulations would apply depends on the minute ventilation and lung size. For example, the ventilatory and anatomic parameters presented by Phalen *et al*. (1985) indicate that our Reynolds number range of 100-500 would encompass generations 1-5, 3-7, and 6 -10 for an adult during quiet breathing, light exertion, and heavy exertion, respectively. On the other hand, the same Reynolds number range would correspond to generations 0-4, 1-6, and 4-8 for a 4-year old child during quiet breathing, light exertion, and heavy exertion, respectively. In addition to the aforementioned considerations for identifying the relevant airway generations, it should also be noted that the results presented here are strictly applicable only to bifurcations of sufficiently high order that the propagated turbulence arising from the laryngeal jet has completely dissipated in the upstream flow. Menon *et al*. (1985) experimentally measured the effect of the larynx on velocity profiles during inspiration in a four-generation model of the human central airways under oscillatory flow conditions equivalent to normal breathing and panting. By comparing velocity profiles with and without a larynx aperture included in the model, they found that even for panting conditions, the presence of the larynx could not be felt beyond the tracheal carina. This was also found to be true during steady flow. Based on their observations, our results should be applicable to airways distal to the trachea.

4.3.2 Flux Distribution and Uptake

The results of the simulations performed in this study are applicable to the transport and uptake of any gas with sufficiently high reactivity at the wall to render the wall concentration of the gas negligibly small. For inspiratory flow, the simulations consistently predicted a hot spot of wall flux at the carina, as well as larger uptake along the inner walls of the daughter branches. This was due to the impingement on the carina of a fluid stream with a relatively high concentration of reactive gas, leading to the formation and development of a new concentration boundary layer along the inner walls of the daughter branches. For expiratory flow, a hot spot of wall flux appeared at the carina for $Re = 500$, but was shifted to the outer wall of the daughter branch (at its junction with the parent branch) as the Reynolds number was reduced to 100. Additional hot spots were found during expiration, along the intersections of the parent branch wall with the $\phi_p = 90^\circ, 270^\circ$ symmetry plane within one parent branch radius of the branching region. Compared to a surface-equivalent straight tube, the presence of branching caused an enhancement in the overall rate of uptake, with the downstream branches being the main sites of increased uptake. This enhanced uptake resulted from the redevelopment of the concentration boundary layer downstream of the carina during inspiration and from the development of high concentration gradients along the parent branch wall during expiration (see Figure **4-7**B).

The simulation results obtained in this study are in good qualitative agreement with the experiments of Mahinpey *et al.* (2004), who studied mass transfer in an idealized human aortic bifurcation using a copper electrodeposition technique. Although the value of the Schmidt number for their system ($Sc = 3600$) was much larger than that used in our simulations, they found similar mass transfer patterns such as higher fluxes at the inner walls of daughter branches and a more uniform flux distribution away from the branching region. Caro and others (2002) carried out an experimental study at a Schmidt number of order 1, conditions that are closer to ours. They flowed an acid vapor through three-generation airway models, the walls of which were coated with a water-litmus paste and observed the time it took for the blue litmus to redden, an indicator of the rate of mass transfer. In the first generation, the initial site of reddening was at the carina, and the outer walls of the first generation daughter branch reddened last. This is consistent with the results of our simulations, which predict that for inspiratory flow the highest mass transfer rates occur at the carina and that the flux along the daughter branch inner wall is greater than that along the outer wall. One-dimensional single-path models are unable to capture such important features of the local flux. Moreover, the overall finding of this study that the rate of uptake in a bifurcation is greater than that in a surface-equivalent straight tube suggests that treating airway generations strictly as tube segments is likely to underestimate uptake in the airways

Using their novel bolus-inhalation method, Hu *et al*. (1994) measured the penetration of a bolus of O_3 into the respiratory tract and reported an increase in the rate of absorption of O_3 with increasing respiratory flow rate in all respiratory tract compartments. They also concluded that an increase in respiratory flow rate decreases the absorbed fraction of O_3 in the more proximal airways, allowing a deeper penetration of O_3 into the respiratory tract. In another study, Postlethwait *et al*. (1994) found that increasing respiratory frequency at a fixed tidal volume (essentially, increasing the breathing flow rate) led to a decrease in the absorbed fraction of O_3 in isolated rat lungs. They attributed this phenomenon to the reduced contact time of O_3 with the mucus lining fluid. The results of single bifurcation simulations in this study are qualitatively consistent with all of the aforementioned experimental observations in that they predict an increase in the overall rate of uptake, accompanied by a reduction in the fractional uptake, as the Reynolds number increases.

4.3.3 Implications for O_3-induced Injury

The ultimate goal of mathematical models of O_3 uptake is to predict the local pattern of O_3-induced damage in the respiratory tract. The simulation results in this study indicate that the total rate of O_3 uptake in the upstream generation is greater than that in the downstream generation, regardless of flow direction. For inspiratory flow, the parent branch had a higher rate of uptake than the two daughter branches combined, while the opposite was found to be true for expiratory flow. Of course, for airways with fixed length-to-diameter ratio, this outcome would depend on the daughter to parent branch length ratio. For the bifurcation used in this study, this quantity had a value of 0.6 which falls well within the range of 0.4-1.7 found in Weibel's anatomical model (1963) and the range of 0.4-1.0 found in Horsefield & Cumming's model (1968). As O_3 is progressively depleted between successive generations, it seems likely that the rate of uptake would also diminish. This expectation has been confirmed with various single path models (Hu *et al.*, 1992; Miller *et al.*, 1978; Overton *et al.*, 1995).

In O_3 exposure studies carried out on isolated rat lungs, Joad *et al.* (2000) and Postlethwait *et al.* (2000) demonstrated that O_3-induced damage is greater in the side branch of monopodial bifurcations compared to that in the main branch. Because of the symmetry of the geometry used in this study, we did not observe such an asymmetry in the uptake pattern. This suggests that the distribution of O_3 absorption may be affected by airway asymmetries or nonuniformities in the flow distribution between daughter branches, neither of which were considered in the current simulations. Other factors that might affect the O_3 uptake distribution and the resulting tissue damage pattern include spatial variations in detoxification reactions that occur in the liquid lining layer and spatial variations in the biological sensitivity of underlying epithelial cells.

4.4 SUMMARY AND CONCLUSIONS

Transport and uptake of a reactive gas in an idealized bifurcation representing a portion of the conducting airways were studied. Both inspiratory and expiratory steady flows were examined. Three-dimensional numerical solutions of the continuity, Navier-Stokes, and convection-diffusion equations were obtained, assuming an infinitely fast surface reaction on the airway walls. Simulation results were used to identify the location of hot spots of flux on the bifurcation wall, as well as the effect of flow rate on the overall rate and efficiency of uptake. Hot spots of wall flux were predicted to occur at the carina for both inspiratory and expiratory flows with $Re > 100$. For an expiratory Reynolds number of 100, however, the location of the hot spot was found to shift to the outer walls of the daughter branches at the junction with the parent branch wall. For expiratory flow, additional hot spots were found to occur on the parent branch wall just downstream of the branching region. Simulations such as those performed in this study are useful and necessary for revealing hot spots of reactive gas uptake that may lead to focal regions of airway tissue injury.

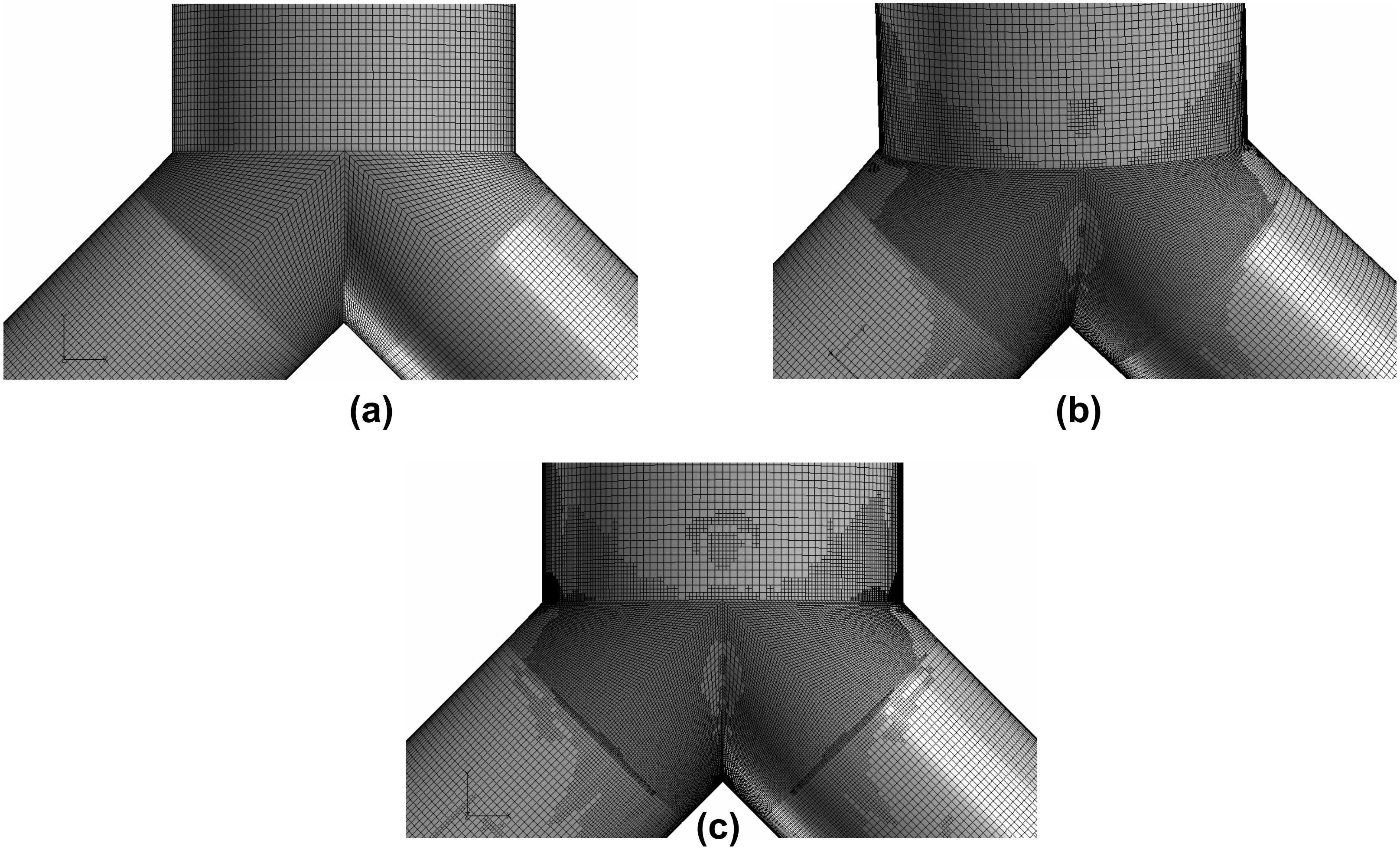

Figure **4-1**: Mesh in the bifurcation region of the 90° symmetric bifurcation. (a) Mesh 1 (b) Mesh 2 (c) Mesh 3

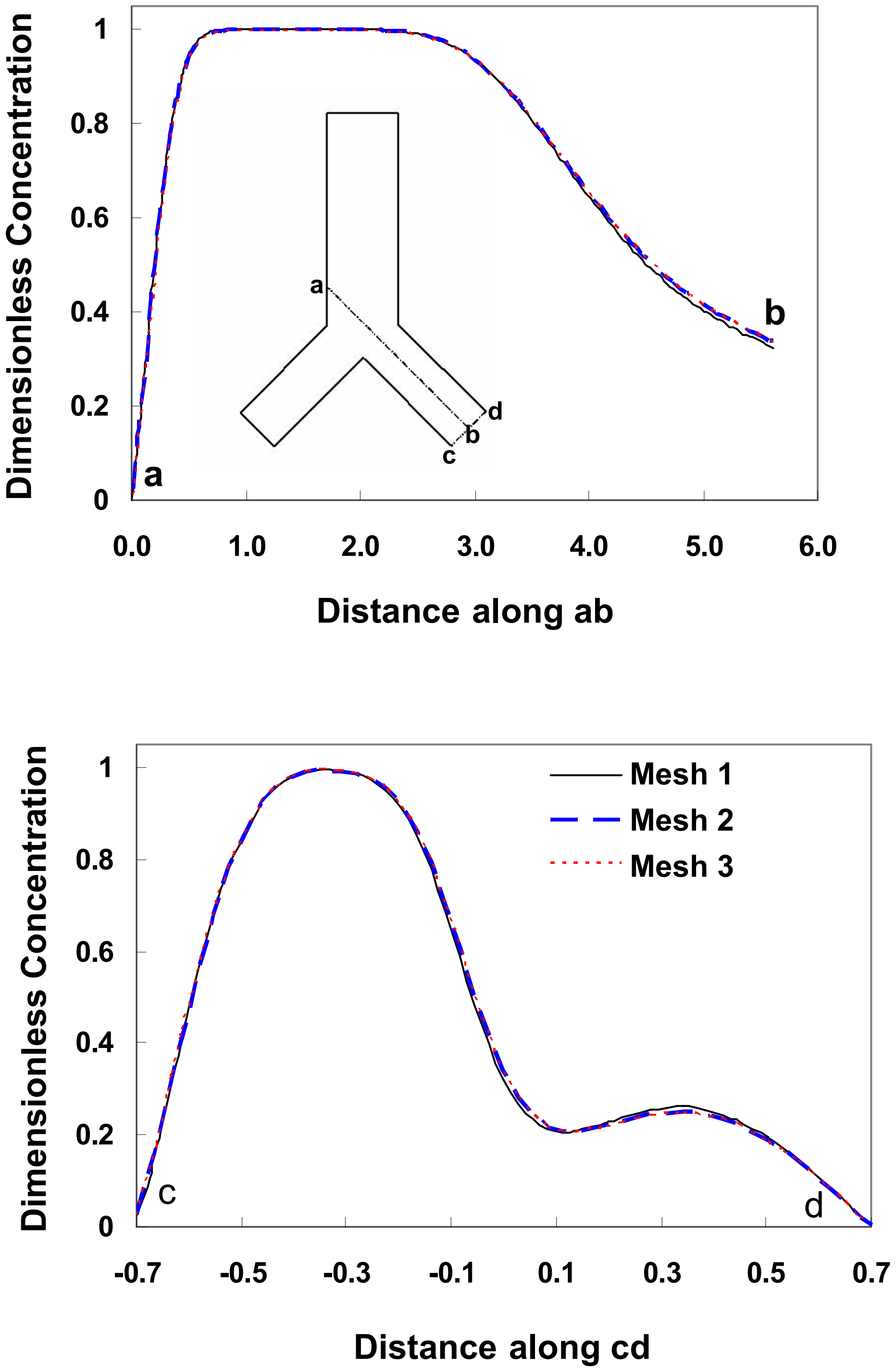

Figure **4-2**: Results of mesh independence study (inspiratory flow). The inset shows the locations used in testing mesh independence. Both lines are in the bifurcation plane.

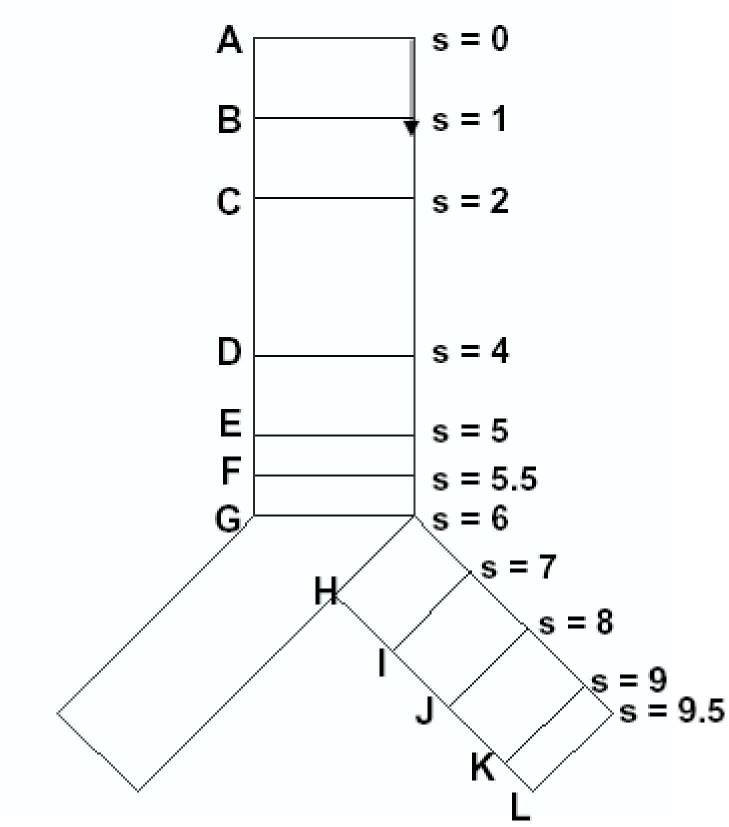
A
s = 0
B
s = 1
C
s = 2
D
s = 4
E
s = 5
F
s = 5.5
G
s = 6
s = 7
H
s = 8
I
s = 9
J
s = 9.5
K
L

Figure **4-3**: Schematic definition of various cross-sections along the wall coordinate *s* on which flux distributions are reported.

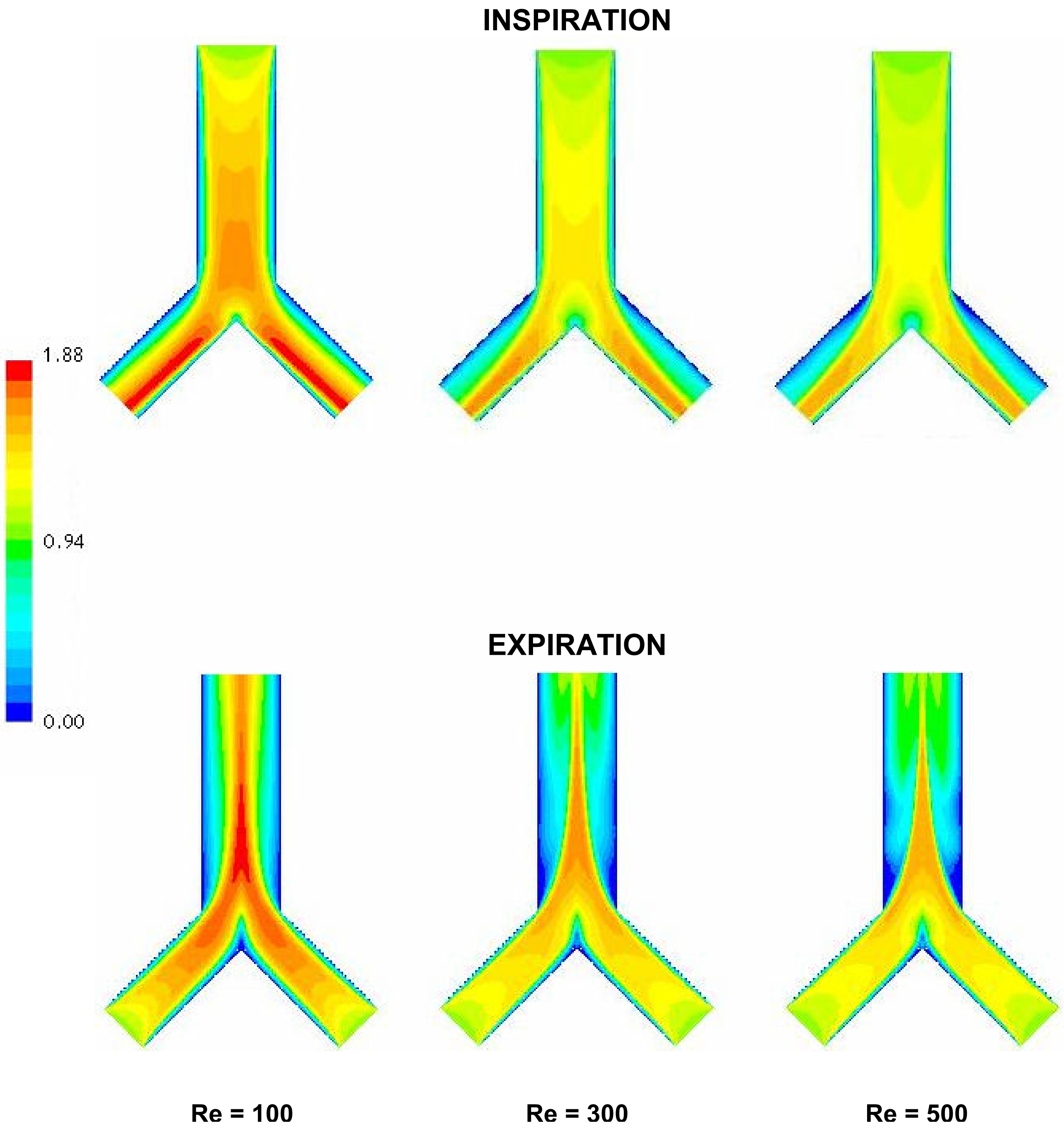

Figure **4-4**: Isocontours of the magnitude of dimensionless velocity in the bifurcation plane for inspiratory and expiratory flows.

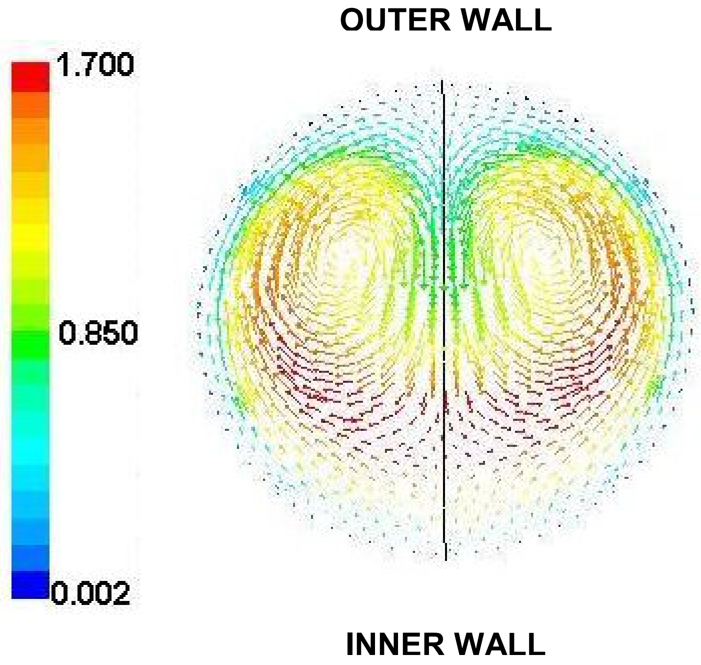

Figure **4-5**: Dimensionless velocity vectors (colored by dimensionless velocity magnitude) in the plane of the outflow boundary of the daughter branch during steady inspiratory flow at $Re = 300$ showing pair of counter-rotating vortices. The line denotes the location of the bifurcation plane.

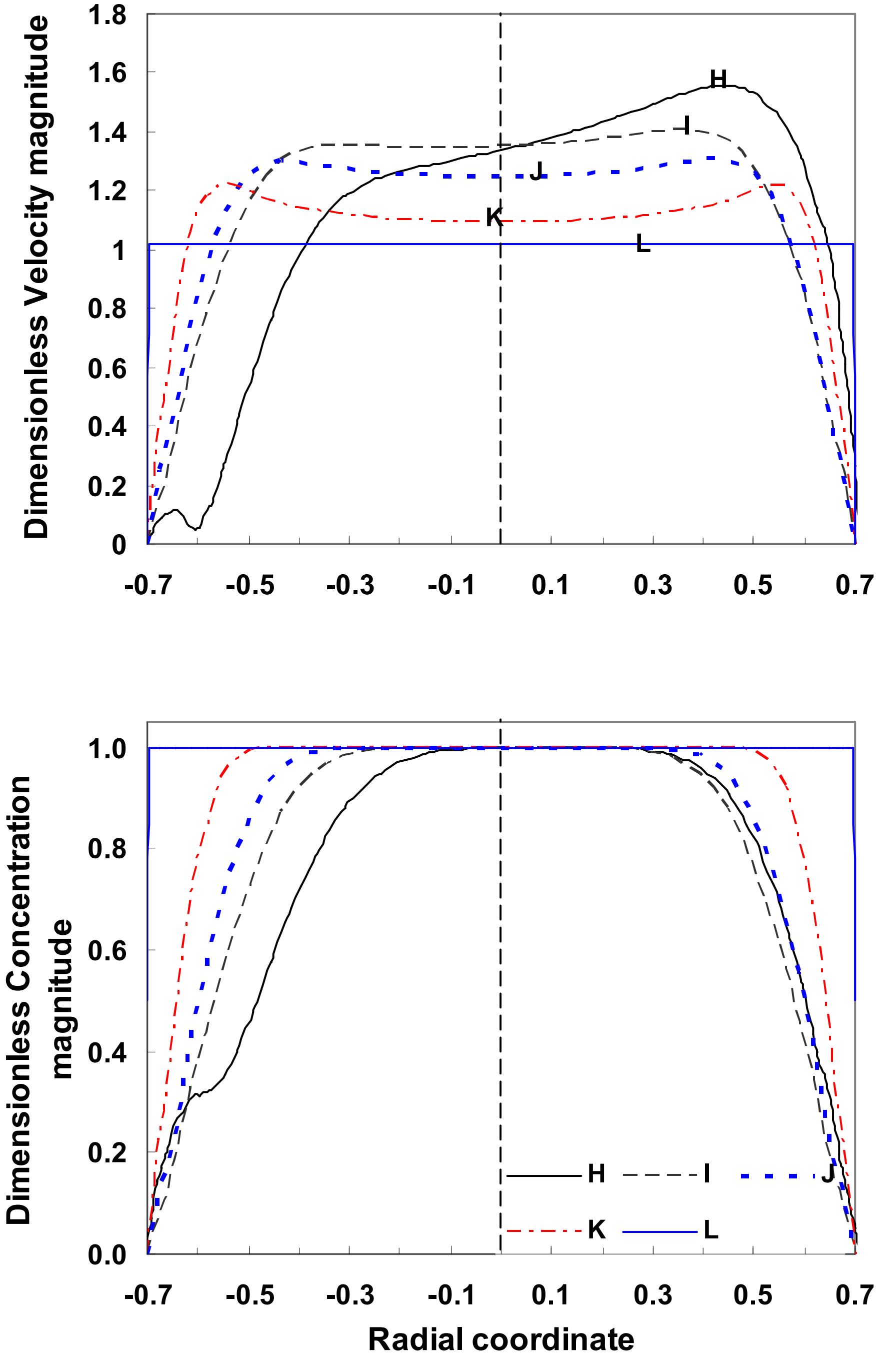

Figure **4-6**: Dimensionless velocity magnitude (top panel) and dimensionless concentration (bottom panel) profiles along the intersections of various cross sections (H, I, J, K, L) and the bifurcation plane for steady expiratory flow in the daughter branch at $Re = 300$. Radial coordinate = -0.7 is intersects the inner wall and radial coordinate = 0.7 intersects the outer wall.

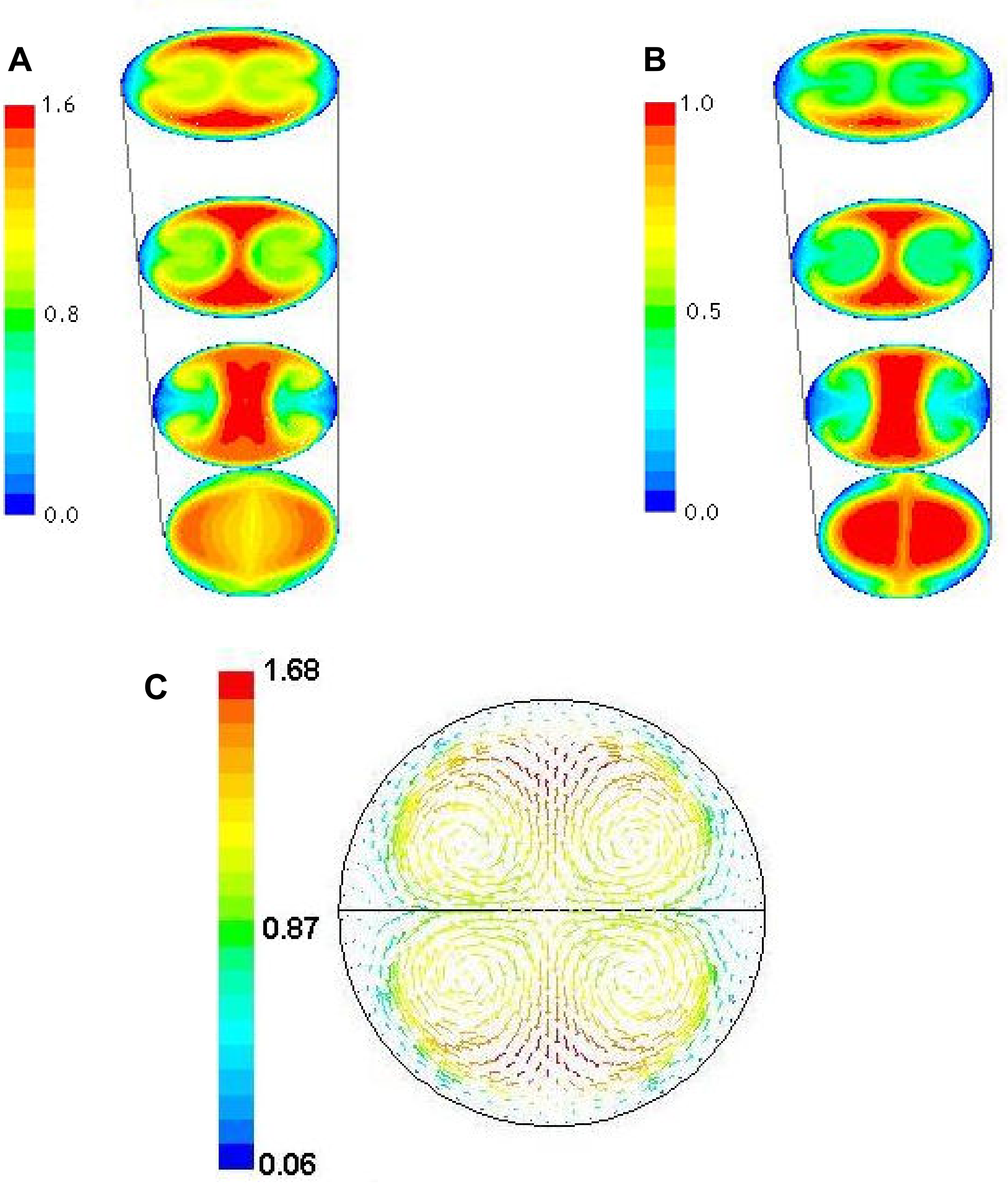

Figure **4-7**: Isocontours of (A) magnitude of dimensionless velocity and (B) dimensionless O_3 concentration on cross-sections *A*, *C*, *D*, and *G* (top to bottom) along the parent branch axis for expiratory flow at $Re = 500$. The lines denote the intersections of the bifurcation plane with the parent branch wall. (C) Dimensionless velocity vectors (colored by dimensionless velocity magnitude) in the plane of the outflow boundary of the parent branch for steady expiratory flow at $Re = 300$ showing the quadruple vortex pattern. The line denotes the location of the bifurcation plane.

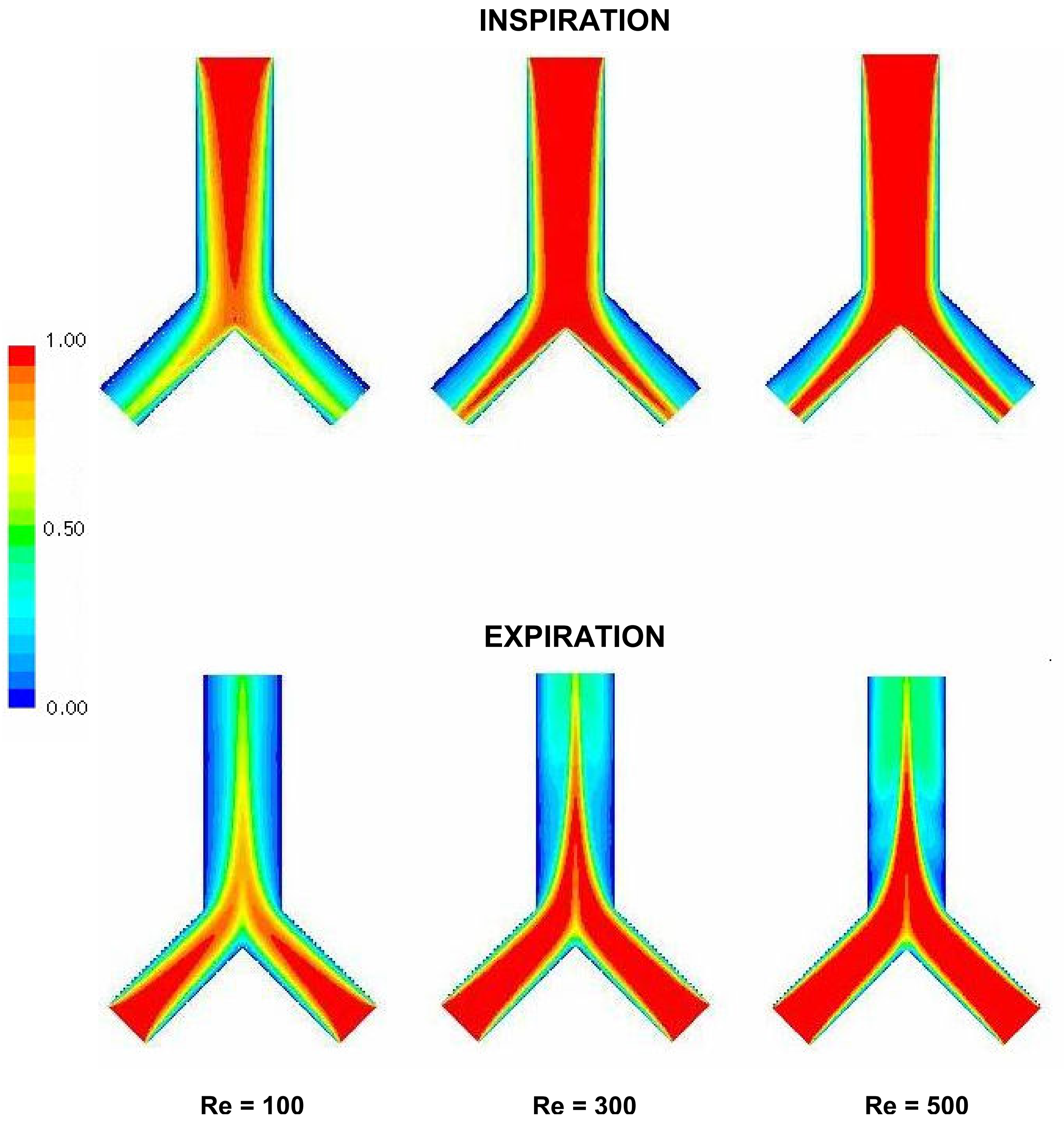

Figure **4-8**: Isocontours of dimensionless O_3 concentration in the bifurcation plane for inspiratory and expiratory flows.

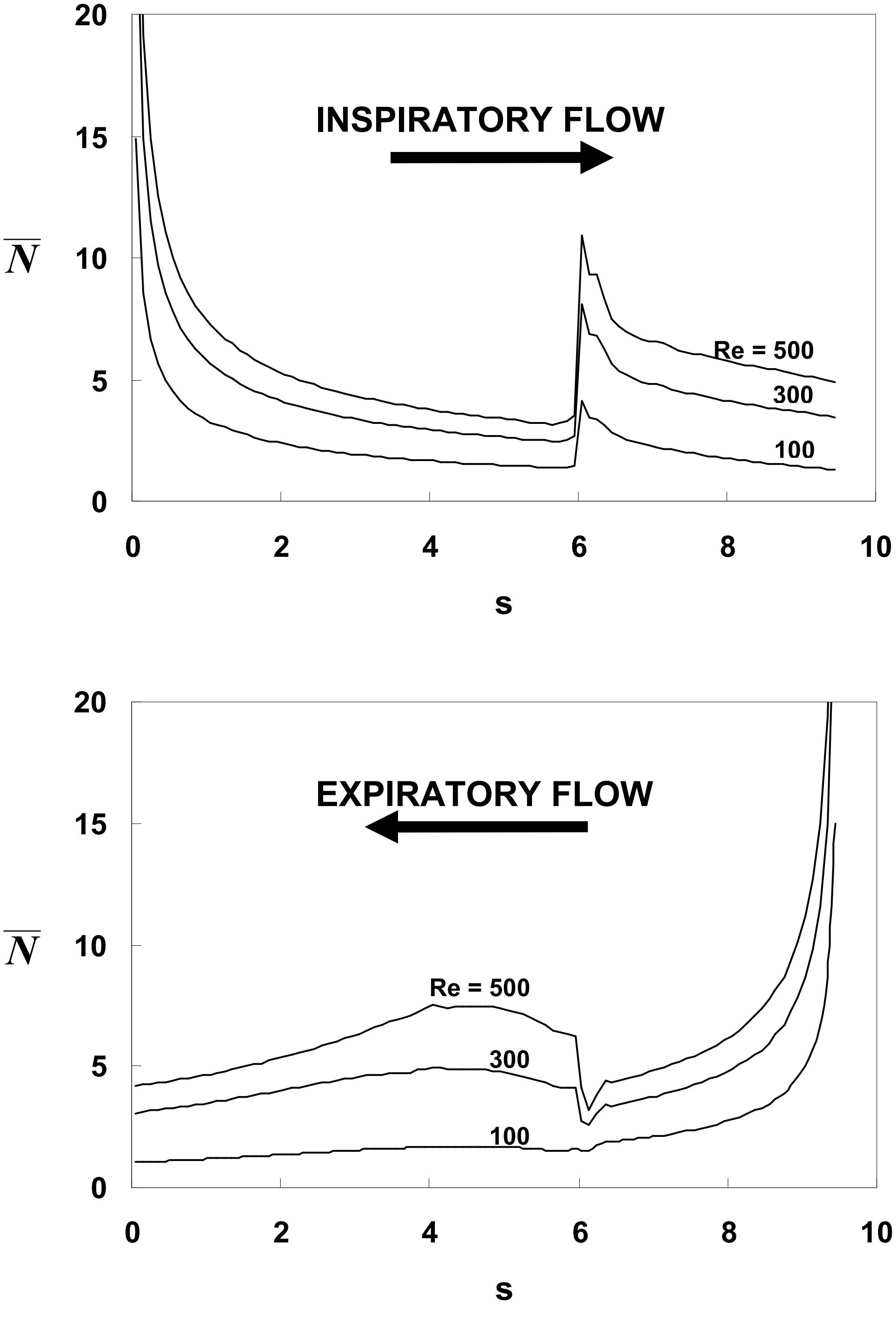

Figure **4-9**: Distribution of the circumferentially-averaged dimensionless flux $\left(\overline{N}\right)$ along the bifurcation wall for inspiratory flow (top panel) and expiratory flow (bottom panel) at three different Reynolds numbers. The arrows indicate the flow direction.

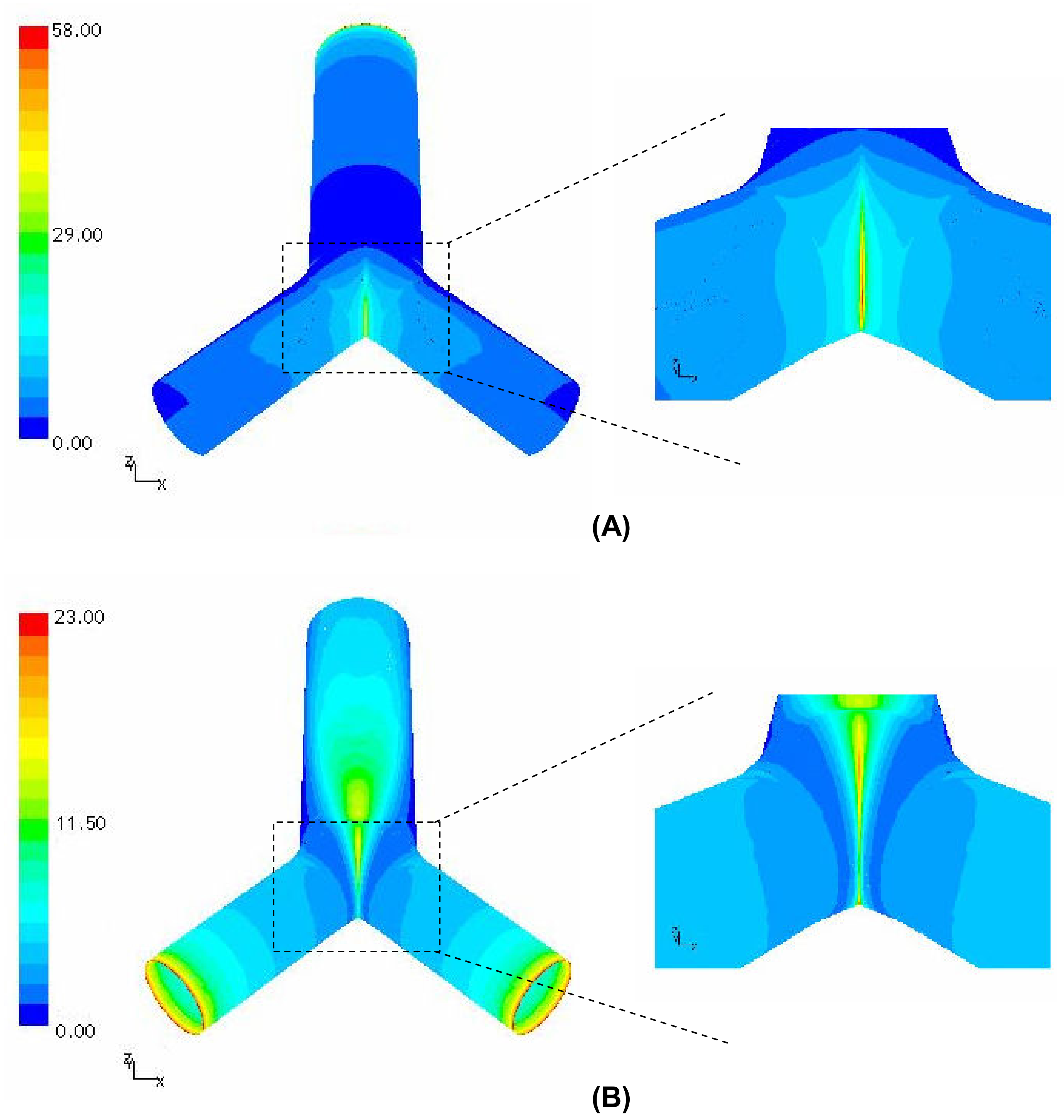

Figure **4-10**: Isocontours of the dimensionless flux (N) along the bifurcation wall for (A) inspiratory flow and (B) expiratory flow ($Re = 300$).

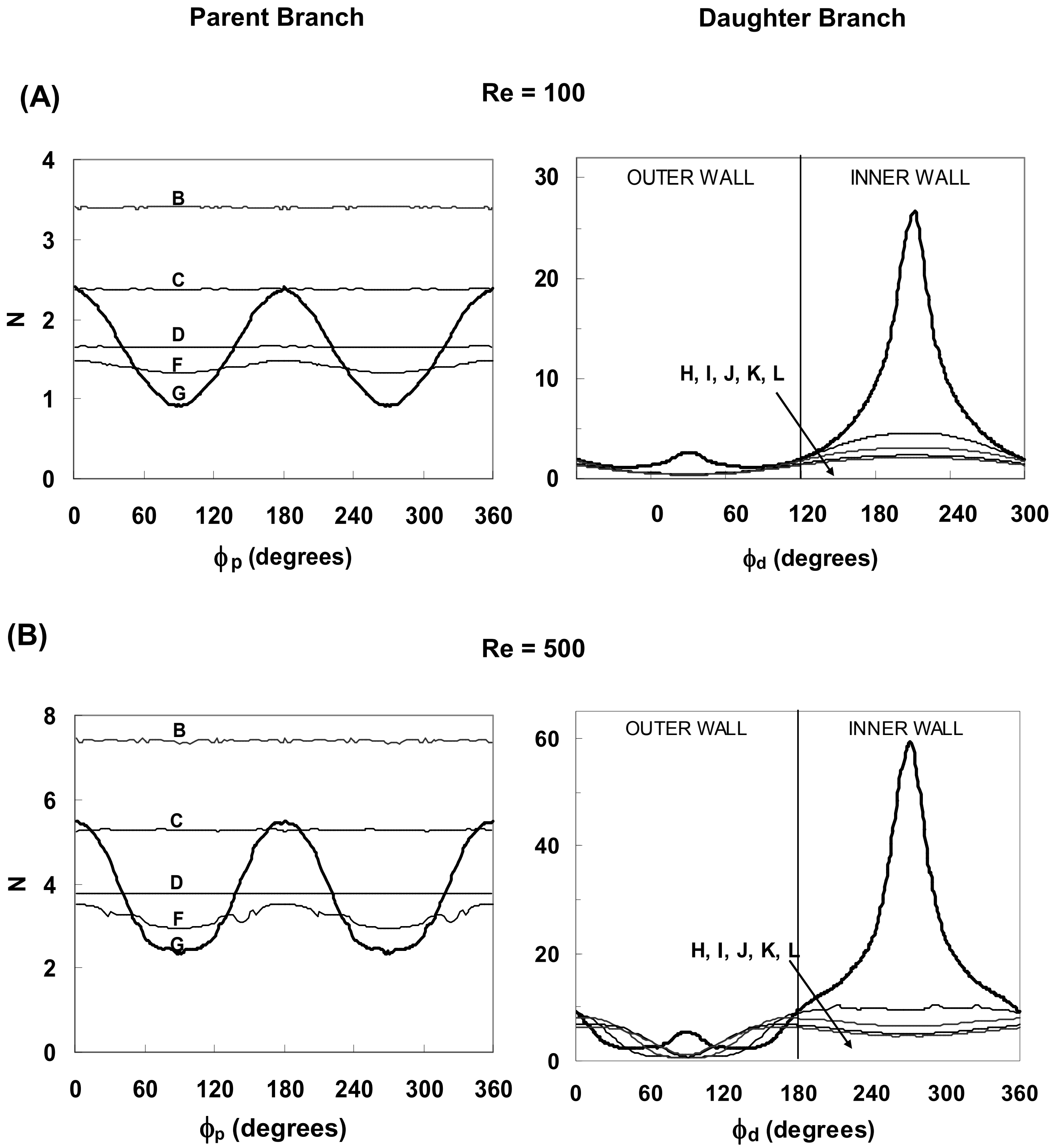

Figure **4-11**: Circumferential variation of the local dimensionless wall flux, N, at various cross-sections in the parent and daughter branches for inspiratory flow at (A) $Re = 100$ and (B) $Re = 500$.

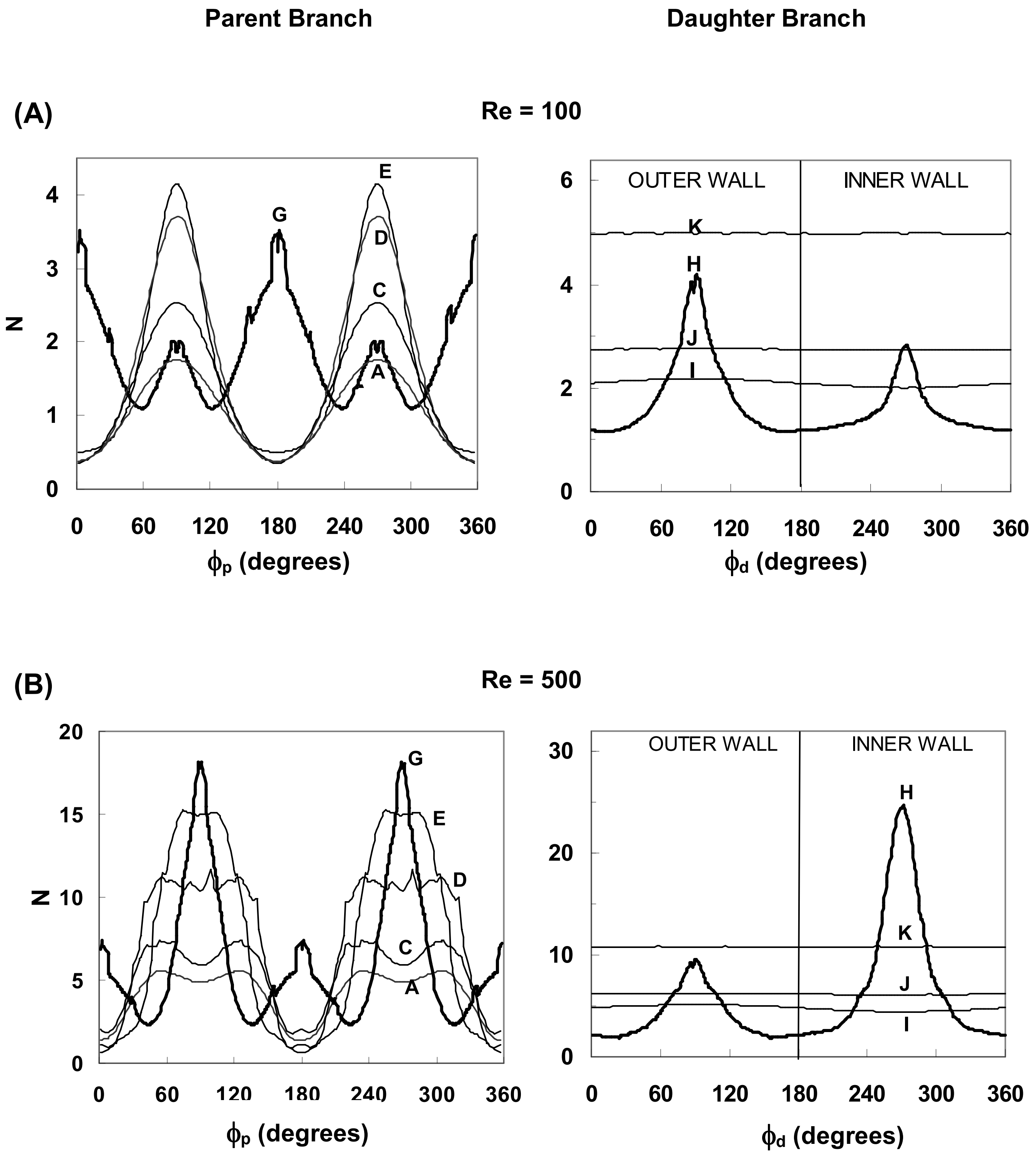

Figure **4-12**: Circumferential variation of the local dimensionless wall flux, N, at various cross-sections in the parent and daughter branches for expiratory flow at (A) $Re = 100$ and (B) $Re = 500$.

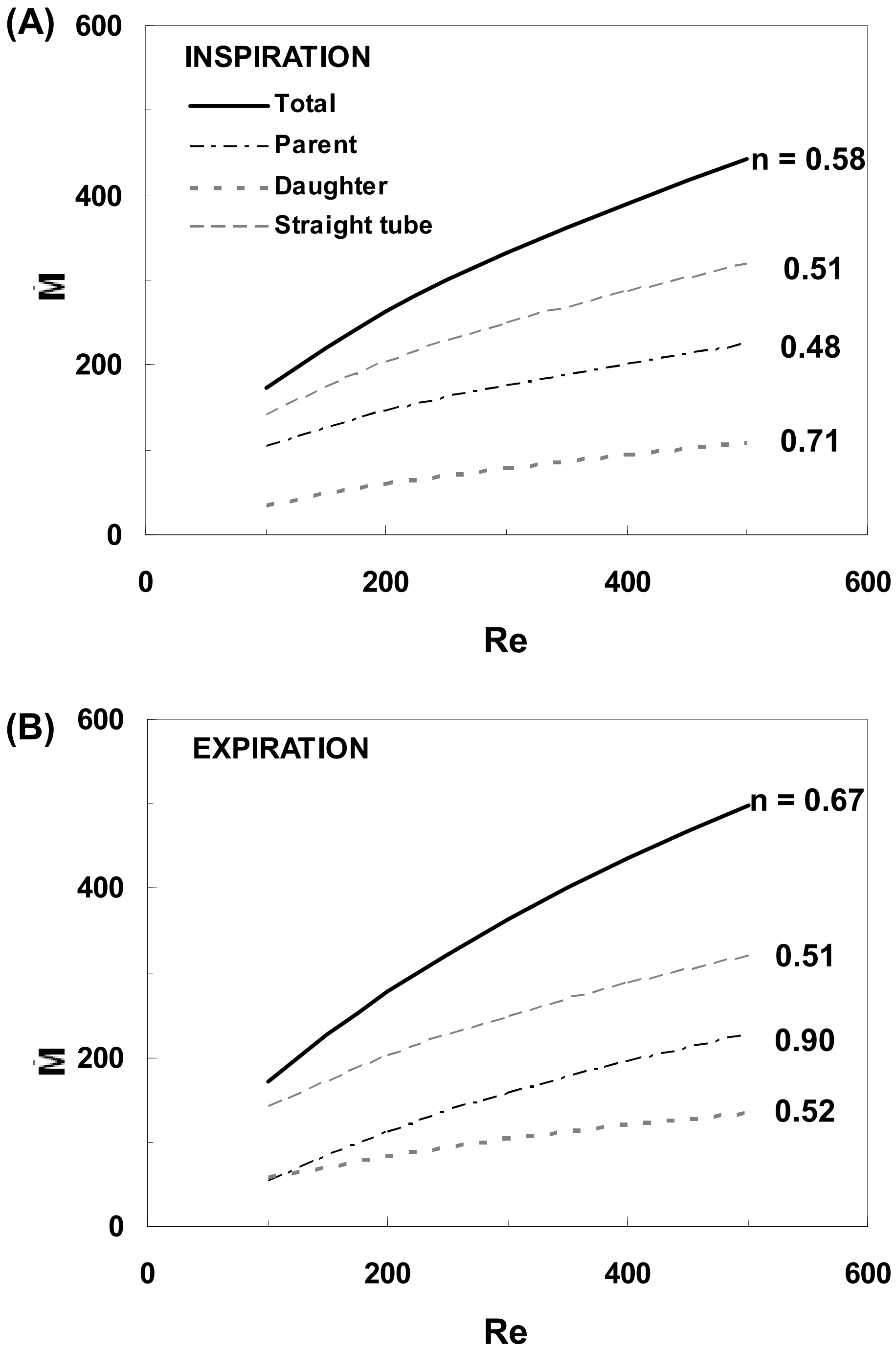

Figure **4-13**: Dependence of the dimensionless rate of O_3 uptake ($\dot{M}$) on Reynolds number for (A) inspiratory flow and (B) expiratory flow. The total rate of uptake for the entire bifurcation, as well as those in the parent branch and in a single daughter branch are shown. Also shown for comparison is the simulated rate of uptake in a straight tube with the same diameter as that of the parent branch and wall surface area equivalent to that of the entire bifurcation. (**NOTE:** The uptake rate reported for the daughter branch includes the uptake rate in half of the transition region.)

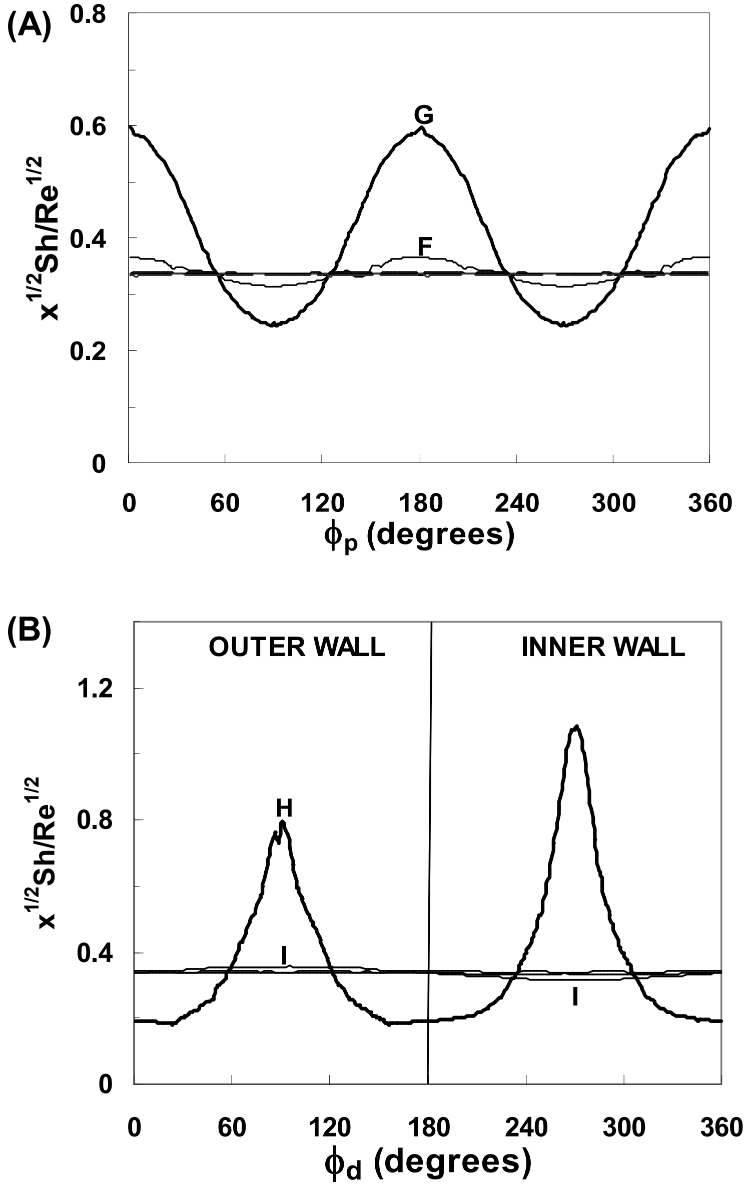

Figure **4-14**: Circumferential variation of the scaled local wall flux, $x^{1/2}\,Sh\big/Re^{1/2}$, at various cross-sections in (A) the parent branch for inspiratory flow at $Re = 300$ and (B) the daughter branch for expiratory flow at $Re = 300$. In the top panel, the lines corresponding to the parent branch cross-sections *B*, *C*, and *D* are not labeled because they are virtually indistinguishable, as are the unlabeled lines in the lower panel representing daughter branch cross-sections *J* and *K*.

Chapter 5

EFFECT OF AIRWAY GEOMETRY ON OZONE UPTAKE

There is great variability in airway branching geometry from generation to generation, lung to lung, and between species. In this chapter, the effects of airway geometry on O_3 uptake distribution will be explored in two respects. First, the effect of branching angle will be examined in symmetric bifurcations. Next, the effect of the type of branching – dichotomous vs. monopodial – will be investigated by comparing O_3 uptake in an idealized symmetric bifurcation and an idealized monopodial bifurcation.

5.1 RESULTS – EFFECT OF BRANCHING ANGLE

In order to examine the effect of branching angle on O_3 uptake, simulations of inspiratory and expiratory flow and O_3 uptake were conducted at a Reynolds number of 300 in three different symmetric bifurcations with branching angles of 45°, 90°, and 135° (Figure **3-1**). An infinitely fast reaction at the gas-RTLF interface was assumed; thus a zero concentration of O_3 at the walls of the bifurcation was specified.

The flow, concentration, and flux distributions for the three branching angles had several features in common with those described in Sections **4.2.1** and **Error! Not a valid link.**, but several differences were observed as detailed in the following sections.

5.1.1 Flow Fields

Contour maps of the dimensionless velocity magnitude in the bifurcation plane are presented in Figure **5-1** for both inspiratory and expiratory flows at a Reynolds number of 300 for symmetric branching angles of 45°, 90°, and 135°. During inspiration, the flow fields in the parent branch were similar for all branching angles, and the maximum dimensionless velocity magnitudes u_{max} attained in the entire bifurcation increased somewhat with branching angle ($u_{max} = 1.67$, 1.68, and 1.72 for branching angles of 45°, 90°, and 135°, respectively). As the branching angle increased, the velocity of the fluid impinging the carina decreased, leading to a thicker momentum boundary layer in the immediate vicinity of the carina. However, further downstream the velocity distribution became more skewed towards the inner wall of the daughter branches as the branching angle increased, leading to a thinner momentum boundary layer along the daughter branch inner wall as the branching angle increased. As the branching angle increased, the region of flow stagnation along the daughter branch outer walls became larger. Additionally, a small region of flow separation that resulted in backflow along the outer wall of each daughter branch was evident in the 135° bifurcation (Figure **5-2**). In the bifurcation plane, the velocity distribution at the outlets was bimodal at 135° but not at the other branching angles (Figure **5-3**). This result suggests that the branching angle will have an impact on the velocity profiles entering the downstream branches.

For expiratory flow, the velocity distributions in the daughter branches became more skewed toward the outer wall and away from the inner wall as the branching angle increased, the latter feature being most pronounced in the carinal region. In addition, at 90° and 135°, but not at 45°, a pair of small counter-rotating vortices present on either side of the carina that was symmetric with respect to the plane normal to the bifurcation plane (normal plane) was observed (Figure **5-4**). These vortices were larger at 135°. The areas of stagnation flow along the parent branch walls near the junction of the parent branch and the transition region became more prominent as the branching angle increased. Regions of flow separation along the parent branch wall, also near the junction of the parent branch and the transition region, that resulted in backflow were evident at branching angles 90° and 135° (Figure **5-4**). These regions were larger for the 135° bifurcation because the incoming flow from the daughter branches deviated more from the parent branch axis for the larger branching angle. In the parent branch, the sheet of high-velocity fluid in the normal plane that was formed by the merging of fluid leaving the daughter branches persisted for a shorter distance as the branching angle increased. The extent of the deviation of the daughter branch axis from the parent branch axis was also responsible for these differences in the high-velocity sheet of fluid. Figure **5-5A** shows that the velocity distribution in the normal plane was different for each branching angle during expiratory flow. In the normal plane, the velocity distribution had a single peak for a branching angle of 45° but two for branching angles of 90° and 135°, with the peaks becoming more pronounced in the 135° bifurcation.

5.1.2 Concentration Distributions

As seen in Figure **5-6**, the dimensionless concentration distributions for inspiratory and expiratory flow in each of the bifurcations are qualitatively similar to their corresponding velocity distributions. Interestingly, for inspiratory flow, the average dimensionless concentration $\langle c \rangle$ exiting each daughter branch did not follow a definite trend. The average concentration exiting the 45° bifurcation ($\langle c \rangle = 0.448$) was less than that exiting the 90° bifurcation ($\langle c \rangle = 0.451$), which was greater than the exit concentration in 135° bifurcation ($\langle c \rangle = 0.432$). These results are not evident from the concentration distributions presented in Figure **5-6**, which shows the concentration distributions only in the bifurcation plane and from which it appears that the average concentration at the outlet decreases as the branching angle increases. The reason for the observed trend in the average concentrations at the outlets can be seen from an examination of the complete concentration distributions at the outflow boundaries, presented in Figure **5-7**. Another trend observed for inspiratory flow was that the newly developing boundary layer along the inner wall of the daughter branches became thinner as the branching angle increases, leading to higher concentration gradients. Furthermore, the size of the regions of low O_3 concentration along the outer walls of the daughter branch that resulted from flow stagnation increased with increasing branching angle, except near the exit of the daughter branch of the 135° bifurcation where there was a higher O_3 concentration in the corresponding higher velocity region (cf. Figure **5-1**).

For expiratory flow, just as with the velocity distributions, the O_3 concentration distribution became more skewed toward the outer daughter branch walls and away from the inner walls as the branching angle increased. Additionally, the regions of low O_3 concentration near the daughter-parent junction, corresponding to the stagnation regions in parent branch that were observed in the velocity distributions, were larger at the higher branching angles. However, the region of low concentration that was located further downstream became smaller at the higher branching angles, leading to higher concentration gradients in that zone. The high concentration sheets within the parent branch possessed the same characteristics as the corresponding high-velocity sheets. The concentration distribution in the normal plane for inspiratory flow is shown for all branching angles in Figure **5-5B**. Again, the concentration distributions were different for each branching angle, but qualitatively similar to their corresponding velocity distributions. The concentration gradient in the region of the carina increased with increasing branching angle.

5.1.3 Flux Distributions

The dimensionless flux distributions in each bifurcation for inspiratory and expiratory flows are presented in Figure **5-8**. There were similarities among the three bifurcations. In all cases, for inspiratory flow the flux distribution in the parent branch was symmetric with respect to both the bifurcation and normal planes, while the flux distributions in the daughter branches were symmetric only with respect to the bifurcation plane. The fluxes through the parent branch walls of each bifurcation progressively decreased in the downstream direction. Close to the exit of the parent branch in the 45° bifurcation, the flux began to increase. This effect was absent in the other two bifurcations. It is unclear whether this was entirely due to the branching angle or to the difference in the manner the bifurcations were constructed (see Section **3.1**). Since the region of high flux around the carina spread more towards the parent branch in the 90° bifurcation than in the 135° bifurcation, it is likely that the aforementioned increase in flux close to the parent branch exit in the 45° geometry was at least partly an effect of the branching angle.

In all cases, local hot spots were located at the carina during inspiratory flow. Furthermore, the flux along the inner walls was greater than that along the outer walls, and as the branching angle increased, the region of high flux along the inner wall spread more towards the outer wall.

For expiratory flow, the flux distribution along the perimeter of the daughter branch cross-sections appeared fairly axisymmetric along most of the daughter branch wall but as the branching angle increased, the areas of axisymmetric flux distribution decreased, indicating that the effect of the bifurcation was felt further upstream as the branching angle increased. Two sets of hot spots were observed. The first was located in the transition region near the carina but displaced towards the parent branch (not readily visible in all cases at the scale and magnification used in Figure **5-8**, but see Figure **4-10B** for a close up of this hot spot in the 90° bifurcation). This hot spot moved closer to the carina and increased in magnitude as the branching angle increased. In the 45° bifurcation, the other hot spot was located on the parent wall distal to the airway opening. As the branching angle increased, this second hot spot increased in intensity and moved more distally, until in the 135° bifurcation it lay entirely in the transition region. The relative magnitudes of the hot spots depended on the branching angle, the magnitude of the second hot spot being higher than the first in the 45° bifurcation and the reverse being true in the 90° and 135° bifurcations. The magnitudes of the flux at the hot spots were greater for inspiratory flow than for expiratory flow.

The distributions of the circumferentially-averaged dimensionless flux ($\overline{N}$) in the parent and daughter branches of the three bifurcations are presented in Figure **5-9**. (Note that the analytical solution for the flux was patched to the numerical solution in the vicinity of the upstream branch flow entrances for both inspiratory and expiratory flow as described in Section **4.1.1**.) During inspiratory flow, the circumferentially-averaged fluxes in the three geometries were virtually identical throughout most of the parent branch ($s < 6$), except that at about $s = 5.5$, $\overline{N}$ in the 45° bifurcation began to rise, as expected from the flux distributions shown in Figure **5-8**. No definite trend in the magnitude of the peak $\overline{N}$ in the daughter branches is evident from Figure **5-9**. $\overline{N}$ was greater for the larger branching angles throughout most of the length of the daughter branch.

For expiratory flow, $\overline{N}$ was identical for all three branching angles throughout most of the length of the upstream branches, i.e., the daughter branches, as was the case for inspiratory flow. The value of $\overline{N}$ reached a minimum at $s = 6$ for the 90° and 135° bifurcations and at $s = 5.5$ for the 45° bifurcation. In the parent branch, $\overline{N}$ increased as the branching angle increased and was fairly uniform through most of the length of the parent branch in the 45° bifurcation, but the distribution of $\overline{N}$ became less and less uniform as the branching angle increased. Furthermore, as the branching angle increased, the relative maximum value of the circumferentially averaged dimensionless flux $\overline{N}_{max}$ in the parent branch increased, and the location of this maximum flux also shifted upstream. The magnitudes and locations of $\overline{N}_{max}$ in each bifurcation are as follows: $\overline{N}_{max} = 3.05$ at $s = 3.05$, $\overline{N}_{max} = 4.96$ at $s = 4.05$, and $\overline{N}_{max} = 6.45$ at $s = 4.95$ in the 45°, 90°, and 135° bifurcations, respectively.

In order to compare the magnitudes of the hot spots at the carina for inspiratory flow in each of the bifurcations, we defined an area along the walls of the transition-daughter branch region surrounding the carina that was symmetric about the bifurcation plane (i.e., symmetric about $\phi_d = 90^\circ$) and spanned a total angle $\boldsymbol{\Phi}$ about this intersection (Figure **5-10A**). The length of this region along the inner wall from the carina to the opposite end was 0.7 units of dimensionless length, i.e., $\frac{1}{5}$ of the daughter branch length. The average dimensionless flux $\langle N \rangle$ over a dimensionless area A is computed as follows

$$\langle N \rangle = \frac{1}{A} \int_A N \, dA \qquad \textbf{5.1}$$

We examined the average dimensionless flux $\langle N \rangle_{\boldsymbol{\Phi}}$ in the above-defined area $A_{\boldsymbol{\Phi}}$ for various values of $\boldsymbol{\Phi}$. The results are presented in Figure **5-10B**.

In the 45° and 90° bifurcations, $\langle N \rangle_{\boldsymbol{\Phi}}$ increased with decreasing $\boldsymbol{\Phi}$ and then began to plateau. On the other hand, in the 135° bifurcation, $\langle N \rangle_{\boldsymbol{\Phi}}$ was insensitive to $\boldsymbol{\Phi}$ for the range of $\boldsymbol{\Phi}$ examined. $\langle N \rangle_{\boldsymbol{\Phi}}$ became more sensitive to $\boldsymbol{\Phi}$ as the branching angle got smaller. The value at which $\langle N \rangle_{\Phi}$ plateaus is an indicator of the magnitude of the hot spot at the carina. Figure **5-10** shows that the magnitude of the hot spot is greatest for the 45° bifurcation and diminishes as the branching angle increases. This effect can be explained by the thickening of the momentum and concentration boundary layers in the immediate vicinity of the carina as the branching angle increased.

5.1.4 Rate of Uptake/Average Fluxes

The slightly different methods of geometry construction, especially in the branching region, that were necessary to create each bifurcation with a different branching angle resulted in the bifurcations having somewhat different areas. (The areas of each region are listed in Table **3-1**.) Therefore, instead of comparing rates of uptake, the average dimensionless fluxes $\langle N \rangle$, which represent the rate of uptake normalized by area, were compared. Because of inaccuracies in the calculation of flux at the flow entrances due to the singularity at that boundary, equation **4.7** was used to calculate the uptake rate in the upstream branches whereas equation **5.1** was used to calculate $\langle N \rangle$ everywhere else.

Figure **5-11** shows the average dimensionless fluxes in the parent and daughter branches and in the transition region, as well as the overall average flux for the entire bifurcation for the three geometries. For inspiratory flow, the overall $\langle N \rangle$ increased with branching angle. This trend was however not as a result of increases in $\langle N \rangle$ over the entire bifurcation but due only to increases in the transition region and daughter branches.

As expected, $\langle N \rangle$ in the parent branch was very similar for all geometries. The greatest differences in $\langle N \rangle$ arose in the transition regions, where there was an almost two-fold increase in $\langle N \rangle$ from 45° to 135°. This increase in $\langle N \rangle$ in the transition region as the branching angle increased occurred in spite of the attenuation of the hot spot at the carina as the branching angle increased.

For expiratory flow, the overall $\langle N \rangle$ also increased with increasing branching angle. As was the case for inspiratory flow, $\langle N \rangle$ in the upstream branches, i.e., the daughter branches, was the essentially the same for all branching angles, and the increase in overall $\langle N \rangle$ as the branching angle increased was due to increases in $\langle N \rangle$ in the transition zone and downstream branch, i.e., the parent branch. In contrast to inspiratory flow, $\langle N \rangle$ in the transition region was considerably smaller than the value in the upstream branches for all branching angles except for 135°, for which $\langle N \rangle$ was comparable to that in the daughter branches. In all cases, the parent branch had the lowest $\langle N \rangle$ of all the zones. The differences in average flux through these zones among the different bifurcations were even more pronounced than for inspiratory flow, leading to a more marked difference in overall $\langle N \rangle$ as the branching angle increased.

5.2 RESULTS – EFFECT OF MODE OF BRANCHING

In order to examine the effect of the mode of branching on O_3 uptake, simulations of inspiratory and expiratory flow and O_3 uptake were conducted at a Reynolds number of 300 in an idealized symmetric bifurcation and an idealized monopodial bifurcation, both with a branching angle 90° and with equal flows in the daughter branches imposed during inspiration as well as expiration (see Section **3.1**). An infinitely fast reaction at the gas-RTLF interface was assumed; thus a zero concentration of O_3 at the walls of the bifurcation was specified.

5.2.1 Flow Fields

Equal flows through both daughter branches of the monopodial bifurcation resulted in Reynolds numbers of 150 and 214 in the major and minor daughters, respectively. The dimensionless velocity distributions in the bifurcation planes of the 90° symmetric dichotomous bifurcation and the 90° monopodial bifurcation are compared in Figure **5-12**. For inspiratory flow, the velocity distributions throughout most of the parent branch are very close in both geometries. However, the flow structure in the monopodial parent branch where the flow bends in order to enter the minor daughter branch is different from that at the same axial position in the parent branch of the symmetric bifurcation. In the minor daughter branch of the monopodial bifurcation, the velocity distribution was skewed toward the inner wall, and a relatively large low-velocity backflow zone was created on the outer wall near the flow entrance because of flow separation as the fluid navigated the bend (Figure **5-12**). Along the outer wall of the major daughter branch of the monopodial bifurcation, the diversion of flow into the minor daughter also resulted in a sizeable zone of stagnant flow, in which there was recirculation and backflow (Figure **5-12**). As in the symmetric bifurcation daughter branches, the flow was skewed toward the inner wall of the major daughter branch, and in addition, a large region of low velocity was found throughout the outer wall of the major daughter branch. As in the symmetric bifurcation, the velocity distribution in the monopodial geometry was symmetric with respect to the bifurcation plane. The maximum velocity within the monopodial bifurcation was greater than that in the symmetric bifurcation.

For expiratory flow, the flow distributions in the daughter branches of the symmetric bifurcation and the minor daughter branch of the monopodial bifurcation were very similar because in both cases the flow rates and cross-sectional areas were the same. The velocity in the major daughter branch was however low in comparison because it had a flow rate equal to that in the minor daughter branch but about twice the cross-sectional area. Just as in the symmetric bifurcation, the fluid from both monopodial daughter branches merged to form a high velocity sheet in the parent branch that followed the curve of that tube, but unlike in the symmetric geometry, this jet was not located on the normal plane but was positioned away from the parent branch axis and toward the outer wall. Thus, the velocity distribution in the monopodial parent branch was symmetric only with respect to the bifurcation plane unlike that in the symmetric bifurcation which was symmetric with respect to both the bifurcation and normal planes. Again, the maximum velocity within the monopodial bifurcation was greater than that in the symmetric bifurcation, but slightly lower than that for inspiratory flow. Similar to what was observed in the symmetric bifurcation, a quadruple vortex pattern was also seen at the outlet of the parent branch (Figure **5-13**). In contrast to the vortices in the symmetric bifurcation, the vortex pattern in the monopodial bifurcation was symmetric only with respect to the bifurcation plane, and the vortices were not equal in size. The two vortices on the outer half of the parent branch were significantly larger and more centered in their respective quadrants than those adjacent to the inner wall, which were very small and located closer to the wall.

5.2.2 Concentration Distributions

The distributions of dimensionless O_3 concentration in the bifurcation planes of the 90° symmetric dichotomous bifurcation and the 90° monopodial bifurcation are displayed in Figure **5-14**. The concentration distributions for both inspiratory and expiratory flows were similar to their corresponding velocity distributions.

For inspiratory flow, the concentration distributions in the parent branches of both geometries were very similar. However, the concentration distribution in the monopodial bifurcation was slightly skewed towards the parent branch inner wall near the entrance of the flow into the transition region. As in the symmetric bifurcation, fluid with a very high O_3 concentration impinged the carina of the monopodial bifurcation, and the concentrations in both monopodial daughter branches were skewed toward the inner walls, leading to high concentration gradients. Stagnation flows and recirculation along the outer walls of both daughter branches also produced low concentrations in those areas because of the increased residence time of O_3.

For expiratory flow, the concentration distribution in the monopodial minor daughter branch was very similar to that in the symmetric daughter branches. The fluid in the high-velocity sheet in the parent branch had a high O_3 concentration. As in the case of inspiratory flow, O_3 concentration was low in the stagnation region in the parent branch near the parent-minor daughter junction. The concentration gradients were higher along the outer parent wall than the inner wall because of the skewing of the concentration toward the outer wall. As with the velocity distribution, the concentration distribution in the monopodial parent branch was symmetric only with respect to the bifurcation plane.

5.2.3 Flux Distributions

The distributions of dimensionless flux along the walls of the symmetric and monopodial bifurcations are shown in Figure **5-15**. For inspiratory flow, the magnitudes of the fluxes in the parent branches of both geometries were similar, were axisymmetric, and steadily decayed in the downstream direction, except near the parent-minor daughter junction in the monopodial parent branch, where the flux along the inner wall increased somewhat. This indicates that the effects of the branching flow were propagated upstream in the monopodial bifurcation. In both the symmetric and monopodial bifurcations, the hot spots of flux downstream of the flow entrance were located at the carina and were of similar magnitude. In both geometries, the fluxes were higher on the inner walls of the daughter branches, but the monopodial major daughter had a larger region of low flux than either the symmetric daughter branches or the minor daughter branch. The lower flux in the major daughter branch was partly attributable to the low Reynolds number in that branch.

During expiratory flow, the flux along the major daughter branch wall was nearly axisymmetric and decayed in the downstream direction, as was the case through most of the daughter branch walls of the symmetric bifurcation. This was not the case, however, in the minor daughter branch, indicating that the effect of the bifurcation was propagated upstream in the minor daughter. This may occur partly because the minor daughter branch is at a larger angle to the parent branch axis than are the major daughter branch and the symmetric daughter branches. In both geometries, the flux distributions were symmetric with respect to the bifurcation plane. The flux distribution in the parent branch of the symmetric bifurcation, but not in the monopodial geometry, was also symmetric about the normal plane. A hot spot of flux was located on either side of the parent branch of the monopodial bifurcation but, in contrast to the symmetric bifurcation, it was not centered on the parent wall. The magnitude of this hot spot was much smaller than the corresponding hot spot in the symmetric bifurcation. A region of low flux that corresponded to the stagnation zone was also found along the inner wall of the monopodial parent branch in the vicinity of the parent-minor daughter junction. In the monopodial bifurcation, another hot spot appeared on the minor daughter branch walls at the parent-minor daughter junction as a result of high concentration gradients created there as the flow navigated the sharp bend to enter the parent branch (Figure **5-14**).

The distributions of the circumferentially-averaged dimensionless flux ($\overline{N}$) in the parent and daughter branches of two types of bifurcations are displayed in Figure **5-16**. (In the upstream branches the analytical solution for the flux was patched to the numerical solution in the vicinity of the flow entrances for both inspiratory and expiratory flows.) For inspiratory flow, the values of $\overline{N}$ in the parent branches of both geometries were nearly identical. However, $\overline{N}$ was different along the daughter branch walls, with the minor and major daughter branches of the monopodial bifurcation having the highest and lowest values of $\overline{N}$, respectively. The peak value of $\overline{N}$ at the entrances to the daughter branches followed the same trend.

For expiratory flow, $\overline{N}$ at the entrance of the major daughter branch was lower than that in both the minor and symmetric daughter branches owing to the low Reynolds number in the major daughter branch. The fluxes at the entrances and along the walls of the minor and symmetric daughter were similar. $\overline{N}$ rose at the outlet of the major daughter branch but dipped at the minor and symmetric daughter outlets. In addition, $\overline{N}$ along the parent walls of the symmetric bifurcation was higher than $\overline{N}$ in the monopodial bifurcation.

5.2.4 Average Fluxes

Because of the dissimilarities in the surface areas of analogous regions of the two geometries, average fluxes $\langle N \rangle$ in a region, rather than rates of uptake, were compared. As expected, for inspiratory flow, $\langle N \rangle$ was similar in both parent branches. The slightly higher value of $\langle N \rangle$ in the monopodial branch was due to the propagation of the effect of the bifurcation, resulting in a higher flux near the parent branch outlet. In contrast to what was observed in the symmetric bifurcations, $\langle N \rangle$ was lower in the monopodial transition region than in either the parent branch or the minor daughter branch and was comparable in magnitude to $\overline{N}$ in the major daughter branch. $\langle N \rangle$ in the transition region of the symmetric bifurcation was about 2.5 times higher than that in the monopodial bifurcation. The monopodial minor daughter branch had the highest average flux of all the regions in both geometries. $\langle N \rangle$ in the major daughter branch was only about half that in the minor daughter. $\langle N \rangle$ was essentially the same in the parent and daughter branches of the symmetric bifurcation. The overall average flux was higher in the symmetric bifurcation than in the monopodial bifurcation.

For expiratory flow, the symmetric daughter and monopodial minor daughter branches had similar values of $\langle N \rangle$ due to equal Reynolds number in those branches, whereas $\langle N \rangle$ was smaller in the monopodial major daughter branch because of its lower Reynolds number. In both geometries, the transition region had a lower $\langle N \rangle$ than the daughter branches, and the average flux in transition region was greater in the symmetric bifurcation than in the monopodial bifurcation. $\langle N \rangle$ in the parent branch was also greater in the symmetric bifurcation. In the monopodial bifurcation, $\langle N \rangle$ in the parent branch was close to the value in the transition region. In the symmetric bifurcation, there was a clear decrease in $\langle N \rangle$ from the entrance of flow to the outlet, but this trend was not observed in the monopodial bifurcation. As was the case for inspiratory flow, the overall

$\langle N \rangle$ in the symmetric bifurcation during expiratory flow was greater than that in the monopodial bifurcation.

5.3 DISCUSSION

5.3.1 Effect of Branching Angle

The works of Horsfield and coworkers (1971) and Raabe and coworkers (1976) reveal a great variability in human airway branching angles from generation to generation. In this chapter, the effect of branching angle on O_3 dose distribution was examined by simulating gas flow and O_3 uptake in three idealized, symmetric dichotomous single airway bifurcations with branching angles of 45°, 90°, and 135°. The simulations predicted a branching angle dependence of total O_3 uptake rates and flux distribution patterns. These effects were due to differences in flow patterns which impacted the concentration distributions in the three bifurcations. The simulations also predicted an enhancement in overall O_3 uptake as the branching angle increased for both inspiratory and expiratory flow, the transition regions and downstream branches being the sites of increased uptake. These results are consistent with the experimental observations of Caro and colleagues (2002), who flowed an acidic vapor in the inspiratory direction through litmus-coated three-generation airway models and observed faster reddening on walls of the daughter branches arising from a bifurcation with a larger branching angle, signifying a higher rate of mass transfer.

For inspiratory flow, the hot spot of flux downstream of the flow entrance was always located at the carina, regardless of the branching angle. Nevertheless, branching angle-dependent features of uptake distribution were observed, namely, the higher magnitude of the flux at the hot spot at the lower branching angles in spite of lower overall average fluxes, and the larger high flux regions along the daughter branch walls at the higher branching angles (Figures **5-8** and **5-10**). Taken together, these results suggest that although O_3-induced tissue damage may generally be more prominent downstream of a bifurcation with a larger branching angle, damage may be more severe immediately surrounding the carina of a bifurcation with a smaller branching angle. However, this conclusion has no experimental support since, to our knowledge, no experimental studies on the effect of airway branching angles on O_3-induced cellular damage has been conducted.

During expiratory there was also an increase in uptake rate with branching angle. In addition, there was a branching angle dependence of the locations of the two sets of local hot spots that were observed downstream of the flow entrance. As the branching angle increased, both sets of hot spots moved closer to the carina. These results, while interesting, are not likely to be important since most O_3 absorption probably occurs during inspiration in most generations.

5.3.2 Effect of Mode of Branching

The selection of appropriate outflow boundary conditions for the monopodial bifurcation is less obvious than for the symmetric bifurcation because of the difference in the cross-sectional areas of the two monopodial daughter branches. While there is still uncertainty regarding the accurate determination of the flow rate of air through a particular airway branch, some investigators have suggested that the flow through an airway branch is proportional to the number of distal terminal bronchioles or alveoli supplied by that segment (Horsfield and Cumming, 1968; Phillips and Kaye, 1998). Since the location of this single monopodial bifurcation depends on the level of physical exertion as well as the lung size (as discussed in Section **4.3.1**), the determination of an appropriate flow split is difficult. An equal flow split was selected for this study to enable direct comparison to the results of the simulations in the symmetric bifurcation. An alternative to this would be to split the flow in proportion to the cross-sectional area of each daughter branch, thereby ensuring equal velocities. Separate simulations conducted with this modified boundary condition (results not shown) predicted the same features described in Section **5.2**, namely, a local hot spot of flux at the carina and higher flux in minor daughter branch compared to that in the major daughter during steady inspiratory flow.

A comparison of O_3 uptake distributions in dichotomous and monopodial bifurcations is especially important since the results of inhalation toxicology studies performed on laboratory animals, which generally possess monopodially branching airways, require extrapolation to humans, who have relatively symmetric dichotomously branching airways. Single path models (SPMs), which have been the main means of numerically predicting O_3 dosimetry in the lower respiratory tract, do not differentiate between dichotomous and monopodial airway structures. Instead, each airway branch is modeled as a right circular cylinder without regard to species. In doing so, SPMs do not account for the effect of the mode of branching on airflow patterns. Differences in the mode of branching led to considerable local differences in O_3 dosimetry predicted by the three-dimensional CFD models that were described in the current chapter.

During inspiratory flow, hot spots of flux were located at the carina in both geometries, but in the monopodial bifurcation the minor daughter branch experienced a higher average flux than the major daughter branch. The latter result is consistent with the observations of Postlethwait and colleagues (2000), who found that O_3 injury, as measured by cell permeability to ethidium homodimer-1 (a permeability marker), was greater in the side branches than along the main axial pathway of isolated rat lung airways exposed to O_3. The specific site of increased injury was however located just downstream of the bifurcation, rather than right at the carina as predicted by our simulations. This slight shift in the location of increased injury may be due to irregular characteristics of real airways such as curvature at the carina and tapering of airway segments, features not represented in the idealized bifurcation.

The simulations also predict that compared to a monopodial bifurcation, the average flux of O_3 is higher in a symmetric bifurcation, suggesting that under equivalent conditions, the overall O_3 dose will be greater in a relatively symmetric dichotomous bifurcation, such as is found in humans, than in a monopodial bifurcation, such as is found in lab animals. Whether or not this translates to increased tissue damage will depend on several additional factors such as the relative sensitivities of the cells of animals of different species to O_3.

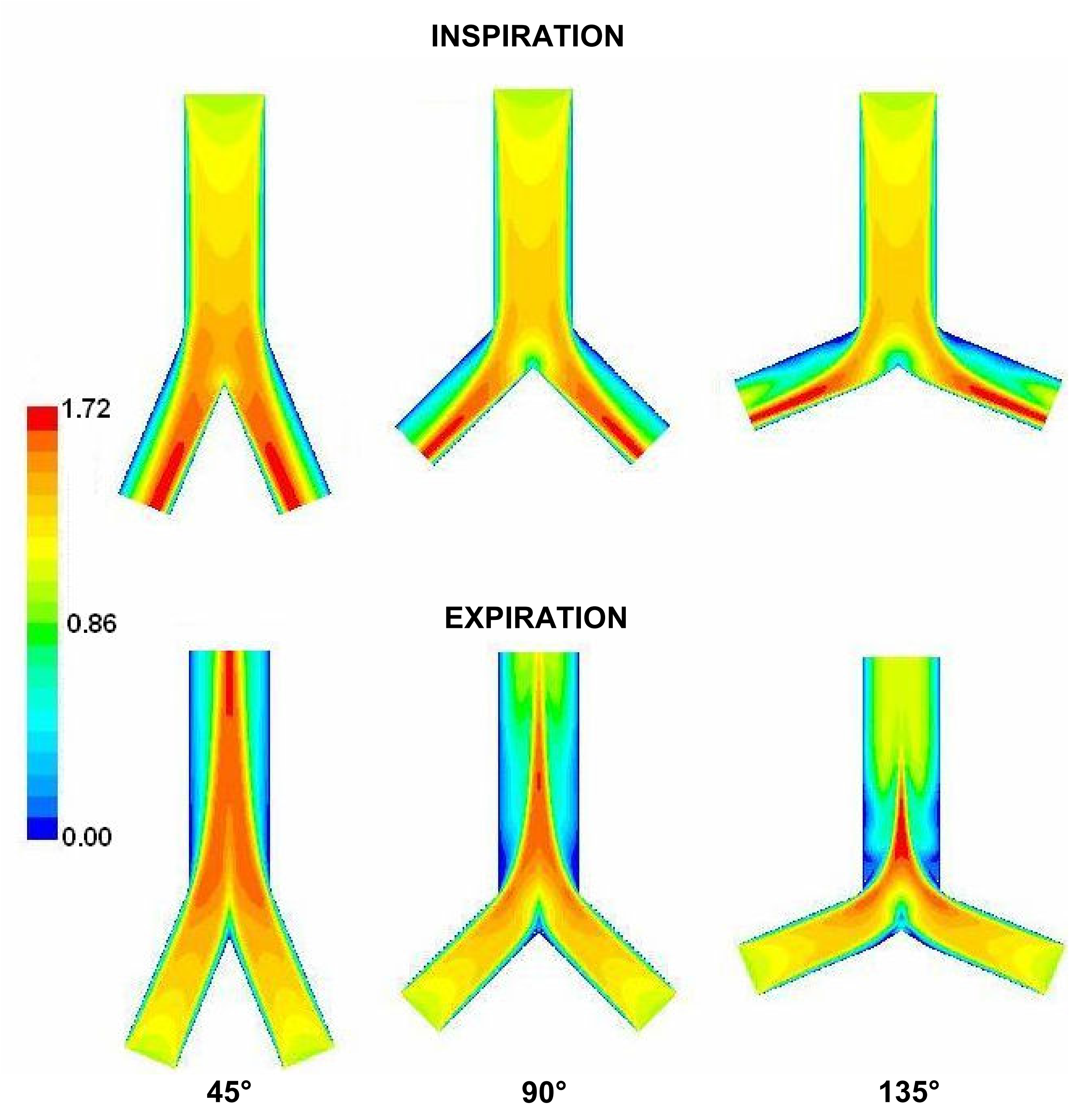

Figure **5-1**: Isocontours of the magnitude of dimensionless velocity in the bifurcation plane for inspiratory and expiratory flows and for three symmetric branching angles ($Re = 300$).

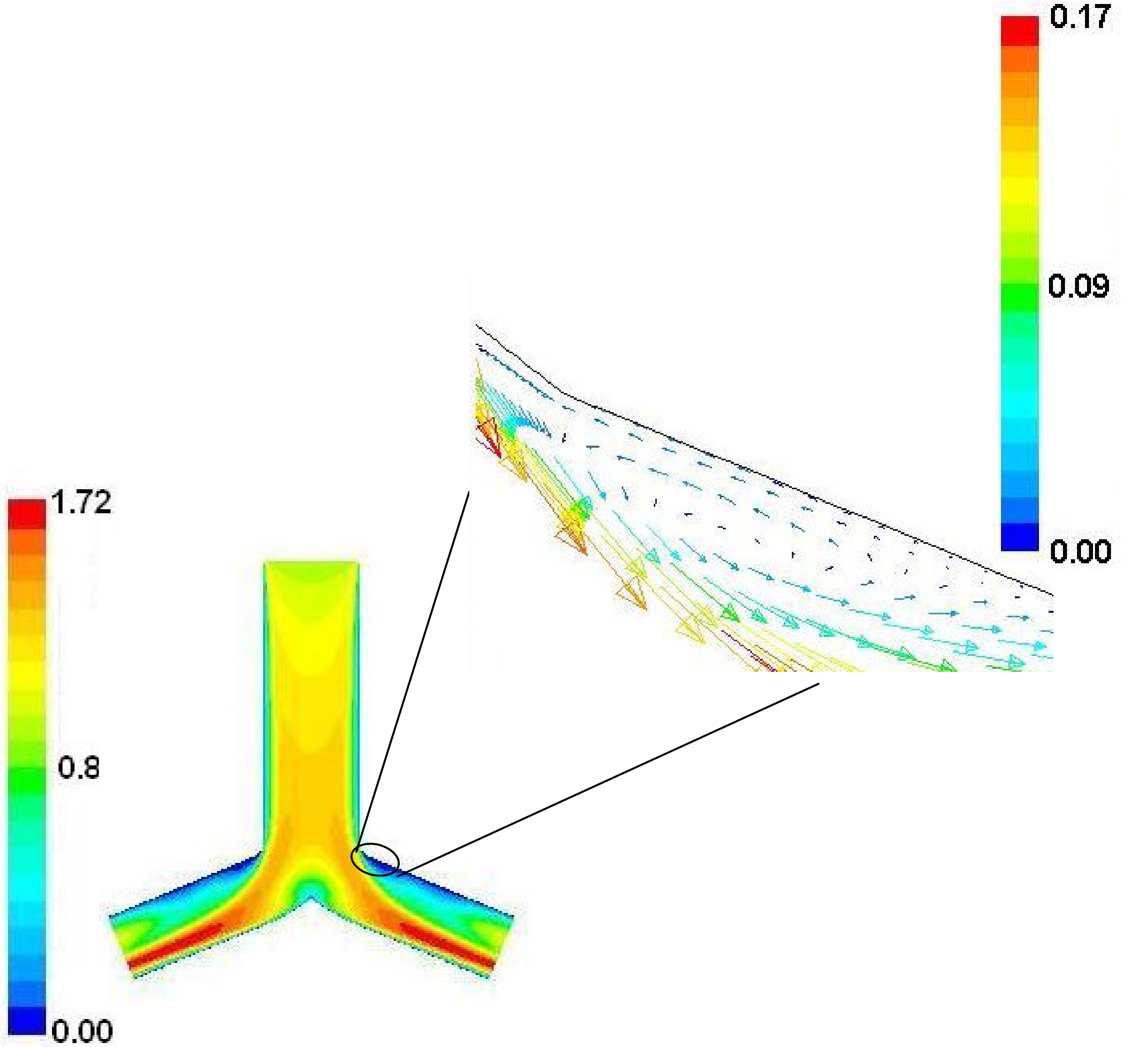

Figure **5-2**: Dimensionless velocity vectors during inspiratory flow in the plane of the bifurcation of the 135° symmetric bifurcation showing the region of backflow along the outer wall of the daughter branch ($Re = 300$). Vectors are colored by dimensionless velocity magnitude.

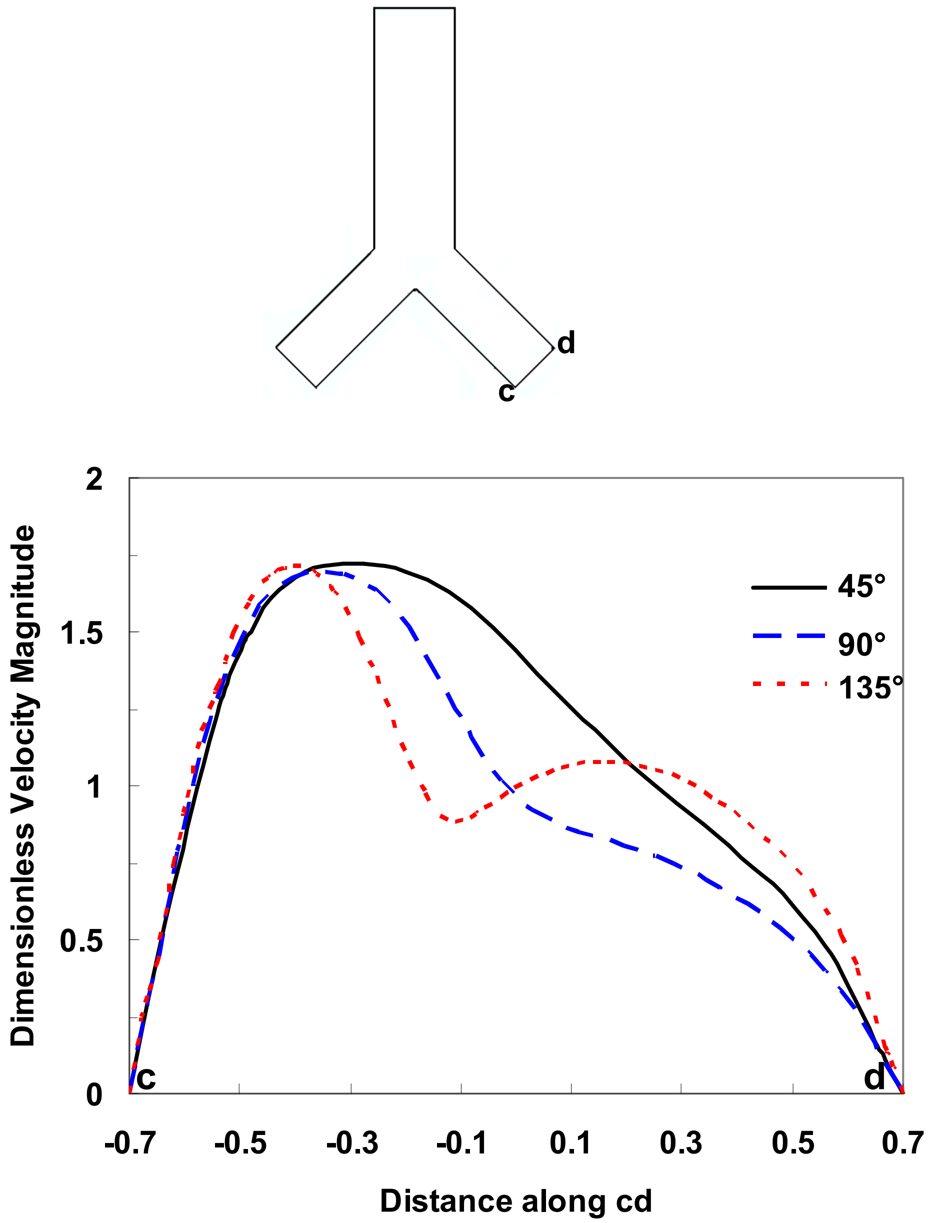

Figure **5-3**: Dimensionless velocity profiles in the bifurcation plane at the outflow boundaries of the daughter branches of the three symmetric bifurcations during inspiratory flow ($Re = 300$).

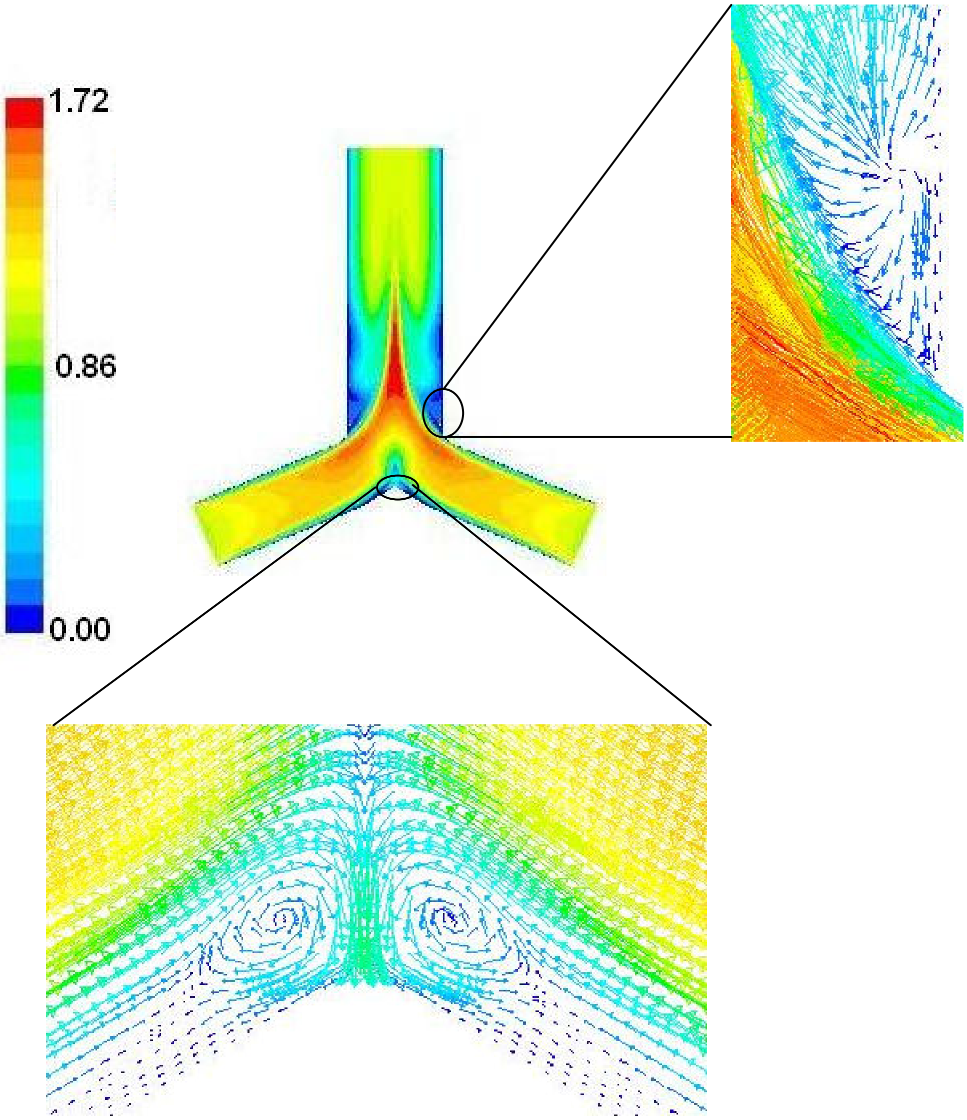

Figure **5-4**: Dimensionless velocity vectors in the bifurcation plane of the 135° symmetric bifurcation during expiratory flow ($Re = 300$) showing (A) the pair of counter-rotating vortices surrounding the carina and (B) the backflow regions along the parent branch walls. Vectors are colored by dimensionless velocity magnitude.

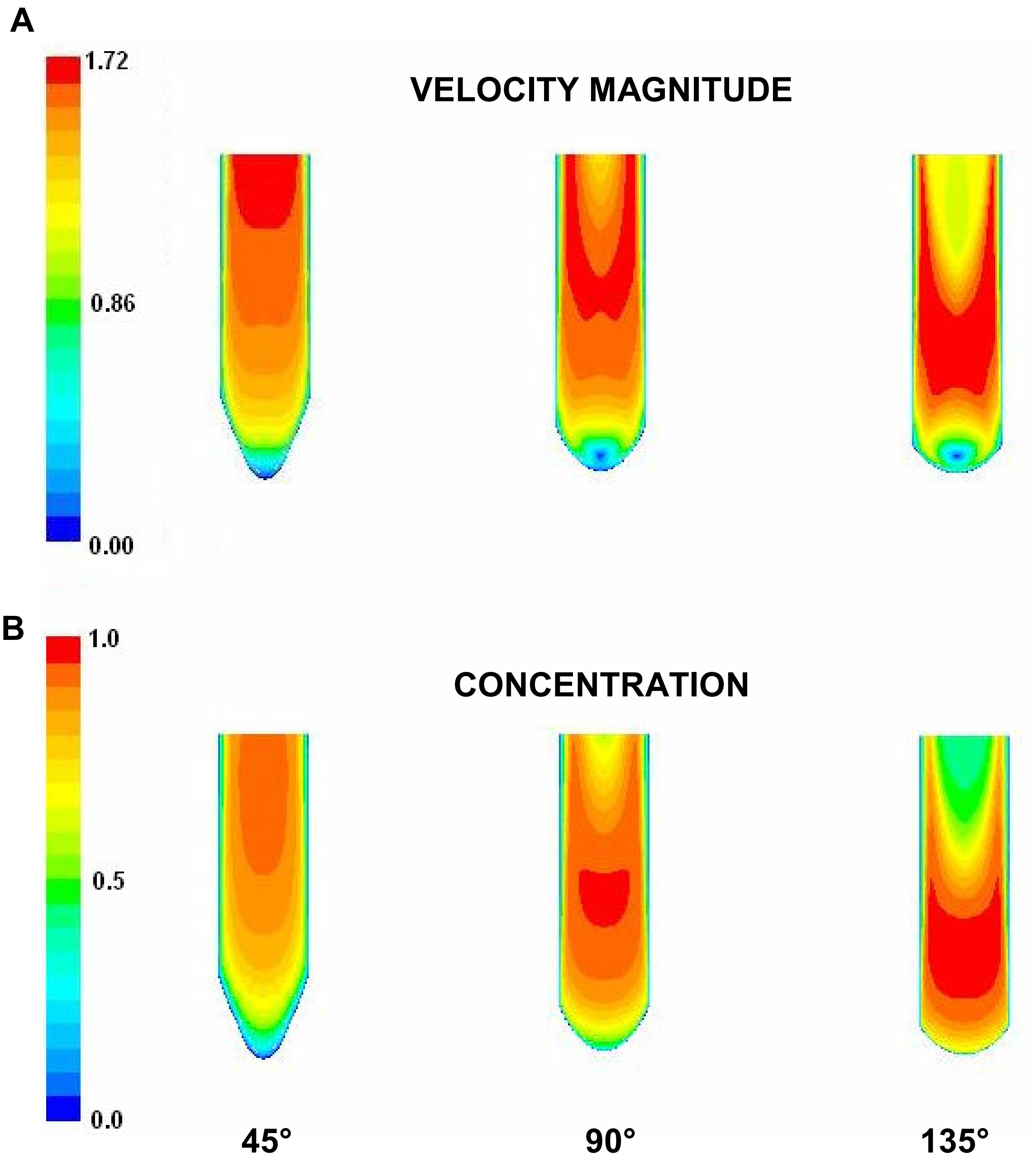

Figure **5-5**: Isocontours of (A) dimensionless velocity magnitude and (B) dimensionless concentration in the plane normal to the bifurcation plane for expiratory flow for three symmetric branching angles ($Re = 300$). The bottom of the cross-section corresponds to the carina.

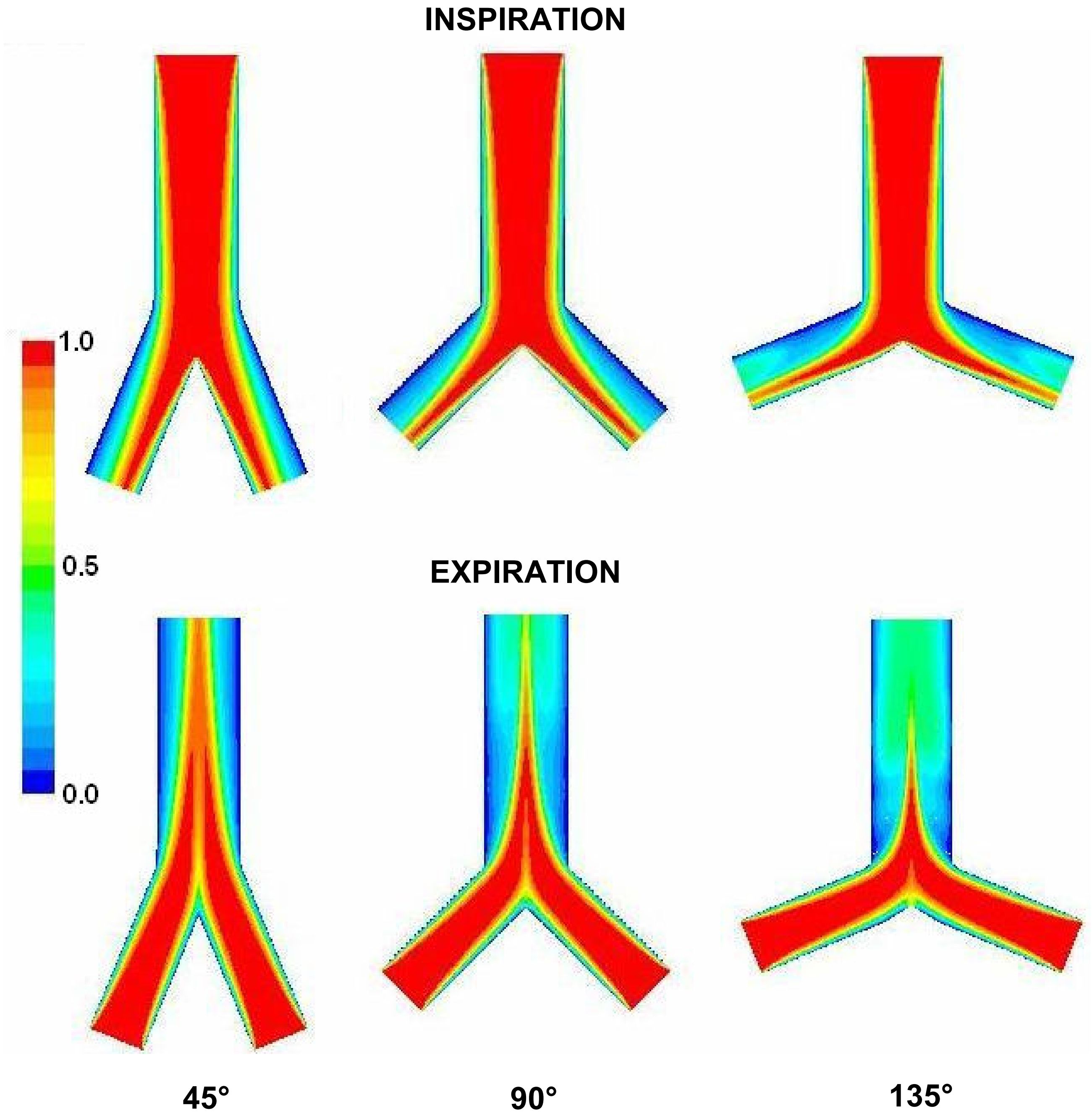

Figure **5-6**: Isocontours of dimensionless concentration in the bifurcation plane for inspiratory and expiratory flows and for three symmetric branching angles ($Re = 300$).

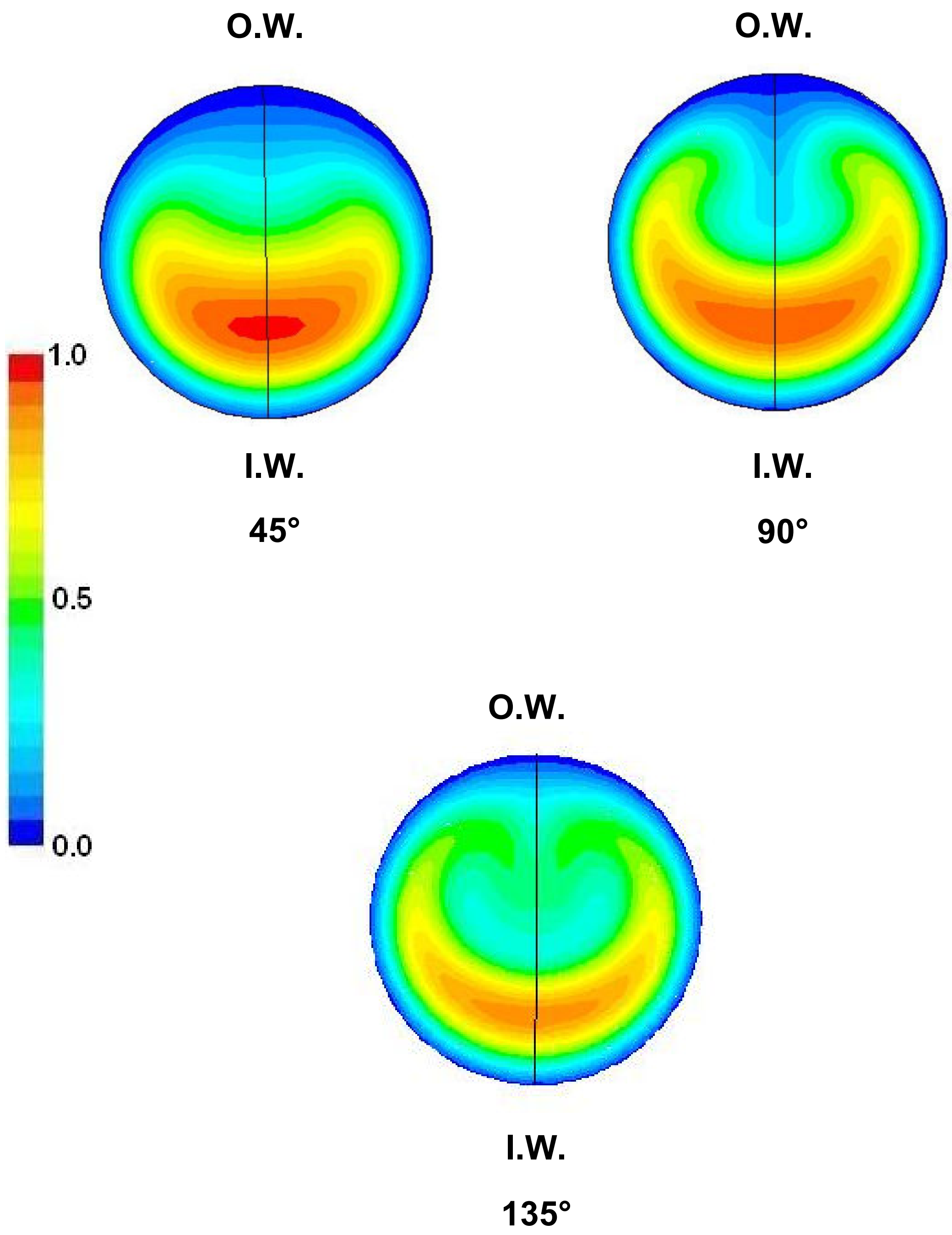

Figure **5-7**: Dimensionless concentration distributions at the outflow boundaries of the daughter branches of the idealized symmetric bifurcations during inspiratory flow ($Re = 300$). The lines denote the location of the bifurcation plane. I.W.: inner wall; O.W.: outer wall.

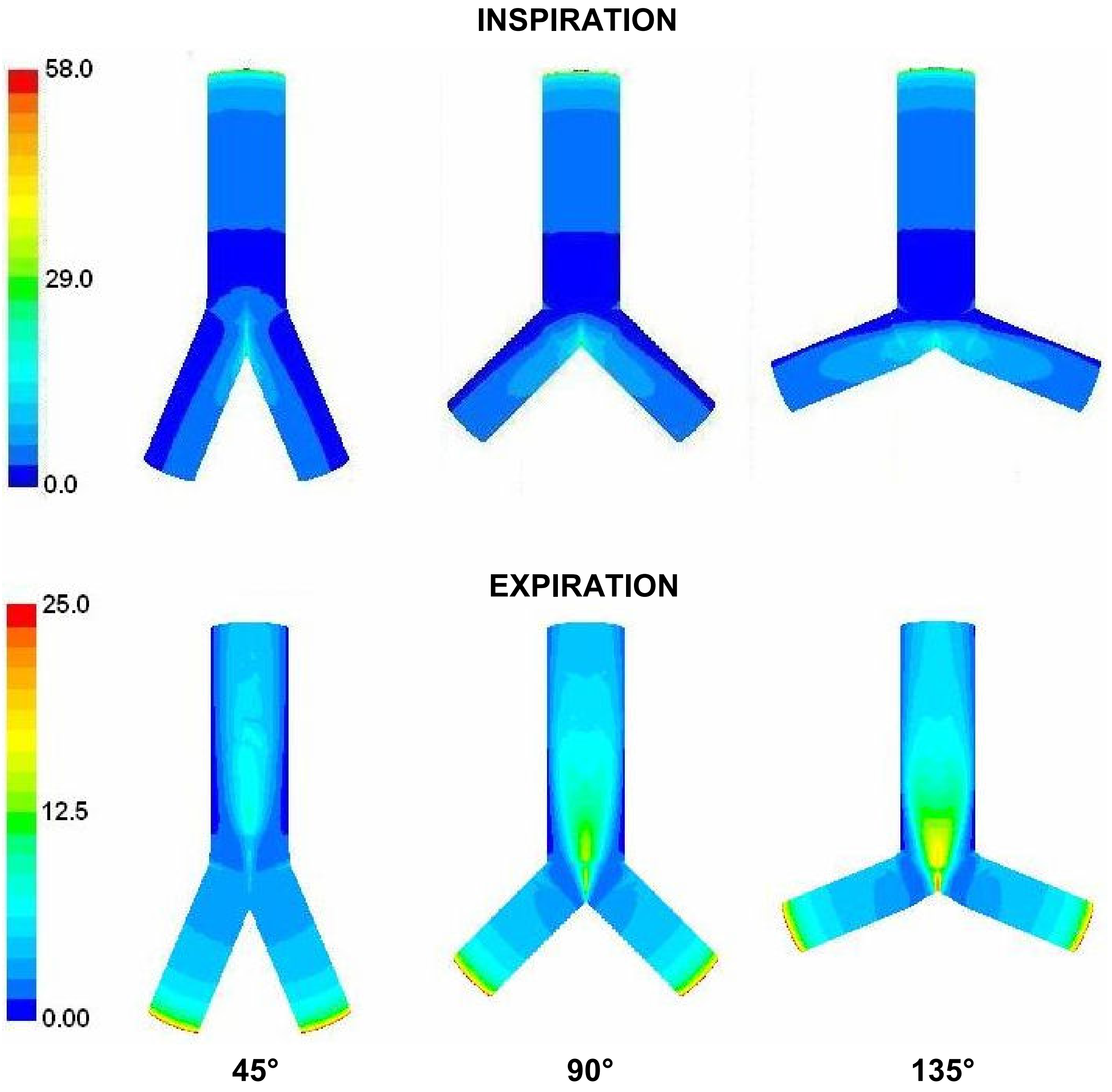

Figure **5-8**: Isocontours of the dimensionless flux N along the bifurcation walls for inspiratory and expiratory flows and for three symmetric branching angles ($Re = 300$).

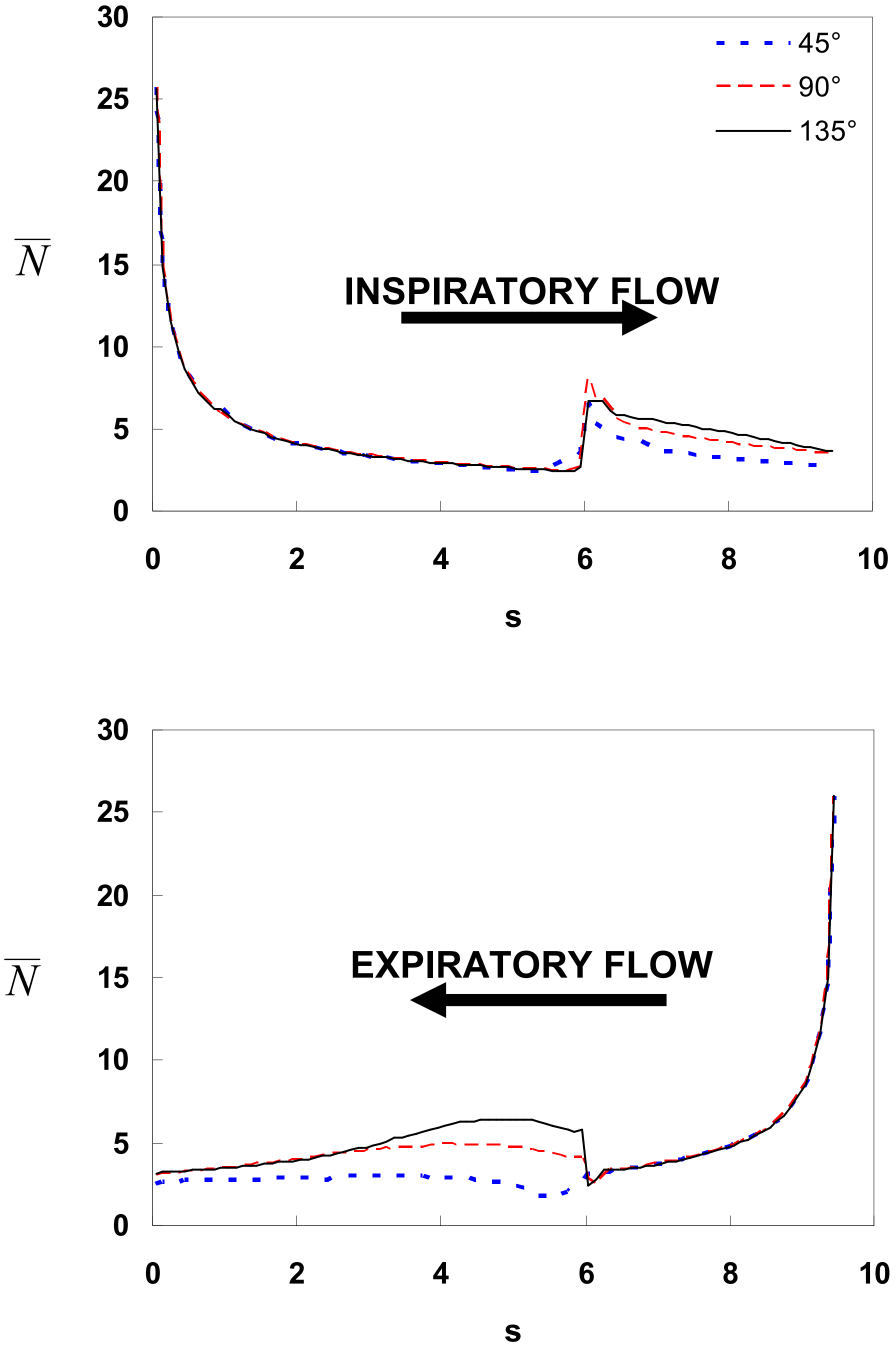

Figure **5-9**: Distribution of the circumferentially-averaged dimensionless flux $\overline{N}$ along the bifurcation walls for inspiratory flow (top panel) and expiratory flow (bottom panel) and for three different branching angles. The arrows indicate the flow direction.

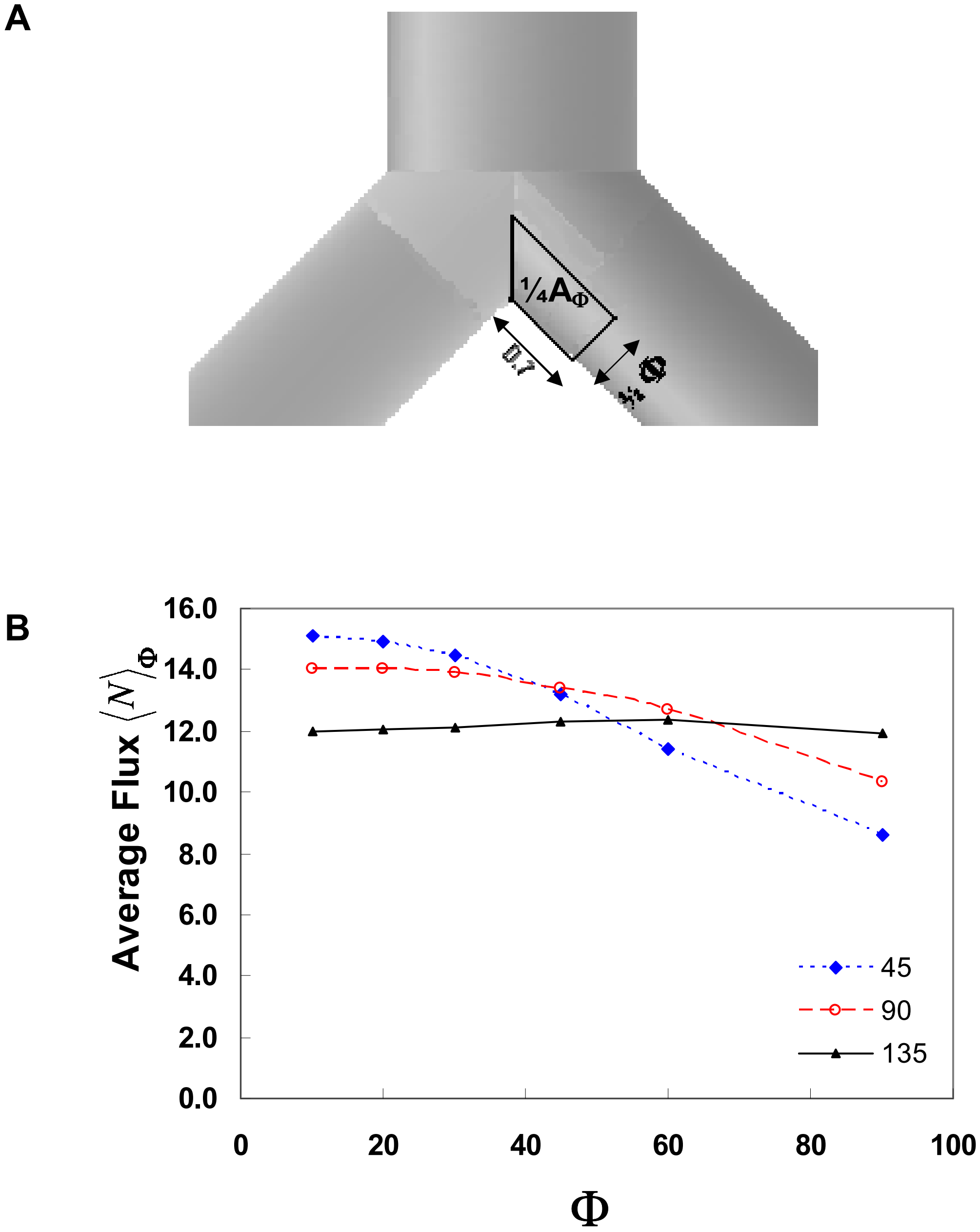

Figure **5-10**: (A) The enclosed area shows one-fourth of the area A_Φ, which is symmetric about both the bifurcation plane and the normal plane. (B) Average dimensionless flux $\langle N \rangle_\Phi$ through area A_Φ as a function of angle $\mathbf{\Phi}$ (all defined in Section **5.1.3**) in the three idealized symmetric bifurcations during steady inspiratory flow.

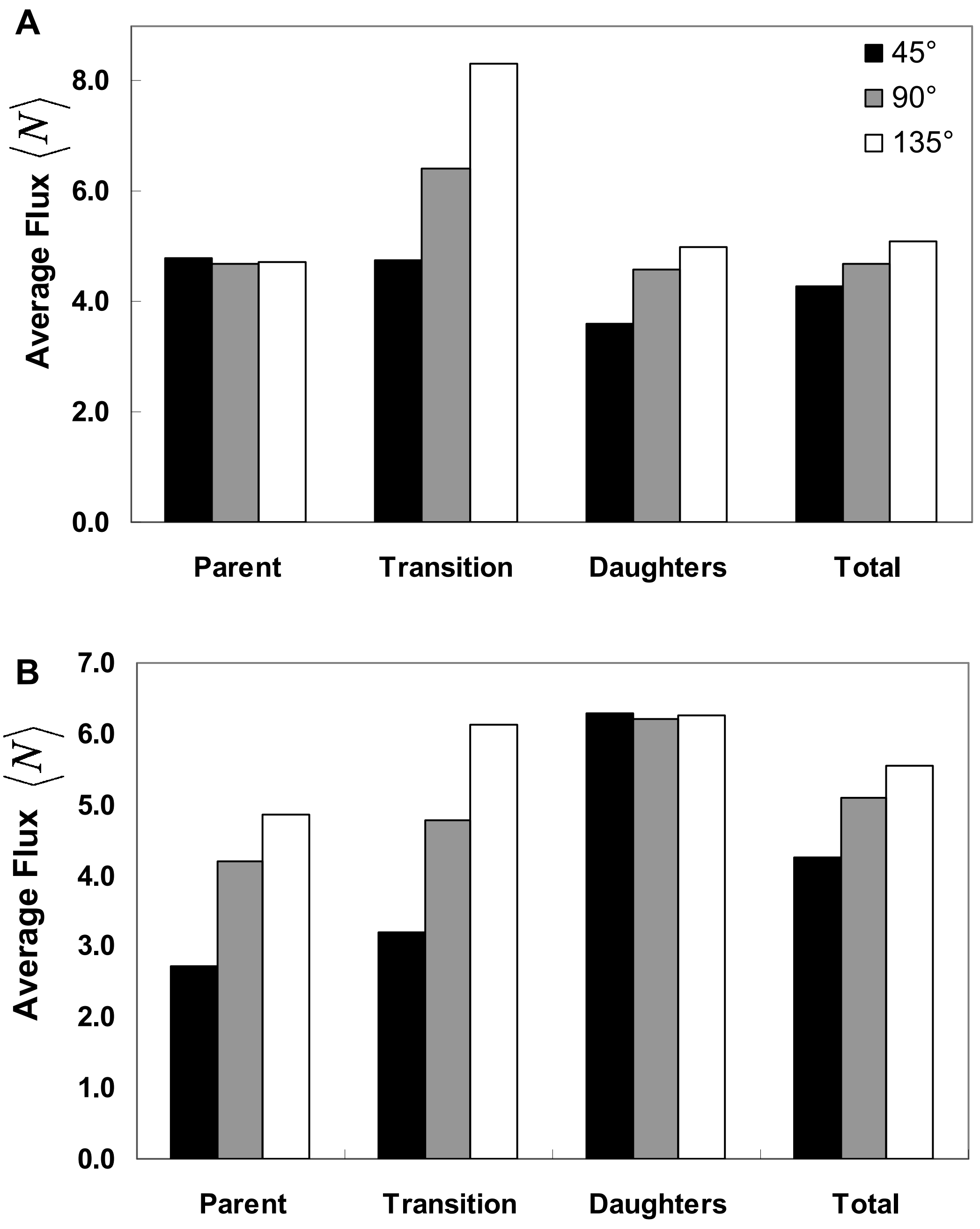

Figure **5-11**: Average dimensionless flux $\langle N \rangle$ in each bifurcation region and in the entire bifurcation for (A) inspiratory flow and (B) expiratory flow for three branching angles.

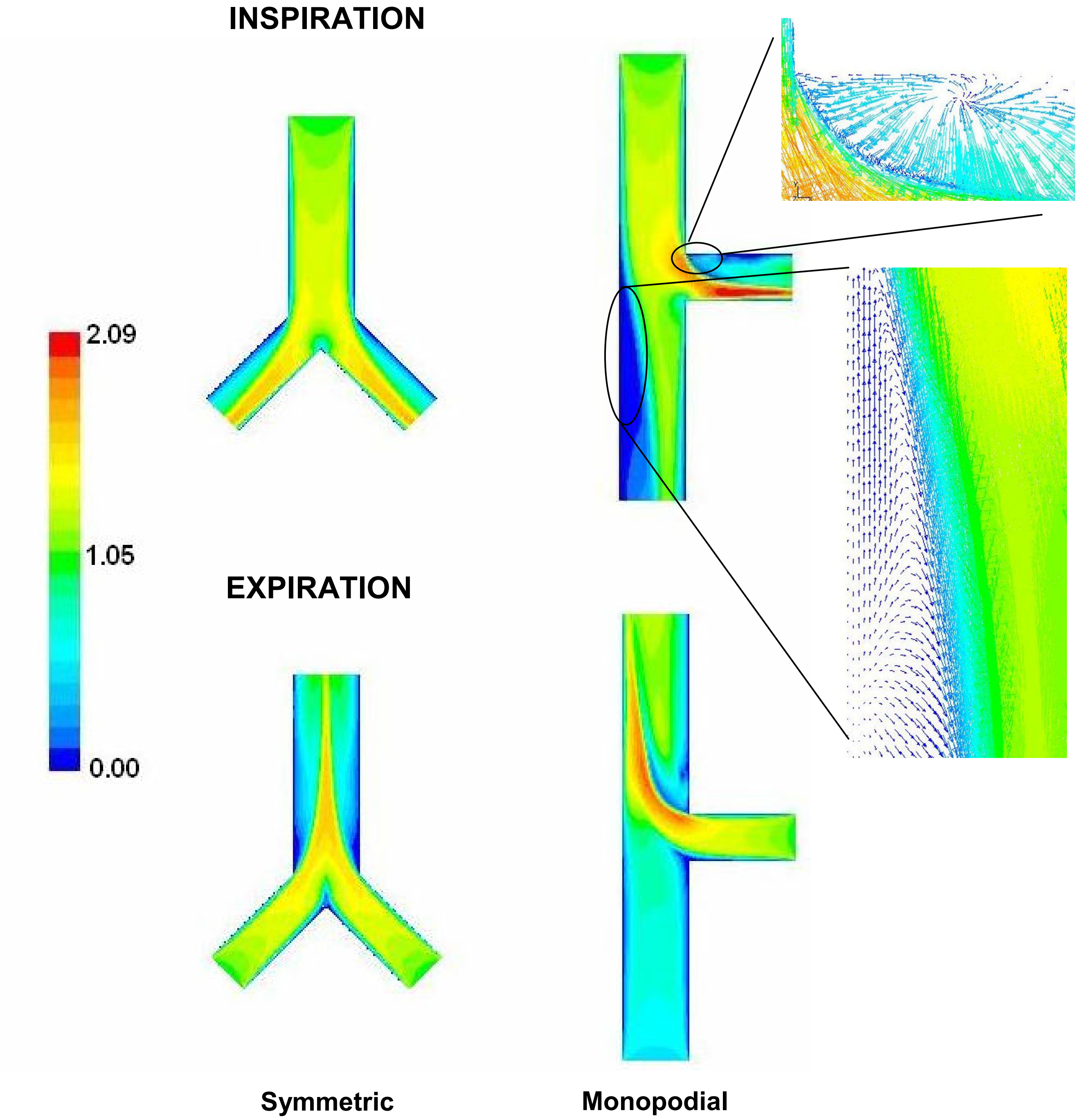

Figure **5-12**: Isocontours of the magnitude of dimensionless velocity in the bifurcation plane for inspiratory and expiratory flows in the symmetric and monopodial bifurcations ($Re = 300$). Also shown are dimensionless velocity vectors (colored by dimensionless velocity magnitude) showing regions of backflow during inspiratory flow in both daughter branches of the monopodial bifurcation.

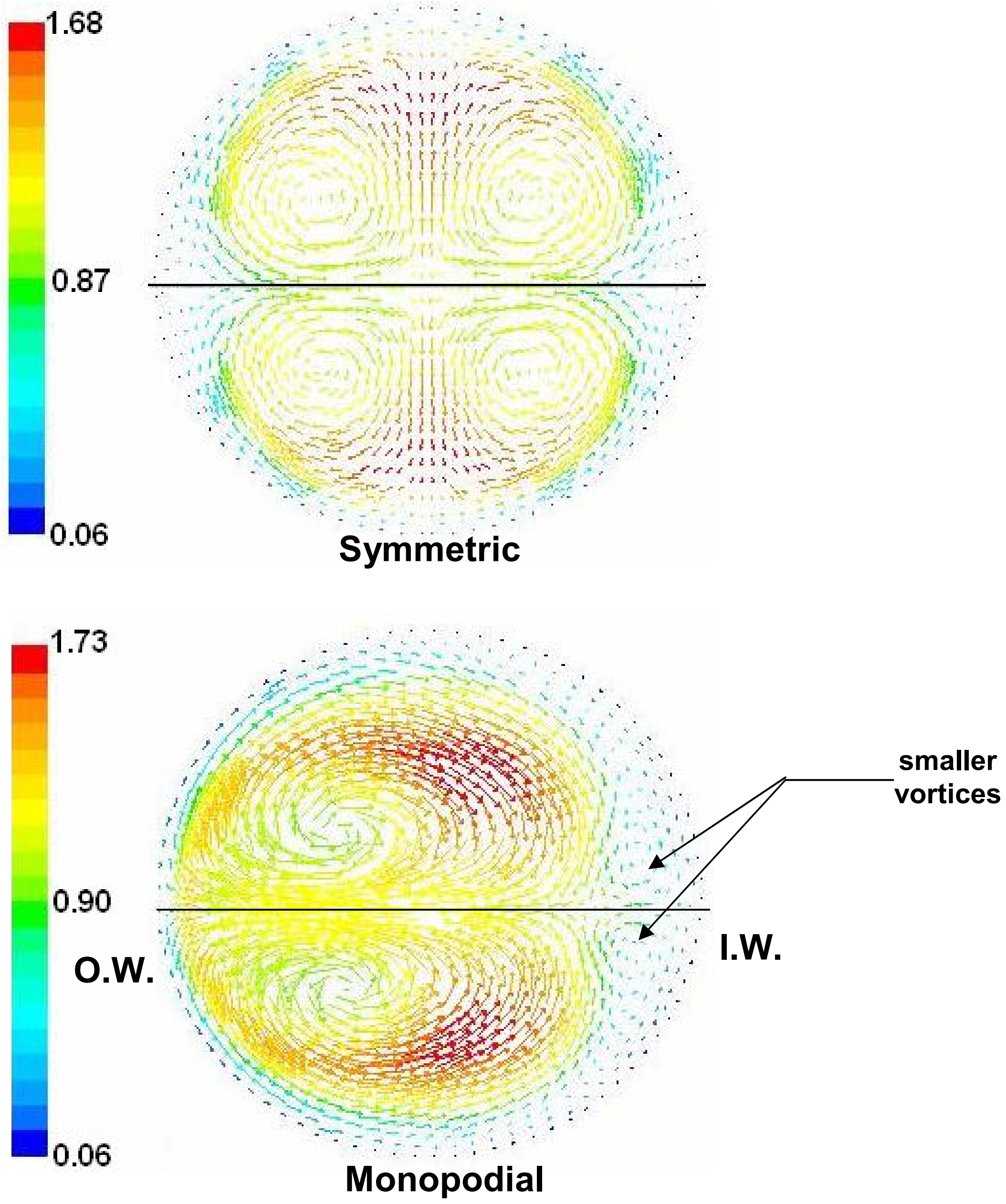

Figure **5-13**: In-plane velocity vectors on the outflow boundary of the parent branch in the symmetric (top panel) and monopodial (bottom panel) bifurcations during steady expiratory flow. Vectors are colored by dimensionless velocity magnitude. O.W.: outer wall, and I.W.: inner wall of monopodial parent branch. The line across each outflow plane marks the location of the bifurcation plane.

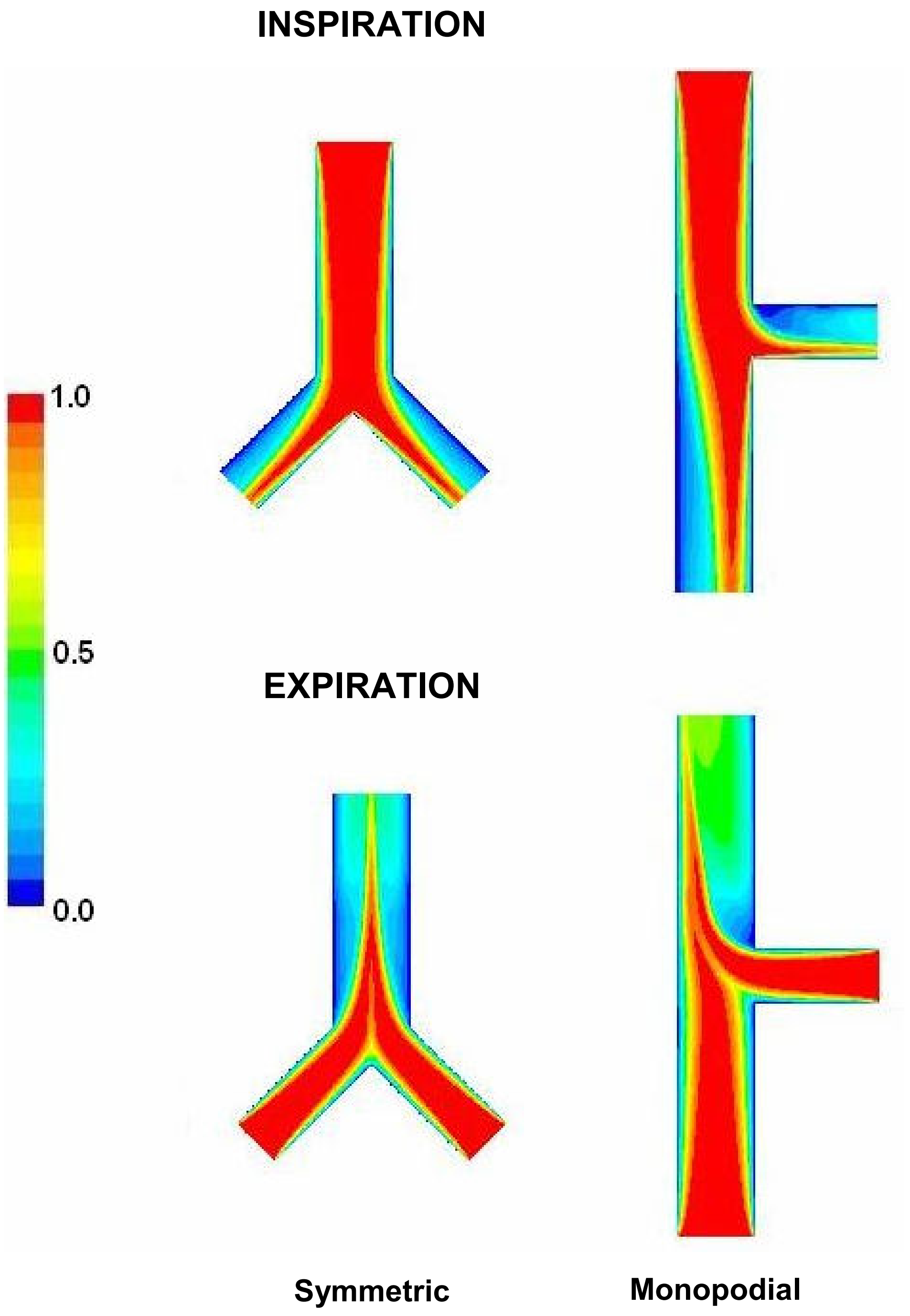

Figure **5-14**: Isocontours of dimensionless O_3 concentration in the bifurcation plane for inspiratory and expiratory flows in the symmetric and monopodial bifurcations ($Re = 300$).

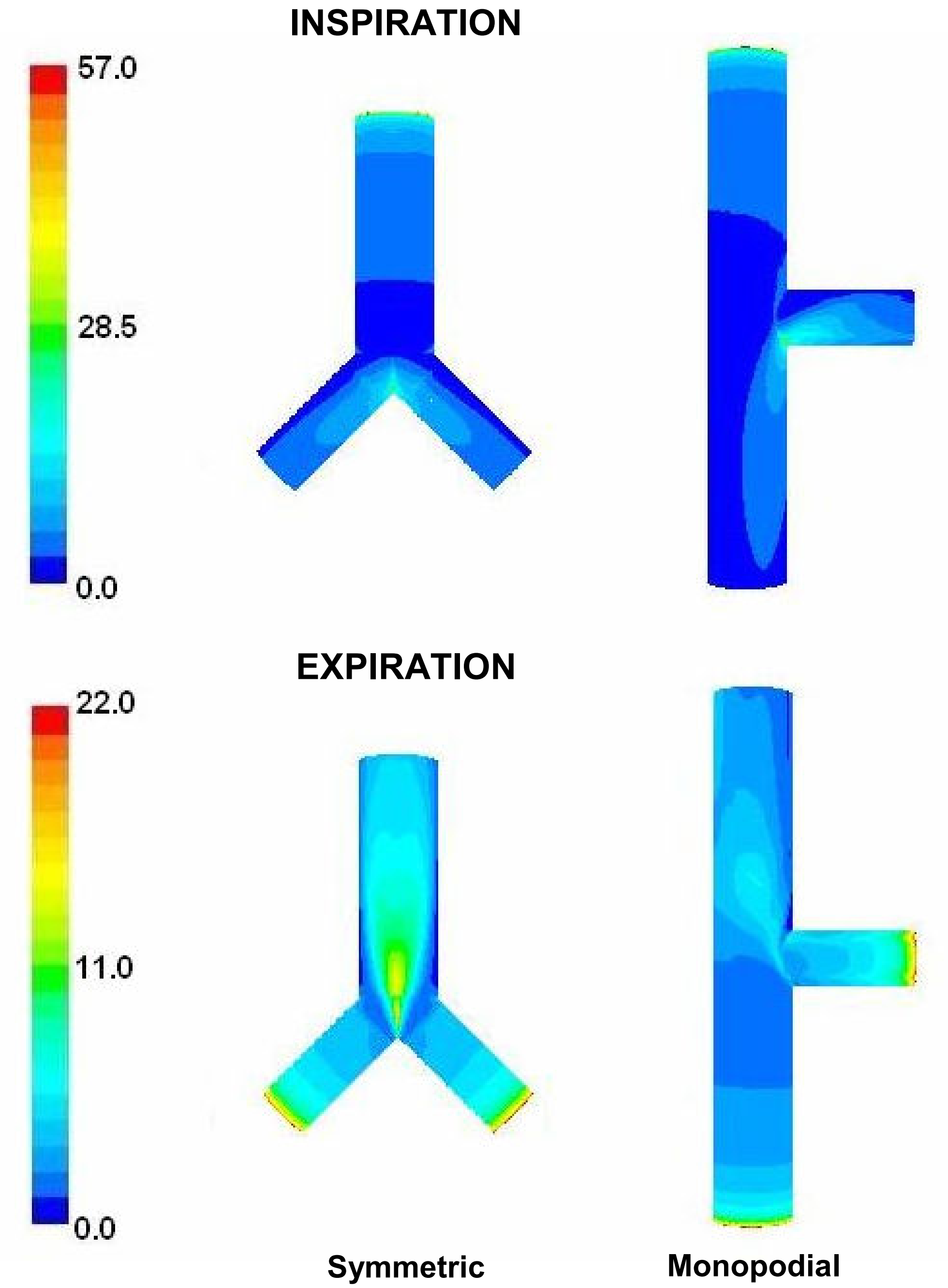

Figure **5-15**: Isocontours of the dimensionless flux N along the bifurcation walls for inspiratory and expiratory flows in the symmetric and monopodial bifurcations ($Re = 300$). Regions with fluxes higher the maximums indicated on the scales are not displayed.

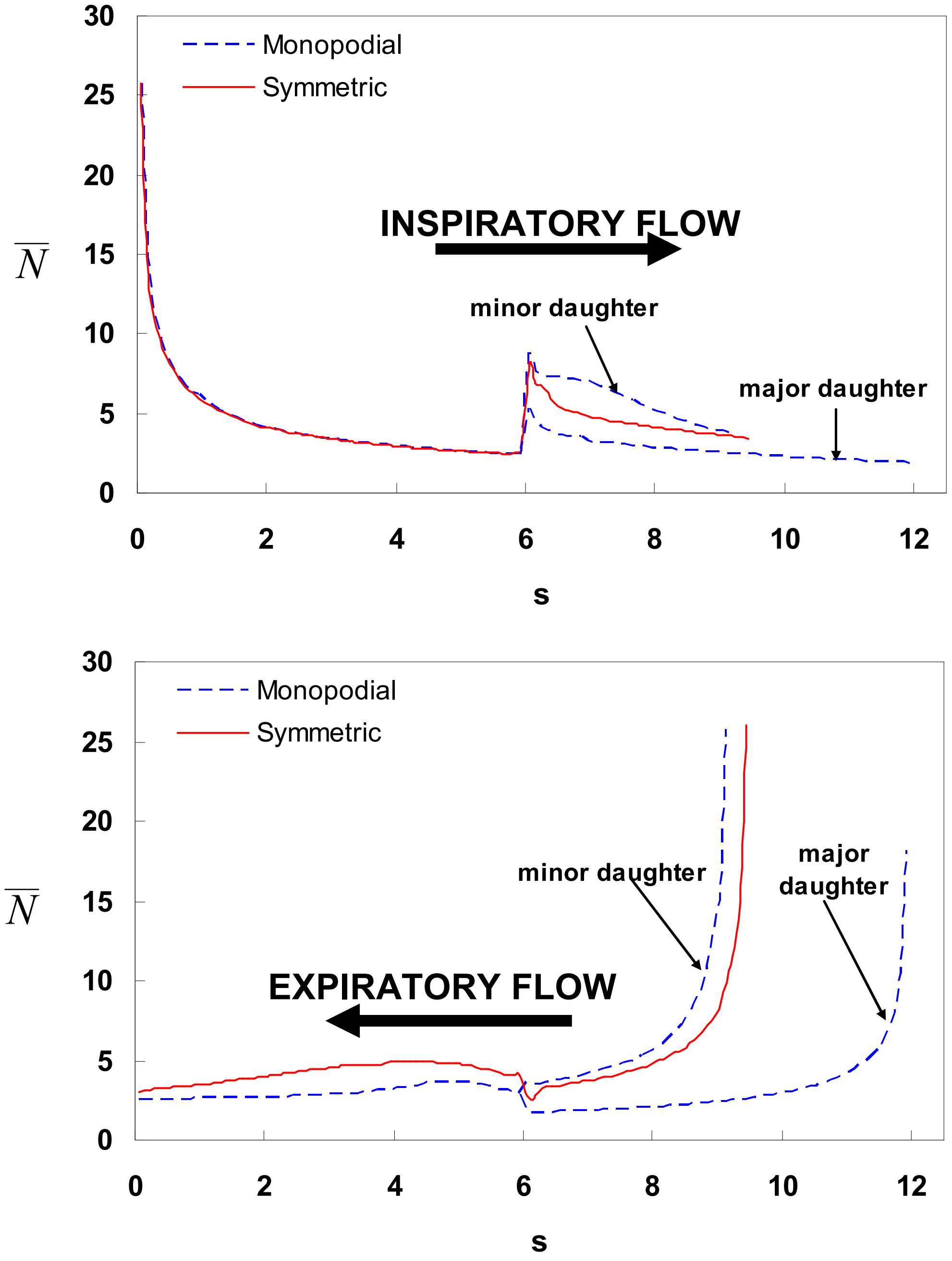

Figure **5-16**: Distribution of the circumferentially-averaged dimensionless flux $\left(\overline{N}\right)$ along the bifurcation wall for inspiratory flow (top panel) and expiratory flow (bottom panel) at three different branching angles. The arrows indicate the flow direction. The monopodial minor daughter branch extends from $6 \le s \le 9.2$ and the major daughter from $6 \le s \le 12$.

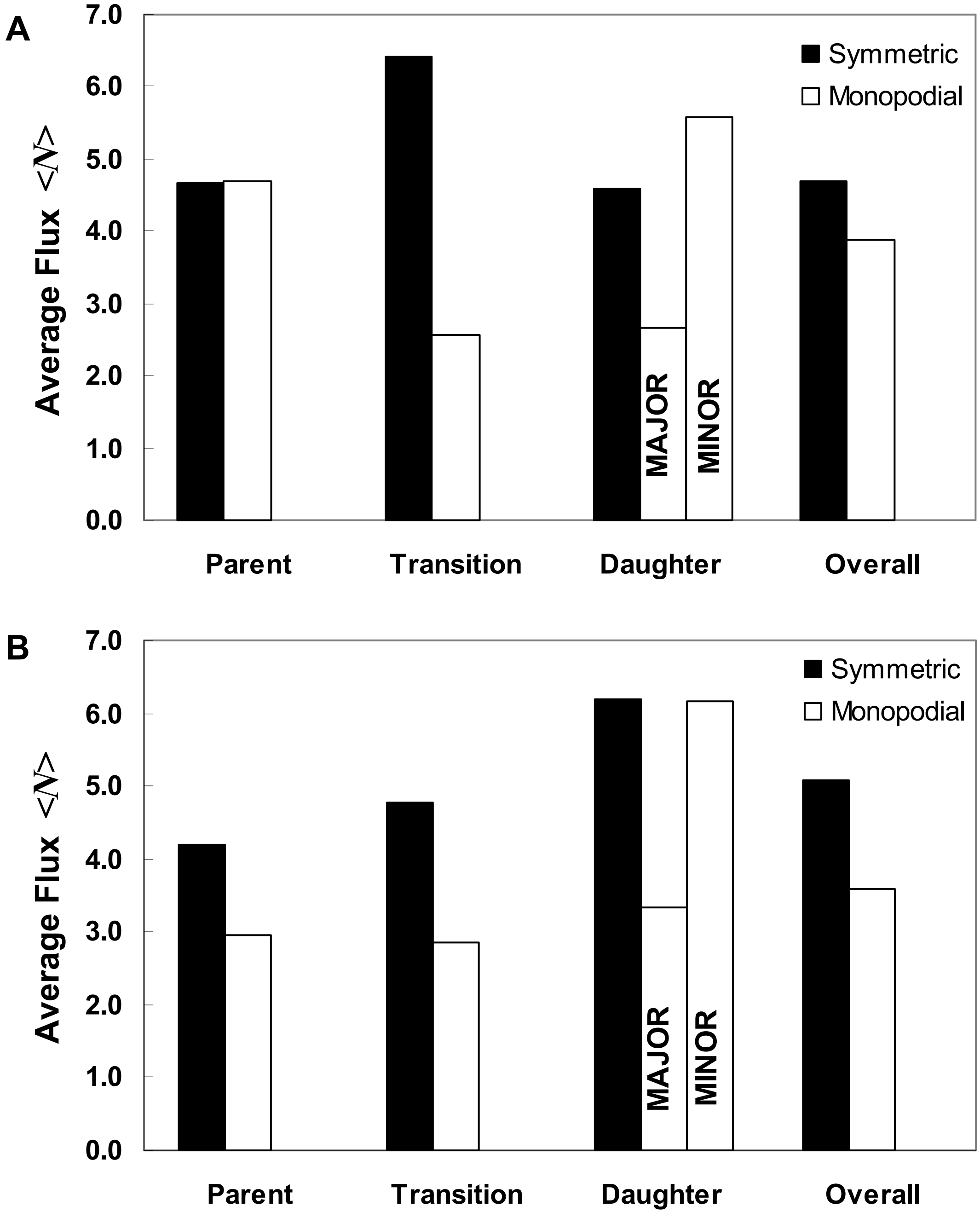

Figure **5-17**: Average dimensionless fluxes $\langle N \rangle$ in each bifurcation region and in the entire bifurcation for (A) inspiratory flow and (B) expiratory flow for three branching angles.

Chapter 6

SELECTION OF AN RTLF REACTION MODEL

In the preceding two chapters, an instantaneous reaction was assumed at the gas-RTLF interface so that the concentration of O_3 at the gas-RTLF interface was driven to zero and no O_3 per se penetrated into the RTLF. In reality, the reaction of O_3 with RTLF substrates occurs at a finite rate, with several of such reactions taking place simultaneously, each with a potentially different reaction pathway and reaction rate. In order to facilitate the prediction of absorbed dose of O_3 along the respiratory tract using mathematical models, several investigators have employed simplifying reaction models.

One such model assumes an instantaneous reaction between O_3 and RTLF reactants so that the reaction is confined to a reaction plane where the concentrations of O_3 and reactant are both zero (Miller *et al.*, 1978; Grotberg *et al.*, 1990; Grotberg, 1990). The reaction plane, which can be located anywhere between the gas-RTLF and the RTLF-lung epithelial tissue interfaces, divides the RTLF into two diffusion layers so that O_3 and reactant do not coexist in the same region.

The other, more commonly used reaction model assumes simultaneous diffusion and homogeneous reaction that is (pseudo-)first order with respect to O_3 concentration in the RTLF, tissue, and/or blood compartments (Miller *et al.*, 1985; Overton *et al.*, 1987; Hu *et al.*, 1992, Hubal *et al.*, 1996). However, the actual reaction rate expression for O_3-substrate reaction is not well-established, and it is unclear whether a first order reaction model in the RTLF is suitable.

In this chapter, two models describing the diffusion-reaction of O_3 in the RTLF are presented and compared in order to select an appropriate model to apply to CFD simulations of O_3 uptake. In both models, the interaction between O_3 and endogenous substrates in the RTLF is modeled as steady one-dimensional diffusion in a thin film with simultaneous reaction. In the first model, the reaction is assumed to be first order with respect to O_3, and in the second model, it is assumed first order with respect to both O_3 and substrate and second order overall.

6.1 GENERAL RTLF SPECIES CONSERVATION EQUATION

The species conservation equation for steady-state O_3 transport in any phase *i*, assuming constant density and diffusivity, is

$$\frac{\partial c_i^*}{\partial t^*} + \left(\mathbf{u}^* \bullet \nabla^* c_i^*\right) = D_i \nabla^{*2} c_i^* + R_{O_3}^* \qquad \textbf{6.1}$$

where c_i^* is the concentration of O_3 in phase *i*, t^* is time, $\mathbf{u}^*$ is the velocity of phase *i*, ∇^* is the gradient operator, D_i is the binary diffusion coefficient of O_3 in phase *i*, and $R_{O_3}^*$ is the molar rate of O_3 production by chemical reaction per unit volume. For simplicity, the RTLF can be idealized as a homogeneous layer. Because the thickness Δ of the RTLF is much smaller than the airway radius R_0, i.e., $\Delta/R_0 \ll 1$ (Table **6-1**), curvature can be neglected and the thin film approximation applied. Consequently, the species conservation equation for O_3 in the RTLF can be written in rectangular coordinates as

$$\frac{\partial c_l^*}{\partial t^*}+u_x^*\frac{\partial c_l^*}{\partial x^*}+u_y^*\frac{\partial c_l^*}{\partial y^*}+u_z^*\frac{\partial c_l^*}{\partial z^*}=D_l\left(\frac{\partial^2 c_l^*}{\partial x^{*2}}+\frac{\partial^2 c_l^*}{\partial y^{*2}}+\frac{\partial^2 c_l^*}{\partial z^{*2}}\right)+R_{O_3}^* \qquad \textbf{6.2}$$

where c_l^* is the concentration of O_3 in the RTLF; u_x^*, u_y^*, and u_z^* are the components of the RTLF velocity in the x^*, y^*, and z^* directions (defined in Figure **6-1**); and D_l is the binary diffusion coefficient of O_3 in the RTLF.

In order to assess the importance of each of the above terms, equation **6.2** can be made dimensionless by scaling t^* by $1/\omega$, where $\omega = 2\pi f$ and f is respiratory frequency, the velocity by the RTLF mucus speed U, x^* by R_0, y^* by Δ, and z^* by the airway length L. If it is assumed that there is no interfacial resistance to O_3 mass transfer at the gas-RTLF interface so that the interfacial O_3 concentrations in the gas and RTLF are at equilibrium, the ratio of the gas phase to mucus phase O_3 concentrations is given by an equilibrium partition coefficient α, i.e.,

$$c_{li}^* = \alpha c_{gi}^* \qquad \textbf{6.3}$$

where c_{li}^* and c_{gi}^* are the RTLF and gas phase O_3 concentrations, respectively, at the gas-RTLF interface. Therefore, c_l^* can be scaled by the RTLF-side interfacial O_3 concentration αc_{gi}^*. Scaling in this manner and dividing by αc_{gi}^* results in the following equation:

$$\omega\frac{\partial c_l}{\partial t}+U\left(\frac{1}{R_0}u_x\frac{\partial c_l}{\partial x}+\frac{1}{\Delta}u_y\frac{\partial c_l}{\partial y}+\frac{1}{L}u_z\frac{\partial c_l}{\partial z}\right)=D_l\left(\frac{1}{R_0^2}\frac{\partial^2 c_l}{\partial x^2}+\frac{1}{\Delta^2}\frac{\partial^2 c_l}{\partial y^2}+\frac{1}{L^2}\frac{\partial^2 c_l}{\partial z^2}\right)+R_{O_3} \qquad \textbf{6.4}$$

where the absence of an asterisk denotes a dimensionless variable and $R_{O_3} = R^*_{O_3} \big/ \alpha\, c^*_{gi}$.

Multiplying equation **6.4** by the quantity $\Delta^2 \big/ D_l$ results in the following dimensionless equation:

$$Wo_l^2 \frac{\partial c_l}{\partial t} + Pe_l \left(\frac{\Delta}{R_0} u_x \frac{\partial c_l}{\partial x} + u_y \frac{\partial c_l}{\partial y} + \frac{\Delta}{L} u_z \frac{\partial c_l}{\partial z} \right) = \frac{\Delta^2}{R_0^2} \frac{\partial^2 c_l}{\partial x^2} + \frac{\partial^2 c_l}{\partial y^2} + \frac{\Delta^2}{L^2} \frac{\partial^2 c_l}{\partial z^2} - Da' \qquad \textbf{6.5}$$

where $Wo_l = \Delta\sqrt{\omega / D_l}$ is the Womersley parameter in the RTLF and represents the ratio of unsteady effects to diffusive effects, $Pe_l = U\Delta / D_l$ is the RTLF Peclet number, and

$$Da' = -R_{O_3} \left(\frac{\Delta^2}{D_l\, \alpha\, c_{gi}} \right).$$

Since $\frac{\Delta}{R_0} \ll 1$ and $\frac{\Delta}{L} \ll 1$ (Table **6-1**), the terms containing $\frac{\Delta}{R_0}$, $\frac{\Delta}{L}$, $\frac{\Delta^2}{R_0^2}$, and $\frac{\Delta^2}{L^2}$ can be neglected. f ranges from about 15 breaths per minute (bpm) during normal breathing to about 30 bpm during heavy exercise (Miller *et al.*, 1985). Using a value of 2.66×10^{-5} cm^2/s for D_l, and the range of values of Δ listed in Table **6-1**, Wo_l^2 can be determined to range from about 9×10^{-6} to about 0.1. Consequently, the unsteady term can be neglected. Finally, mean mucus velocities in the lower respiratory tract of humans range from 2.4 mm/min in the main bronchi to 0.01 mm/min in the bronchioles (Schlesinger, 1982). These values, together with the range of Δ listed in Table **6-1**, result in values of Pe_l ranging from about 0.15 to about 8×10^{-6}. Thus, all terms containing Pe_l, i.e., the convective terms, can also be neglected. Therefore, the species conservation equation in the RTLF can be approximated as

$$\frac{\partial^2 c_l}{\partial y^2} = Da' . \qquad \textbf{6.6}$$

Therefore, O_3 transport at any (*x,z*) position in the RTLF can be approximated by quasi-steady lateral diffusion (LHS of equation **6.6**) and simultaneous chemical reaction (RHS term). Equation **6.6** is written using a partial derivative with respect to y because Da' depends upon αc^*_{gi} which varies with (*x,z*) position along the gas-RTLF interface.

Table **6-1**: Ratio of RTLF thickness to Airway Radius and Length in the Respiratory Tract

Generation[a]	R_0[a] (cm)	L[a] (cm)	Δ[b] (μm)	$\Delta/R_0 \times 10^3$	$\Delta/L \times 10^3$
0	0.9	12	10	1.11	0.08
1	0.61	4.76	8.6	1.41	0.18
2	0.415	1.9	7.2	1.73	0.38
3	0.28	1.76	6.81	2.43	0.39
4	0.225	1.27	6.41	2.85	0.51
5	0.175	1.07	6.02	3.44	0.56
6	0.14	0.9	5.63	4.02	0.63
7	0.115	0.76	5.23	4.55	0.69
8	0.093	0.64	4.84	5.21	0.76
9	0.077	0.54	4.45	5.78	0.82
10	0.065	0.46	4.06	6.24	0.88
11	0.0545	0.39	3.66	6.72	0.94
12	0.0475	0.33	3.27	6.88	0.99
13	0.041	0.27	2.88	7.02	1.07
14	0.037	0.23	2.48	6.71	1.08
15	0.033	0.2	2.09	6.33	1.05
16	0.03	0.165	1.70	5.66	1.03
17	0.027	0.141	1.30	4.83	0.92
18	0.025	0.117	0.91	3.64	0.78
19	0.0235	0.099	0.52	2.20	0.52
20	0.0225	0.083	0.125	0.56	0.15
21	0.0215	0.07	0.125	0.58	0.18
22	0.0205	0.05	0.125	0.61	0.25
23	0.0205	0.05	0.125	0.61	0.25
			Mean	3.80	0.63

[a] Source: Weibel, 1963. In Weibel's model A, the conducting airways extend from generations 0 (trachea) to 16, the respiratory bronchioles from generations 17 to 19, and the alveolar ducts and sacs from generations 20 to 23.

[b] Based on Miller et al. (1985).

6.2 PSEUDO-FIRST ORDER REACTION MODEL

6.2.1 Model Description

In this model, O_3 is consumed in the RTLF via a homogeneous irreversible reaction that is first order with respect to O_3 concentration and has a reaction rate constant k_{r1} (Figure **6-2**) so that $R^*_{O_3} = -k_{r1} c^*_l$, where c^*_l is the concentration of O_3 in the RTLF. Therefore equation **6.6** becomes

$$\frac{\partial^2 c_l}{\partial y^2} = Da\, c_l \qquad \mathbf{6.7}$$

where $Da = k_{r1}\Delta^2 / D_l$ is the Damkohler number for the pseudo-first order reaction and is the ratio of the time scale for diffusion to the time scale for reaction. $Da \gg 1$ indicates that reaction is dominant over diffusion and $Da \ll 1$ signifies the reverse.

The following Dirichlet boundary conditions are imposed:

1. No interfacial resistance at the gas-RTLF interface, so that equation **6.2** holds, i.e., $c_l\left(y=0,z\right)=1$.
2. Zero O_3 concentration at the RTLF-tissue interface, representing an infinitely fast/instantaneous reaction of O_3 with tissue components, i.e., $c^*_l\left(y^*=\Delta, z^*\right)=c_l\left(y=1,z\right)=0$.

Equation **6.7** together with the above boundary conditions can be solved analytically for the concentration profile of O_3 to yield the following result:

$$c_l\left(y,z\right) = \cosh\left(\sqrt{Da}\,y\right) - \coth\sqrt{Da}\,\sinh\left(\sqrt{Da}\,y\right) \qquad \textbf{6.8}$$

where cosh, coth, and sinh are the hyperbolic cosine, hyperbolic cotangent, and hyperbolic sine, respectively.

Two quantities of interest are the flux of O_3 into the RTLF and the flux into the lung epithelial tissue. The dimensionless form of the former quantity can be calculated thus:

$$N_{RTLF} \quad = \quad -\left.\frac{\partial c_l}{\partial y}\right|_{y=0} = \sqrt{Da}\,\coth\sqrt{Da} \qquad \textbf{6.9}$$

where N_{RTLF} is the RTLF-side dimensionless flux of O_3 into the RTLF and is equal to the negative of the RTLF-side dimensionless concentration gradient of O_3. The RTLF-side dimensionless flux of O_3 into the epithelial tissue N_{tissue} can be computed by evaluating the RTLF-side concentration gradient at the RTLF-tissue interface:

$$N_{tissue} \quad = \quad -\left.\frac{\partial c_l}{\partial y}\right|_{y=1} = \sqrt{Da}\left[\coth\sqrt{Da}\,\cosh\sqrt{Da}\, - \sinh\sqrt{Da}\,\right] = \sqrt{Da}\,\operatorname{csch}\sqrt{Da} \qquad \textbf{6.10}$$

where csch is the hyperbolic cosecant. The ratio of the tissue flux to the RTLF flux is a function only of Da and is equal to

$$N_{tissue}/N_{RTLF} = \operatorname{sech}\sqrt{Da} \qquad \textbf{6.11}$$

where sech is the hyperbolic secant. The RTLF-side dimensionless RTLF and tissue fluxes are related to their dimensional counterparts by the following equations:

$$N^*_{RTLF} \quad = \frac{D_l\,\alpha\,c^*_{gi}(z)}{\Delta}N_{RTLF} \qquad \textbf{6.12}$$

and

$$N^*_{tissue} = \frac{D_l \, \alpha \, c^*_{gi}(z)}{\Delta} N_{tissue}, \qquad \textbf{6.13}$$

where the asterisk denotes a dimensional flux.

6.2.2 Sensitivity of O_3 Concentration and Uptake to Damkohler Number

The concentration and flux of O_3 are functions of the Damkohler number Da, which depends on both the reaction rate constant k_{r1} and RTLF thickness Δ. Before assessing the effect of Da on the concentration profile of O_3 in the RTLF and the flux of O_3 into the RTLF and tissue compartments, it is necessary to evaluate the effect of k_{r1} and Δ on Da.

Figure **6-3** shows that Da increases with increasing k_{r1} and with increasing RTLF thickness. Moreover, the rate of increase of Da with k_{r1} is greater for a thicker RTLF.

Figure **6-4** indicates that the rate of increase of Da with RTLF thickness increases with k_{r1}. As is apparent from the definition of Da given in Section **6.2.1**, Da is more sensitive to Δ than to k_{r1}; a ten-fold increase in k_{r1} leads to a ten-fold increase in k_{r1}, whereas a ten-fold increase in Δ results in a 100-fold increase in Da.

Pseudo-first order reaction rate constants in the literature for the reaction of O_3 in the RTLF range from about 10^3 s^{-1} (Miller *et a*l., 1985) to about 10^7 s^{-1} (Bush *et al.*, 2001). Assuming a diffusivity of 2.66×10^{-5} cm^2/s for O_3 in the RTLF (Miller *et al.*,

1985) and using the range of RTLF thicknesses given in Table **6-1**, lower and upper bounds of Da in the human respiratory tract can be estimated to be on the order of 10^{-3} and 10^{6}, respectively. Figure **6-5** shows that at low Da, the concentration profile of O_3 in the RTLF is approximately linear, close to what would be observed for pure diffusion ($Da = 0$). This is because diffusion dominates in the low Da regime. As Da increases, O_3 is consumed by chemical reaction increasingly rapidly so that O_3 penetrates to shallower and shallower depths. At $Da = 100$, the concentration of O_3 is very nearly zero beyond a depth of about half of the RTLF thickness. As Da increases further, the penetration depth of O_3 becomes smaller and smaller until at $Da = 10^{6}$, virtually all the O_3 is consumed in the vicinity of the gas-RTLF interface. Consequently, at higher Da, the RTLF can be regarded as being infinitely thick.

As Da increases, the dimensionless flux of O_3 into the RTLF increases while the dimensionless flux of O_3 into the lung epithelial tissue decreases (Figure **6-6A**). At high Da, the fast reaction maintains a high concentration gradient at the gas-RTLF interface but most of the absorbed O_3 is consumed before it can reach the underlying tissue. Conversely, at low Da, smaller concentration gradients result in less O_3 uptake, but the very low reaction rates allow O_3 to penetrate to the tissue. Either larger RTLF thicknesses or higher k_{r1}, both resulting in larger Da, will increase the relative time for O_3 consumption by chemical reaction, thus preventing O_3 from reaching the tissue. At low Da, almost all the O_3 absorbed from the gas phase reaches the underlying tissue (99.5% at $Da = 0.01$), but as Da increases, less and less O_3 reaches the tissue, until at

$Da \geq 100$, virtually none of the absorbed O_3 reaches the tissue compartment (Figure **6-6B**).

Note that even though a thicker RTLF results in a larger Da and a larger dimensionless flux at the RTLF surface, the actual flux of O_3 is also inversely proportional to Δ (equations **6.12** and **6.13**). Consequently, at higher Δ there is a tradeoff between the effect of increasing Da (which acts to increase the flux) and decreasing the quantity $1/\Delta$ (which acts to decrease the flux). This will be evident in Section **7.2.1**.

6.3 SECOND ORDER REACTION MODEL

6.3.1 Model Description

The second order reaction model is similar to the pseudo-first order model, except that O_3 is consumed via an irreversible reaction that is second order overall – first order with respect to both the O_3 concentration and the effective substrate concentration c_s^* – with a second order reaction rate constant k_{r2} (Figure **6-7**). The reaction is assumed to occur with 1:1 stoichiometry so that

$$R_{O_3}^* = R_S^* = -k_{r2} c_l^* c_S^* . \qquad \textbf{6.14}$$

where R_S^* is the molar rate of substrate production by chemical reaction per unit volume. At the RTLF-tissue interface, the substrate concentration is assumed to be maintained at a constant concentration $c_{S\Delta}^*$. By separately applying equation **6.7** to O_3 and to substrate, the dimensionless species conservation equations can be written as follows:

$$\left(\frac{\partial^2 c_l}{\partial y^2}\right) = Da_2\, c_l\, c_S \qquad \textbf{6.15}$$

$$\left(\frac{\partial^2 c_S}{\partial y^2}\right) = Da_2\, \beta\, c_l\, c_S \qquad \textbf{6.16}$$

where c_S is the dimensionless substrate concentration obtained by scaling c_S^* by $c_{S\Delta}^*$, $Da_2 = k_{r2}\, c_{S\Delta}^*\, \Delta^2 / D_l$ is the second order reaction Damkohler number, and $\beta(z) = \dfrac{D_l}{D_S} \dfrac{\alpha\, c_{g,i}^*(z)}{c_{S\Delta}^*}$ is the relative diffusion rate of O_3 and substrate, where D_S is the effective diffusivity of substrate in the RTLF. All other variables were scaled as in Section **6.1**. The same boundary conditions imposed in the pseudo-first order reaction model are applied to the O_3 concentration field:

1. $c_l^*\left(y^*=0, z^*\right) = \alpha\, c_{g,i}^*\left(z^*\right)$ or $c_l\left(y=0, z\right) = 1$
2. $c_l^*\left(y^*=\Delta, z^*\right) = c_l\left(y=1,\, z\right) = 0$

The following boundary conditions are applied on the substrate concentration field:

1. No flux of substrate from the RTLF into the gas phase, i.e., $-D_S \left.\dfrac{\partial c_S^*}{\partial y^*}\right|_{y^*=0} = \left.\dfrac{\partial c_S}{\partial y}\right|_{y=0} = 0$.
2. A constant substrate concentration $c_{S\Delta}^*$ at the RTLF-tissue interface, i.e., $c_S^*\left(y^*=\Delta, z^*\right) = c_{S\Delta}^*$ or $c_S\left(y=1, z\right) = 1$.

Equations **6.15** and **6.16** together with the boundary conditions represent a boundary value problem (BVP) comprised of two coupled nonlinear second-order ordinary differential equations (ODEs). This system of equations was solved numerically in Mathematica (Wolfram Research, Inc., Champaign, IL) using the shooting method (Appendix D). N_{RTLF} and N_{tissue} can be calculated in the same manner outlined in Section **6.2.1** .

Briefly, the shooting method involves transforming a BVP consisting of an nth order ODE into an initial value problem (IVP) with $n-1$ estimated parameters (i.e., guessed initial conditions) and iteratively adjusting these parameters to satisfy the original BVP. For example, to solve the second order ordinary differential equation $x''(t)=f\left(t, x(t), x'(t)\right)$ on the interval $a \le t \le b$ with boundary conditions $x(a)=x_a$ and $x(b)=x_b$, the boundary condition at $t=b$ can be replaced with a guessed initial condition $x'(a)=\Omega$. This substitution transforms the original BVP into an IVP, which can then be solved using an ODE solver. The value of Ω is adjusted iteratively until the solution of the corresponding IVP satisfies the boundary condition $x(b)=x_b$. If a function $F(\Omega)$ is defined as

$$F(\Omega)=x(b;\Omega)-x_b, \qquad \mathbf{6.17}$$

then the value of Ω that satisfies the original BVP is the root of $F(\Omega)$, which can be determined by iterative methods such as the secant method.

In order to test the accuracy of the algorithm for the shooting method implemented in Mathematica, asymptotic methods were used to solve equations **6.15** and **6.16** for the small Da_2 limit when $\beta = 1$ (Appendix D). For $Da_2 \ll 1$, the asymptotic solutions of equations **6.15** and **6.16** are

$$c_l\left(y; Da_2\right) = \left(1 - y\right) - \tfrac{1}{6} Da_2\left(2y - 3y^2 + y^3\right) + \mathrm{O}\left(Da_2^2\right) \qquad \textbf{6.18}$$

$$c_S\left(y; Da_2\right) = 1 - \tfrac{1}{6}\beta\, Da_2\left(2 - 3y^2 + y^3\right) + \mathrm{O}\left(Da_2^2\right) \qquad \textbf{6.19}$$

Figures **6-8** and **6-9** compare the numerical and asymptotic solutions for the dimensionless O_3 and substrate concentrations at $Da_2 = 0.001$ and $Da_2 = 0.01$ ($\beta = 1$ in both cases). The dimensionless concentrations computed using both methods are virtually indistinguishable, and the RTLF and tissue O_3 fluxes obtained from both methods differed by less than 0.001%.

6.3.2 Sensitivity of O_3 Concentration and Uptake Rate to Reaction Model Parameters

The exact values (or range of values) needed to determine Da_2 and β, namely k_{r2}, $c^*_{S\Delta}$, D_S, Δ, and c^*_{gi}, are not well-established and/or vary along the respiratory tract and among individuals; therefore, it is necessary to determine the sensitivity of O_3 flux into the RTLF and underlying epithelial tissue to model parameters over a range of possible physiologically relevant conditions.

In order to determine an appropriate range of values of β, it was necessary to estimate D_S, $c^*_{S\Delta}$, and c^*_{gi}. The diffusivities of uric acid, ascorbic acid, linoleic acid, and glutathione were estimated to be 1.1×10^{-5}, 9.9×10^{-6}, 6.2×10^{-6}, and 7.0×10^{-6} $\mathrm{cm^2/s}$, respectively, using the Wilke-Chang correlation (Wilke and Chang, 1955). D_S was assumed to be $8.5\times10^{-6}\ \mathrm{cm^2/s}$, the average of these values.

The total RTLF concentration of low molecular weight antioxidants determined by Van der Vliet and colleagues (1999) was about $360\ \mu$M. For the purposes of identifying a range of $c^*_{S\Delta}$, the antioxidant concentration was assumed to vary over two orders of magnitude of so that $c^*_{S\Delta}$ ranges between 36 and 3600 μM.

If c^*_{gi} is estimated to range from 1% to 100% (representing no gas phase resistance) of the bulk concentration c^*_{bulk} in the gas phase, and c^*_{bulk} is estimated as the ambient concentration of O_3, which at O_3 levels of 0.1 ppm and an ambient temperature of 25°C is $4.9\times10^{-3}\ \mu$M, the lower and upper bounds of c^*_{gi} can be estimated to be $4.9\times10^{-5}\ \mu$M and $4.9\times10^{-3}\ \mu$M, respectively. (But note that the actual bulk O_3 concentration will be lower because a portion of the inhaled O_3 would have been absorbed by the upper airways and the airways proximal to the generation of interest.)

Using the estimated values of the relevant parameters given above and in Table **6-1**, the lower and upper bounds of β were determined to be 6.2×10^{-9} and 6.2×10^{-5}, respectively. Since Mathematica was unable to solve equations **6.15** and **6.16** for Da_2 greater than about 250 for $\beta = 6.2\times10^{-5}$, sensitivity studies were limited to the range $0.01 \le Da_2 \le 250$. Over the range of Da_2 studied, the concentrations of O_3 and substrate are both insensitive to β (Figure **6-10**). At the lower and upper bounds of Da_2, the substrate concentration was practically constant throughout the RTLF. At $Da_2 = 250$, the substrate concentration at the gas-RTLF for $\beta = 6.2\times10^{-5}$ ($c_S = 0.999$) is very slightly less than that for $\beta = 6.2\times10^{-9}$ ($c_S = 1.000$), but this variation with β can be considered insignificant since a 10,000-fold increase in β resulted in a difference of only about 0.1%.

Similarly, the dimensionless fluxes of O_3 into the RTLF and tissue were also insensitive to β. For both values of β, the dimensionless fluxes into the RTLF and tissue were 1.003 and 0.998, respectively at a Da_2 of 0.01. For $Da_2 = 250$ and for both values of β, the dimensionless tissue fluxes were 0.000, and the dimensionless RTLF fluxes differed only slightly at the different values of β: 15.811 for $\beta = 6.2\times10^{-9}$ and 15.804 for $\beta = 6.2\times10^{-5}$, a difference of only about 0.04%.

Just as in the case of the pseudo-first order reaction model, the O_3 concentration profile in the RTLF is approximately linear at low Damkohler numbers, but O_3 penetrates only to a shallow depth at the higher Damkohler numbers, for the same reasons given in Section **6.2.2**. Likewise, the dimensionless flux of O_3 into the RTLF from the gas phase increases and the dimensionless flux into the epithelial tissue decreases with increasing Da_2.

Note that it is the RTLF-side dimensionless fluxes that were found to be insensitive to β. The effect of β on the actual flux will depend on the origin of the difference in β, i.e., whether it is due to a difference in the interfacial O_3 concentration, which depends on the Damkohler number and the ambient concentration of O_3, or to the substrate concentration at the RTLF-tissue interface. If Da_2 is fixed and β varies due to a change in the ambient concentration of O_3, then a smaller β will result in a smaller RTLF flux since RTLF flux is proportional to c_{gi}^*. In order to maintain the same Da_2 while varying $c_{S\Delta}^*$ (and keeping all other variables constant), k_{r2} must be changed in the opposite direction, changes which would have no effect on c_{gi}^*. Thus, at a fixed Da_2, a change in β resulting from a change in $c_{S\Delta}^*$ has little effect on the actual flux of O_3 into the RTLF or lung epithelial tissue, at least within the range of Da_2 examined.

β is an indicator of the relative diffusion rates of O_3 toward tissue and substrate toward the gas-RTLF interface. High values of β signify relatively higher fluxes of O_3 into the RTLF, which will lead to increased depletion of substrate, making less substrate available for reaction at the gas-RTLF interface (Figure **6-10B**) and leading to decreased flux. This effect is unimportant at lower reaction rates since relatively little substrate would be consumed by chemical reaction, but it becomes more pronounced as the reaction rate (and thus Da_2) increases.

6.4 COMPARISON OF REACTION MODELS

For the following comparison, Da and Da_2 were considered to be equivalent, so that $k_{r1} = k_{r2}\, c_{S\Delta}^*$. Since concentration profiles and dimensionless fluxes were largely insensitive to β, and lowering the value of β enabled Mathematica to solve the second-order reaction problem at higher values of Da_2, the lower bound calculated for β

(6.2×10^{-9}) was used in the comparisons. At this value of β, the second-order reaction model could be solved up to a maximum Da_2 of about 750.

Figure **6-11** shows O_3 concentration profiles obtained from the pseudo-first order and second order reaction models at various Damkohler numbers. At each Damkohler number, the concentration profiles from both reaction models are indistinguishable. A deviation of the second order model from the pseudo-first order model is expected at higher β, but this difference is not likely to be significant for physiologically relevant values of β, even at Damkohler numbers higher than those shown here. The RTLF and tissue fluxes determined from both models were also virtually identical. (See Figure **6-6** for flux values.) These results indicate that at levels of O_3 typical during episodes of air pollution, the two reaction models can be considered to be equivalent. However, care should be taken when applying these findings to studies in which animals are exposed to much higher concentrations of O_3.

6.5 DISCUSSION

The purpose of this study was to develop and compare two alternative models of homogeneous reaction between O_3 and RTLF constituents. Most mathematical O_3 dosimetry models that have incorporated a homogenous reaction between O_3 and RTLF constituents have assumed a pseudo-first order reaction. However, the actual reaction kinetics of O_3 in the RTLF has not been established. Most experimental studies in the literature measure consumption rates of antioxidants, and a few report reaction rate constants, but hardly any provide a reaction rate expression.

To the author's knowledge, the only investigators who have determined a reaction rate expression for the reaction of O_3 with RTLF antioxidants are Kermani and collaborators (2006). They exposed solutions of pure antioxidant (UA, AH_2, or glutathione) to O_3 while monitoring both the antioxidant concentration and the exit O_3 concentration and obtained rate expressions for the reaction of O_3 with UA and AH_2 that were first order with respect to O_3 and antioxidant concentrations and second order overall. They also found the respective reactions to occur with 1:1 stoichiometry. On the other hand, they concluded that the reaction rate for the reaction of O_3 with glutathione (GSH) was proportional to $[O_3]^{0.5}[GSH]^{1.25}$. Since UA and AH_2 have been shown to be the most reactive RTLF constituents (Kelly *et al.*, 1996; Mudway and Kelly, 1998; Postlethwait *et al.*, 1998), this study, together with the others, suggests that it is reasonable to assume a second order reaction between O_3 and RTLF constituents.

In several other experimental studies, the rates of consumption of antioxidants by reaction with O_3 appeared to be linear with respect to time, which would support a pseudo-first order reaction model (Mudway and Kelly, 1998; Kelly *et al.*, 1996; Mudway *et al.*, 1996). However, the rates of consumption of O_3 and RTLF substrates such as ascorbic acid (AH_2) and uric acid (UA) have also been found to be positively related to O_3 concentration and initial substrate concentrations (Cross *et al.*, 1992; Kelly *et al.*, 1996; Mudway *et al.*, 1996; Langford *et al.*, 1995; Giamalva *et al.*, 1985; Kanofsky and Sima, 1995), consistent with a reaction rate that is dependent on both O_3 and substrate concentrations. These observations appear to support a pseudo-first order reaction model.

Any RTLF reaction model must include appropriate boundary conditions. The boundary conditions applied for the concentration of O_3 in the two models were a concentration in equilibrium with the interfacial gas phase concentration at the gas-RTLF interface and a zero concentration at the RTLF-tissue interface.

When O_3 reaches the lung epithelial tissue, it reacts with the unsaturated fatty acids (UFA) in the cell membrane. Miller and colleagues (1985) reported an effective UFA concentration of 50,000 μM in lung tissue and a second order reaction rate constant of about $10^6\ \mathrm{M}^{-1}\,\mathrm{s}^{-1}$ for the reaction of UFAs with O_3. This will result in a much higher reaction rate than in the RTLF, where the total substrate concentration can be estimated to be about 360 μM (van der Vliet *et al.*, 1999) and the highest second order reaction rate constant reported for a reactive RTLF substrate is $4.8\times10^7\ \mathrm{M}^{-1}\,\mathrm{s}^{-1}$ for ascorbic acid (Kanofsky and Sima, 1995). Although a reaction rate constant of about$10^9\ \mathrm{M}^{-1}\,\mathrm{s}^{-1}$ has been reported for glutathione (Pryor *et al.*, 1984), this antioxidant has been shown to be relatively unreactive with O_3 in bronchoalveolar lavage and physiologically relevant mixtures of RTLF substrates (Kelly *et al.*, 1996; Mudway *et al.*, 1996; Postlethwait *et al.*, 1998). Hence it is reasonable to assume that the reaction of O_3 with lung tissue is fast enough to drive the concentration of O_3 to zero at the RTLF-tissue interface.

The second order reaction model also required boundary conditions on the substrate concentration. A zero flux condition was imposed at the gas-RTLF interface and a constant substrate concentration was maintained at the tissue surface. While it is reasonable to assume that no RTLF substrate will be transported from the RTLF into the gas phase, what happens to the concentration or flux of substrate at the other end of the RTLF layer is not clear. However, it is believed that plasma exudation and/or cellular mechanisms maintain antioxidant concentrations in the RTLF (Persson *et al.*, 1991; van der Vliet and Cross, 2001; Peden *et al.*, 1993; Cross *et al.*, 1994). Furthermore, human and animal O_3 exposure studies have also reported little or no antioxidant depletion during or after O_3 exposure but before the onset of inflammation (Mudway *et al.*, 1999a; Mudway *et al.*, 1999b; Long *et al.*, 2001; Crissman *et al.*, 1989). Therefore, it is not unreasonable to assume a constant substrate concentration at the RTLF-tissue interface.

A comparison between the pseudo-first and second order models revealed no difference in the resulting O_3 concentration profiles in the RTLF or in the fluxes into the RTLF and lung tissue over the range of Damkohler numbers examined. This is because the pseudo-first order reaction model is an extreme case of the second order reaction that assumes an excess of substrate, as is the case in the RTLF, so that the substrate concentration remains essentially constant and $k_{r1} = k_{r2} c_S^* \simeq k_{r2} c_{S\Delta}^*$. As both the Damkohler number and β increase, the results of the two models can be expected to diverge, although the extent of the deviation cannot be ascertained from our results due to the limitations of the ODE solver that was used. At higher Damkohler numbers, the substrate concentration may vary throughout the RTLF because of increased consumption and/or diffusion distance. But in the RTLF, $\beta \ll 1$ so that the substrate concentration can always be considered to be in excess. Consequently, the deviation between the two models may not be significant even at high Damkohler numbers.

Because of its simplicity and ease of implementation in FLUENT, the pseudo-first order reaction model will be used in subsequent chapters.

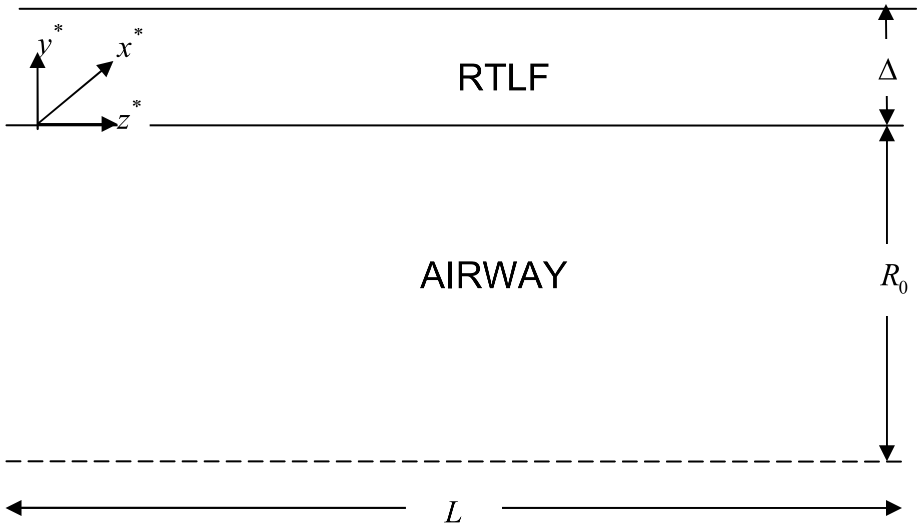

Figure **6-1**: Schematic of half of the cross-section along the length L of an airway with ELF thickness Δ and radius R_0. The x^* direction is perpendicular to both the y^* and z^* directions and parallel to the circumference of the tube.

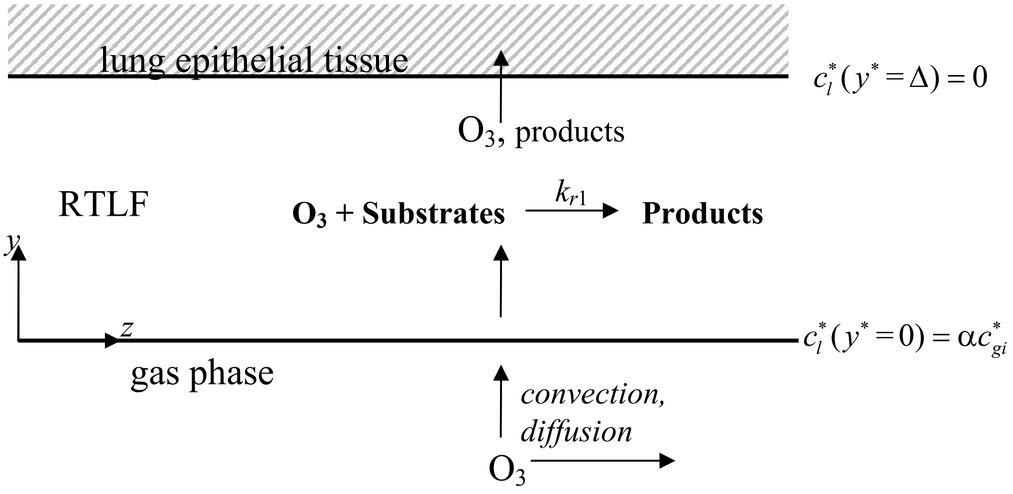
lung epithelial tissue
$c_l^*(y^*=\Delta)=0$
O_3, products
RTLF
O_3 + Substrates $\xrightarrow{k_{r1}}$ Products
y
z
$c_l^*(y^*=0)=\alpha c_{gi}^*$
gas phase
convection, diffusion
O_3

Figure **6-2**: Pseudo-first order reaction model for the consumption of O_3 in the RTLF. Symbols are defined in the text.

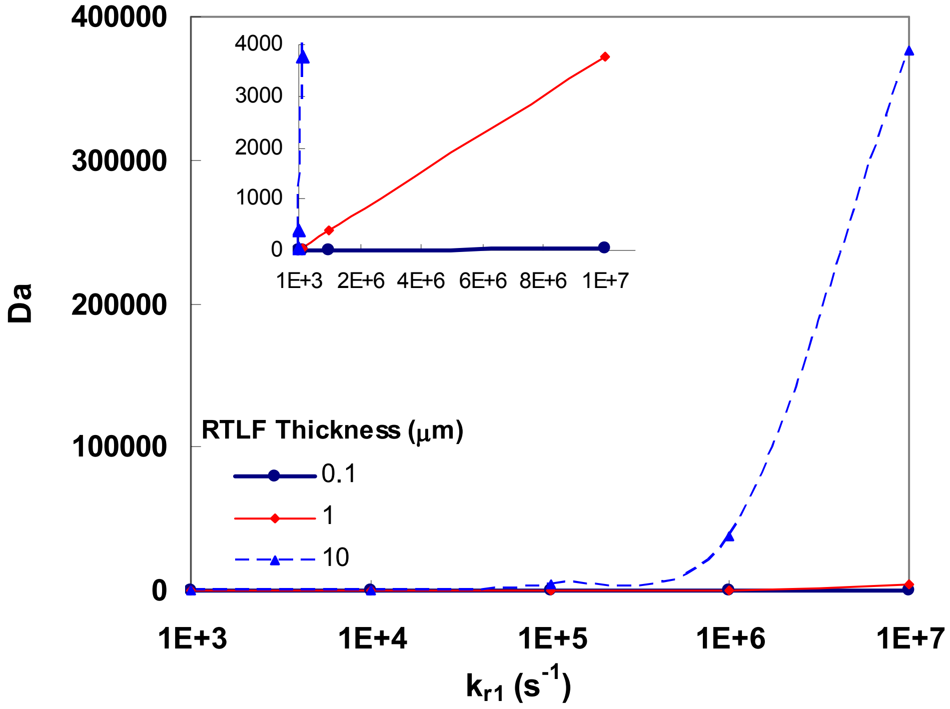

Figure **6-3**: Sensitivity of the Damkohler number Da to the reaction rate constant at different RTLF thicknesses. $D_l = 2.66\times10^{-5}$ cm^2/s .

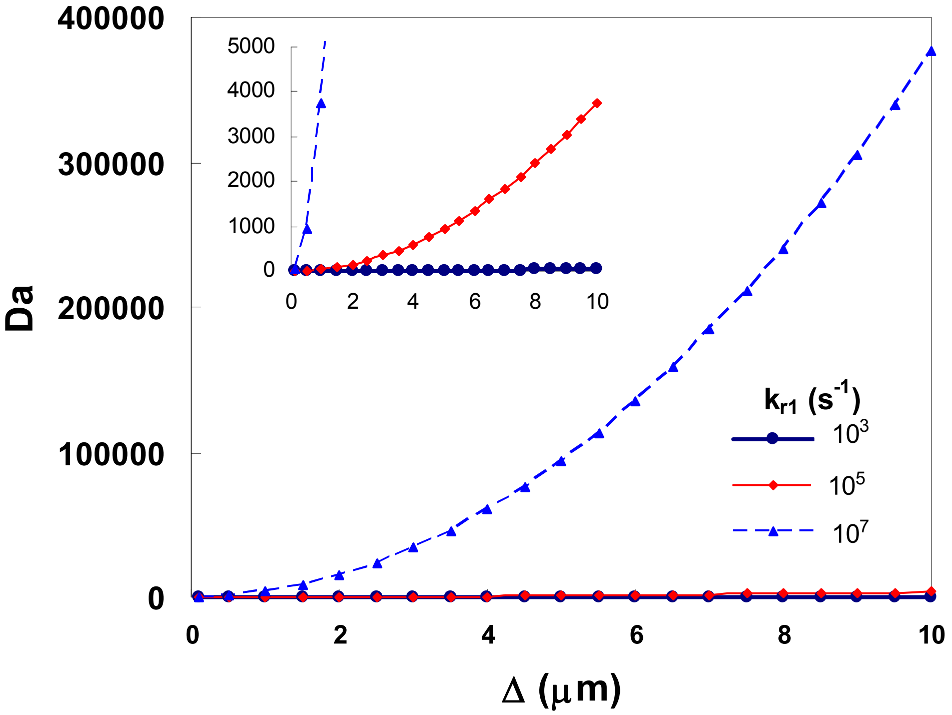

Figure **6-4**: Sensitivity of the Damkohler number to RTLF thickness at different reaction rates. $D_l = 2.66 \times 10^{-5}\ \text{cm}^2/\text{s}$.

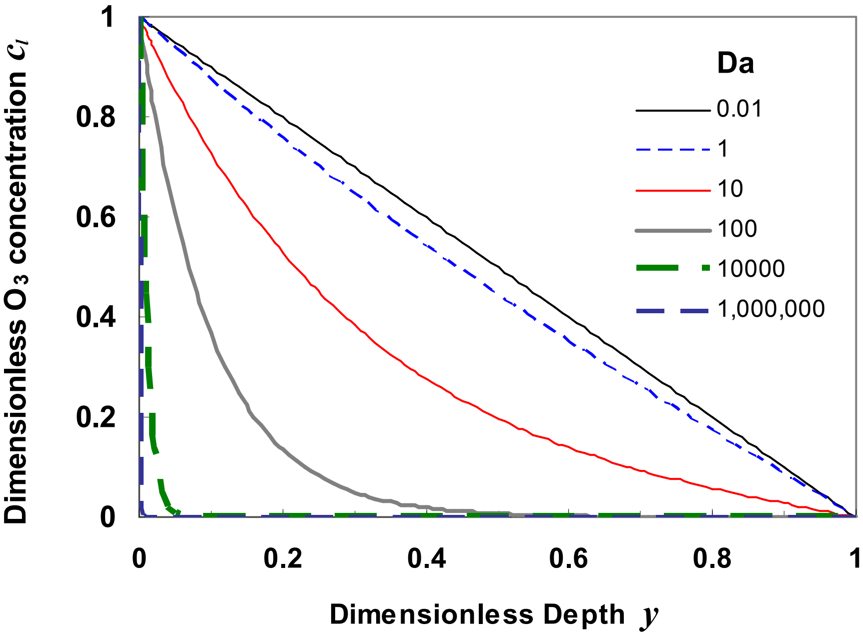

Figure **6-5**: Effect of the Damkohler number Da on the O$_3$ concentration profile in the RTLF. $y = 0$ corresponds to the gas-RTLF interface, and $y = 1$ corresponds to the RTLF-tissue interface.

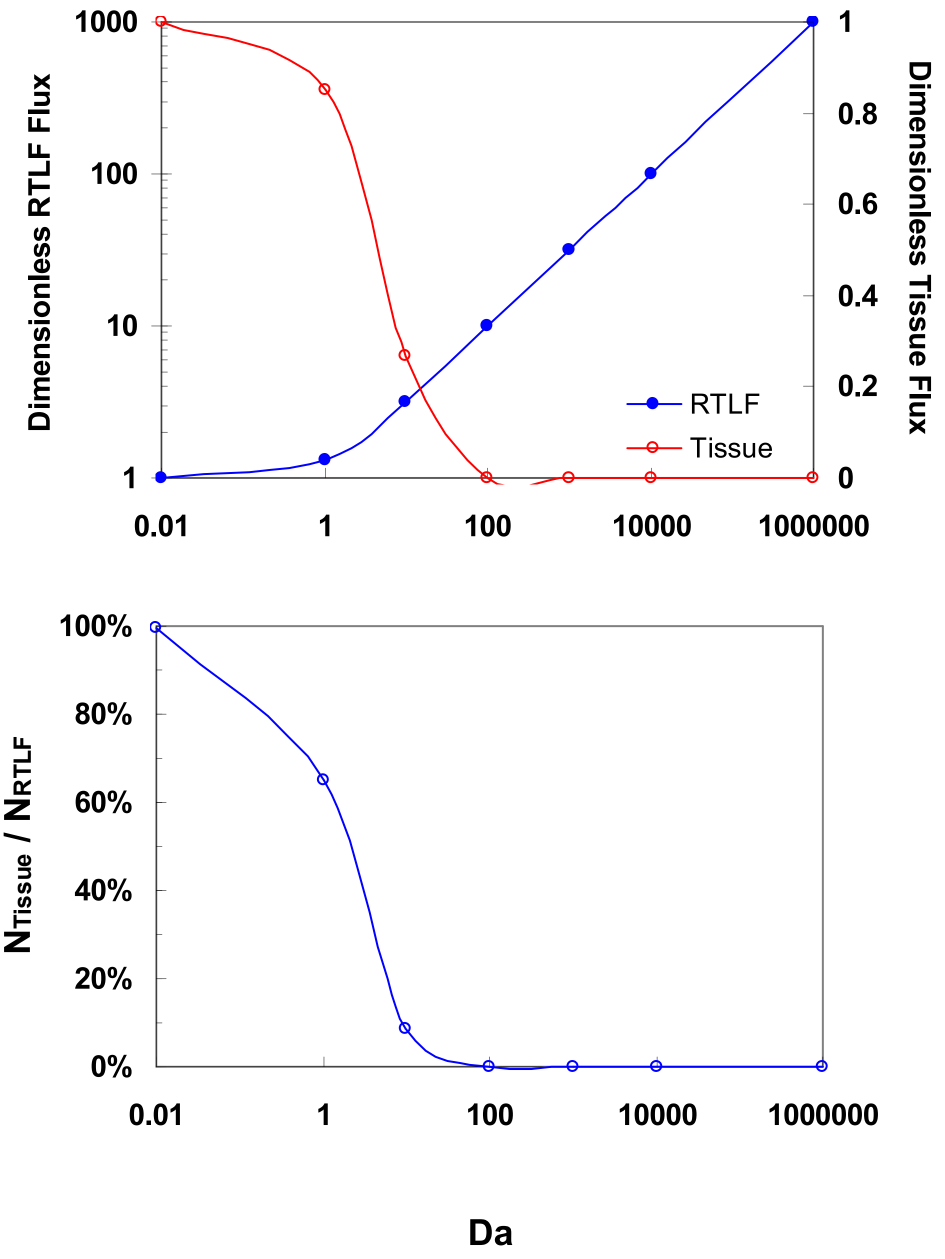

Figure **6-6**: Dependence on the Damkohler number Da of (top panel) the dimensionless flux of O_3 into the RTLF (N_{RTLF}) and tissue (N_{tissue}) and (bottom panel) the amount of O_3 that reaches the tissue.

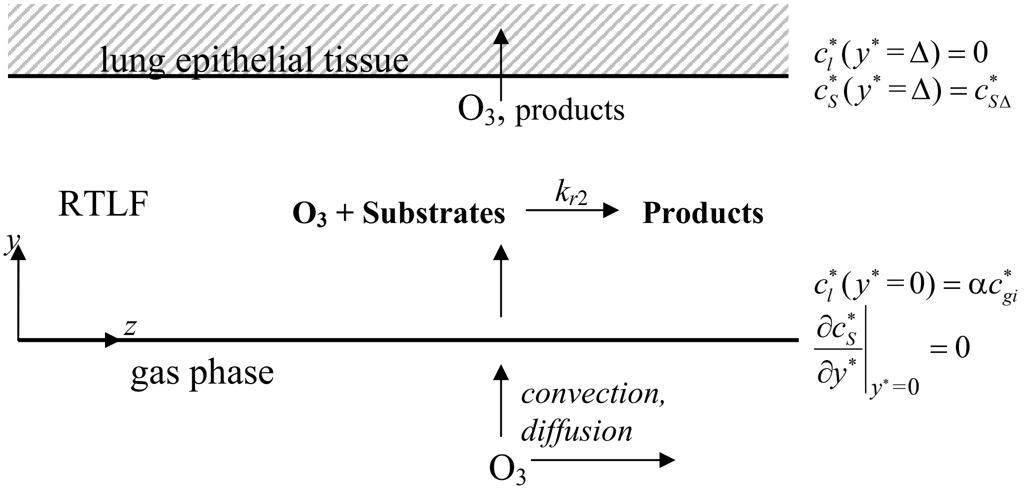
lung epithelial tissue
$c_l^*(y^*=\Delta)=0$
$c_S^*(y^*=\Delta)=c_{S\Delta}^*$
O_3, products
RTLF
O_3 + Substrates $\xrightarrow{k_{r2}}$ Products
y
z
$c_l^*(y^*=0)=\alpha c_{gi}^*$
$\left.\frac{\partial c_S^*}{\partial y^*}\right|_{y^*=0}=0$
gas phase
convection,
diffusion
O_3

Figure **6-7**: Second order reaction model for the consumption of O_3 reaction and diffusion in the RTLF. Symbols are defined in the text.

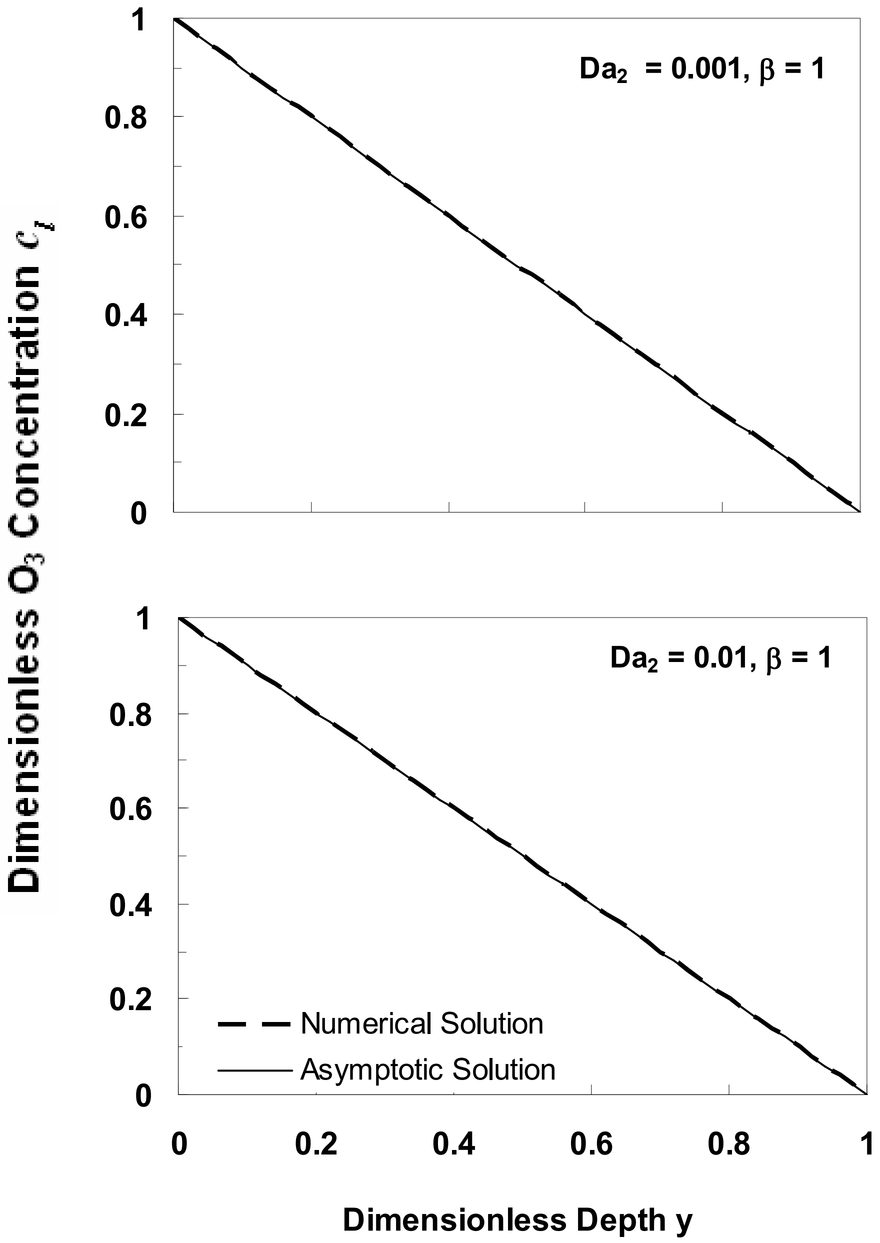

Figure **6-8**: Comparison of numerical and asymptotic solutions of O$_3$ concentration for $Da = 0.001$ and $Da = 0.01$, $\beta = 1$. $y = 0$ corresponds to the gas-RTLF interface, and $y = 1$ corresponds to the RTLF-tissue interface.

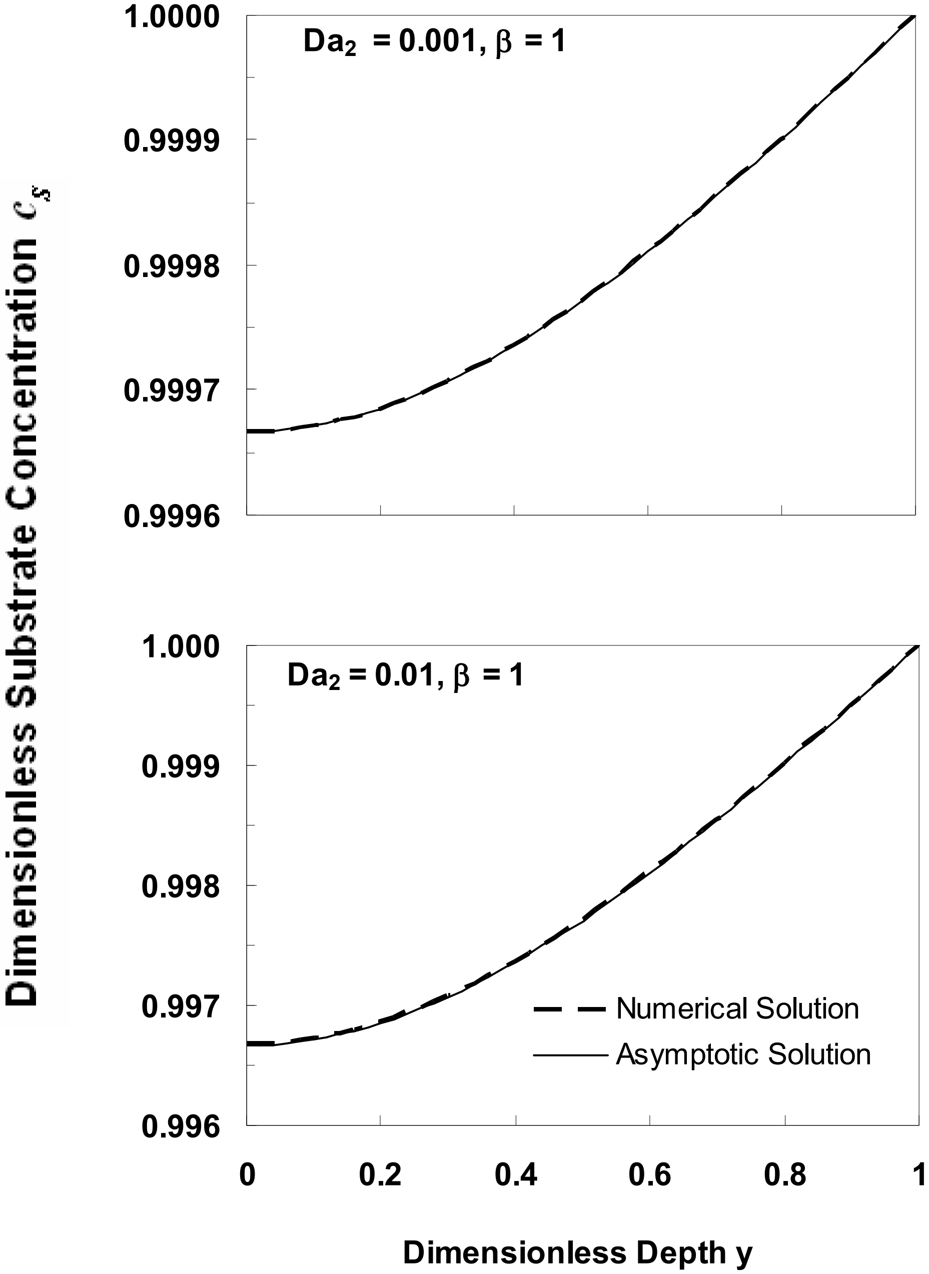

Figure **6-9**: Comparison of numerical and asymptotic solutions of substrate concentration for $Da=0.001$ and $Da=0.01$, $\beta=1$. $y=0$ corresponds to the gas-RTLF interface, and $y=1$ corresponds to the RTLF-tissue interface.

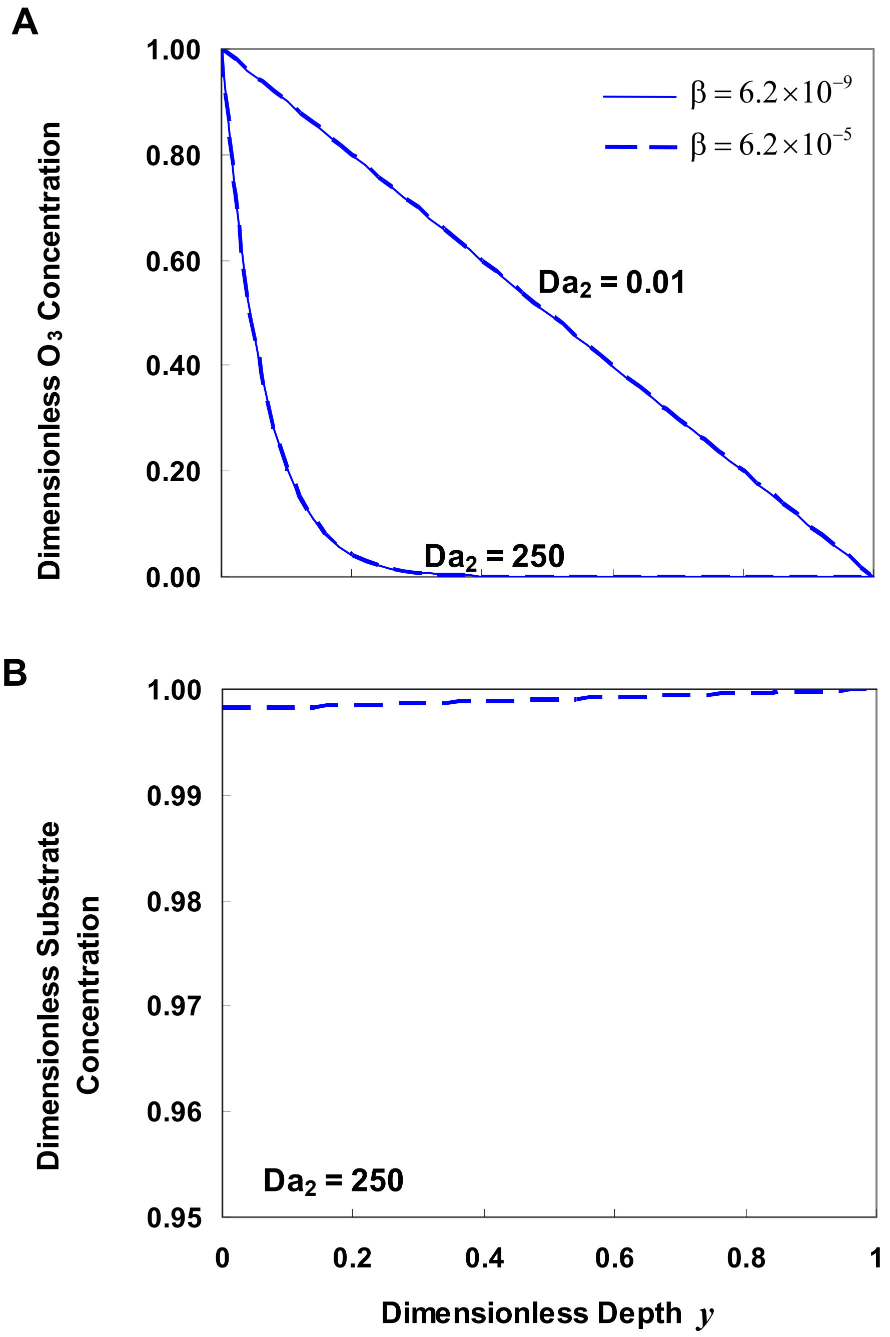

Figure **6-10**: Sensitivity of (A) O_3 and (B) substrate concentration profiles to β. For the substrate concentration, only the results for $\mathrm{Da}_2 = 250$ are shown. For $\mathrm{Da}_2 = 0.01$, c_S maintained a value of 1.00 throughout the RTLF for both values of β, as was the case when $\mathrm{Da}_2 = 250$ and $\beta = 6.2\times10^{-9}$. y = 0 corresponds to the gas-RTLF interface, and y = 1 corresponds to the RTLF-tissue interface.

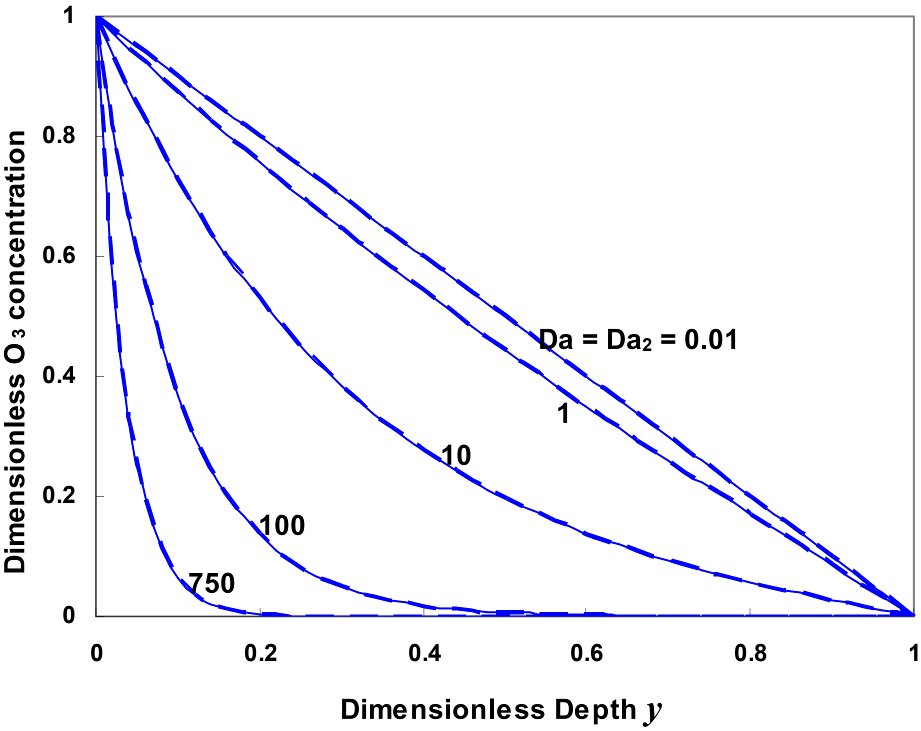

Figure **6-11**: Comparison between O_3 concentration profiles from the pseudo-first order and second order reaction models. The solid lines represent the pseudo-first order model and the dashed lines the second order model.

Chapter 7

SENSITIVITY OF OZONE UPTAKE TO RTLF DIFFUSION-REACTION PARAMETERS IN SINGLE AIRWAY BIFURCATIONS

The respiratory tract lining fluids (RTLF) act as a barrier between O_3 in inspired air and lung epithelial cells, and RTLF constituents mediate the transport of O_3 and O_3-derived reaction products to the tissue. In this chapter, the effects of the RTLF, specifically, the RTLF thickness and reaction rate, on O_3 uptake into the RTLF and tissues will be examined.

7.1 IMPLEMENTATION OF RTLF REACTION IN FLUENT

At steady-state, the continuity of flux requires that the flux of O_3 out of the gas phase equals the flux O_3 into the RTLF:

$$-D_g \left(\mathbf{n} \bullet \nabla^* c^*\right)_{wall} = -D_l \left.\frac{\partial c_l^*}{\partial y^*}\right|_{y^*=0} \qquad \mathbf{7.1}$$

where D_g is the gas phase diffusivity of O_3, **n** is the outward unit normal vector, c^* is the gas phase concentration of O_3, c_l^* is the concentration of O_3 in the RTLF, and the subscript "*wall*" refers to the gas-RTLF interface. The LHS of equation **7.1** represents the flux of O_3 out of the gas phase and the RHS the flux of O_3 into the RTLF. In light of equation **6.9**, equation **7.1** can be written as a function of the dimensionless gas-phase concentration at the bifurcation wall $c_{gi}(z)$:

$$N \equiv -(\mathbf{n} \bullet \nabla c)_{wall} = K\, c_{gi}(z), \qquad \textbf{7.2}$$

where N is the gas-side dimensionless flux into the RTLF, ∇ is the dimensionless gradient operator obtained by scaling ∇^* by the parent branch radius R_0, $c = c^*/c_0$ and $c_{gi}(z) = c_{gi}(z)/c_0$, c_0 is the O_3 concentration at the flow entrance of the bifurcation, and

$$K = \frac{D_l}{D_g}\frac{R_0}{\Delta}\alpha\sqrt{Da}\coth\sqrt{Da} \qquad \textbf{7.3}$$

Therefore, N is a function of the dimensionless parameters $\frac{D_l}{D_g}$, $\frac{\Delta}{R_0}$, α, and Da.

Because FLUENT does not provide for the direct specification of a non-zero flux at the walls, the boundary equation represented by equation **7.2** was applied by specifying the following surface reaction at the bifurcation walls:

$$O_3(g) \quad + \quad \text{air}(s) \quad \xrightarrow{k_{f,r}} \quad O_3(s) \quad + \quad \text{air}(g) \qquad \textbf{7.4}$$

where g represents a gas phase species, s represents a surface-adsorbed species, and $k_{f,r}$ is a reaction rate constant to be input into FLUENT. The above reaction was defined as a first order reaction with respect to O_3 concentration. FLUENT defines $k_{f,r}$ as follows:

$$k_{f,r} = A_r T^{\beta_r} \mathrm{e}^{-E_r/RT} \qquad \textbf{7.5}$$

where A_r is a pre-exponential factor, T is temperature, β_r is the temperature exponent (dimensionless), E_r is the activation energy for the reaction, and R is the universal gas constant. The following mass balance on a reacting species i is applied by FLUENT at the reacting surface:

$$\rho_i D_i \left(\nabla^* Y_i \bullet \mathbf{n}\right)_{wall} = M_{w,i} \hat{R}_i \qquad \mathbf{7.6}$$

where ρ_i and D_i are the density and gas phase diffusivity, respectively, input to FLUENT, Y_i is the FLUENT mass fraction, $M_{w,i}$ is the molecular weight of species i, and $\hat{R}_i$ is the rate of production of species i per unit area into the gas phase. If species i is being consumed according to a first order reaction, then

$$\hat{R}_i = -k_{f,r} \left[i\right]_{wall} \qquad \mathbf{7.7}$$

where $\left[i\right]_{wall}$ is the FLUENT concentration of species i at the reacting surface. Since $\left[i\right] = \rho_i Y_i / M_{w,i}$, we can write

$$\left(\nabla^* Y_i \bullet \mathbf{n}\right)_{wall} = k_{f,r} Y_{i,\, wall} / D_i \qquad \mathbf{7.8}$$

where $Y_{i,\, wall}$ is the FLUENT mass fraction of species i at the reacting surface. Recognizing that Y_i in FLUENT is equivalent to the dimensionless concentration c and $1/Pe$ was substituted for the FLUENT diffusivity D_i (see Section **3.3**), a comparison of equations **7.2** and **7.8** reveals that the following substitution should be made in FLUENT:

$$k_{f,r} = K/Pe \qquad \mathbf{7.9}$$

Therefore, in the simulations incorporating a pseudo-first order reaction of O_3 in the RTLF, the constant K was computed from equation **7.3**, and $k_{f,r}$ was input into FLUENT by setting $A_r = K/Pe$ and $\beta_r = E_r = 0$.

7.2 RESULTS – SYMMETRIC BIFURCATIONS

7.2.1 Sensitivity of Uptake Rate to RTLF Thickness

In order to examine the effect of the RTLF thickness on uptake, we simulated inspiratory flow and O_3 uptake at a Reynolds number of 300 in a single 90° bifurcation at Δ/R_0 ranging from 1.41×10^{-4} to 2.82×10^{-3}. According to equations **7.2** and **7.3**, the flux of O_3 into the RTLF is a function of both the RTLF relative thickness (Δ/R_0) and the Damkohler number Da, which itself is a function of the RTLF thickness Δ. In order to isolate the influence of the RTLF thickness in this analysis, a new dimensionless parameter Da_R was defined thus

$$Da_R = \frac{Da}{\left(\Delta/R_0\right)^2} = \frac{k_{r1}R_0^2}{D_l}. \qquad \textbf{7.10}$$

In all subsequent studies, Δ/R_0 and k_{r1} will both be assumed to be constant throughout the bifurcation, which implies that the thickness of the RTLF scales with the parent branch airway radius. Da_R can be considered to be representative of the reaction rate constant.

The sensitivity to Δ/R_0 of the total uptake rate into the RTLF and lung epithelial tissue in a 90° symmetric bifurcation at $Da_R = 1.7\times10^7$ and 1.7×10^{10} are compared in Figure **7-1**. At both Da_R, the dimensionless RTLF uptake rate was rather insensitive to Δ/R_0, except in the lower range of relative RTLF thicknesses at the lower Da_R of 1.7×10^7, where a five-fold increase in Δ/R_0 from 1.4×10^{-4} to 7.0×10^{-4} resulted in a 47% decrease in the RTLF uptake rate. Above a Δ/R_0 of 7.0×10^{-4}, this uptake rate remained insensitive to the relative RTLF thickness. According to Weibel's model of the airways (1963) and Miller *et al.* (1985), Δ/R_0 in the human airways ranges from 5.6×10^{-4} to 7.0×10^{-3} (Table **6-1**). Therefore, the simulation results predict that even for low reaction rate constants, O_3 uptake into the RTLF will be insensitive to the RTLF thickness.

At the higher Da_R, no O_3 penetrated to the tissue; naturally, the tissue uptake rate was insensitive to Δ/R_0. At the lower Da_R, the tissue uptake rate was more sensitive to Δ/R_0 than the RTLF uptake rate. A five-fold increase in Δ/R_0 from 1.4×10^{-4} to 7.0×10^{-4} resulted in a 93% decrease in the RTLF uptake rate. As Δ/R_0 increased, the tissue uptake rate became less and less sensitive to the RTLF thickness. Similar trends in RTLF and tissue uptake rates were observed for simulations performed for flow at Reynolds numbers of 10 and 1000.

Therefore, at low reaction rates, increasing the RTLF thickness will lead to decreased RTLF and tissue uptake rates until both rates no longer respond to increases in RTLF thickness. If the reaction rate is high enough, the RTLF uptake rate will not be affected by the liquid lining thickness, and no O_3 will penetrate to the lung epithelial tissue. These results suggest that under conditions for which O_3 uptake is sensitive to the liquid lining thickness, i.e., at lower reaction rates and for thinner lining layers, a thicker RTLF is protective against direct O_3 damage to the tissue.

7.2.2 Sensitivity to Da

In order to assess the sensitivity of RTLF and tissue uptake rates to Da, which is a measure of the dominance of reaction over diffusion, flow and O_3 uptake in a single 90° bifurcation at Reynolds numbers of 10, 100, and 1000 were simulated with Da ranging from 1 to 10^6. Because the earlier simulations were conducted in a mesh that was refined using curvature-based adaption carried out at $Re = 500$, additional mesh refinement was required for the simulations at $Re = 1000$. Instead of using curvature-based adaption, mesh refinement was performed in GAMBIT by remeshing the original geometry with what GAMBIT refers to as "boundary layers" (GAMBIT 2.2 Modeling Guide). These boundary layers increased the mesh density along the walls where high velocity and concentration gradients are expected. Outside the boundary layer, the mesh size was maintained at 0.04 dimensionless units. The results of the simulations using Mesh 2 (described in Section **4.1.1**) and those using the grids generated with boundary layers were very close (within 1% - see Appendix E). Mesh 2 was therefore considered adequate and was used for the simulations at $Re = 1000$.

For comparison, additional simulations that assumed an infinitely fast reaction rate ($Da \to \infty$) at the RTLF-gas interface, i.e., zero concentration at the bifurcation walls, were carried out. For finite values of Da, the RTLF and tissue flux distributions along the walls were obtained using a user-defined function based on equations **6.9** and **6.10** (see Appendix C) and the total uptake rates were calculated by integrating the flux over the bifurcation surfaces since the use of the finite wall reaction condition eliminates the singularity associated with the zero-concentration wall condition at the flow inlet. For $Da \to \infty$, total uptake rates were determined using the material balance relationship given in equation **4.7**. Note that at $Re = 10$, the diffusive flux at the inlet, while small, was no longer negligible, and was therefore included in the material balance used for the total uptake rate calculations when $Da \to \infty$.

Having established that for higher reaction rates and RTLF thicknesses, the absorption rates of O_3 into both the RTLF and tissue are insensitive to the RTLF thickness, a fixed Δ/R_0 of 4.6×10^{-3} (the average for the conducting airways based on Table **6-1**) was assumed in all simulations.

7.2.2.1 RTLF and Tissue Uptake Rates

The total uptake rates into the RTLF and tissue for different Re at various Da are presented in Figure **7-2**. At all Re, the total RTLF uptake rate rose as Da increased. However, in contrast to what was observed in Chapter 4 for an infinitely fast reaction in the RTLF, the RTLF uptake rates at low Da ($1 < Da < 100$) were insensitive to Re, even over two orders of magnitude of Re. As Da increased further, the uptake became increasingly sensitive to Re. The difference in uptake rate was greater going from $Re = 10$ to $Re = 100$ than from $Re = 100$ to $Re = 1000$, and these respective differences increased as Da increased. The percent changes in uptake rate from $Re = 10$ to $Re = 100$ and $Re = 100$ to $Re = 1000$ were 0.75% and 0.15%, respectively, when $Da = 1$ and 299.5% and 83.5%, respectively, when $Da \to \infty$. At $Re = 10$, a Da of 10^6 approached the behavior at an infinite Da. The Da that would be equivalent to or approach $Da \to \infty$ increased with increasing Re.

Although the total RTLF uptake rates were insensitive to Re at low Da, the fractional uptakes θ demonstrated a high sensitivity to the Reynolds number because the total flow rate of O_3 into the bifurcation increased as Re rose while the total rate of O_3 absorption remained the same, leading to lower fractional uptakes. The sensitivity of θ to Re decreased as Da increased since the amount of O_3 absorbed became more and more proportional to the amount of O_3 passing through the bifurcation.

As expected, tissue uptake rates decreased with increasing Da, and above a Da of 100, virtually none of the O_3 absorbed into the RTLF reached the tissue. Whereas at $Da = 1$, about 65% of absorbed O_3 penetrated to the tissue, at $Da = 100$ only 0.01% did, and above that, none of the absorbed O_3 reached the lung tissue. Under conditions for which O_3 was able to reach the tissue, the tissue uptake rate was insensitive to Re.

These results indicate that at low Da O_3 uptake is limited by diffusion and reaction in the lining fluid and the gas phase mass transfer resistance is unimportant. As Da increases, the gas phase resistance becomes more and more dominant, and uptake becomes completely gas phase diffusion limited as $Da \to \infty$.

7.2.2.2 Flux Distributions

The dimensionless RTLF flux distributions for various Da at the three Re simulated are displayed in Figure **7-3**. The flux magnitudes at each Re increased as anticipated and the range of fluxes through the bifurcation walls became greater and greater as Da increased, and in all cases, the hot spots of flux downstream of the flow entrances were located at the carina. Interestingly, even though the total uptake rate was basically insensitive to Re at low Da, the flux distributions at the different Re showed marked differences at all Da.

On the other hand, the RTLF flux distributions at each Re exhibited qualitatively similar patterns regardless of Da. At the lowest Reynolds number ($Re = 10$), the flux of O_3 through the bifurcation walls was axisymmetric, except near the bifurcation region, and decayed in the downstream direction in both the daughter and parent branches. At $Da = 10^6$ virtually all the O_3 that entered the bifurcation in the respired gas had been absorbed by the time the gas exited the bifurcation. At $Re = 100$, as at all other Reynolds numbers, the flux distribution on the parent branch walls was also axisymmetric, but in the daughter branches, the flux was higher along the inner walls as was predicted in the case of an infinite Da (Section **4.2.2**). The region of high flux along the inner walls of the daughter branches extended more to the outer walls at $Re = 1000$ so that only a relatively small region of very low flux was found along the daughter branch outer walls near the junction of the parent and daughter branches (Figure **7-4**).

From Figure **7-3** it is evident that at $Da = 100$ and $Da = 10^4$ the maximum fluxes (which occur at the flow entrance) at all Re are very similar in magnitude. These are the

Da values at which total uptake rates were shown in the previous section to be insensitive to Re. However, an inspection of the flux distribution isocontours reveals that the flux distribution becomes more uniform and the magnitude of the hot spot becomes greater relative to the fluxes in the bifurcation as the Reynolds number increases. At all Re, but especially evident at the two higher Re, the regions of relatively high flux surrounding the carina became more and more focused and the regions of low flux along the outer wall became larger as Da increased.

When O_3 was able to penetrate to the tissue ($Da \leq 1000$), the tissue flux distribution patterns were qualitatively identical to the corresponding RTLF flux distributions (Figure **7-5**). The ratio of the magnitude of the RTLF flux to the tissue flux is constant for any given Da (see equation **6.11**).

The source of the flux distribution patterns can be deduced from the velocity and concentration fields.

7.2.2.3 Flow and Concentration Fields

The dimensionless velocity magnitude distributions on the bifurcation plane at the three Re examined are displayed in Figure **7-6**. At $Re = 10$, the flow becomes fully developed in the parent branch about 2.3 parent branch radii downstream of the flow entrance. The flow is also fully developed through most of the daughter branches, and the dimensionless velocity magnitude distribution is not skewed towards the inner wall, in contrast to what is found at higher Re but instead is very nearly symmetric with respect to the daughter branch axes. At the higher Re, the flow never fully develops before exiting the parent branch, but is closer to being fully developed at $Re = 100$ than at $Re = 1000$. Consequently, since entry length is proportional to Re, the maximum dimensionless velocity in the bifurcation decreased with increasing Re.

An interesting flow feature observed at $Re = 1000$ but not at the lower Re was the presence of two stagnation zones in which there was reversed flow along the daughter branch outer walls (Figure **7-7**). The first region was located near the entrance to the daughter branch and extended from the junction of parent branch and the outer wall of the daughter branch to one parent radius downstream. A second smaller region of backflow was located about halfway down the outer daughter wall.

Finally, whereas the velocity profile in the bifurcation plane at the daughter branch outflow boundaries exhibited a single peak velocity at $Re = 10$ and $Re = 100$, two peaks were observed at $Re = 1000$, one smaller than the other (Figure **7-8**).

The dimensionless O_3 distributions in the bifurcation plane at the three Re and at three Da are presented in Figure **7-9**. Like the flux distributions, the dimensionless concentration distributions at the same Re were qualitatively similar to each other, regardless of Da; the main differences were in the magnitudes of the minimum and maximum concentrations. At all Re, the impingement of high concentration fluid on the carina led to the formation of local hot spot of flux there, and the amount of O_3 exiting the bifurcation decreased with increasing Da because higher reaction rates resulted in increased O_3 absorption.

Similar to what was observed in previous chapters, the concentration distributions at $Re = 100$ and $Re = 1000$ were qualitatively similar to their corresponding flow fields.

This was, however, not the case at $Re = 10$. At $Re = 10$, the concentration distributions in the parent and daughter branches, like the velocity distributions, were very nearly symmetric about their respective axes, except in the bifurcation region, leading to the axisymmetric flux distributions seen in Figure **7-3**. However, unlike the velocity distributions, the same high concentration was not maintained at the center of the parent and daughter branches; rather, the peak O_3 concentration at each axial cross-section decayed in the downstream direction because of the increased residence time for the reaction of O_3 with RTLF constituents at the gas-RTLF. As Da increased, the amount of O_3 exiting the bifurcation decreased until at $Da = 10^6$, very little O_3 was present in the exiting gas, indicating that most of the O_3 entering the bifurcation has been absorbed into the RTLF.

The concentration distributions at $Re = 100$ are similar to those described in Section **4.2.2**). At $Re = 1000$, the concentration distributions are similar to the corresponding flow field. In the bifurcation plane, two regions of relatively low O_3 concentration were present in the stagnation zones, leading to low fluxes (see Figure **7-4**). Downstream of this region was a zone of relatively high O_3 concentration, resulting in a relatively high flux along the outer wall close to the outflow boundaries of the daughter branches.

7.3 RESULTS – MONOPODIAL BIFURCATION

The effect of finite reaction in the RTLF on the distribution of O_3 uptake was also investigated in a single idealized monopodial bifurcation by simulating inspiratory flow and O_3 uptake at $Re = 10$ and $Re = 100$ at Da of 100, 10^4, and 10^6, assuming a fixed Δ/R_0 of 4.6×10^{-3}. These results were compared to those obtained with an infinite Da. Simulations at $Re = 1000$ were not carried out because of difficulties with solution convergence in the monopodial geometry at such a high Reynolds number.

7.3.1 Sensitivity to Da

7.3.1.1 Total Uptake Rates

The total rates of O_3 absorption into the RTLF at various Da are presented in Figure **7-10**. As with the symmetric bifurcations, the total rate of O_3 uptake was insensitive to Re at low Da. In addition, the sensitivity to Re became greater with increasing Da, indicating that O_3 uptake was becoming more gas phase diffusion controlled. At $Re = 10$, the total uptake rate at $Da = 10^6$ was very close to the uptake rate with an infinitely fast reaction occurring at the gas-RTLF interface. The tissue uptake rates (not shown) followed the same trends observed in the symmetric bifurcation.

7.3.1.2 Flux Distributions

The dimensionless flux distributions in the monopodial bifurcation are displayed in Figure **7-11** and are similar in several respects to those observed in the symmetric bifurcations. Local hot spots of O_3 flux were located at the carina and were more prominent at the higher Re, and the relative intensity of the hot spots increased with increasing Da. As in the symmetric bifurcation, the flux distribution at $Re = 10$ was axisymmetric, except near the branching region, and decayed in the downstream direction in the parent and daughter branches.

At $Re = 100$, the flux distribution patterns along the daughter branch walls were also similar to those in the symmetric bifurcation in that the flux was higher along the inner walls. As Da rose, this region of high flux became less spread out and more focused, leaving a larger region of relatively low flux along the outer walls. Another characteristic of the flux distribution at $Re = 100$ is that the low flux zone along the outer wall of the major daughter branch was larger than the low flux region on the minor daughter branch outer wall.

The source of the flux distribution patterns can be deduced from the velocity and concentration fields.

7.3.1.3 Flow Fields and Concentration Distributions

The flow fields at the two Reynolds numbers simulated are presented in Figure **7-12**. The velocity distributions shared several features in common with those of the symmetric bifurcations. As was the case in the symmetric bifurcation, the velocity field became fully developed within the parent and daughter branches and was symmetric all branch axes throughout most of the lengths of the branches at $Re = 10$ but not at $Re = 100$. An interesting feature at $Re = 10$ was the skewing of the velocity distribution towards the inner wall of the minor daughter branch very near its flow entrance, but this feature persisted for only a short distance, after which the flow field became axisymmetric. At $Re = 100$, the velocity distribution was axisymmetric in the parent branch but was skewed toward the inner walls in both daughter branches. This bending of the higher velocity fluid to maneuver the turn into the minor daughter branch led to a jet of high velocity fluid in the minor daughter branch so that the maximum dimensionless velocity magnitude at $Re = 100$ was very close to that at $Re = 10$, despite the higher Reynolds number. The bending of fluid also resulted in a region of stagnation and recirculation at $Re = 100$ (cf. Figure Figure **5-128**) along the upstream section of the outer minor daughter wall that was not present in the daughter branches of the symmetric bifurcation.

The corresponding dimensionless O_3 concentration distributions are shown in Figure **7-13**. The concentration distributions have many similarities with those in their symmetric counterparts. At $Re = 10$, the concentration distributions were symmetric about the branch axes, and for $Da = 10^6$, most of the O_3 entering the bifurcation had been absorbed before the respired gas exited the bifurcation. At $Re = 100$, the concentration distribution was skewed toward the inner walls of both daughter branches. As Da increased, the higher concentration gradients at the walls led to higher fluxes.

7.4 COMPARISON OF SYMMETRIC AND MONOPODIAL BIFURCATIONS

The overall average dimensionless fluxes $\langle N \rangle$ of O_3 through the walls of the symmetric and monopodial bifurcations are compared in Figure **7-14**. For all Da at both flow conditions, the average flux in the symmetric bifurcation was greater than that in the monopodial bifurcation. These differences were enhanced at the lower Reynolds number and grew as Da increased. Nevertheless, both bifurcation geometries had similar overall average fluxes at $Da = 100$ for flow at $Re = 10$ and at Da of 100 and 10^4 for flow at $Re = 100$, signifying comparable efficiencies in O_3 absorption.

7.5 DISCUSSION

Not only are the concentrations of O_3-reactive substrates in the RTLF and the RTLF thicknesses along the respiratory tract not precisely known, but the reaction rate constants for the reaction of RTLF substrates with O_3 have also not been established in the literature. Moreover, RTLF thickness and the concentrations of RTLF constituents vary along the respiratory tract of an individual organism, among individuals within the same species, and among different species. Consequently, a sensitivity analysis to investigate the effects of the reaction rate constant and RTLF thickness on O_3 uptake was needed.

Chapters 4 and 5 presented flux patterns during both steady inspiratory and expiratory flow. Since the primary purpose of this chapter was to investigate the effects of RTLF reaction and diffusion parameters, only inspiratory flow was simulated. In light of the fact that the patterns of O_3 distribution were similar for reactions in the RTLF occurring at finite and infinite rates, it is conceivable that for expiratory flow the same would be true and the effects of Da would be similar to those predicted in this chapter would be observed for expiratory flow.

The ranges of Δ/R_0, k_{r1}, and Da reported in humans were given in Chapter 6. If the parent branch is assumed to be a primary bronchus, which in Weibel's model is assumed to have a radius of 0.61 cm (Weibel, 1963), then the values of $Da_R = 1.7\times10^4$ and $Da_R = 1.7\times10^7$ used to investigate sensitivity to Δ/R_0 correspond to pseudo-first order reaction rate constants k_{r1} of 1.2×10^3 s^{-1} and 1.2×10^6 s^{-1}, respectively. Our results demonstrate that only for small RTLF thicknesses is the total uptake rate of O_3 into the RTLF responsive to RTLF thickness. On the other hand, the tissue uptake rate was sensitive to RTLF thicknesses over a greater range of Δ/R_0. The same trends were reported by Hubal *et al*., (1996) in their study of O_3 uptake in the nasal passages of the rat using three-dimensional CFD.

Therefore, at low reaction rates, increasing the RTLF thickness will lead to decreased RTLF and tissue uptake rates until these rates no longer respond to increases in RTLF thickness. If the reaction rate is high enough, the RTLF uptake rate will not be affected by the liquid lining thickness, and no O_3 will penetrate to the lung epithelial tissue. These results suggest that under conditions for which O_3 uptake is sensitive to the liquid lining thickness, a thicker RTLF is protective against direct O_3 damage to the tissue.

The implications of these results for O_3-induced injury depend on the nature of the reactions of O_3 with RTLF components. If the reactions of RTLF components with O_3 quench the air pollutant, then in airways where the reaction rate constant is low, for example in the distal airspaces which are lined with surfactant, a thicker RTLF would provide protection against O_3-induced damage. (At high reaction rates, all the O_3

absorbed into the RTLF is consumed before it can reach the tissue.) On the other hand, if the reactions of O_3 with RTLF substrates produce mostly toxic compounds, then, except for low Δ/R_0 and low reaction rate constants, the thickness of the RTLF would have no effect on damage to the tissue since the amount of toxic compounds, including O_3, reaching the epithelial cells would depend only on the rate of O_3 uptake into the RTLF, assuming that one molecule of O_3 produces one molecule of toxic compounds and that the toxic byproducts are equally as damaging to cells as O_3.

This study also examined the effect of Da on O_3 uptake at $Re = 10$, 100, and 1000. According to the anatomical parameters of Weibel (1963), in adult airways Reynolds numbers of 10, 100, and 1000 correspond to the following generations: 11, 7, and 1, respectively, during light exertion (minute ventilation MV = 20 L min^{-1}); and 4, 10, and 14, respectively during heavy exertion (MV = 60 L min^{-1}). Reynolds numbers of 10 and 100 roughly correspond to generations 10 and 5, respectively, during quiet breathing (MV = 10 L min^{-1}). The Reynolds number in the trachea during quiet breathing is about 660 (Table **7-1**). Assuming that Δ/R_0 has a representative value of 4.6×10^{-3} in all airways of the bifurcation, then Da is indicative of the reaction rate constant alone when the same airway segments are being considered such that R_0 is constant. Damkohler numbers along selected airway generations, assuming an intermediate k_{r1} of 10^5 s^{-1}, are also listed in Table **7-1**.

Table **7-1**: Re and Da (assuming $k_{r1} = 10^5$ s^{-1}) at different levels of exertion in selected lower conducting airway generations along the respiratory tract. Reynolds numbers in generations roughly corresponding to the Re simulated in this chapter are highlighted in boldface. Weibel's model A (Weibel, 1963) was used to define airway diameters, and thickness scheme A of Miller *et al.* (1985) was used to define RTLF thicknesses.

	Reynolds Numbers			
Generation	Quiet Breathing	Light Exercise	Heavy Exercise	Da ($k_{r1} = 10^5\ \mathrm{s}^{-1}$)
0	659	1390	4169	3759
1	512	**1023**	3070	2780
4	178	356	**1068**	1547
5	**111**	222	667	1363
6	70	139	418	1191
7	44	**87**	262	1031
9	16	32	**95**	744
10	**9**	19	57	618
11	5	**11**	33	504
13	3	4	**11**	311

The uptake rate of O_3 into the RTLF was found to depend on Re, with the RTLF uptake rate being more sensitive to Da (or equivalently, k_{r1}) as Re increased. Another interesting finding was that at low values of Da, the RTLF uptake rate was insensitive to Re, unlike what was observed in Chapter 4, where reactions in the RTLF were assumed to be infinitely fast. These results indicate that at low Da, O_3 uptake is limited by diffusion and reaction in the RTLF, and the gas phase mass transfer resistance is unimportant. As Da increases, the gas phase resistance becomes more dominant, and uptake becomes completely gas phase diffusion controlled as $Da \to \infty$. This indicates that obtaining accurate airway geometries is more important in predicting O_3 uptake for higher values of Da than for low values.

The distributions at $Re = 10$ were very different from those at the higher Reynolds numbers, which were more similar to each other. The predicted flux patterns suggest that at $Re = 10$, injury at the carina would be less focused compared to injury in the immediate surrounding regions than at the higher Re.

The effects of Da on the rates and distributions of RTLF and tissue uptake rates in the monopodial bifurcation were similar to those in its symmetric counterpart. However, the overall average RTLF flux of O_3 was always greater in the symmetric bifurcation, and this effect became more pronounced at lower Re, suggesting that if O_3 reaction in the RTLF yields toxic products, then O_3-related damage in symmetric bifurcations would be greater than in a comparable monopodial bifurcation. On the other hand, if the reactions in the RTLF are protective, the airways downstream of the symmetric bifurcation would be more protected against O_3 compared to airways distal to the monopodial bifurcation because of the more efficient scrubbing of O_3 in the symmetric bifurcation. These effects would be more pronounced in the distal branches, where Re is low, all other factors being equal.

As discussed above, whether or not a high Da is protective against O_3 damage also depends on the nature of the reactions taking place in the RTLF. According the predictions of the CFD simulations, very little O_3, if any, will actually be able to penetrate to the tissue, except at the smallest values of the reaction rate constant. These findings are in agreement with those of Pryor (1992), who compared the time it would take for O_3 to cross the RTLF to the half-life of O_3 within that compartment and concluded that no O_3 would reach lung epithelial cells lined by RTLF layers with thicknesses greater than 0.1 μm. However, O_3-related damage has been observed to occur throughout the lower respiratory tracts of laboratory animals (Plopper et al., 1998; Joad et al., 2000; Postlethwait et al., 2000), suggesting that O_3-related damage may primarily be due to the production of cytotoxic compounds when O_3 reacts with substrates in the RTLF. This conclusion is supported by the work of Connor and fellow researchers (2004), who observed that the addition of ascorbic acid (AH_2) to medium covering human embryonic lung fibroblast cells resulted in cell injury when the system was exposed to O_3. However, they found that when the cells were covered with AH_2-free medium, very little injury resulted from exposure of the system to O_3, and this amount of injury was no different from that caused by exposure of the system to pure air. Accordingly, they concluded that cell injury was a result of the production of toxic products from the reaction of O_3 with RTLF components and not from the diffusion of O_3 to the cells. This may be because O_3 is a relatively insoluble gas, and without the presence of reactive substrates to drive the absorption of O_3, the amount of O_3 able to diffuse to the cell would be insufficient to cause damage.

According to many experimental studies, uric acid (UA) and AH_2 are the most O_3-reactive substances in the RTLF. Both are thought by a good number of researchers to be protective against O_3 damage in the lungs; however the author was unable to find in the literature the products of the reaction of O_3 with these antioxidants. Nonetheless, besides the study of Connor et al. (2004), Ballinger and colleagues (2005) have also shown that the reactions of O_3 with AH_2 as well as glutathione (GSH), but not UA or Trolox (vitamin E), produce toxic products that cause cell injury, specifically, oxidation of membrane proteins and lipids. They found, however, that membrane oxidation as a result of the reaction of O_3 with AH_2 was dose dependent in a complex manner, with the degree of membrane oxidation increasing with rising AH_2 concentration until it reached a maximum at 200 μM AH_2, and then decreasing as the AH_2 concentration was further increased. They hypothesized that at AH_2 concentrations higher than 200 μM, quenching of toxic products resulted in reduced cell membrane oxidation. The addition of UA or bovine serum albumin (BSA) to AH_2 in the medium led to a modest decrease in membrane oxidation, which they theorized could have been due to either the competitive reactions of UA and BSA with O_3, thus reducing the amount of O_3 that reacted with AH_2 or to the reduction of cytotoxic products from the reaction between AH_2 and O_3 by UA and BSA.

The study described above reveals additional complexities in the interaction of O_3 with RTLF substrates, namely, that the extent of cell injury may not display a simple dependence on the concentration of certain RTLF substrates, that there may be competition between substrates that have opposite effects on cell injury, and/or that some RTLF antioxidants may quench toxic products arising from other reactions in the RTLF. These conclusions indicate that it may be an oversimplification to predict cell injury based on either the total RTLF uptake rate (i.e., to assume that all reactions in the RTLF lead to cell injury), the amount of molecular O_3 reaching the epithelial cells (i.e., to assume that all reactions are protective), or even a simple ratio of quenching to toxic reactions. This suggests that a more complex model of reactions in the RTLF that also accounts for interactions between RTLF antioxidants and toxic reaction products and that includes the prediction of the concentrations of toxic reaction products and their diffusion towards lung epithelial tissue may be needed.

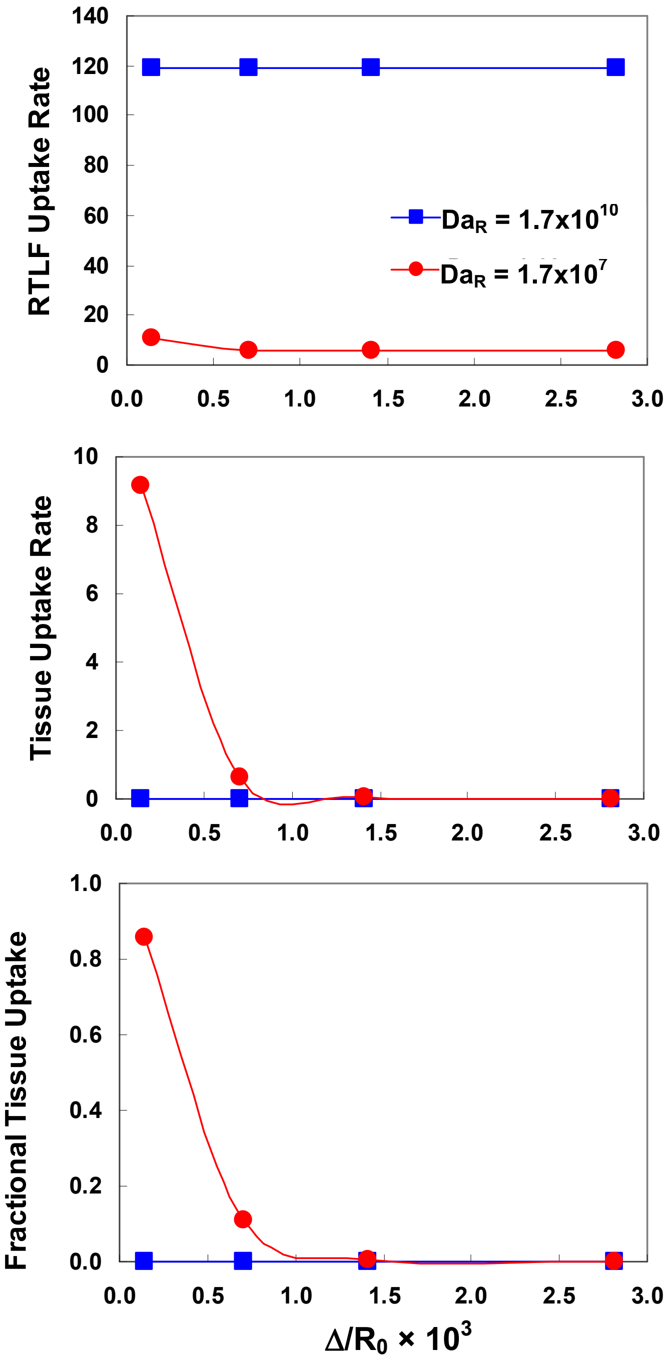

Figure **7-1**: Sensitivity to Δ / R_0 of the dimensionless RTLF (top panel) and tissue (middle panel) uptake rates and the fraction of ozone absorbed that penetrates to the tissue (bottom panel).

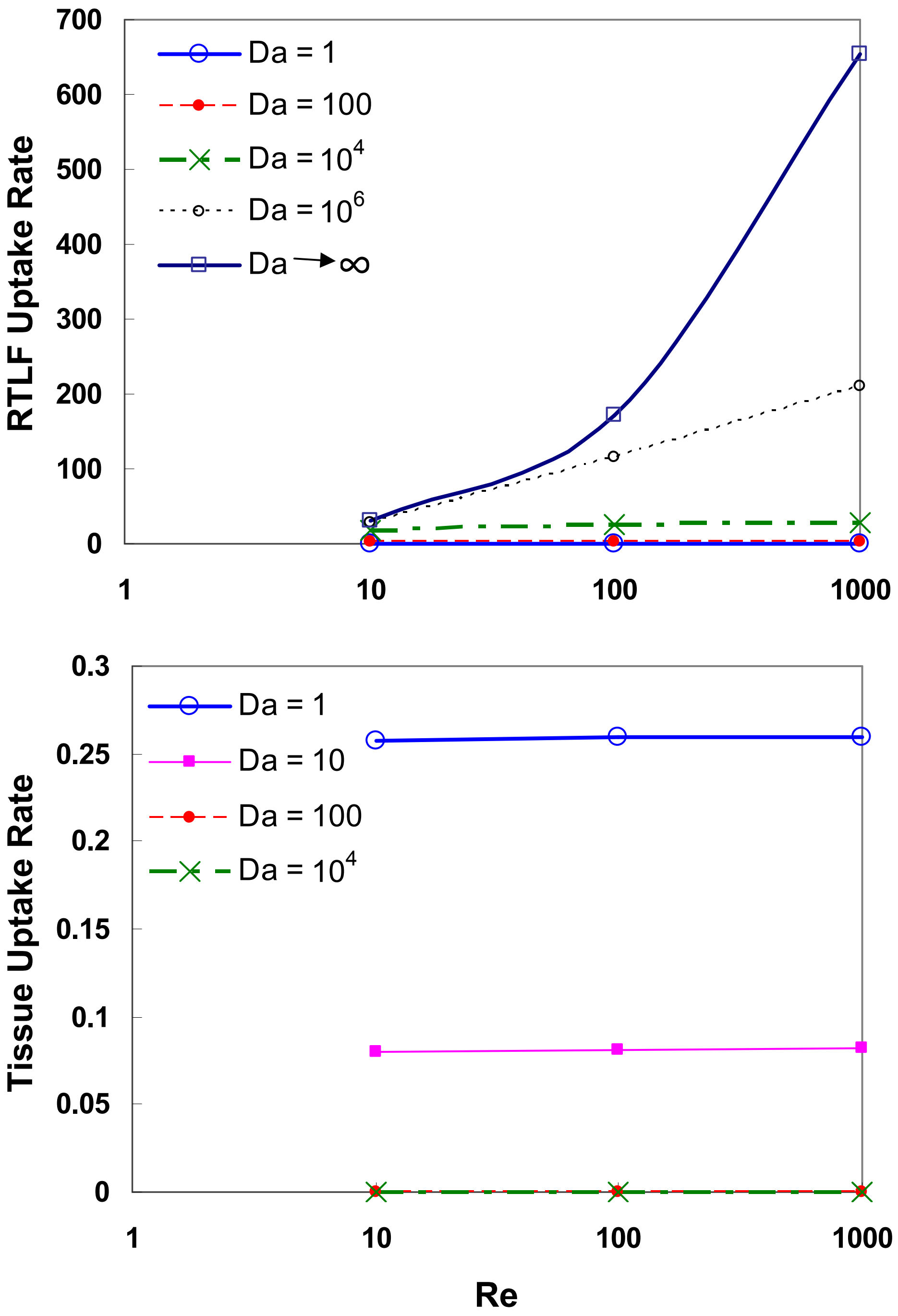

Figure **7-2**: Sensitivity of the dimensionless RTLF and tissue uptake rates to Da and Re in a symmetric bifurcation. The dimensionless RTLF uptake rates for an infinitely fast reaction at the gas-RTLF interface ($Da \to \infty$) are shown for comparison.

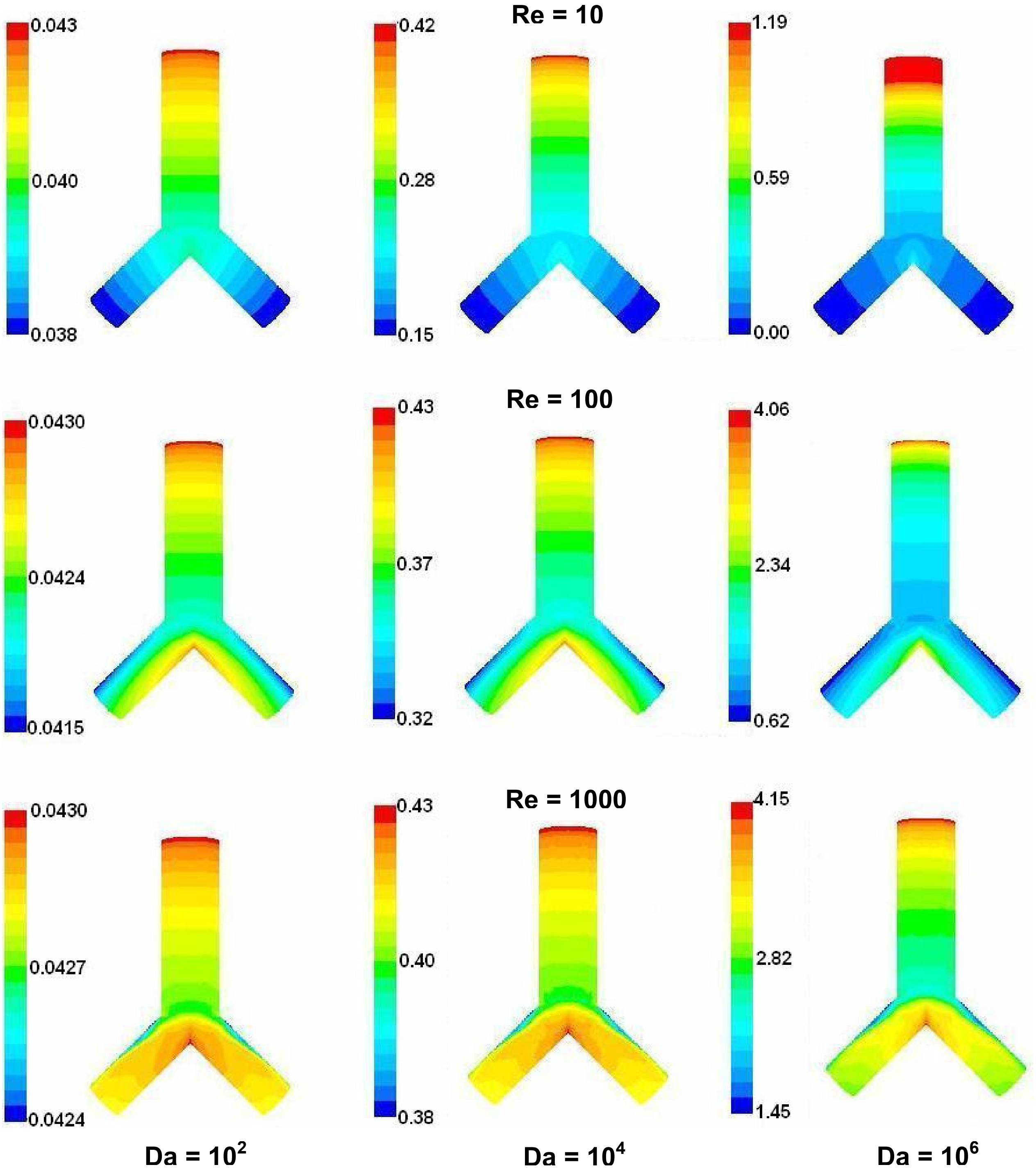

Figure **7-3**: Isocontours of the dimensionless flux into the RTLF (N) for various Re and Da in a symmetric bifurcation.

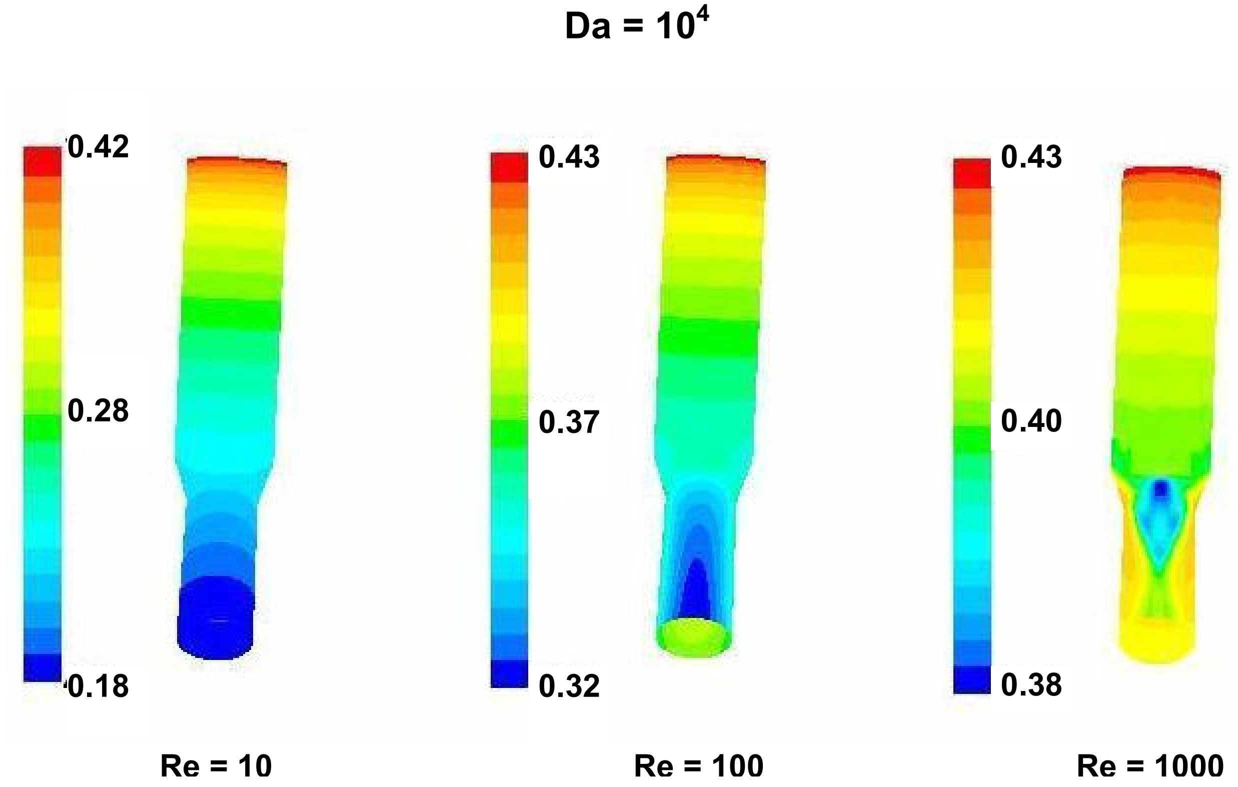

Figure **7-4**: Side views of isocontours of dimensionless flux into the RTLF (N) for three Re when $Da = 10^4$ in a symmetric bifurcation. The views in this figure are rotated 90° about the parent branch axes from those in Figure **7-3**.

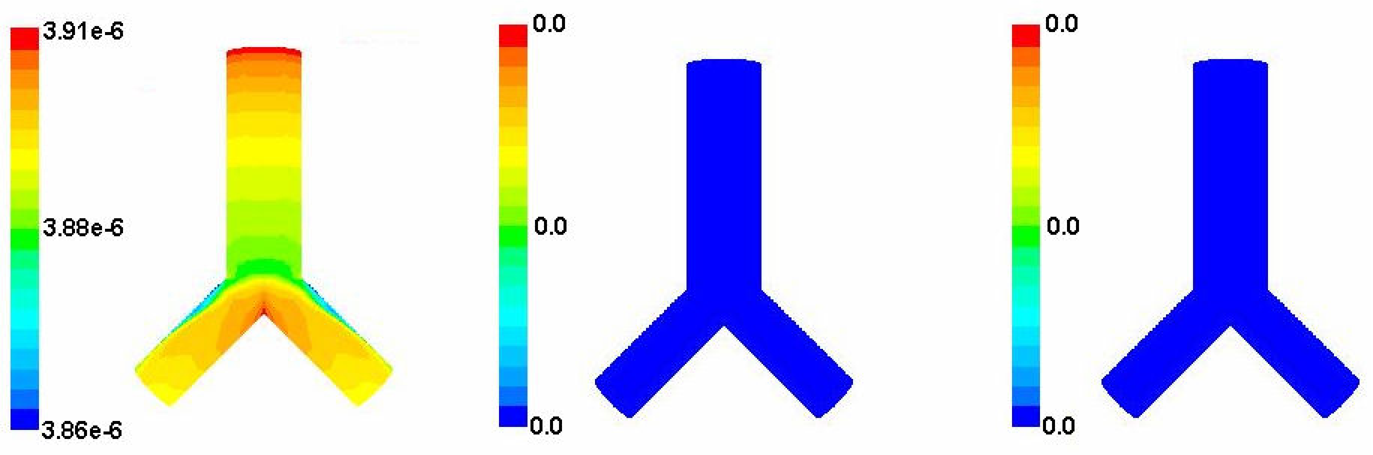

Da = 10^2 **Da = 10^4** **Da = 10^6**

Figure **7-5**: Isocontours of the dimensionless flux into tissue for various Da at $Re = 1000$ in a symmetric bifurcation.

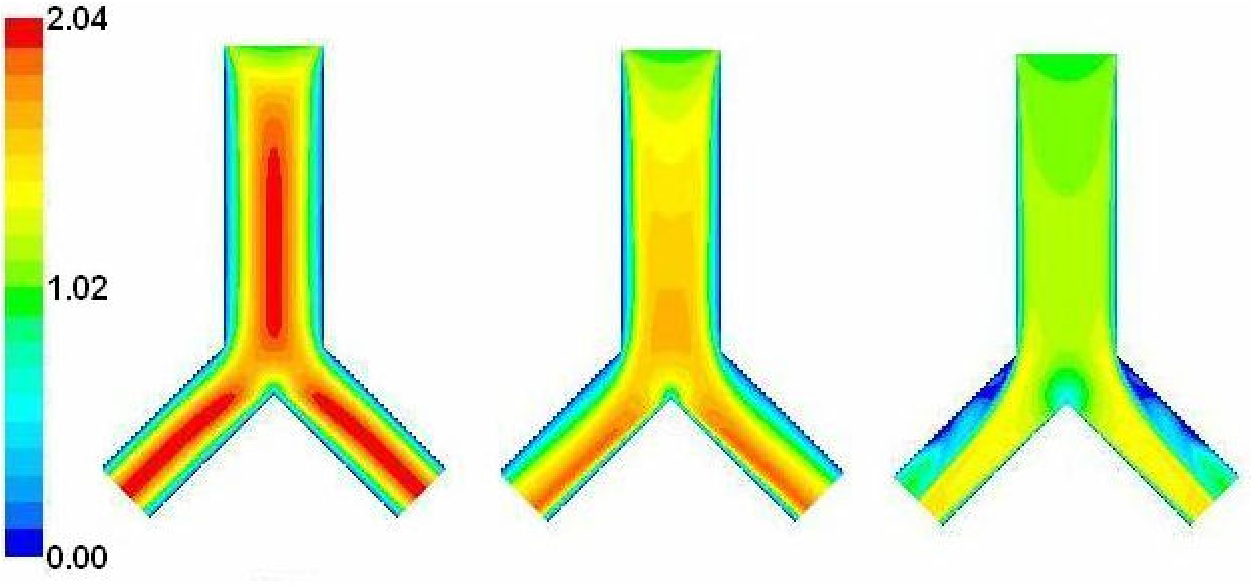

Re = 10 Re = 100 Re = 1000

Figure **7-6**: Isocontours of dimensionless velocity magnitude for *Re* = 10, 100, and 1000 in the bifurcation plane for inspiratory flow in a symmetric bifurcation.

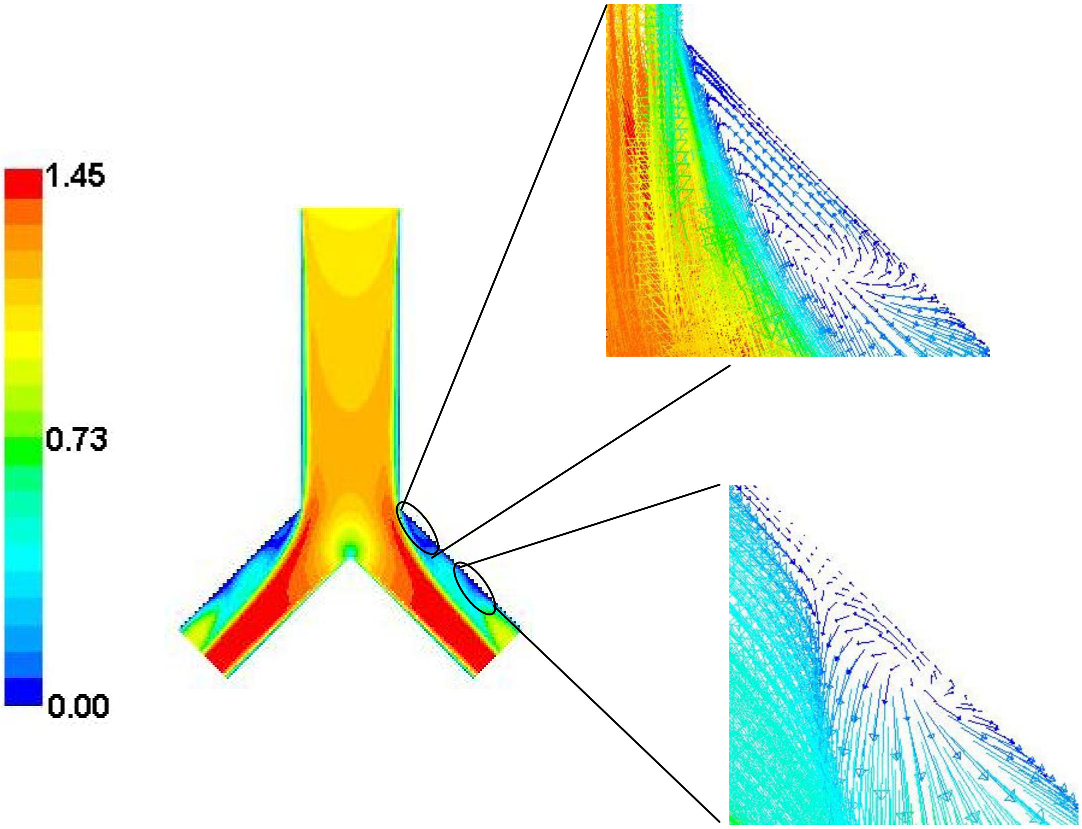

Figure **7-7**: Velocity vector plot in the bifurcation plane (colored by dimensionless velocity magnitude) for inspiratory flow at $Re = 1000$. The magnified regions show the two areas of backflow along the daughter branch walls.

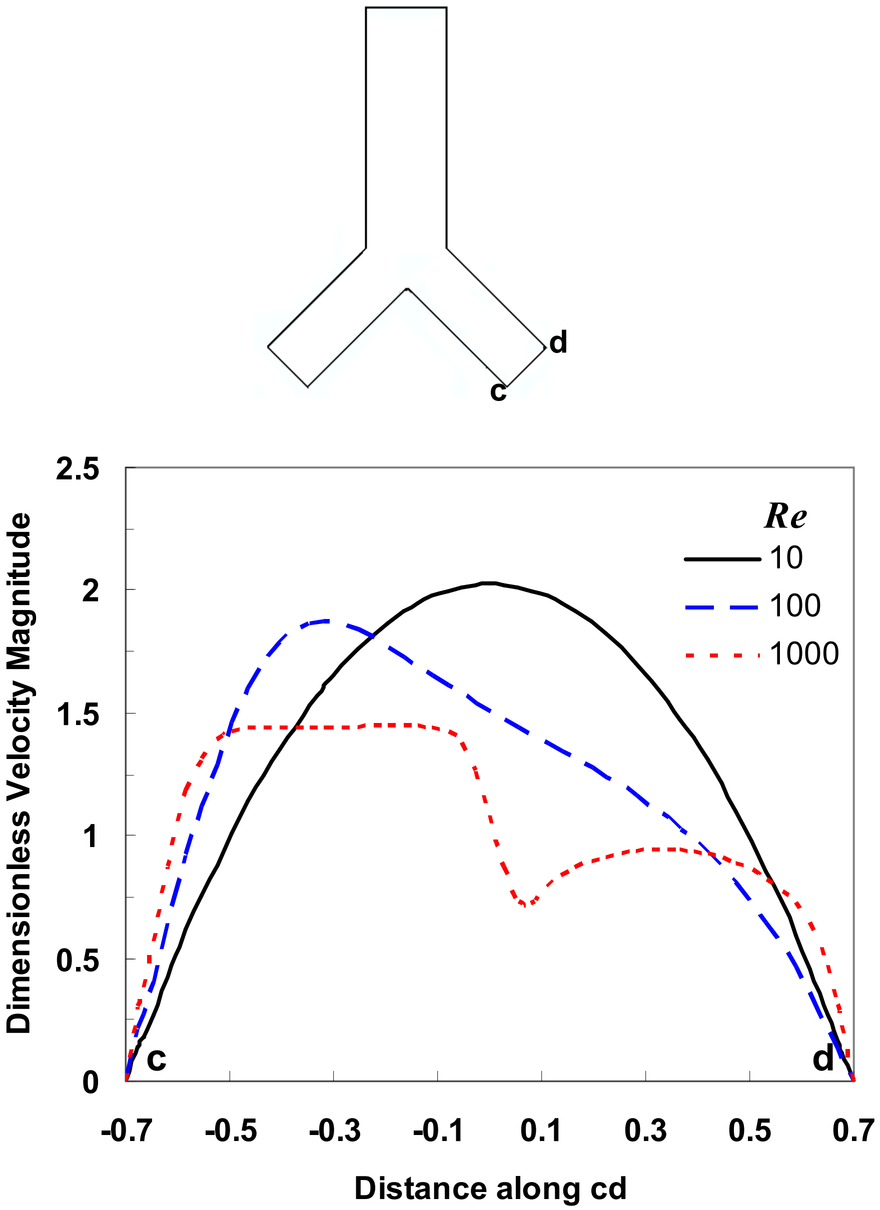

Figure **7-8**: Dimensionless velocity profiles in the plane of the bifurcation at the outflow boundaries of the daughter branch at *Re* = 10, 100, and 1000.

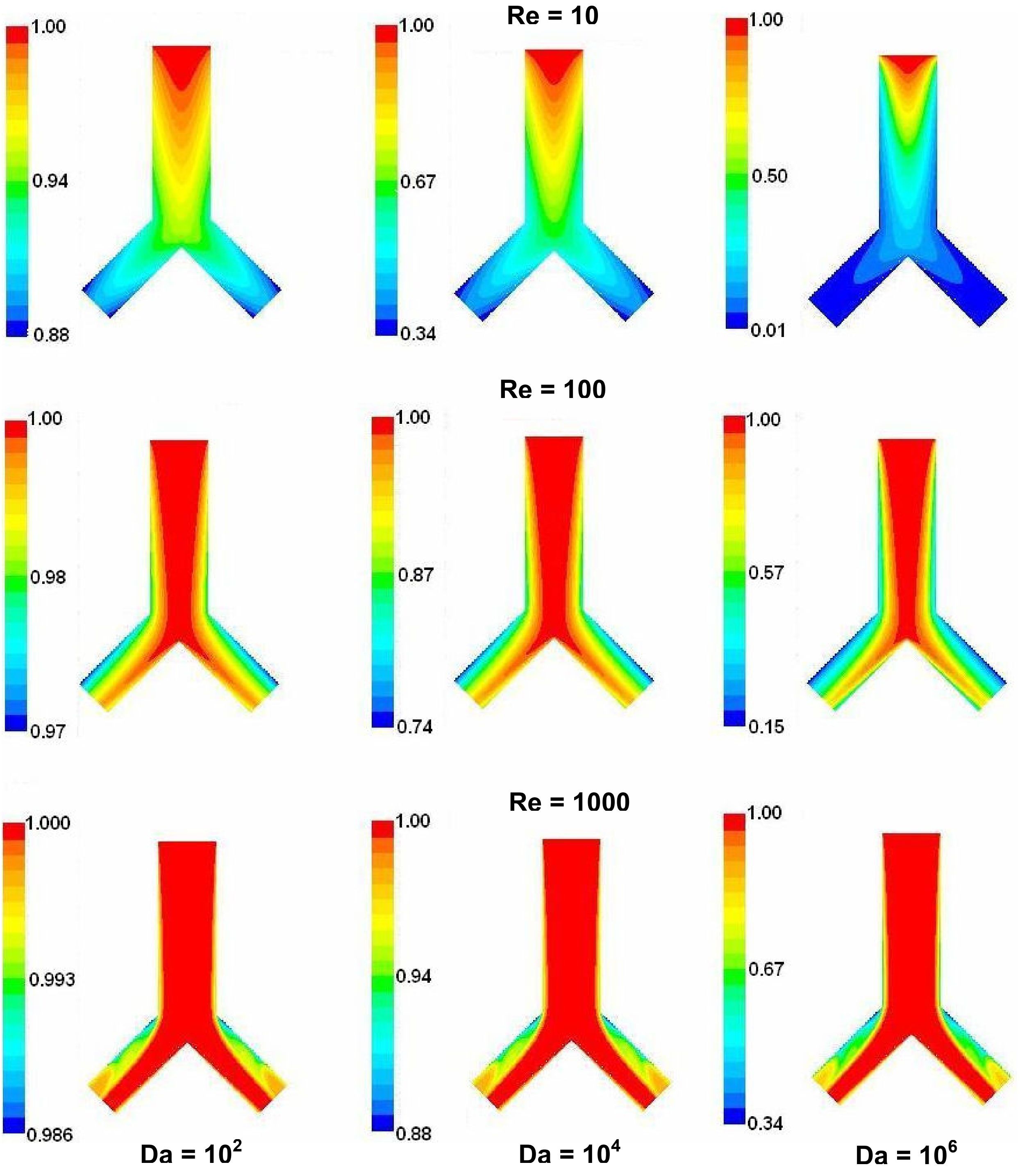

Figure **7-9**: Isocontours of dimensionless O_3 concentration in the bifurcation plane at various Re and Da for inspiratory flow in a symmetric bifurcation.

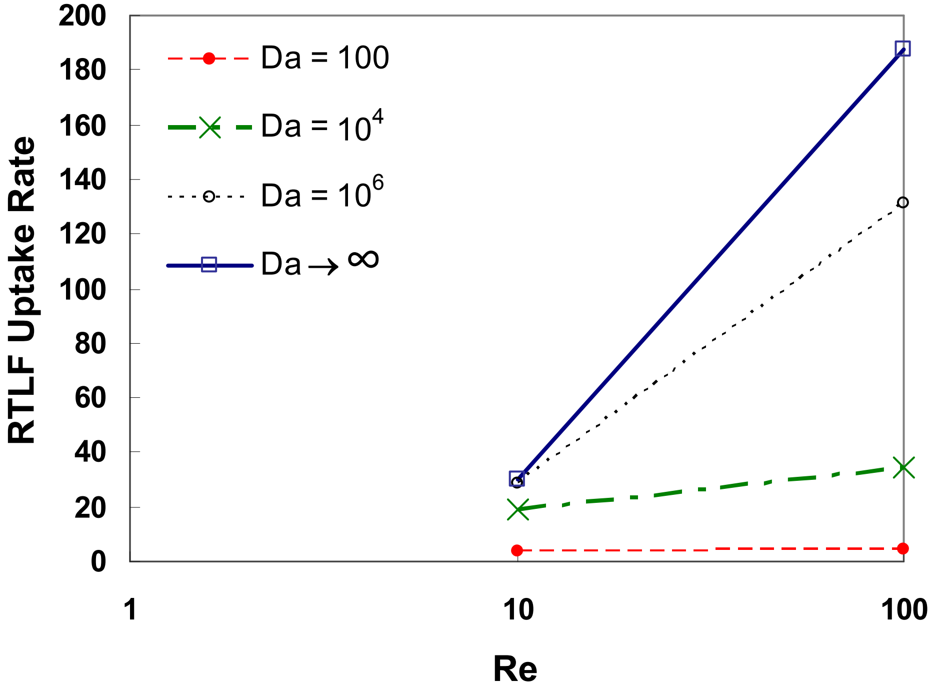

Figure **7-10**: Sensitivity of the dimensionless RTLF uptake rate to Da and Re in a monopodial bifurcation. The dimensionless RTLF uptake rates for an infinitely fast reaction at the gas-RTLF interface ($Da \to \infty$) are shown for comparison.

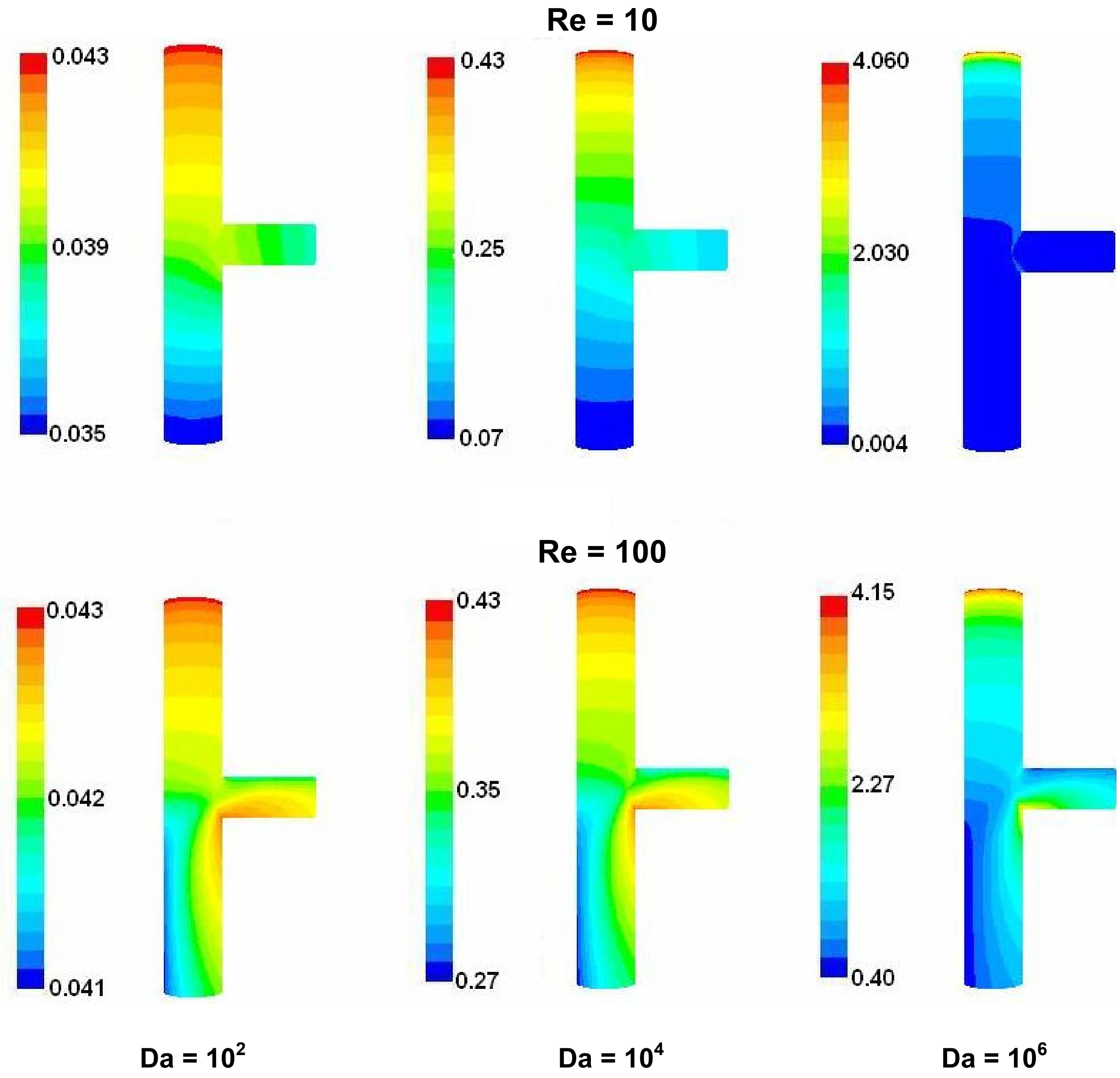

Figure **7-11**: Isocontours of dimensionless RTLF flux for $Re = 10$ and $Re = 100$ at various Da in a monopodial bifurcation.

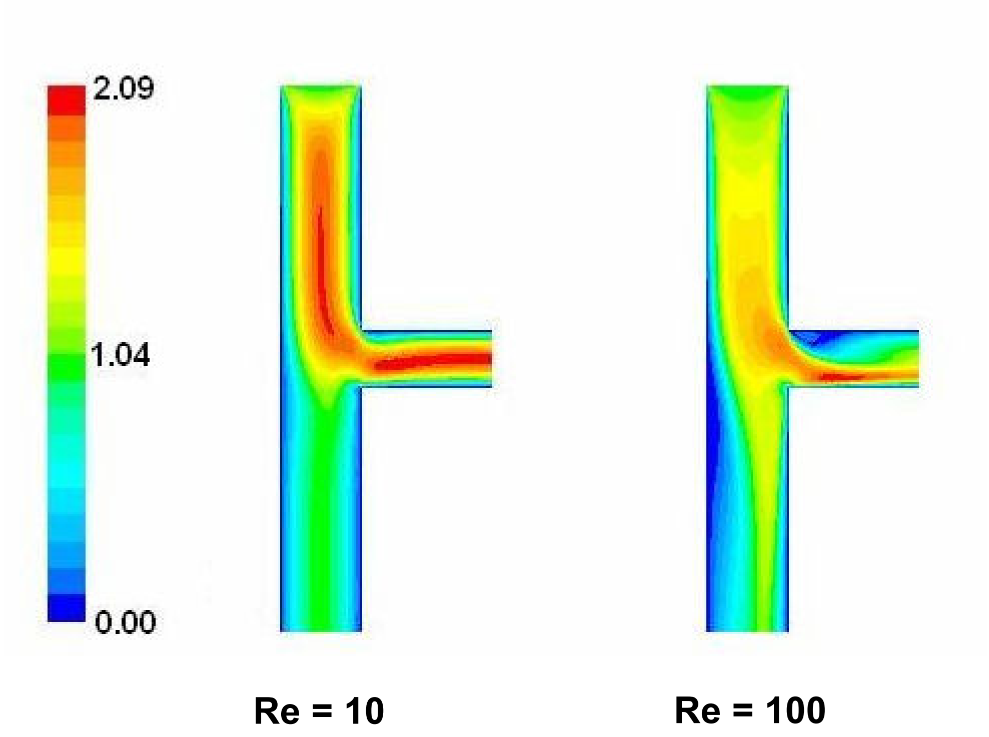

Figure **7-12**: Isocontours of dimensionless velocity magnitude in the bifurcation plane at *Re* = 10 and 100 for inspiratory flow in a monopodial bifurcation.

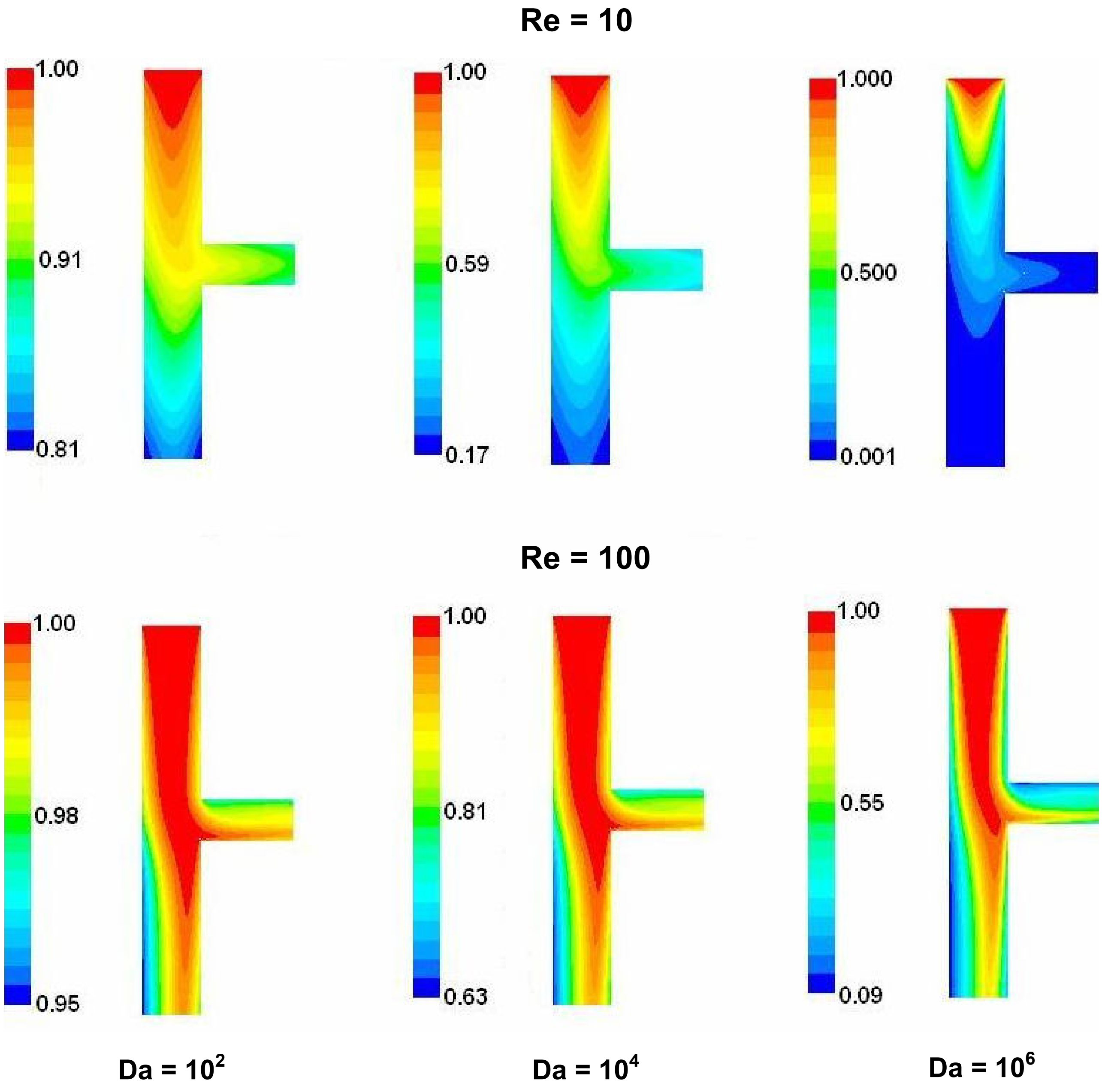

Figure **7-13**: Isocontours of the dimensionless O_3 concentration in a monopodial bifurcation for $Re = 10$ and $Re = 100$ at various Da in the bifurcation plane for inspiratory flow.

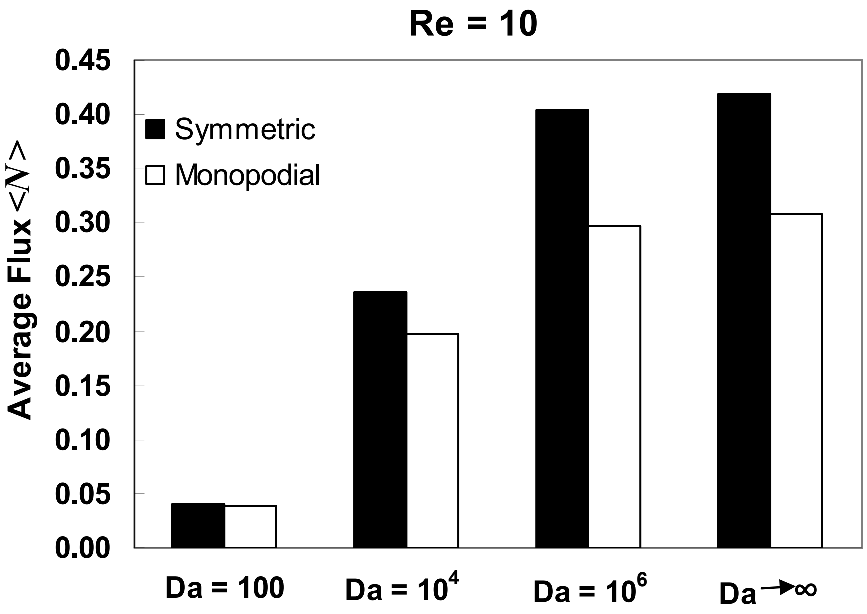

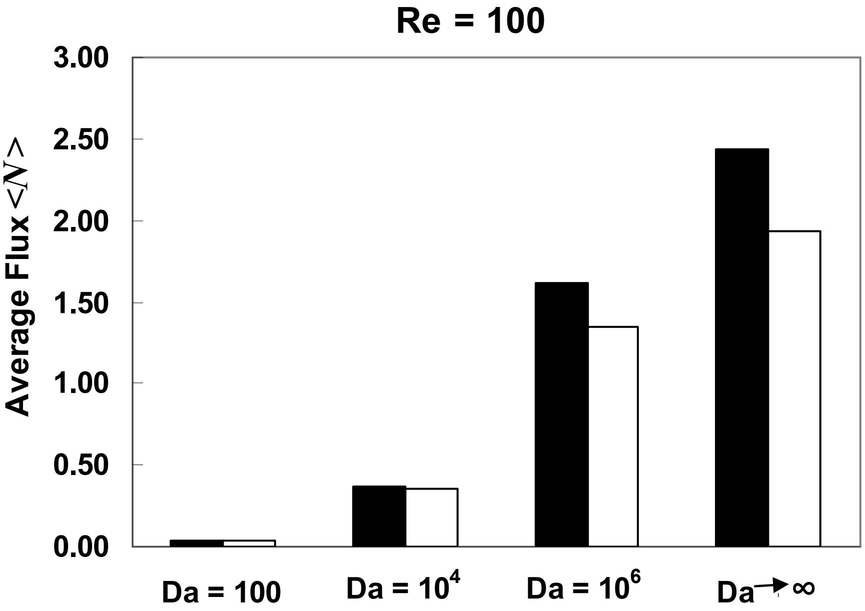

Figure **7-14**: Comparison of average fluxes $\langle N \rangle$ in the symmetric and monopodial bifurcations for different Da and at Re of 10 and 100.

Chapter 8

OZONE UPTAKE IN AN ANATOMICALLY ACCURATE AIRWAY MODEL

The preceding chapters investigated O_3 uptake in idealized airway bifurcations. While useful for elucidating the mechanisms responsible for O_3 dose distribution, idealized geometries do not reflect the more complex features present in real airways that will affect air flow patterns and consequently, O_3 uptake. Such features include the cartilaginous rings along the walls of the trachea and bronchi, carina curvature, and noncircular cross-sections of varying diameter along individual airway segments. This chapter will describe the construction of an anatomically accurate three-generation airway model, and the O_3 dose distribution in this geometry will be investigated.

8.1 CONSTRUCTION AND MESHING OF AN ANATOMICALLY ACCURATE GEOMETRY

The CFD simulations required the creation of an anatomically accurate volume in GAMBIT (ANSYS Inc., Lebanon, NH) that would be meshed and exported to FLUENT (ANSYS Inc., Lebanon, NH). This process involved two stages.

8.1.1 Surface Generation

The first stage involved the generation of a surface from MRI data that would be exported to GAMBIT. Since data for the human respiratory tract were not available, the

MRI data used were for the airway cast (lower respiratory tract) from a 29 day old, 0.52 kg male rhesus monkey (*Macaca mulatta*) and consisted of 512 transverse slices, each with a square field of 7cm on a side. The resolution in each slice and the thickness of a single slice were both 273 μm. Each slice was originally stored as an 8-bit TIFF file containing 256 × 256 pixels, and the data were compiled in DDV (Digital Data Viewer) format (DDV, Computational Geometry Consulting, Inc., www.compgeomco.com). The imaging and conversion to DDV format were carried out by Dr. Kevin Minard at Pacific Northwest National Laboratory, Richland, WA. The compiled raw MRI data were imported into AMIRA™ version 4.0 (Mercury Computer Systems, Inc., Chelmsford, MA), a commercial 3D visualization and volume modeling software package.

The desired airways were then segmented in AMIRA™ using the brush and magic wand tools in the *image segmentation editor*. Segmentation is the process of partitioning an image into constituent components and involves the grouping of pixels/voxels defining a desired region, in this case, the lumina of the first three airway generations, i.e., the trachea, the primary bronchi, and the secondary bronchi. The *brush* tool was used to manually select the desired pixels, and the *magic wand* tool was used to perform 2D or 3D region growing. The latter procedure involved selecting a range of gray values to define the desired region and clicking on a pixel/voxel. The largest area connected to that pixel/voxel that contained pixels/voxels within the specified range of gray values was selected. In order to facilitate a potentially long and tedious segmentation process, the complete MRI data were cropped to remove slices that did not contain the first three airway generations. It was this reduced data set that was segmented.

The selected voxels were grouped to define a separate "material." Since some defects may have arisen during the preceding steps, corrections of such potential defects were performed by filling in any existing holes, removing islands of unconnected pixels or voxels and assigning them to one of the materials, and smoothing the boundaries of the segmented region.

The next step was to generate a triangulated surface from the segmented data using the *SurfaceGen* module. Constrained smoothing using a lesser degree of smoothing than the default was applied during surface generation. Some of the preceding steps are illustrated in Figure **8-1**. In addition, the *add border* option was not selected in order to ensure an open surface at the entrance of the trachea and the exits of the terminal airway segments. However, one of the terminal airway segments did not extend to the boundaries of the cropped data set. Terminating segmentation at the end of this airway segment would result in a curved closed surface at the corresponding exit, making subsequent volume creation in GAMBIT virtually impossible. To avoid this difficulty, the data set was segmented before surface generation in order to create an artificial airway wall that extended from the edge of the actual airway wall to the boundary of the data set. This resulted in an open surface at the end of the artificial extension, which was later removed in GAMBIT. The generated surface was saved in STL (sterolithography) format and imported as an STL surface mesh into GAMBIT (Figure **8-2A**).

8.1.2 Construction and Meshing of Airway Volume

STL files consist of a list of coordinates defining triangles that characterize a surface. The surface in GAMBIT possessed a triangulated surface mesh consisting of the triangles describing the topology of the imported airway model geometry. This surface mesh was deleted, and the geometry was then cleaned up by eliminating short and dangling edges. A flow inlet (into the trachea) and flow outlets (out of the terminal airway segments) that were perpendicular to the axes of their respective airway branches were created by truncating the surface using planar cuts. One of the planar cuts eliminated the artificial airway wall created in a previous step. Faces were then created at these new inlet and outlet boundaries, and all of the faces (including the airway wall) were stitched together to create an enclosed volume (Figure **8-2B**).

Before the volume meshing and exportation to FLUENT, the volume was scaled. When the surface mesh was imported into GAMBIT, one pixel was equal to one unit of length. Taking into account the resolution of the original MRI images, the volume was scaled by a factor of 0.0273 in order for one unit of length in GAMBIT to be equivalent to 1 cm. Because of the complexity of the anatomically accurate geometry, a fully hexahedral mesh could not be generated. On the other hand, using a tetrahedral mesh would result in significantly more elements, leading to increased computational cost. Moreover, tetrahedral elements are not as accurate as hexahedral elements of the same size. A compromise was achieved by using the *hexcore* meshing scheme, which creates a core of hexahedral elements surrounded by an outer layer of pyramidal and tetrahedral elements. The volume was initially meshed with a *hexcore* mesh 0.03 cm in size, and grid convergence studies were later conducted. The resulting meshed geometry is displayed in Figure **8-2B** and Figure **8-2C**. Approximate airway dimensions are listed in Table **8-1**. Airway segments were labeled in a binary fashion, similar to that found in Raabe *et al.* (1976), using the digits 1 and 0, with the trachea being labeled as 1. The identification labels of the downstream segments were formed by taking the ID of the parent branch and adding either a 1 if the given segment was the daughter branch with the larger diameter, or a 0 otherwise. The meshed geometry was exported to FLUENT for simulation, where they were rescaled in order to ensure correct dimensions.

Table **8-1**: Rhesus monkey airway dimensions. The radius is defined as half the hydraulic diameter, which is defined in equation **8.3**. The airway segment length measurements are very approximate. The radii and cross-sectional areas of only the inflow and outflow boundaries are given.

Airway Segment	**Length (cm)**	**Radius (cm)**	**Cross-sectional Area (cm^2)**
1 (Trachea)	2.028	0.166	0.090
11	0.218		
10	0.657		
111	0.335	0.117	0.048
110	0.403	0.078	0.020
101	0.399	0.094	0.029
100	0.346	0.085	0.025

8.2 CFD SIMULATIONS

8.2.1 Governing Equations and Boundary Conditions

The governing equations were solved in dimensional form, with the exception that the concentration was scaled with the tracheal inlet concentration c_0 so that an inlet concentration of 1 was input into FLUENT. Accordingly, the continuity and Navier-Stokes equations were solved as written in equations **3.1** and **3.2**, and the modified convection-diffusion that was solved is

$$\mathbf{u}^* \bullet \nabla^* c = D_g \nabla^{*2} c \qquad \mathbf{8.1}$$

where all the variables were defined in Section **3.2**.

The governing equations were solved applying the boundary conditions listed in Table **8-2**.

Table **8-2**: Boundary conditions for steady inspiratory flow and O_3 transport in the anatomically-accurate airway geometry.

Airway walls	$\mathbf{u}^* = \mathbf{0}$	$c = 0$ or $-D_g\left(\mathbf{n}\bullet\nabla^* c\right)_{wall} = K^* c_{gi}$
Inflow boundary	$\mathbf{u}^*\bullet\mathbf{n} = 152\ \text{cm/s}$ $\mathbf{u}^*\times\mathbf{n} = \mathbf{0}$	$c = 1$
Outflow boundaries	$p^* = 0$	$\nabla^* c\bullet\mathbf{n} = 0$

At the inflow boundary to the trachea, zero radial velocity, a uniform velocity of 152 cm/s normal to the boundary (corresponding to a volumetric flow rate of 13.64 ml/s), and a scaled concentration of 1 were imposed. At the outlets of the terminal airway segments, zero pressure and a zero diffusive flux of O_3 were imposed. At the airway walls, the no-slip condition (zero velocity) was imposed, and either an infinitely fast RTLF reaction (zero O_3 concentration) or a pseudo-first order RTLF reaction resulting in a scaled flux of $K^* c_{gi}$ at the gas-RTLF interface, where K^* and c_{gi} are defined in Sections **8.4** and **7.1**, respectively, was imposed.

The inlet flow rate was calculated from the following correlation for rhesus monkeys given by Blackburn (1988):

$$I(\text{m}^3/\text{day}) = 0.81 W^{0.4862} \qquad \textbf{8.2}$$

where I is the respired volume of air per day and W is the weight of the animal in kg. The calculated flow rate of 13.64 ml/s resulted in $Re = 152$, where the Reynolds number is based on the radius R_0 of the trachea inlet. The radii of the inflow and outflow boundaries were defined as half the hydraulic diameter D_H, given by

$$D_H = \frac{4A^*}{P^*} \qquad \textbf{8.3}$$

where A^* is the cross-sectional area of the inlet/outlet and P^* is the perimeter.

8.5.2 Grid Resolution

Simulations with an infinite infinitely fast reaction at the wall (zero wall concentration) were carried out on three meshes of increasing refinement in order to ensure that the results were independent of mesh size. Mesh 1 was a uniform *hexcore* mesh with elements of size 0.03 cm (dimensionless size of 0.181 based on the radius of the inlet to the trachea) and consisted of 530,828 mesh elements. In generating Mesh 2, also a *hexcore* mesh, an element size of 0.008 cm (dimensionless size of 0.048) was specified at the airway walls and moving away from the walls, the element size was gradually increased by a factor of 1.05 until a maximum size of 0.03 cm was reached. This resulted in a mesh with 669,802 cells. Both Mesh 1 and Mesh 2 were created in GAMBIT. Mesh 3 was composed of 1,505,035 elements and was generated in FLUENT by curvature-based adaptive refinement of Mesh 2. (See Section **4.1.1**.)

In order to assess the sensitivity of the numerical predictions to mesh size, the circumferentially averaged flux of O_3 on the airway wall assuming an axis roughly parallel to the axis of the trachea. All three meshes gave very similar results downstream of the flow entrance, where a singularity existed on the airway walls (see Section **4.1.1**). Downstream of the flow entrance, the maximum variations in circumferentially-averaged fluxes between Mesh 1 and Mesh 2 was 7.72% (average variation = 1.04% ± 0.89), and that between Mesh 2 and Mesh 3 was 4.10% (average variation = 1.01% ± 0.87). Macroscopic quantities such as average velocities and O_3 flow rates at outflow boundaries were also compared, and the maximum differences between Meshes 1 and 2 and Meshes 2 and 3 were 6.9% and 2.0%, respectively. Therefore, Mesh 3 was considered to provide adequate resolution and was used in subsequent simulations.

8.6 RESULTS – INFINITELY FAST REACTION IN RTLF

Simulations were carried for $Re = 152$ assuming an infinitely fast reaction in the RTLF, leading to a zero-concentration at the gas-liquid interface. Figure **8-3** shows the flow field at three cross-sections through the anatomically-accurate airway model. The trachea was sufficiently long for the flow to become fully developed within that airway segment at $Re = 152$. (Note that the velocity magnitude at the bottom portion of the cross-section shown in Figure **8-3A** is small because that part of the cross-section is very close to the airway wall.) Furthermore, the outflow Reynolds numbers, i.e., the Reynolds numbers based on half the outlet hydraulic diameter, increased with increasing cross-sectional area (Figure **8-3c**, cf. Table **8-1**).

The flow distribution was skewed toward the inner walls of the first generation daughter branches (branches 10 and 11) and three of the second generation daughter branches (branches 100, 101, and 110). In contrast, the flow distribution in branch 111 was skewed toward its outer wall. This is because its parent branch, branch 11, was very short, and the inner wall of this branch became the outer wall of branch 111. The flow distributions at the airway outlets are presented in Figure **8-4** and show that until the flow exits the airway model, the flow distributions remain skewed toward the inner walls in branches 100, 101, and 110 and toward the outer wall in branch 111.

The scaled concentration distributions were also similar to the velocity magnitude distributions (Figures **8-5** and **8-6**) in that the concentration distributions in all branches except branch 111 were skewed toward the inner walls, and the concentration distribution in branch 111 was skewed towards the outer walls. Moreover, the average concentrations exiting the terminal branches increased with increasing outlet Reynolds number (Figure **8-5**). This is because at the lower Reynolds numbers, the residence time of the O_3-air mixture in those terminal branches was longer, providing more time for O_3 to be absorbed into the RTLF.

The distribution of scaled flux N^*/c_0, where N^* was defined in Section **3.2**, along the walls of the airways are presented in Figure **8-7**. Unlike what was observed in the idealized bifurcations, the flux of O_3 through the wall of the trachea did not decay monotonically with axial position. Instead there were large areas of low flux surrounded by regions of higher flux along the trachea walls. This is because the trachea wall featured irregularities such as the undulations caused by the cartilaginous rings, whereas the idealized bifurcations possessed smooth walls. Moreover, each branch was modeled as a right circular cylinder in the idealized bifurcations whereas the trachea was curved in the axial direction.

Similar to what was predicted in the idealized bifurcations, in most cases, regions of high flux were found along the inner wall of each branch downstream of the trachea (Figure **8-8** – it is difficult to see this in branch 100 because of the color scale used), even along the inner wall of branch 111. The region of high flux along the walls of this branch extended almost all around the branch except for a small, low flux region along a small portion of its inner wall near the back of the airway. Hot spots of flux were predicted to occur at all the carinas, and the second generation carina hot spots were smaller magnitude of the hot spots of the first generation carina. In addition, the magnitude of the hot spot at the carina that formed the junction between branches 100 and 101 was greater than that at the carina that formed the junction between the other second generation daughter branches.

8.4 RESULTS – FINITE REACTION IN RTLF

The incorporation of a finite reaction in the RTLF was accomplished in a manner similar to that outlined in Section **7.1**. The condition for continuity of flux was expressed in equation **7.1**. The scaled form of the continuity of flux may be written

$$N^*/c_0 = -D_g\left(\mathbf{n}\bullet\nabla^* c\right)_{wall} = K^* c_{g,i}(z)\,. \qquad \mathbf{8.4}$$

Recognizing that $N^*_{RTLF} = N^*$, a comparison of equations **6.9**, **6.12**, and **7.1** reveals that

$$K^* = \frac{D_l\,\alpha}{\Delta}\sqrt{Da}\coth\sqrt{Da}\ . \qquad \mathbf{8.5}$$

Using a derivation similar to that outlined in Section **7.1**, the value $k_{f,r}$ to be input into FLUENT was determined to be equal to K^*, i.e.,

$$k_{f,r} = \frac{D_l\,\alpha}{\Delta}\sqrt{Da}\coth\sqrt{Da}\ . \qquad \mathbf{8.6}$$

In order to facilitate later comparisons with the idealized bifurcations, a relative RTLF thickness Δ/R_0 of 4.6×10^{-3} was used, which was equivalent to an RTLF thickness of $7.65\ \mu\text{m}$ in all airway segments. All simulations were carried out for $Da = 1000$, corresponding to a first order reaction rate constant of about $4.54\times10^4\ \text{s}^{-1}$.

The scaled concentration contours are presented in Figure **8-9**. These concentration distribution patterns were similar to those in Figure **8-5**, except that, because of the slower reaction in the RTLF, the scaled concentrations were higher than those in the simulations that assumed an infinitely fast reaction rate.

The distributions of scaled flux along the airway walls are shown in Figures and **8-11**. Although the fluxes were about two orders of magnitude smaller than those predicted from the simulations that assumed an infinitely fast reaction in the RTLF, the flux distribution were very similar to those described in Figures **8-7** and **8-8**. However, the hot spots of flux were less focused than those predicted assuming a zero concentration of O_3 at the wall, and the range of flux magnitudes in the entire airway model was much smaller, indicating a relatively uniform distribution of flux. When $Da = 1000$, no O_3 reached the tissues.

8.8 DISCUSSION

Unlike the simulations in the idealized bifurcations, which assumed equal flow rates through each daughter branch and zero normal viscous stress, the simulations in the anatomically accurate airway model imposed equal pressures at all the flow outlets. As discussed in Section **5.3.2**, the flow splits have been theorized to depend on the number of terminal bronchioles or alveoli supplied by the branches in question. Because of the limited resolution of the MRI data, it was not possible to determine the number of terminal bronchioles or alveoli in this model, and doing so would be extremely time consuming even if the resolution were adequate. Several other investigators who have simulated flow and particle deposition in anatomically accurate airway models have also assumed equal pressures at all flow outlets (Cebral and Summers, 2004; Robinson et al., 2006; Nowak et al., 2003). Cebral and Summers (2004) justified the use of this outlet boundary condition by stating that most of the pressure drop in the lung occurred distal to their airway models, which encompassed about 3 to 4 generations, beginning at the trachea.

The flow split is defined as the flow rate through an outflow boundary divided by the total flow rate through the bifurcation. Table **8-3** compares the flow splits predicted by the simulations to those that would occur if the flow rates through the branches obeyed Poiseuille's law, i.e., if the flow rates were proportional to the airway radius raised to the fourth power (assuming equal pressure gradients through all terminal airway segments). The flow splits predicted by the simulations and those predicted by Poiseuille's law were very close.

Table **8-3**: Comparison of the flow splits predicted by the simulation (zero pressure at outflow boundaries) and flow splits based on Poiseuille flow.

Outflow Boundary	**PREDICTED FLOW SPLITS**	
	Simulation	**Poiseuille**
100	0.151	0.148
101	0.232	0.221
110	0.105	0.105
111	0.512	0.526

Despite the presence of an additional upstream branch, the velocity magnitude, scaled concentration and flux distributions compared well with those observed in the idealized bifurcations, except for branch 111 due to the shortness of its parent branch (branch 11). This suggests that for convection-dominated flows, such as the flow simulated in the present study, idealized single airway bifurcations may do an adequate job of predicting the main features of O_3 flux distributions along the walls of airway segments if airway branches are long enough. Simulations on models possessing more generations are needed to verify this hypothesis.

As was the case with idealized bifurcations, local hot spots of flux always occurred at the carina; however, these hot spots were less focused and more spread out than those in the idealized airway bifurcations because, unlike the carinas of the idealized bifurcations, the carinas in the anatomically accurate airway models had finite curvature. The anatomically accurate airways exhibited surface irregularities such as protrusions on the airway walls arising from the cartilaginous rings and axial curvature of the airway segments, especially the trachea, features which impact flow and flux distribution patterns. Therefore, the idealized bifurcations were unable to exactly predict the patterns of uptake distribution in the anatomically accurate airways. Differences between model predictions of airways represented by smooth tubes and airways lined by cartilaginous rings were also found by Martonen et al. (1995). These investigators obtained an analytical solution of particle diffusion in an idealized model of an airway branch lined by cartilaginous rings and determined that the presence of these rings enhanced particle dose to large bronchi compared to that for airways that were modeled as having smooth walls.

Further comparisons were performed by analyzing the overall average dimensionless fluxes and the fractional uptake in the idealized symmetric 90° bifurcation and the anatomically accurate airway model. In the anatomically accurate geometry, the overall dimensionless uptake $\dot{M}$ was determined from the following equation:

$$\dot{M} = \frac{\left\langle \int_{A^*} c\mathbf{u}^* \bullet \mathbf{n} \, dA^* \right\rangle}{D_g \, R_0} \qquad \mathbf{8.7}$$

where the brackets denote the jump in the value of the integral from the inflow boundary to the outflow boundaries, A^* is the (dimensional) surface area of the walls of the geometry and $\mathbf{n}$ is the unit vector normal to the boundary. The dimensionless surface area A was calculated thus:

$$A = A^* / R_0^2 \qquad \mathbf{8.8}$$

For the simulations assuming an infinitely fast reaction in the RTLF, the average flux in an idealized bifurcation at $Re = 152$ was determined by regressing the dimensionless uptake rate $\dot{M}$ with Re (see Figure **4-13**, Section **4.2.3**) to obtain the following correlation:

$$\dot{M} = 11.84\,Re^{0.58} \qquad \textbf{8.9}$$

For the simulations with $Da = 1000$, the uptake rate in the idealized bifurcation at $Re = 152$ was assumed to be equal to that at $Re = 100$ since at that Da, uptake was essentially insensitive to Re at such small values of Da. The results of the comparison are presented in Table **8-4**.

For an infinitely fast RTLF reaction, the total dimensionless uptake rate and the fractional uptake in the anatomically accurate airway model were about 37% and 32% greater, respectively, than the corresponding values in the idealized airway bifurcation. This is at least partly because the dimensionless surface area of the anatomically accurate airway model is a little more than twice that of the idealized bifurcation. For the same reason, the overall average flux $\langle N \rangle = \dot{M}/A$ in the anatomically accurate bifurcation was less than that in the idealized bifurcation since the flux along the airway walls generally decreased in the downstream direction. It is unclear to what extent the surface irregularities of the anatomically accurate geometries contribute to these differences.

Table **8-4**: Comparisons of the dimensionless uptake rate $\dot{M}$, overall average dimensionless flux, and fractional uptake in the idealized 90° symmetric bifurcation and the anatomically accurate airway model.

	$Da \to \infty$		$Da = 1000$	
	Idealized	Anatomically Accurate	Idealized	Anatomically Accurate
$\dot{M}$	222.5	304.3	9.2	19.3
Dimensionless Area	71.0	150.2	71.0	150.2
$\langle N \rangle$	3.13	2.03	0.13	0.13
θ	0.56	0.74	0.023	0.046

An interesting result found for $Da = 1000$ was that the overall average dimensionless fluxes in both geometries were virtually identical. This finding is not entirely surprising if one considers that, as was shown in Chapter 7, the flux distribution was fairly uniform throughout the idealized bifurcation at smaller values of Da and that gas phase resistance is unimportant at low Da. Therefore, for low values of Da, it may not be very important to obtain highly accurate airway geometries.

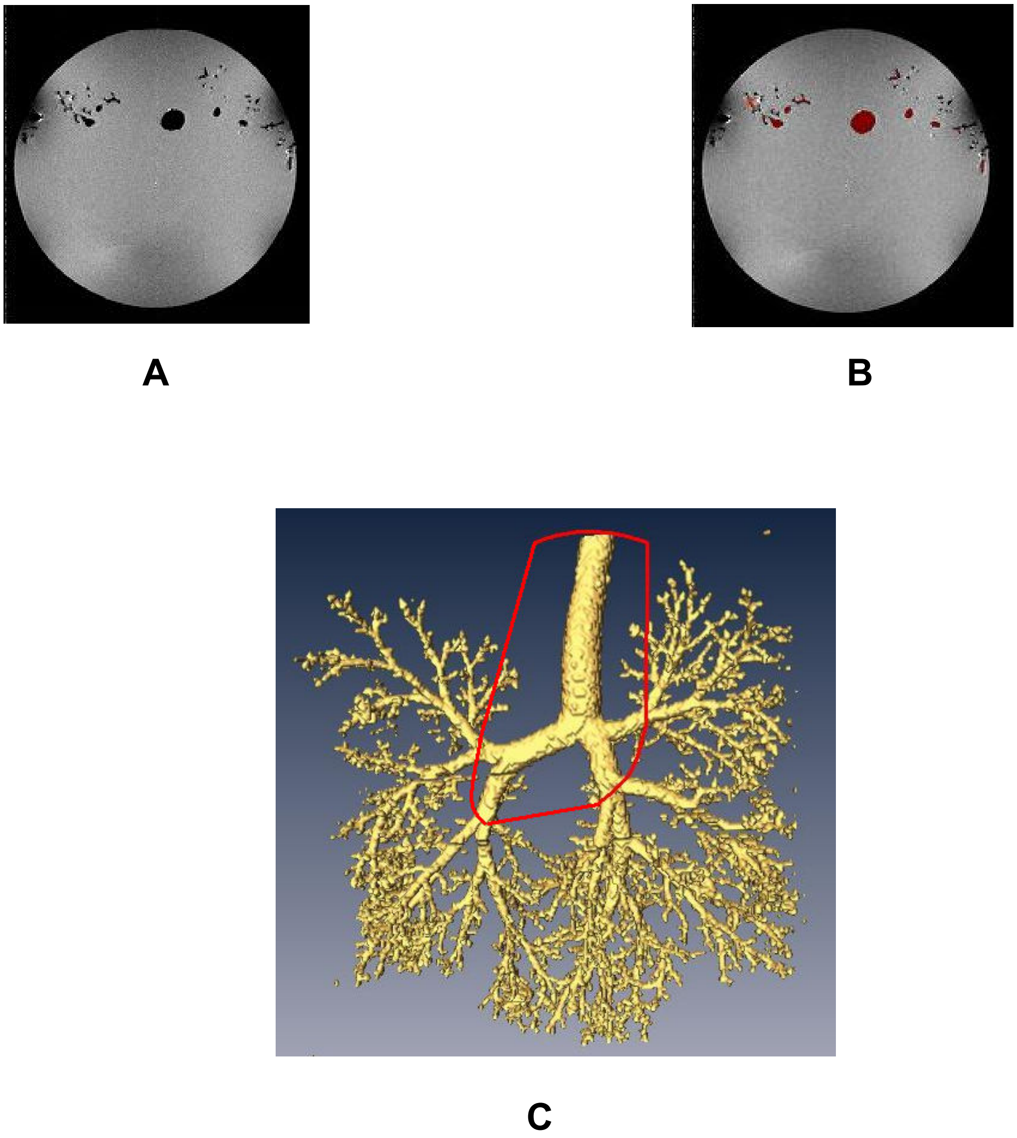

Figure **8-1**: (A) A slice of MRI data. The dark holes that are surrounded by the gray region represent airway lumina. (B) Segmentation of the MRI data slice. The segmented airways are colored red. (C) Isosurface of tracheobronchial tree of the rhesus monkey. The red loop identifies the airways that were used in the simulations.

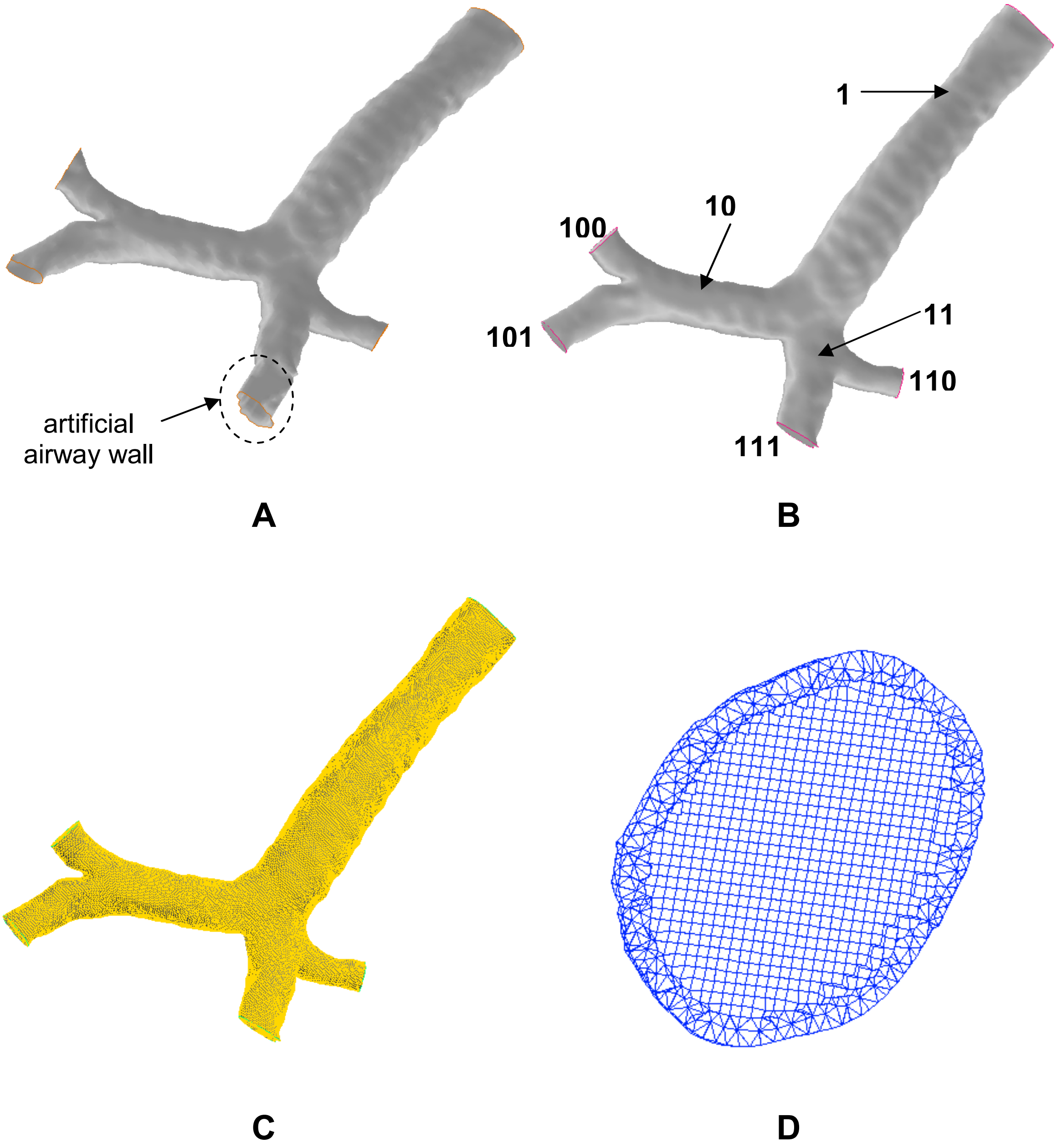
artificial
airway wall
A
1
10
100
101
11
110
111
B
C
D

Figure **8-2**: (A) Surface imported from AMIRA™. The artificial airway wall is marked. (B) Truncated airway geometry. The pink outlines identify the perimeters of the inflow and outflow boundaries. (C) Meshed airway volume. (D) Cross-section through meshed volume showing *hexcore* mesh.

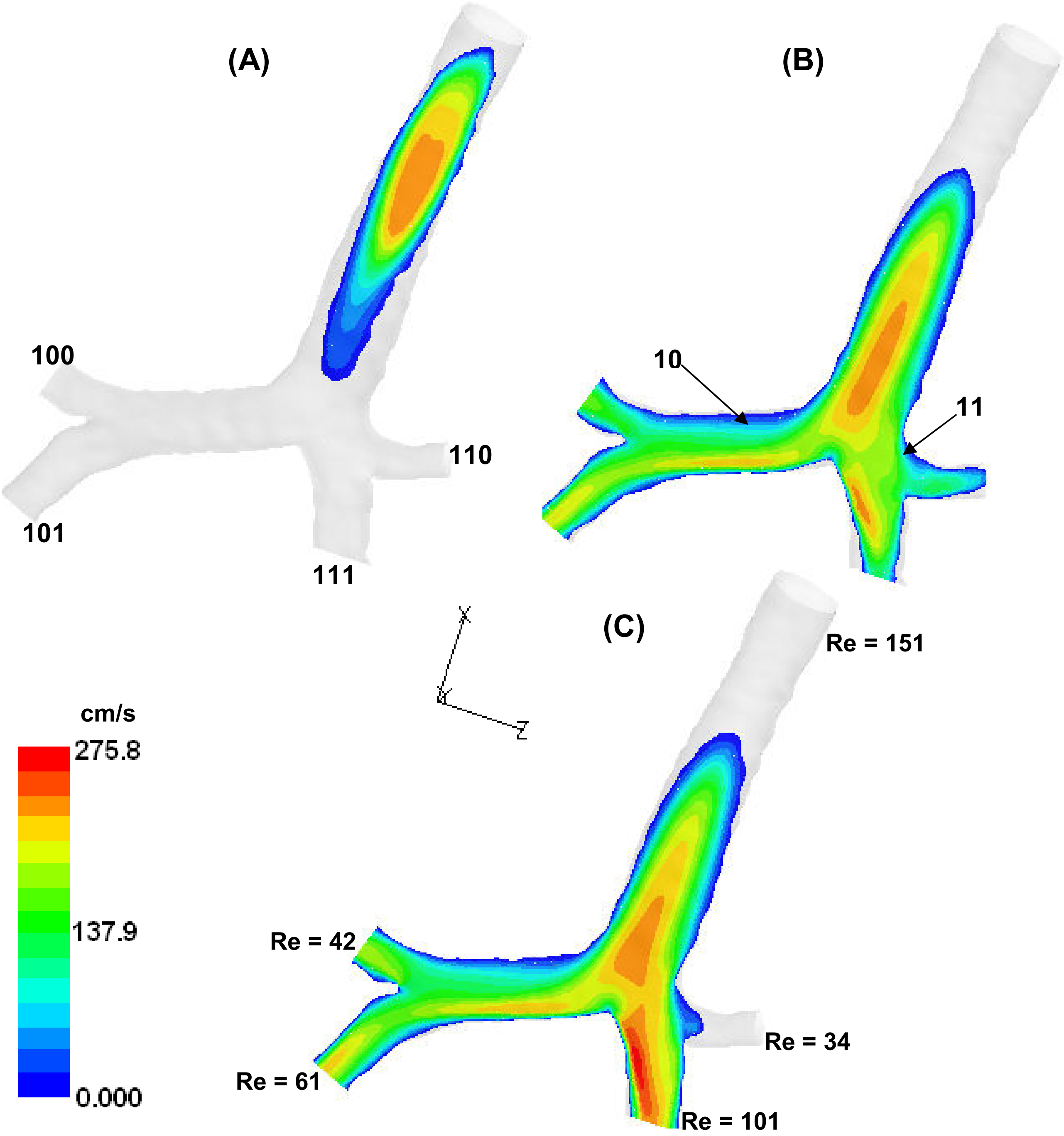

Figure **8-3**: Isocontours of velocity magnitude at three cross-sections through the anatomically accurate airway model. (a) $y = 0.01$ cm, (b) $y = 0.29$ cm, (c) $y = 0.33$ cm. The y coordinate increases in the direction pointing out of the page and the airway spans y = -0.271 (anterior–behind the page) to y = 0.503 cm (posterior–in front of the page). The terminal airway segments are labeled in (a) and the Reynolds numbers (based on the inlet radius R_0 or outlet radius R^*, where the radius is defined as half the hydraulic diameter) in the trachea and each of the terminal airways are labeled in (c).

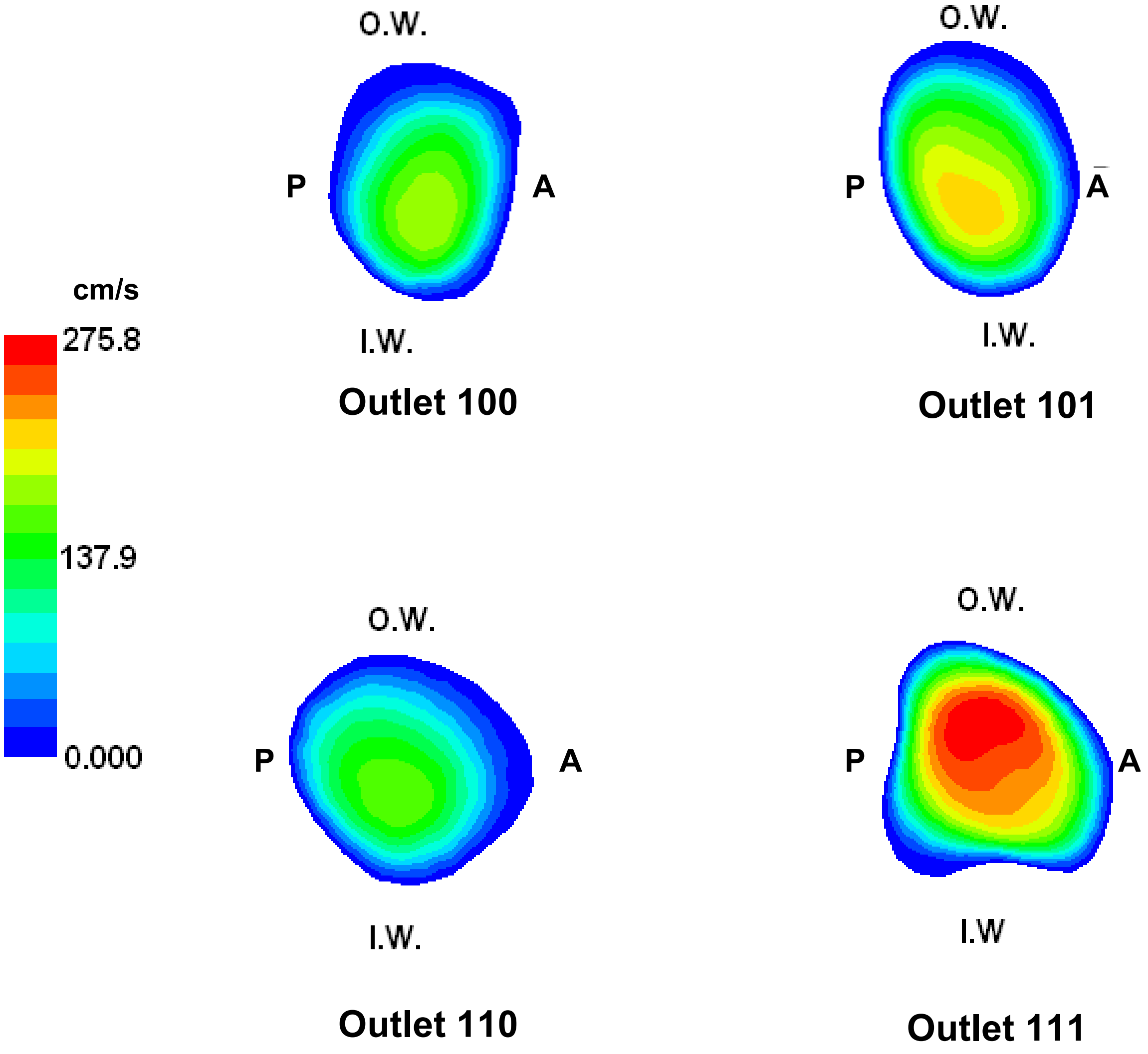

Figure **8-4**: Isocontours of velocity magnitude at each of the outlets of the anatomically accurate airway model. O.W.: outer wall, I.W.: inner wall, P: posterior, A: anterior. Outlets are not all represented at the same scale. The posterior and anterior of the geometry are defined in the caption of Figure **8-3**.

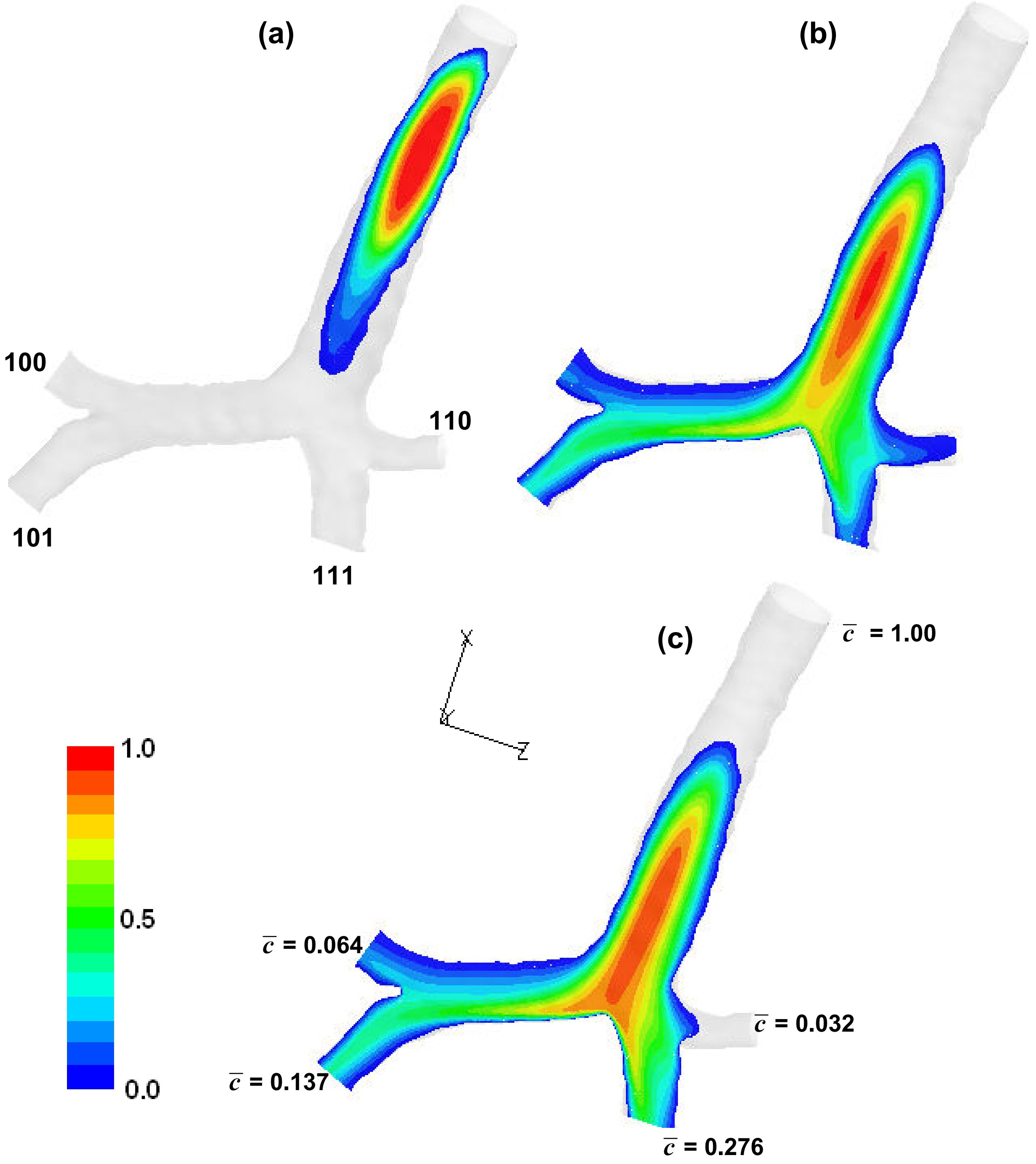
(a)
(b)
(c)
100
101
110
111
$\overline{c}$ = 1.00
$\overline{c}$ = 0.064
$\overline{c}$ = 0.032
$\overline{c}$ = 0.137
$\overline{c}$ = 0.276
1.0
0.5
0.0
X
Z

Figure **8-5**: Isocontours of scaled concentration for an infinitely fast RTLF reaction at three cross-sections through the anatomically accurate airway. (a) y = 0.01 cm, (b) y = 0.29 cm, (c) y = 0.33 cm. The y coordinate increases in the direction pointing out of the page and the airway spans y = -0.271 (anterior–behind page) to y = 0.503 cm (posterior–in front of page). The terminal airway segments are labeled in (a) and the average concentration $\overline{c}$ in (c).

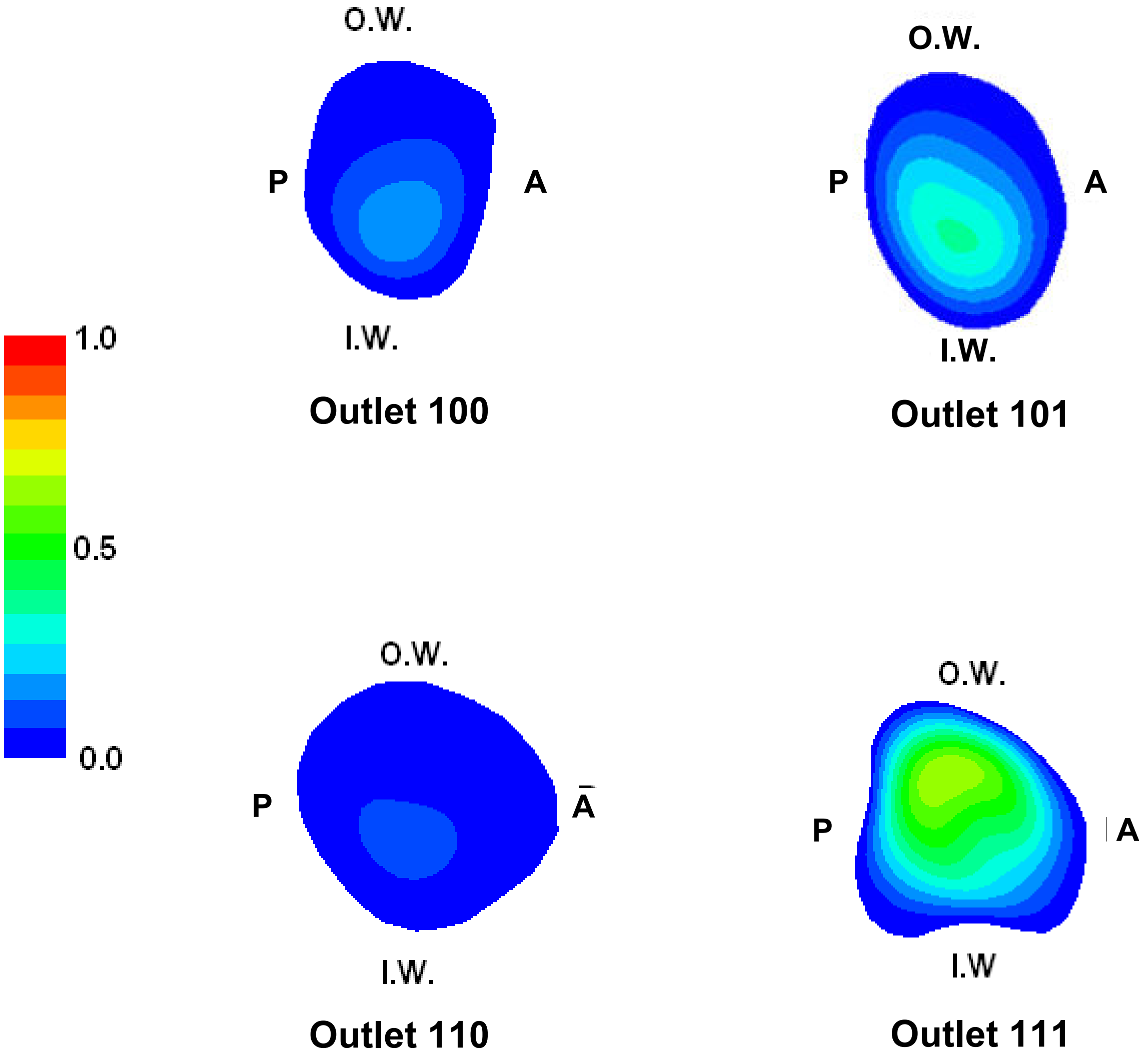

Figure **8-6**: Isocontours of scaled concentration for an infinitely fast RTLF reaction at each of the outlets of the anatomically accurate airway model. O.W.: outer wall, I.W.: inner wall, P: posterior, A: anterior. Outlets are not all represented at the same scale. The posterior and anterior of the geometry are defined in the caption of Figure **8-3**.

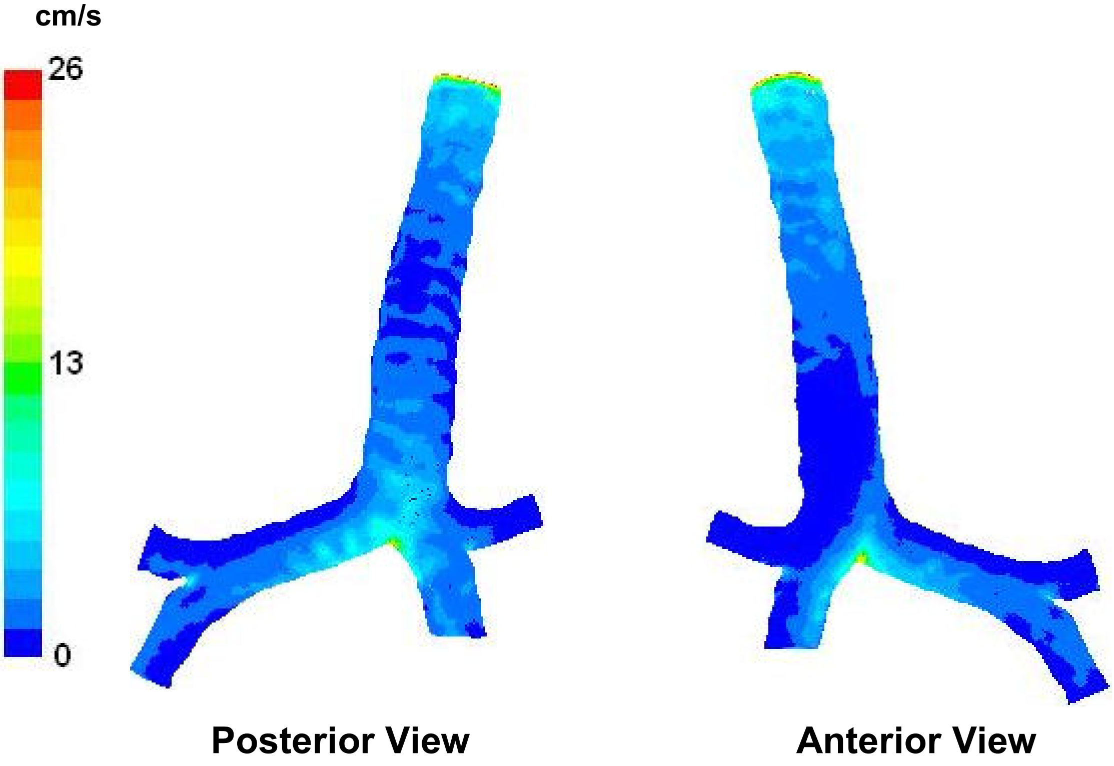

Figure **8-7**: Isocontours of scaled flux (N^*/c_0) for an infinitely fast RTLF reaction in the anatomically accurate airway model.

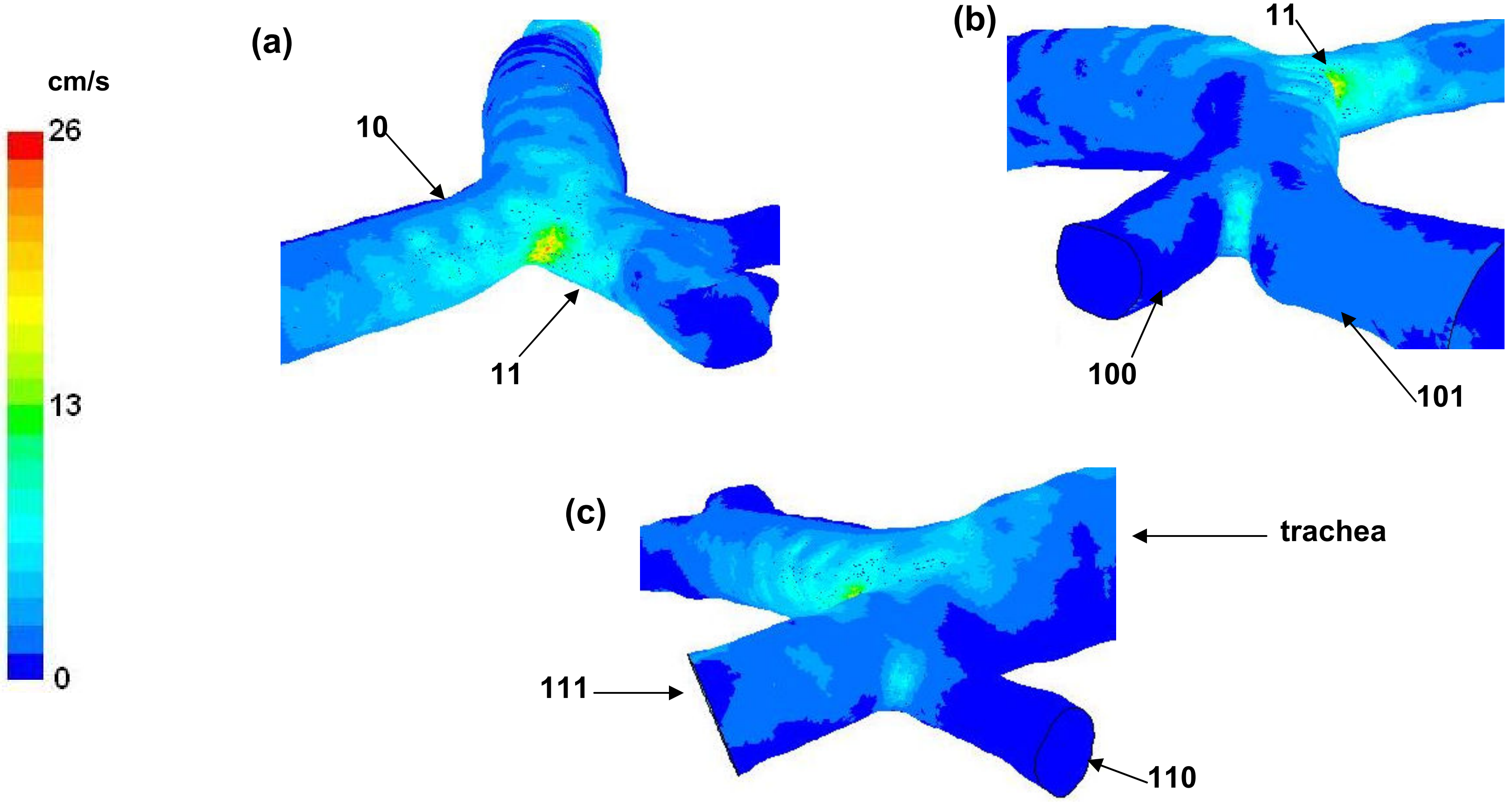
cm/s
26
13
0
(a)
10
11
(b)
11
100
101
(c)
trachea
111
110

Figure **8-8**: Scaled flux distributions in branching regions for an infinitely fast RTLF reaction. (a) First generation branching (b) Minor second generation branching (c) Major second generation branching. Airway segments are labeled. The dark lines mark the perimeters of the outflow boundaries.

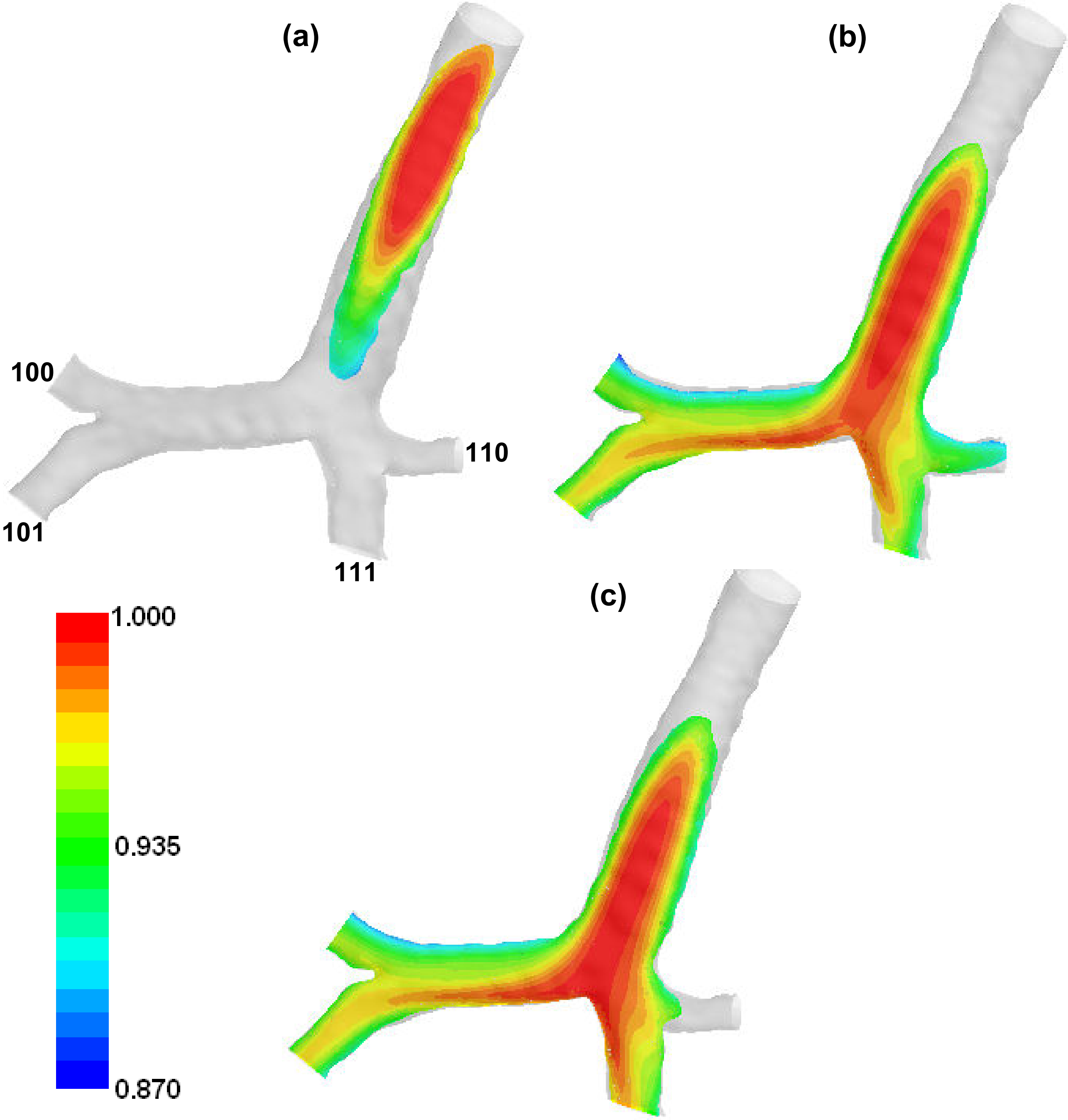

Figure **8-9**: Isocontours of scaled concentration for $Da = 1000$ at three cross-sections through the anatomically accurate airway. (a) y = 0.01 cm, (b) y = 0.29 cm, (c) y = 0.33 cm. The terminal airway segments are labeled in (a).

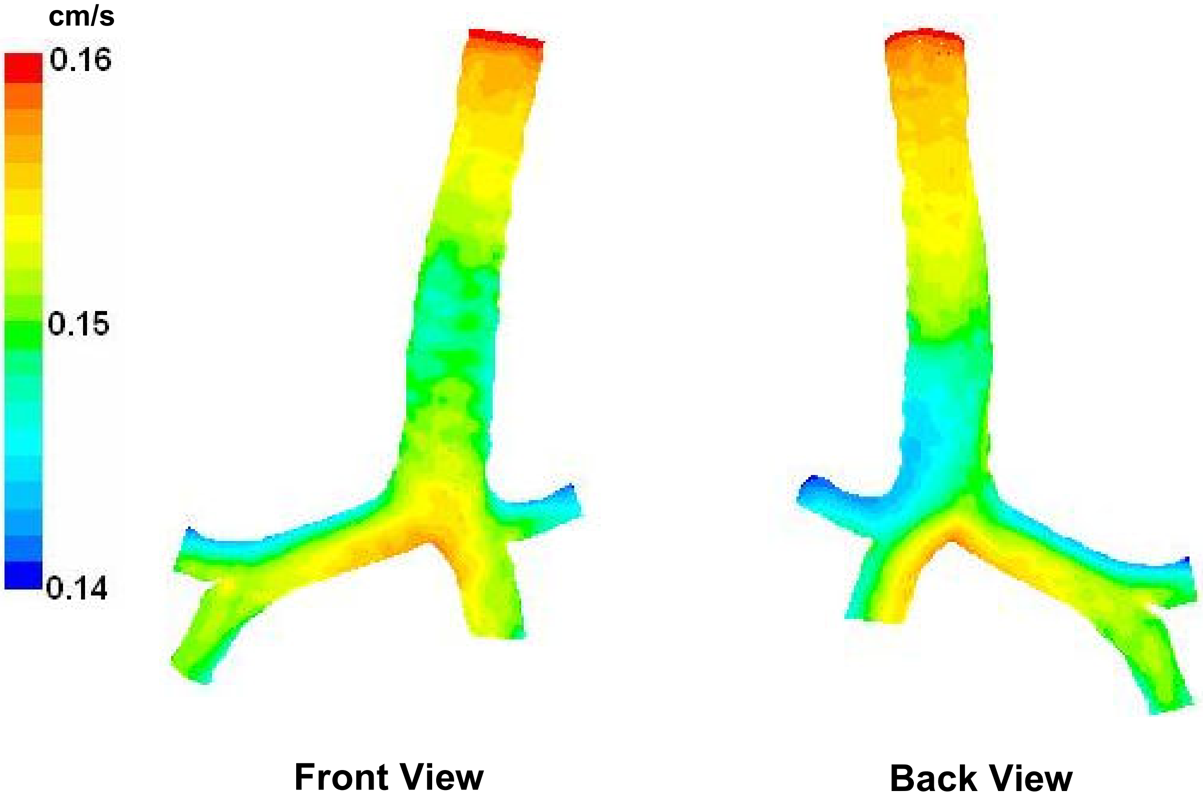

Figure **8-10**: Isocontours of scaled flux for $Da = 1000$ in the anatomically accurate airway model.

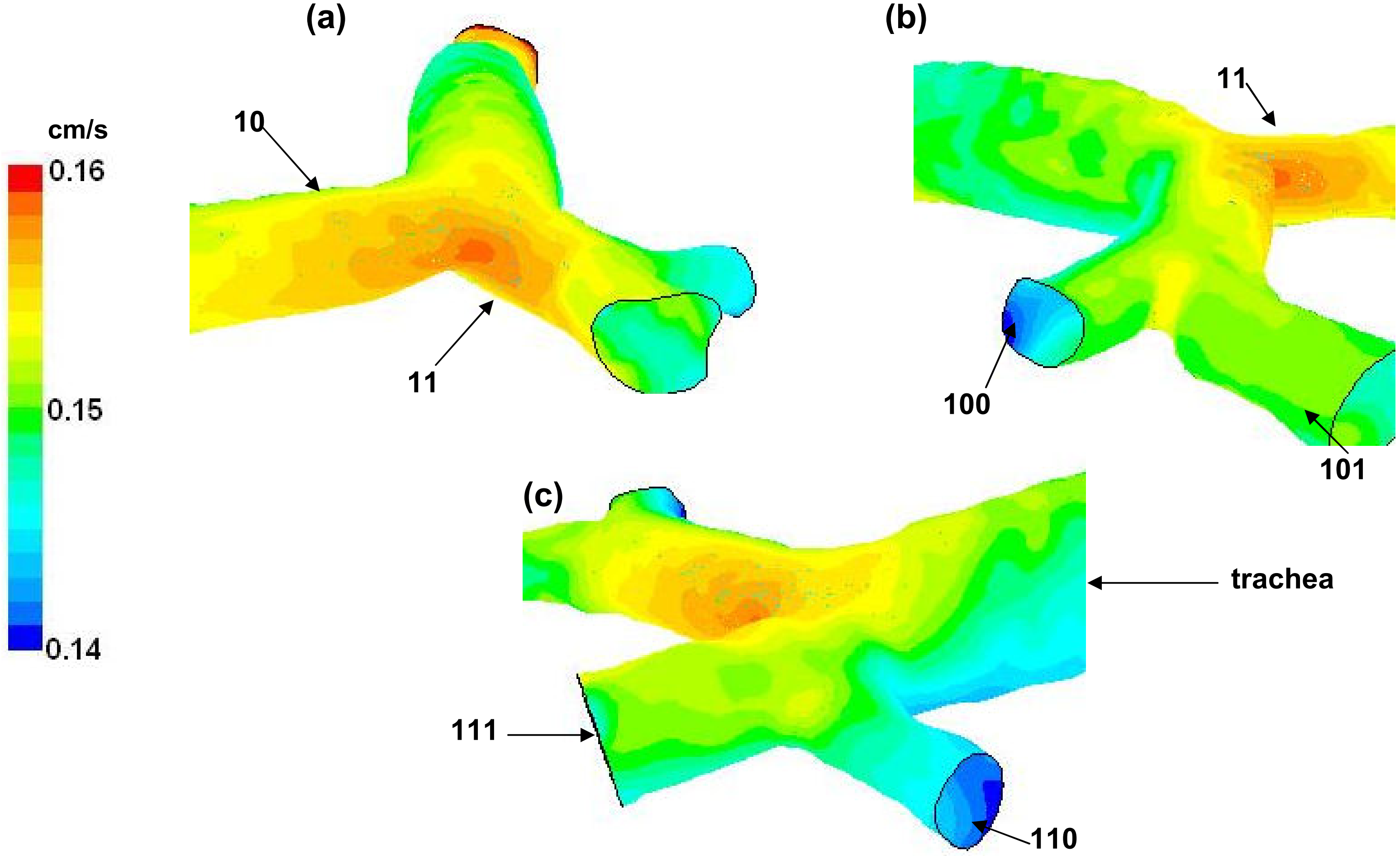

Figure **8-11**: Scaled flux distributions in branching regions for for $Da = 1000$. (a) First generation branching (b) Minor second generation branching (c) Major second generation branching. Airway segments are labeled. The dark lines mark the perimeters of the outflow boundaries.

Chapter 9

SUMMARY AND RECOMMENDATIONS FOR FUTURE WORK

The goal of this thesis was to study O_3 dose distribution in the respiratory tract and investigate the effects of factors influencing O_3 uptake into the surrounding respiratory tract lining fluid (RTLF) and underlying epithelial tissue. This goal was developed in light of the hypothesis that the reproducible differences in O_3 induced injury along the respiratory tract are due to differences in O_3 dose to different tissue sites. The aims of this thesis were accomplished by using the commercial computational fluid dynamics (CFD) package FLUENT (Fluent Inc., Lebanon, NH) to solve the three-dimensional forms of the continuity, Navier-Stokes, and convection-diffusion in representative airway geometries.

The first study examined the effect of flow rate on O_3 uptake. Steady inspiratory and expiratory flow in an idealized symmetric 90° single airway bifurcation were simulated at parent branch radius-based Reynolds numbers (Re) ranging from 100 to 500 assuming an infinitely fast reaction of O_3 in the RTLF, rendering the O_3 concentration negligible on the bifurcation walls. During inspiratory and expiratory flows, an increase in flow rate resulted in an increase in the total uptake rate of O_3 into the RTLF. During inspiratory flow at all Re, hot spots of O_3 flux were located at the carina. Two sets of hot spots were predicted during expiratory flow – one set in the immediate vicinity of the carina and another along the parent branch walls. The flow rate was also found to have an effect on the location of the maximum flux; the location of the maximum flux shifted from the region of the carina to the outer wall of the daughter branch at the lowest Re. In all cases, O_3 uptake in the single bifurcation was larger than that in a straight tube of equal inlet radius and wall surface area, suggesting that single path models underestimate the O_3 uptake rate.

The second study examined the influence of airway branching structure on O_3 uptake in two respects: the effect of the branching angle in a symmetric bifurcation and the effect of the mode of branching. To investigate the effect of the branching angle, steady inspiratory and expiratory flows in idealized single symmetric airway bifurcations with total branching angles of 45°, 90°, and 135° were simulated at $Re = 300$, assuming an instantaneous reaction at the bifurcation walls. The average flux $\langle N \rangle$ of O_3 was predicted to increase with increasing branching angle during both inspiratory and expiratory flows, with the main sites of increased $\langle N \rangle$ being the transition region and the downstream branches. These findings were consistent with the results of the experimental study of Caro *et al.* (2002), who observed an increased rate of mass transfer for a larger branching angle. During inspiratory flow, the magnitude of the flux of the hot spot at the carina decreased with increasing branching angle. These findings suggest that while under equivalent conditions, O_3-induced injury may generally be greater in an airway bifurcation with a greater branching angle, the tissue damage in the vicinity of the carina may be more serious in an airway bifurcation with a smaller branching angle.

The effect of the mode of branching was examined by comparing simulation predictions of steady inspiratory and expiratory flows and O_3 uptake at $Re = 300$ in an idealized 90° single symmetric bifurcation and an idealized 90° monopodial bifurcation, assuming a zero concentration of O_3 on the bifurcation walls. During inspiratory flow, hot spots of flux were predicted at the carinas of the two geometries. During expiratory flow, a hot spot of O_3 flux appeared along the outer wall of the monopodial parent branch. Overall $\langle N \rangle$ was greater in the symmetric bifurcation, but the minor daughter branch of the monopodial bifurcation had the highest $\langle N \rangle$ of all the individual regions in the two bifurcations. This result was consistent with the findings of Postlethwait *et al.* (2000), who observed greater O_3-induced cell injury in the side branches than along the main axial pathway in isolated rat lungs.

Because the reaction of O_3 with endogenous RTLF substrates actually occurs at a finite rate, the next task was to select an appropriate RTLF reaction model. Two reaction models were compared, both of which assumed quasi-steady lateral diffusion with simultaneous homogeneous reaction. In the first model, the substrate concentration was assumed to be in excess of the concentration O_3; thus, the reaction rate of O_3 with RTLF substrates was assumed to be pseudo-first order with respect to O_3 concentration. The second model assumed a reaction rate that was first order with respect to both the concentration of O_3 and the concentration of substrate, and second order overall. In both models, the RTLF concentration of O_3 at the gas-RTLF interface was assumed to be in equilibrium with the gas phase concentration, and the O_3 concentration at the RTLF-tissue interface was assumed to be negligible due to a very fast reaction in the tissue. In the second order reaction model, a constant substrate concentration was assumed at the tissue surface and the gas-RTLF interface was assumed to be impermeable to substrate. Over a range of physiologically relevant conditions, the two reaction models yielded O_3

concentration profiles in the RTLF and O_3 fluxes into the RTLF and tissue that were virtually identical, indicating that RTLF substrates are indeed in excess of O_3 concentration in the RTLF. Because of its simplicity and ease of implementation in FLUENT, the pseudo-first order reaction model was selected for use in the simulations that incorporated an RTLF reaction occurring at a finite rate.

In the next study, the effect of RTLF reaction-diffusion parameters on O_3 uptake distribution was investigated. To examine the effect of RTLF thickness, O_3 uptake during steady inspiratory flow in an idealized single 90° symmetric bifurcation at $Re = 300$ and at two representative reaction rate constants was simulated. O_3 uptake into the RTLF was found to be largely insensitive to RTLF thickness, except for low reaction rate constants and very small RTLF thicknesses, in which case a reduction in RTLF thickness led to an increase in O_3 uptake. The tissue uptake rates proved to be more sensitive to RTLF thickness, with a thicker RTLF resulting in less O_3 absorbed by the tissue, but as the thickness of the RTLF layer increased, the tissue uptake rate became less and less sensitive to changes in RTLF thickness. This effect was evident only at the lower reaction rate because at the higher reaction rate, all the absorbed O_3 reacted within the RTLF before it could reach the tissue.

To examine the sensitivity of O_3 uptake to the RTLF reaction rate constant, steady inspiratory flow in an idealized single 90° symmetric bifurcation at Reynolds numbers of 10, 100, and 1000 was simulated assuming Da ranging from 1 to 10^6. The RTLF uptake rate of O_3 increased and the tissue uptake rate decreased as Da increased. An interesting observation was that at low Da, the O_3 uptake rates were insensitive to Re, but as Da increased, the RTLF uptake rates became more and more sensitive to Da. These results indicate that at low Da, the uptake of O_3 into the RTLF is controlled by the mass transfer resistance in the RTLF, and as Da rises, the gas phase resistance becomes increasingly important. Steady inspiratory flow simulations at Reynolds numbers of 10 and 100 and Da ranging from 1 to 10^6 were also conducted in the idealized monopodial bifurcation. At the lowest Da, the uptake rates of O_3 into the RTLF were very close for the idealized symmetric and monopodial bifurcations, but as Da increased, the differences between the uptake rates in the two geometries grew, with the uptake rate in the symmetric bifurcation always being greater than that in the monopodial geometry. The implications for O_3-induced injury of the results of the studies examining the effect of RTLF reaction-diffusion parameters depends on the nature of the reactions occurring in the RTLF, which is not completely clear.

In the final study, an anatomically accurate geometry representative of the first three generations of the lower respiratory tract of a one month old rhesus monkey was constructed from MRI data, and O_3 uptake during steady inspiratory flow at $Re = 152$ was simulated under two RTLF reaction conditions, namely, an infinitely fast reaction in the RTLF (resulting in a zero O_3 concentration at the airway walls) and a pseudo-first order reaction occurring at a finite rate with a Da of 1000. Although the flux distributions in the anatomically accurate airways differed in some respects from those in the idealized bifurcations, some similarities between the two geometries existed. In both cases, hot spots of fluxes were predicted to be located at the carina, and the inner walls of the daughter branches were predicted to have higher fluxes than the outer walls. The only exception to the latter pattern was that higher fluxes were found along the outer walls of one of the second generation daughter branches which had a very short parent branch. A comparison of average dimensionless fluxes in the idealized and anatomically accurate geometries revealed that the average dimensionless flux was less than that in an idealized symmetric 90° bifurcation when an instantaneous RTLF reaction was assumed but identical to that in the idealized bifurcation when $Da = 1000$.

The work presented in this thesis is a preliminary study that demonstrates the successful use of CFD to predict the transport of a reactive gas in the lower conducting airways as demonstrated by the consistency of the simulation predictions with various experimental results from other researchers. This study, like any other, can be improved. Some recommendations for future work are as follows.

First of all, in most of the studies, flow in single bifurcations was simulated. It would be desirable to study flow in multiple generations and perhaps study the effects of the rotation angles of daughter branches on O_3 uptake distribution. Moreover, it will prove interesting to simulate flow and O_3 uptake in an anatomically accurate geometry with several more generations. Perhaps O_3 transport in a complete anatomically accurate lower conducting airway model will be possible in the near future, considering the exponential increase in computational power with time.

Although under quiet breathing conditions, flow can be considered to be quasi-steady throughout much of the respiratory tract, flow in the more proximal airways, especially during exercise, is not likely to be quasi-steady, as large values of the Womersley parameter ($= \sqrt{R^2\omega/\nu}$, where R is the airway radius, ω is the angular frequency of respiration, and ν is the kinematic viscosity) are expected under these conditions. In this case, it will be important to conduct time-dependent simulations of O_3

uptake during cyclic breathing. Furthermore, at these high respiratory flow rates, the turbulent jet resulting from flow through the larynx can be expected to propagate further into the lower respiratory tract, and incorporating flow through the larynx into the simulations with the appropriate turbulence model becomes important.

One feature absent from the studies was the validation of the simulation predictions with results from experiments that exactly replicate the simulation conditions. One way to accomplish this would be to construct bifurcations like those described in this thesis, coat the bifurcation walls with agarose gel, flow a formaldehyde-air mixture through the bifurcations, and determine the uptake of formaldehyde into the uptake gel. Regional (e.g., inner daughter wall, outer daughter wall, transition region) and overall mass transfer coefficients determined from the experiments and three-dimensional CFD simulations can then be compared.

Finally, the end purpose of using CFD simulations to predict O_3 dose distribution in the RTLF and tissues is to eventually predict the tissue response. In order to accomplish this goal, more knowledge about the nature of the reactions occurring between O_3 and RTLF substrates crucial, for example, knowledge about reaction products, RTLF reaction kinetics, possible interactions between RTLF substrates, as well as whether the flux of O_3 predicted by these simulations is sufficient to cause cellular damage. Unfortunately, these details have not been well-established. As more of this information becomes available, it should be incorporated into the RTLF reaction model. This would most likely necessitate a more complex reaction model and call for creative ways of incorporating the RTLF reaction model into the CFD simulations.

Bibliography

Alfaro, M., L. Putney, B. Tarkington, G. Hatch, D. Hyde, and E. Schelegle. Effect of rapid shallow breathing on the distribution of ^{18}O-labeled ozone reaction product in the respiratory tract of the rat. *Inhal. Toxicol.* 16(2):77-85, 2004.

Balásházy, I., Á. Farkas, I. Szöke, W. Hofmann, and R. Sturm. Simulation of deposition and clearance of inhaled particles in central human airways. *Radiat. Prot. Dosim.* 105:129-132, 2003a.

Balásházy, I., W. Hofmann, and T. Heistracher. Local particle deposition patterns may play a key role in the development of lung cancer. *J. Appl. Physiol.* 94:1719-1725, 2003b.

Ballinger, C. A., R. Cueto, G. Squadrito, L. M. Connor, J. J.Coffin, L.W. Velsor, W. A. Pryor, and E. M. Postlethwait. Antioxidant-mediated augmentation of ozone-induced membrane oxidation. *Free Radical Biol. Med.* 38:515-526, 2005.

Blackburn, K. *Recommendations for and Documentation of Biological Values for Use in Risk Assessment*, EPA/600/6-87/008. Washington DC: US Environmental Protection Agency Office of Research and Development, 1988, 4.16 pp.

Blomberg, A., I. S. Mudway, C. Nordenhäll, H. Hedenström, F. J. Kelly, A .J. Frew, S. T. Holgate, and T. Sandström. Ozone-induced lung function decrements do not correlate with early airway inflammatory or antioxidant responses. *Eur. Respir. J.* 13:1418-1428, 1999.

Boyden, E. A. The programming of canalization in fetal lungs of man and monkey. *Am. J. Anat.* 145(1):125-127, 1976.

Bush, M. L., T. Raybold, S.-C. Abeles, S. Hu, A. Ben-Jebria, and J. S. Ultman. Longitudinal distribution of ozone absorption in the lung: simulation with a single-path model. *Toxicol. Appl. Pharmacol.* 140:219-226, 1996.

Bush, M. L., W. Zhang, A. Ben-Jebria, and J. S. Ultman. Longitudinal distribution of ozone and chlorine in the human respiratory tract: simulation of nasal and oral breathing with the single-path diffusion model. *Toxicol. Appl. Pharmacol.* 173(3):137-145, 2001.

Calay, R. K., J. Kurujareon, and A.E. Holdø. Numerical simulation of respiratory flow patterns within human lung. *Resp. Physiol. Neurobiol.* 130:201-221, 2002.

Caro, C. G., R. C. Schroter, N. Watkins, S. J. Sherwin, and V. Sauret. Steady inspiratory flow in planar and non-planar models of human bronchial airways. *Proc. R. Soc. Lond. A.* 58:791-809, 2002.

Castleman, W. L., W. S. Tyler, and D. L. Dungworth. Lesions in respiratory bronchioles and conducting airways of monkeys exposed to ambient levels of ozone. *Exp. Mol. Pathol.* 26(3):384-400, 1977.

Cebral, J. R. and R. M. Summers. Tracheal and central bronchial aerodynamics using virtual bronchoscopy and computational fluid dynamics. *IEEE T. Med. Imaging* 23(8):1021-1033, 2004.

Chang, L., F. J. Miller, J. Ultman, Y. Huang, B. L. Stockstill, E. Grose, J. A. Graham, J. J. Ospital, and J. D. Crapo. Alveolar epithelial cell injuries by subchronic exposure to low concentrations of ozone correlate with cumulative exposure. *Tox. Appl. Pharmacol.* 109(2):219-334, 1991.

Comer, J. K., C. Kleinstreuer, S. Hyun, and C. S. Kim. Aerosol transport and deposition in sequentially bifurcating airways. *J. Biomech. Eng.* 122(2):152-158, 2000.

Connor, L. M., C. A. Ballinger, T. B. Albrecht, and E. M. Postlethwait. Interfacial phospholipids inhibit ozone-reactive absorption-mediated cytotoxicity in vitro. *Am. J. Physiol. Lung Cell. Mol. Physiol.* 286:1169-1178, 2004.

Crissman, K., J. Norwood, R. Slade, J. Highfill, H. Koren, and G. Hatch. Acute ozone (O_3) effects on lavage fluid antioxidants in humans, rats, and guinea pigs. *Toxicologist* 9:46, 1989.

Cross, C. E. and B. Halliwell. Evaluation of biomolecular damage by ozone. *Methods Enzymol.* 234: 252-256, 1994.

Cross, C. E., P. A. Motchnik, B. A. Bruener, D. A. Jones, H. Kaur, B. N. Ames, and B. Halliwell. Oxidative damage to plasma constituents by ozone. *FEBS Lett.* 298(2,3):269-272, 1992.

Cross, C. E., A. van der Vliet, C. A. O'Neill, S. Louie, and B. Halliwell. Oxidants, antioxidants, and respiratory tract lining fluids. *Environ. Health Perspect.*, 102(Suppl. 10):185-91, 1994.

Davis, W. B. and E. R. Pacht. “Extracellular antioxidant defenses.” In: R. G. Crystal, J. B. West, eds. *The Lung: Scientific Foundations*. New York: Raven Press; 1991, pp. 1821-1827.

Farag, A., J. Hammersley, D. Olson, and T. Ng. Mechanics of the flow in the small and middle human airways. *J. Fluid Eng.* 122(3):576-584, 2000.

FLUENT 6.2 User’s Guide.

Fresconi, F. E., A. S.Wexler, and A. K. Prasad. Expiration flow in a symmetric bifurcation. *Exp. Fluids.* 35(5):493-501, 2003.

GAMBIT 2.2 Modeling Guide.

Geankoplis C. J. *Transport Processes and Unit Operations*. Englewood Cliffs: Prentice Hall, 1993, 866 pp.

Gerrity, T.R., R.A. Weaver, J. Bernsten, D.E. House, and J.J. O’Neil. Extrathoracic and intrathoracic removal of O_3 in tidal-breathing humans. *J. Appl. Physiol.* 65(1):393-400, 1998.

Giamalva, D., D. F. Church, and W. A. Pryor. A comparison of the rates of ozonation of biological antioxidants and oleate and linoleate esters. *Biochem. Biophys. Res. Commun.* 133(2):773-779, 1985.

Goddard, J.B. and Acrivos, A. Asymptotic expansions for laminar forced-convection heat and mass transfer. Part II. Boundary layer flows. *J. Fluid Mech.* 24: 339-366, 1966.

Grotberg, J. B. Gas absorption in pulmonary airways at low Peclet number. *J. Biomech. Eng.* 112(2):177-182, 1990.

Grotberg, J. B., B. V. Sheth, and L. F. Mockros. An anlaysis of pollutant gas transport and absorption in pulmonary airways. *J. Biomech. Eng.* 112(2):168-176, 1990.

Hatch, G.E. “Comparative biochemistry of the airway lining fluid.” In: *Treatise on Pulmonary Toxicology. Vol. 1. Comparative Biology of the Normal Lung,* edited by R. A. Parent. Boca Raton: CRC Press, 1992, pp. 617-632.

Heyder, J., S. Takenaka. Long-term canine exposure studies with ambient air pollutants. *Eur. Respir. J.* 9:571-584, 1996.

Hofmann, W., L. Koblinger, and T. B. Martonen. Structural differences between human and rat lungs: implications for Monte Carlo modeling of aerosol deposition. *Health Phys.* 57(Suppl. 1): 41-47, 1989.

Horsfield, K. and G. Cumming. Morphology of the bronchial tree in man. *J. Appl. Physiol.* 24(3):373-383, 1968.

Horsfield, K, G. Dart, D. E. Olson, G. F. Filley, and G. Cumming. Models of the human bronchial tree. *J. Appl. Physiol.* 31(2):207-217, 1971.

Hu, S. C., A. Ben-Jebria, and J. S. Ultman. Simulation of O_3 uptake distribution in the human airways by orthogonal collocation on finite elements. *Comput. Biomed. Res.* 25(3):264-278, 1992.

Hu, S. C., A. Ben-Jebria, and J. S. Ultman. Longitudinal distribution of ozone absorption in the lung: effects of respiratory flow. *J. Appl. Physiol.* 77(2):574-583, 1994.

Hubal, E. A., J. S. Kimbell, and P. S. Fedkiw. Incorporation of nasal-lining mass-transfer resistance into a CFD model for prediction of ozone dosimetry in the upper respiratory tract. *Inhal. Toxicol.* 8:831-857, 1996.

Joad, J. P., J. M. Bric, A. J. Weir, L. Putney, D. M. Hyde, E. M. Postlethwait, and C. G. Plopper. Effect of respiratory pattern on ozone injury to the airways of isolated rat lungs. *Toxicol. Appl. Pharmacol.* 169(1):26-32, 2000.

Kabel, J. R., A. Ben-Jebria, and J. S. Ultman. Longitudinal distribution of ozone absorption in the lung: comparison of nasal and oral quiet breathing. *J. Appl. Physiol*. 77:2584–2592, 1994.

Kanofsky, J. R. and P. D. Sima. Reactive absorption of ozone by aqueous biomolecule solutions: implications for the role of sulfhydryl compounds as targets for ozone. *Arch. Biochem. Biophys.* 316(1):52-62, 1995.

Kelly, F. J. Oxidative stress: its role in air pollution and adverse health effects. *Occup. Environ. Med*. 60:612-616, 2003.

Kelly, F. J., M. Cotgrove, I. S. Mudway. Respiratory tract lining fluid antioxidants: the first line of defence against gaseous pollutants. *Cent. Eur. J. Public Health* 4(Suppl.):11-14, 1996.

Kepler, G. M., R. B. Richardson, K. T. Morgan, and J. S. Kimbell. Computer simulation of inspiratory nasal airflow and inhaled gas uptake in a rhesus monkey. *Toxicol. Appl. Pharmacol.* 150(1):1-11, 1998.

Kermani, S., A. Ben-Jebria, J. S. Ultman. Kinetics of ozone reaction with uric acid, ascorbic acid, and glutathione at physiologically relevant conditions. *Arch. Biochem. Biophys.* 451:8-16, 2006.

Kimbell, J. S., E. A. Gross, D. R. Joyner, M. N. Godo, and K. T. Morgan. Application of computational fluid dynamics to regional dosimetry of inhaled chemicals in the upper respiratory tract of the rat. *Toxicol. Appl. Pharmacol*. 121(2):253-263, 1993.

Kimbell, J. S. and F. J. Miller. "Regional respiratory-tract absorption of inhaled reactive gases: a modeling approach." In: D. E. Gardner, J. D. Crapo, R. O. Mcclellan, eds. *Toxicology of the Lung.* 3rd ed. Philadelphia: Taylor & Francis, 1999, pp. 557-597.

Kimbell, J. S., R. P. Subramaniam, E. A. Gross, P. M. Schlosser, and K. T. Morgan. Dosimetry modeling of inhaled formaldehyde: Comparisons of local flux predictions in the rat, monkey, and human nasal passages. *Toxicol. Sci.* 64:100–110, 2001.

Kott, K. S., K. E. Pinkerton, J. M. Bric, C. G. Plopper, K. P. Avadhanam, and J. P. Joad. Methacholine responsiveness of proximal and distal airways of monkeys and rats using videomicrometry. *J. Appl. Physiol.* 92(3):989-996, 2002.

Langford, S. D., A. Bidani, and E. M. Postlethwait. Ozone-reactive absorption by pulmonary epithelial lining fluid constituents. *Toxicol. Appl. Pharmacol.* 132(1):122-130, 1995.

Lieber, B. B. and Y. Zhao. Oscillatory flow in a symmetric bifurcation airway model. *Ann. Biomed. Eng.* 26(5):821-830, 1998.

Long, N.C., J. Suh, J. D. Morrow, R. H. Shiestl, G. G. Krishna Murthy, J. D. Brain, and B. Frei. Ozone causes lipid peroxidation but little antioxidant depletion in exercising and nonexercising hamsters. *J. Appl. Physiol.* 91:1694-1700, 2001.

Lui, Y., R. M. So, and C. H. Zhang. Modeling the bifurcating flow in a human lung airway. *J. Biomech.* 35(4):465-473, 2002.

Madasu, S., A. Borhan, J. S. Ultman. An axisymmetric single-path model for gas transport in the conducting airways. *J. Biomech. Eng.*128(1):69-75, 2006.

Mahinpey, N., R. Leask, M. Ojha, K.W. Johnston, and O. Trass. Experimental study on local mass transfer in a simplified bifurcation model: potential role in atherosclerosis. *Ann. Biomed. Eng.* 32(11):1504-1518, 2004.

Martonen, T. B., X. Guan, and R. M. Schreck. Fluid dynamics in airway bifurcations: I. Primary flows. *Inhal. Toxicol.* 13(4):261-279, 2001a.

Martonen, T. B., X. Guan, and R. M. Schreck. Fluid dynamics in airway bifurcations: II. Secondary Currents. *Inhal. Toxicol.* 13(4):281-289, 2001b.

Martonen, T. B., X. Guan, and R. M. Schreck. Fluid dynamics in airway bifurcations: III. Localized flow conditions. *Inhal. Toxicol.* 13(4):291-305, 2001c.

Martonen, T., Z. Zhang, Y. Yang, and G. Bottei. Airway surface irregularities promote particle diffusion in the human lung. *Radiat. Prot. Dosim.* 59:5-14, 1995.

McDonnell, W. F., D. H. Horstman, M. J. Hazucha, E. Seal, Jr., E. D. Haak, S. A. Salaam, and D. E. House. Pulmonary effects of ozone exposure during exercise: dose-response characteristics. *J. Appl. Physiol.* 54:1345-1352, 1983.

Menon, A. S., M. E.Weber, and H. K. Chang. Effect of the larynx on oscillatory flow in the central airways: a model study. *J. Appl. Physiol.* 59(1):160-169, 1985.

Miller, F. J. Uptake and fate of ozone in the respiratory tract. *Toxicol. Lett.* 82-83:277-285, 1995.

Miller, F. J., D. B. Menzel, and D. L. Coffin. Similarity between man and laboratory animals in regional pulmonary deposition of ozone. *Environ. Res.* 17(1):84-101, 1978.

Miller, F. J., J. H. Overton Jr, R. H. Jaskot, and D. B. Menzel. A model of the regional uptake of gaseous pollutants in the lung: I. The sensitivity of the uptake of ozone in the human lung to lower respiratory tract secretions and exercise. *Toxicol. Appl. Pharmacol.* 79(1):11-27, 1985.

Miller, F. J., J. H. Overton, J. S. Kimbell, and M. L. Russell. "Regional respiratory tract absorption of inhaled reactive gases" In: D. E. Gardner, J. D. Crapo, R. O. McClellan, eds. *Toxicology of the Lung.* 2nd ed. New York: Raven Press, 1993, pp. 485-525.

Moulin, F. J. M., K. A. Brenneman, J. S. Kimbell, R. A James, and D. C. Dorman. Predicted regional flux of hydrogen sulfide correlates with distribution of nasal olfactory lesions in rats. *Toxicol. Sci.* 66: 7 – 15, 2002.

Mudway, I. S., A. Blomberg, A. J. Frew, S. T. Holgate, T. Sandström, and F. J. Kelly. Antioxidant consumption and repletion kinetics in nasal lavage fluid following exposure of healthy human volunteers to ozone. *Eur. Respir. J.* 13:1429-1438, 1999a.

Mudway, I. S., M. T. Krishna, A. J. Frew, D. MacLeod, T. Sandström, S. T. Holgate, and F. J. Kelly. Compromised concentrations of ascorbate in fluid lining the respiratory tract in human subjects after exposure to ozone. *Occup. Environ. Med.* 56:473-481, 1999b.

Mudway, I. S., D. Housley, R. Eccles, R. J. Richards, A. K. Datta, T. D. Tetley, and F. J. Kelly Differential depletion of human respiratory tract antioxidants in response to ozone challenge. *Free Radic. Res.* 25:499–513, 1996.

Mudway, I. S. and F. J. Kelly. Modeling the interaction of ozone with pulmonary epithelial lining fuid antioxidants. *Toxicol. Appl. Pharmacol.* 148:91-100, 1998.

Mudway, I. S., F. J. Kelly. Ozone and the lung: a sensitive issue. *Mol. Aspect. Med.* 21:1-48, 2000.

Mustafa, M. G. Biochemical basis of ozone toxicity. *Free Radical Biol. Med.* 9:245–265, 1990.

Nowak, N., P. P. Kakade, and Ananth V. Annapragada. Computational fluid dynamics simulation of airflow and aerosol deposition in human lungs. *Ann. Biomed. Eng.* 31(4):374-390, 2003.

Overton Jr, J. H. Physicochemical processes and the formulation of dosimetry models. *J. Toxicol. Environ. Health* 13(2-3):273-294, 1984.

Overton, J. H. and R. C. Graham. Simulation of the uptake of a reactive gas in a rat respiratory tract model with an asymmetric tracheobronchial region patterned on complete conducting airway cast data. *Comput. Biomed. Res.* 28(3):171-190, 1995.

Overton, J. H., R. C. Graham, and F. J. Miller. A model of the regional uptake of gaseous pollutants in the lung: II. The sensitivity of ozone uptake in laboratory animal lungs to anatomical and ventilatory parameters. *Toxicol. Appl. Pharmacol.* 88(3):418-432, 1987.

Patankar S. V. A calculation procedure for two-dimensional elliptic situations. *Numer. Heat Transfer* 4:409-425, 1981.

Peden, D. B., M. Swiersz, K. Ohkubo, B. Hahn, B. Emery, and M. A. Kaliner. Nasal secretion of the ozone scavenger uric acid. *Am. Rev. Respir. Dis.* 148:455-461, 1993.

Persson, C. G., I. Erjefält, U. Alkner, C. Baumgarten, L. Greiff, B. Gustafsson, A. Luts, U. Pipkorn, F. Sundler, C. Svensson, and P. Wollmer. Plasma exudation as a first line respiratory mucosal defence. *Clin. Exp. Allergy* 21:17-24, 1991.

Phalen, R. F., M. J. Oldham , C. B. Beaucage , T. T. Crocker, J. D. Mortensen. Postnatal enlargement of human tracheobronchial airways and implications for particle deposition. *Anat. Rec.* 212(4):368-380, 1985.

Plopper, C. G., G. E. Hatch, V. Wong, X. Duan, A. J. Weir, B. K Tarkington, R. B. Devlin, S. Becker, and A. R. Buckpit. Relationship of inhaled ozone concentration to acute tracheobronchial epithelial injury, site-specific ozone dose, and glutathione depletion in rhesus monkeys. *Am. J. Respir. Cell Mol. Biol.* 19:387-399, 1998.

Postlethwait, E. M., R. Cueto, L. W. Velsor, and W. A. Pryor. O_3-induced formation of bioactive lipids: estimated surface concentrations and lining layer effects. *Am. J. Physiol.-Lung. Cell. Mol. Physiol.* 274:L1006–L1016, 1998.

Postlethwait, E. M., J. P. Joad, D. M. Hyde, E. S. Schelegle, J. M. Bric, A. J. Weir, L. F. Putney, V. J. Wong, L. W. Velsor, and C. G. Plopper. Three-dimensional mapping of ozone-induced acute cytotoxicity in tracheobronchial airways of isolated perfused rat lung. *Am. J. Respir. Cell Mol. Biol.* 22(2):191-199, 2000.

Postlethwait, E. M., S. D. Langford, and A. Bidani. Determinants of inhaled ozone absorption in isolated rat lungs. *Toxicol. Appl. Pharmacol.* 125(1):77-89, 1994.

Pryor, W. A. How far does O_3 penetrate into the pulmonary air-tissue boundary before it reacts? *Free Radical Biol. Med.* 12:83–88, 1992.

Pryor, W. A., D. H. Giamalva, and D. F. Church. Kinetics of ozonation. 2. Amino acids and model compounds in water and comparison to rates in nonpolar solvents. *J. Am. Chem. Soc.* 106:7094-7100, 1984.

Pryor, W. A., G. L. Squadrito, and M. Friedman. The cascade mechanism to explain ozone toxicity: the role of lipid ozonation products. *Free Radical Biol. Med.* 19: 935-941, 1995.

Raabe, O. G., H. C. Yeh, G. M. Schum, and R. F. Phalen. *Tracheobronchial Geometry: Human, Dog, Rat, Hamster.* Albuquerque: Inhalation Toxicology Research Institute, Lovelace Foundation for Medical Evaluation and Research, 1976, Report LF-53.

Robinson, R. J., M. J. Oldham, R. E. Clinkenbeard, and P. Rai. Experimental and numerical smoke carcinogen deposition in a multigenerational human replica tracheobronchial model. *Ann. Biomed. Eng.* 34(3):373-383, 2006.

Santiago, L. Y. *Absorption of ozone in the human nose during unidirectional airflow.* PhD Thesis. University Park: The Pennsylvania State University, 2001.

Santiago, L. Y., M. C. Hann, A. Ben-Jebria, and J. S. Ultman. Ozone absorption in the human nose during unidirectional airflow. *J. Appl. Physiol.* 91:725-732, 2001.

Schlesinger, R. B. Defense mechanisms of the respiratory system. *BioScience.* 32(1):45-50, 1982.

Schlosser, P.M.. Relative roles of convection and chemical reaction for the disposition of formaldehyde and ozone in nasal mucus. *Inhal. Toxicol.* 11: 967-980, 1999.

Schock, B. C., J. Koostra, S. Kwack, R. M. Hackman, A. Van Der Vliet, and C. E. Cross. Ascorbic acid in nasal and tracheobronchial airway lining fluids. *Free Radical Biol. Med.* 37(9):1393-1401, 2004.

Schreck, R. M. *Laminar flow through bifurcations with applications to the human lung*. PhD thesis. Evanston: Northwestern University, 1972.

Silverthorn, D.U. (2001). *Human Physiology: An Integrated Approach*. Upper Saddle River: Prentice Hall, 2001, 498-502 pp.

Slade, R., K. Crissman, J. Norwood, and G. Hatch. Comparison of antioxidant substances in bronchoalveolar lavage cells and fluid from humans, guinea pigs, and rats. *Environ. Lung Res.* 19:469-484, 1993.

Tyler, N. K., D. M. Hyde, A. G. Hendrickx, and C.G. Plopper. Morphogenesis of the respiratory bronchiole in Rhesus monkey lungs. *Am. J. Anat.* 182:215-223, 1988.

van der Vliet, A. and C. E. Cross. Innate antioxidant defense systems in the respiratory tract. *Biofactors* 15:83-86, 2001.

van der Vliet, A., C.A. O'Neill, C.E. Cross, J.M. Koostra, W.G. Volz, B. Halliwell, and S. Louie. Determination of low-molecular-mass antioxidant concentrations in human respiratory tract lining fluids. *Am. J. Physiol. Lung Cell. Mol. Physiol.* 276{2):L289-L296, 1999.

Weibel, E. R. *Morphometry of the Human Lung*. New York: Academic Press Inc., 1963, 139 pp.

West, J.B. *Respiratory Physiology: The Essentials.* 6th ed. Baltimore: Williams and Wilkins, 1999.

Wilke, P. R. and C. Chang. Correlation of diffusion coefficients in dilute solutions. *A.I.Ch.E. J.* 1: 264-270, 1955.

Zhang, C. H., Y. Liu, R. M. C. So, and N. Phan-Thien. The influence of inlet velocity profile on three-dimensional three-generation bifurcating flows. *Comput. Mech.* 29(4-5):422-429, 2002.

Zhang, Z., C. Kleinstreuer, and C. S. Kim. Effects of asymmetric branch flow rates on aerosol deposition in bifurcating airways. *J. Med. Eng. Technol.* 24(5):192-202, 2000.

Appendix A

NOMENCLATURE

A^*, A	surface area, dimensionless surface area
A_r	FLUENT pre-exponential factor
c^*, c	O_3 concentration, dimensionless/scaled concentration
$\langle c \rangle$	average dimensionless O_3 concentration
c_{gi}^*, c_{gi}	gas phase concentration, dimensionless concentration at the gas-RTLF interface
c_0	inlet O_3 concentration
c_l^*, c_l	concentration, dimensionless concentration of O_3 in the RTLF
c_{li}^*	RTLF phase concentration at the gas-RTLF interface
c_S^*, c_S	concentration, dimensionless concentration of RTLF substrate
$c_{S\Delta}^*$	concentration of substrate at RTLF-tissue interface
D_g	gas phase diffusivity of O_3 in air
D_H	hydraulic diameter
D_i	FLUENT diffusivity (Section **3.3**) OR binary diffusion coefficient of O_3 in phase *i* (Section **6.1**)
D_l	diffusivity of O_3 in the RTLF

D_S	effective diffusivity of substrate in the RTLF
Da	pseudo-first order reaction model Damkohler number (defined in Section **6.2.1**)
Da_2	second order reaction model Damkohler number (defined in Section **6.3.1**)
Da'	dimensionless reaction parameter (defined in Section **6.1**)
Da_R	dimensionless quantity representative of reaction rate constant (defined in equation **7.10**)
E_r	FLUENT activation energy
f	respiratory frequency
$[i]_{wall}$	FLUENT concentration of species i at a reacting surface
I	respired volume of air per day (m^3/day)
$J^*_{O_3}$	diffusive flux of O_3 into the RTLF
$k_{f,r}$	FLUENT reaction rate constant
k_{r1}	pseudo-first order reaction rate constant
k_{r2}	second order reaction rate constant
K	dimensionless mass transfer parameter (equations **7.2** and **7.3**)
K^*	mass transfer parameter (equations **8.4** and **8.5**)
L	airway length
$\dot{M}$	dimensionless rate of O_3 uptake
$M_{w,i}$	molecular weight of species i
$\mathbf{n}$	unit normal vector

$N^*,\ N$	flux, dimensionless flux of O_3 into the RTLF
$\overline{N}$	circumferentially-averaged dimensionless flux
$\langle N \rangle$	average dimensionless flux (equation **5.1**)
N^*_{RTLF}	flux of O_3 into the RTLF
N_{RTLF}	RTLF-side dimensionless flux of O_3 into the RTLF
N^*_{tissue}	flux of O_3 into the tissue
N_{tissue}	RTLF-side dimensionless flux of O_3 into the tissue
$p^*,\ p$	pressure, dimensionless pressure
P^*	perimeter of inflow or outflow boundary
Pe	gas phase Peclet number (defined in Section **3.2**)
Pe_l	RTLF Peclet number (defined in Section **6.1**)
Q_0	volumetric flow rate through parent branch
R	universal gas constant
R_0	radius of parent branch or trachea
$\hat{R}_i$	FLUENT rate of production of species i per unit area into the gas phase
$R^*_{O_3}$	molar rate of O_3 production by chemical reaction per unit volume
R^*_S	molar rate of substrate production by chemical reaction per unit volume
Re	Reynolds number (defined in Section **3.2**)
s	dimensionless wall coordinate (Figure **3-3B**)
Sc	Schmidt number (defined in Section **3.2**)

Sh	local Sherwood number (defined in equation **4.1**)
$\overline{Sh}$	average Sherwood number (defined in equation **4.3**)
t^*, t	time, dimensionless time
T	temperature
$\mathbf{u}^*$, $\mathbf{u}$	velocity vector, dimensionless velocity vector
U	RTLF mucus speed
V_{cell}	volume of a mesh element
V_0	average axial velocity magnitude in parent branch
W	weight of rhesus monkey (in kg)
Wo_l	RTLF Womersley parameter (defined in Section **6.1**)
x	dimensionless axial position (Section **4.1.1**)
Y_i	FLUENT mass fraction

Greek and Other Symbols

∇^*, ∇	gradient operator, dimensionless gradient operator
∇^{*2}, ∇^2	Laplace operator, dimensionless Laplace operator
α	RTLF-gas equilibrium partition coefficient
Δ	RTLF thickness
β	relative diffusion rate of O_3 and substrate (defined in Section **6.3.1**)
β_r	FLUENT dimensionless temperature exponent
ϕ_p, ϕ_d	azimuthal angle in parent branch, daughter branch

κ	dimensionless daughter branch radius
λ	dimensionless tube length
μ	dynamic viscosity of O_3-air mixture
θ	fractional uptake of O_3
ρ	density of O_3-air mixture
ρ_i	FLUENT density
ω	angular respiratory frequency = $2\pi f$

Acronyms

A	anterior
AH_2	ascorbic acid
BSA	bovine serum albumin
egg PC	egg-phosphatidylcholine
GSH	reduced glutathione
I.W.	inner wall
O.W.	outer wall
P	posterior
RTLF	respiratory tract lining fluid
UA	uric acid

Appendix B

NUMERICAL SOLUTION OF GOVERNING EQUATIONS WITH FLUENT

The integral form of the steady-state conservation equation for a scalar quantity ϕ can be written for an arbitrary control volume V as

$$\oint \rho \phi \mathbf{u} \bullet d\mathbf{A} = \oint \left[\left(\Gamma_{\phi} \nabla \phi \bullet d\mathbf{A} - \left(\psi \, p\mathbf{I} \right) \bullet d\mathbf{A} \right) \right] + \int_{V} S_{\phi} \, dV \qquad \mathbf{B.1}$$

where **A** is the surface area vector, Γ_{ϕ} is the diffusivity coefficient for the scalar ϕ, and S_{ϕ} is the source of ϕ per unit volume (FLUENT 6.2 User's Guide). The term on the LHS represents the convective flux of the scalar ϕ, while the first term on the RHS represents its diffusive flux. $\psi = 0$ for all equations except the Navier-Stokes equation. In the continuity equation, ϕ is equal to unity, and all RHS terms are zero. For the Navier-Stokes equation, three separate equations can be written for each of the velocity component. Each of the velocity components is represented by ϕ, Γ_{ϕ} represents the dynamic viscosity μ, **I** is the identity matrix, $\psi = 1$, and the source term includes body forces (e.g., gravity). In the simulations, the effects of gravity were neglected. In the convection-diffusion equation, ϕ represents the concentration of O_3, Γ_{ϕ} represents the gas phase diffusivity of O_3 in air, $\psi = 0$, and the source term is the rate of production of O_3 due to homogeneous reaction in the gas phase, which in all simulations was equal to zero. The finite volume discretization of equation **B.1** is

$$\sum_{f}^{N_{faces}} \rho_f \mathbf{u}_f \phi_f \bullet \mathbf{A}_f = \sum_{f}^{N_{faces}} \Gamma_\phi (\nabla\phi)_n \bullet \mathbf{A}_f - \sum_{f}^{N_{faces}} \psi \, p_f \left|\mathbf{A}_f\right| + S_\phi V \qquad \textbf{B.2}$$

where N_{faces} is the number of faces enclosing the control volume, ϕ_f is the value of the scalar convected through face *f*, $\mathbf{A}_f$ is the area vector of face *f*, the direction of which is normal to *f* and the magnitude of which is $\left|\mathbf{A}_f\right|$, and $(\nabla\phi)_n$ is the magnitude of the gradient of ϕ normal to *f*. Because the concentration of O_3 in air is so small, the velocity field can be considered to be uncoupled from the gas phase composition. Therefore, FLUENT's segregated implicit solver, which solves each of the governing equations sequentially, was used.

In the finite volume method, all flow variables are stored at the cell centers, therefore ϕ_f has to be determined by interpolation of cell-centered values using an upwind scheme. Several schemes are available in FLUENT, and a flux-limiting second-order upwind scheme was used in order to reduce numerical diffusion while maintaining numerical stability. FLUENT's standard scheme was used for pressure interpolation to determine p_f. In solving the continuity and Navier-Stokes equations sequentially, a pressure equation develops from the requirement that the momentum equation must satisfy continuity. Pressure-velocity coupling was achieved by employing SIMPLE (Semi-Implicit Method for Pressure-Linked Equations) algorithm to introduce pressure into the continuity equation. Node-based evaluations of derivatives were employed in all simulations.

After the equations represented by equation **B.2** are linearized and assembled, an algebraic equation can be written for each scalar in each control volume:

$$a_P \, \phi_P = \sum_{nb} a_{nb} \phi_{nb} + b \qquad \mathbf{B.3}$$

where the subscripts *p* and *nb* signify the current cell under consideration and the neighboring cells, respectively, and a_P and a_{nb} are linearized coefficients for ϕ_P and ϕ_{nb}, respectively. When all the equations for all control volumes for a single scalar are combined, a matrix equation results:

$$\mathbf{a} \, \boldsymbol{\phi} = \mathbf{b} \qquad \mathbf{B.4}$$

where $\boldsymbol{\phi}$ is the vector of all scalar cell-center values $\{\phi_P\}$. Each scalar matrix equation was solved using a point implicit (Gauss-Seidel) linear equation solver in combination with an algebraic multigrid (AMG) method. In order to avoid numerical instability in the solution of the non-linear, coupled set of equations represented by equation **B.4**, the value of ϕ was updated to ϕ_{new} after each iteration:

$$\phi_{new} = \phi_{old} + \alpha \; \Delta\phi \qquad \mathbf{B.5}$$

where ϕ_{old} is the value of ϕ at the beginning of the previous iteration, $\Delta\phi$ is the computed change in ϕ, and α is the under-relaxation factor, $0 < \alpha < 1$. The default values of the relaxation factors in FLUENT are 0.3 for pressure, 0.7 for the velocity components, and 1.0 for all other variables. These values were adjusted as necessary to facilitate solution convergence.

To start the computations, the velocity and O_3 concentrations in the entire domain were initialized to their respective values at the inflow boundary. The average velocity and flow rate of O_3 at an outflow plane were monitored in order to determine convergence, and convergence was considered to be achieved when the change in these values did not exceed 5×10^{-5} for at least 50 iterations. In FLUENT, the scaled residuals R^{ϕ} for all equations except the continuity equation are calculated as follows:

$$R^{\phi} = \frac{\sum_{cells\ P}\left|\sum_{nb} a_{nb}\phi_{nb} + b - a_P\phi_P\right|}{\sum_{cells\ P}\left|a_P\phi_P\right|} \qquad \textbf{B.6}$$

The scaled residual R^c for the continuity equation is defined as

$$\frac{R^c_{iteration\ N}}{R^c_{iteration\ 5}} \qquad \textbf{B.7}$$

where R^c is defined as the sum of the rate of mass creation in all cells and the denominator is the maximum of the absolute value of R^c in the first 5 iterations. When the convergence criteria stated above were satisfied, the scaled residuals for the governing equations were all less than 10^{-5}.

Appendix C

USER-DEFINED PROGRAMS FOR CALCULATING O_3 FLUX

The determination of the flux of O_3 into the RTLF required the evaluation of ∇c^* at the gas-RTLF interface; however, the gradients of each variable are stored at the cell center. Therefore, the flux calculation used the following approximation to calculate the flux at the gas-RTLF interface for an infinitely fast reaction at the wall (FLUENT 6.2 User's Guide):

$$N^*\left|\mathbf{A}_f^*\right| = D_g\left[\frac{(c_f^*-c^*)}{ds^*}\frac{\mathbf{A}_f^*\bullet\mathbf{A}_f^*}{\mathbf{A}_f^*\bullet\mathbf{e}_\mathrm{s}} + \left(\nabla^* c^*\bullet\mathbf{A}_f^* - \nabla^* c^*\bullet\mathbf{e}_\mathrm{s}\frac{\mathbf{A}_f^*\bullet\mathbf{A}_f^*}{\mathbf{A}_f^*\bullet\mathbf{e}_\mathrm{s}}\right)\right] \qquad \mathbf{C.1}$$

where $\mathbf{A}_f^*$ represents the dimensional face area vector, ds^* is the magnitude of the vector $\mathbf{ds}^*$, which is the vector from the cell centroid and the face centroid, and $\mathbf{e}_\mathrm{s}$ is the unit vector in the direction of $\mathbf{ds}^*$ (Figure **C-1**). Again, an asterisk denotes a dimensional variable. In order to calculate the dimensionless flux N, a modification of equation **C.1** was used:

$$N\left|\mathbf{A}_f\right| = \left[\frac{(c_f-c)}{ds}\frac{\mathbf{A}_f\bullet\mathbf{A}_f}{\mathbf{A}_f\bullet\mathbf{e}_\mathrm{s}} + \left(\nabla c\bullet\mathbf{A}_f - \nabla c\bullet\mathbf{e}_\mathrm{s}\frac{\mathbf{A}_f\bullet\mathbf{A}_f}{\mathbf{A}_f\bullet\mathbf{e}_\mathrm{s}}\right)\right] \qquad \mathbf{C.2}$$

where the absence of an asterisk denotes dimensionless variables. Note that c^* and ∇c^* and their dimensionless counterparts are the values stored in the cell center (Figure **C-1**), and c_f^* and c_f are the values stored at the face centroid. The first term on the RHS represents the primary gradient in the direction that connects the cell and face centroids, and the second term represents the “cross” diffusion term.

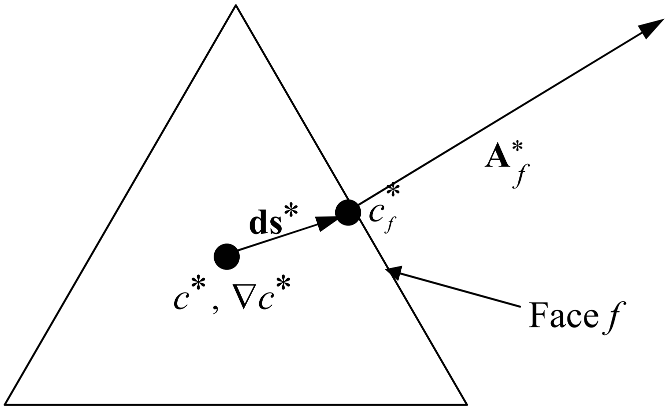

Figure **C-1**: Vectors used to calculate the flux through the gas-RTLF interface. The triangle represents a cell/control volume adjacent to the gas-RTLF interface, a portion of which is spanned by face *f*. The dark circles represent a cell or face centroid.

C.1 USER-DEFINED FUNCTION FOR CALCULATING FLUX FOR THE CASE OF AN INFINITE WALL REACTION

For the case of an infinite wall reaction, $c_f^* = c_f^* = 0$, and the following user-defined function (UDF) was written in C to calculate the dimensionless flux:

```
/**********************************************************

This program calculates the diffusive flux of ozone through a wall in
two different ways: wall_flux1 using equation 5.2-3 and wall_flux2
equation 5.2-2 in the FLUENT UDF documentation.
NOTE 1: Run the case first, specifying (tui): solve/set/expert.  Answer
yes for the 4th question.
NOTE 2: Allocate 2 memory locations for the face UDMs before you start.

**********************************************************/

#include "udf.h"
```

```
#include "sg.h"

DEFINE_ON_DEMAND(N_D_wall_flux)
{
  Domain *d;
  Thread *tf, *tc0;
  face_t f;
  cell_t c0;
  int i = 0; /*species index for ozone*/


  real wall_flux1, wall_flux2;
  real area, delYI_A, delYI_es;
  real A[ND_ND], ds, es[ND_ND], A_by_es, dr0[ND_ND];
  real test;

  d = Get_Domain(1);

  thread_loop_f(tf, d)
  {
        Message("%d \n",tf);

    /*Check to see if tf references a boundary thread*/
      if (BOUNDARY_FACE_THREAD_P(tf))
      {

            if (THREAD_TYPE(tf) == THREAD_F_WALL)
            {

            Message("%d \n",tf); /*Prints the face pointer*/

            begin_f_loop(f,tf)
            {
                  c0 = F_C0(f,tf); /*obtain cell index for cell adjacent
                                     to face f*/
                  tc0 = THREAD_T0(tf); /*obtain cell thread of cells
                                     adjoining boundary face*/

                  BOUNDARY_FACE_GEOMETRY(f, tf, A, ds, es, A_by_es,
dr0);

                  area = NV_MAG(A); /*magnitude of area vector*/
                  delYI_A = NV_DOT(C_YI_RG(c0, tc0, i), A);
                  delYI_es = NV_DOT(C_YI_RG(c0, tc0, i), es);

                  wall_flux1 = (-C_YI(c0, tc0, i)*A_by_es/ds +(delYI_A
- delYI_es*A_by_es));
                  /*The above is really the wall flux times area*/

                  wall_flux1 /= area; /*actual wall flux*/

                  wall_flux2 = delYI_A/area;

                  F_UDMI(f,tf,0) = wall_flux1;
                  F_UDMI(f,tf,1) = wall_flux2;
```

```
                C_UDMI(c0,tc0,0) = wall_flux1;
                C_UDMI(c0,tc0,1) = wall_flux2;

          }
          end_f_loop(f,tf)

          }

    }

  }
}
```

---

wall_flux1 was calculated using equation **C.2** to solve for N, and *wall_flux2* was calculated using equation **3.8**, but using the value of ∇c, i.e. the gradient stored at the cell-center, to approximate the O_3 concentration gradient at the gas-RTLF interface. The fluxes calculated using both methods were virtually indistinguishable. For example, see Figure **C-2**.

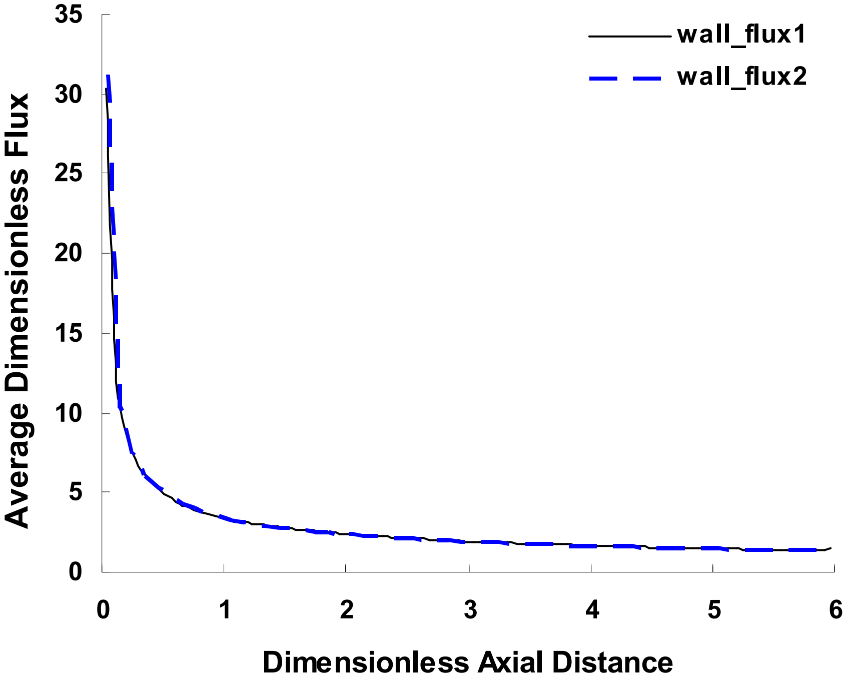

Figure **C-2**: Comparison of the circumferentially averaged dimensionless fluxes along the parent branch of an idealized symmetric bifurcation (90° branching angle, Re = 100) calculated using equation **C.2** (wall_flux1) and an approximation of equation **3.8** (wall_flux2).

C.2 USER-DEFINED FUNCTION FOR THE CASE OF A FINITE PSUEDO-FIRST ORDER REACTION IN THE RTLF

In the case of reaction in the RTLF occurring at a finite reaction rate, the UDFs used to compute the RTLF and tissue fluxes were used equations **6.9**, **6.10**, **7.2**, and **7.3**. In order to obtain the values of the dimensionless fluxes reported in Chapter 7, the values returned by the UDF were multiplied by $\frac{D_l}{D_g}\frac{R_0}{\Delta}$ (cf. equation **7.3**).

```
#include "udf.h"
#include "sg.h"

DEFINE_ON_DEMAND(N_D_wall_flux)
{
  Domain *d;
  Thread *tf, *tc0;
  face_t f;
  cell_t c0;
  int i = 0; /*species index for ozone*/

  real cO3;
  real alpha = 0.145;  /*RTLF-gas partition coefficient for O3*/
  real D;
  real tissue_flux, elf_flux;


  d = Get_Domain(1);

  D = RP_Get_Real("da");

  Message("Damkohler number is:  %f", D);

  thread_loop_f(tf, d)
  {
        Message("%d \n",tf);

    /*Check to see if tf references a boundary thread*/
      if (BOUNDARY_FACE_THREAD_P(tf))
      {

            if (THREAD_TYPE(tf) == THREAD_F_WALL)
    /*Check to see if tf references a wall*/
```

```
            {

            Message("%d \n",tf);

            begin_f_loop(f,tf)
            {
                  cO3 = F_YI(f, tf, i);

                  elf_flux = alpha * cO3 * sqrt(D)/tanh(sqrt(D));
                  tissue_flux = alpha* cO3 * sqrt(D) *
(cosh(sqrt(D))/tanh(sqrt(D)) - sinh(sqrt(D)));

                  F_UDMI(f,tf,2) = elf_flux;
                  F_UDMI(f,tf,3) = tissue_flux;

                  C_UDMI(c0,tc0,2) = elf_flux;
                  C_UDMI(c0,tc0,3) = tissue_flux;


            }
            end_f_loop(f,tf)

            }

      }

  }
}
```

Appendix D

SOLUTION OF 2ND ORDER REACTION MODEL

D.1 MATHEMATICA CODE USED TO IMPLEMENT THE SHOOTING METHOD

```
Directory[]
(* c - ozone concentration, s - substrate concentration, x - direction perpendicular to
RTLF - gas interface *)

(* Set values of parameters *)
Da = 1000;
β = 2.4*^-11;

xinit  =  1;  (* Value of x for guess "initial" condition *)
cinit  =  0;   (* Actual boundary  condition for c at x  =  xinit *)
sinit  = 1;   (* See above *)
targetx  = 0;   (* Value of x for other boundary condition *)
targetc  =  1;   (* Value of boundary condition for c.   Note:  Not necessarily the same as
   value of c at targetx *)
targets  =  0;   (* Value of b.c. for s. See note above *)

(* 2nd order ODEs to be solved *)
f[c_, s_, x_] := c"[x] - Da c[x] s[x];
g[c_, s_, x_] := s"[x] - β Da c[x] s[x];

Print["Da = ",  Da,  "     β = ", β];
?f
?g

ShootingMeth2[guessc0_, guessc1_, guesss0_, guesss1_, maxerror_, maxiter_] :=
Module[{},
   j = 1;  k = 1;
   c0 = N[guessc0];
   c1 = N[guessc1];
   s0 = N[guesss0];
   s1 = N[guesss1];
```

```
(* Note:  the order in the final curly brackets in NDSolve may have to be changed
   depending on whether xinit > targetx or not *)
sol0 = NDSolve[{    f[c, s, x] == 0, g[c, s, x] == 0,  c[xinit] == cinit,  c'[xinit] == c0,
   s[xinit] == sinit,  s'[xinit] == s0},  {c, s}, {x, targetx,  xinit}];
sol1 = NDSolve[{f[c, s, x] == 0, g[c, s, x] == 0,  c[xinit] == cinit,  c'[xinit] == c1,
   s[xinit] == sinit,  s'[xinit] == s1},  {c, s}, {x, targetx,  xinit}];

(* You need to put in the correct form of the  known boundary condition at the other
   end *)
cboundaryval0 = Evaluate[c[targetx] /. sol0];
cboundaryval1 = Evaluate[c[targetx] /. sol1];
sboundaryval0 = Evaluate[s'[targetx] /. sol0];
sboundaryval1 = Evaluate[s'[targetx] /. sol1];
cerror0 = N[targetc - cboundaryval0];
cerror1 = N[targetc - cboundaryval1];
serror0 = N[targets - sboundaryval0];
serror1 = N[targets - sboundaryval1];


Print[0, "c:    " , c0,  cboundaryval0,  cerror0];
Print[0, "s:    ", s0,  sboundaryval0,  serror0];
Print[1, "c:    " , c1, cboundaryval1,  cerror1];
Print[1, "s:    ", s1,  sboundaryval1,  serror1];

cerror  =  cerror1;
serror  =  serror1;
c2  = c1; s2  = s1;
c1 = c0; s1 = s0;

While[(j  <  maxiter)  &&  (maxerror <  Abs[First[cerror]]  ||  maxerror  <
   Abs[First[serror]]),
   k = 1;
   c0 = c1;
   c1 = c2;
   Print[" "];
   Print["j = ",  j];


   While[(k  <  maxiter) &&  (maxerror < Abs[First[cerror]]  ||  maxerror  <
      Abs[First[serror]]),
      sol0 = NDSolve[{f[c, s, x] == 0, g[c, s, x] == 0, c[xinit] == cinit, c'[xinit] == c0,
         s[xinit] == sinit,  s'[xinit] == s2}, {c, s}, {x, targetx, xinit}];
      sol1 = NDSolve[{f[c, s, x] == 0, g[c, s, x] == 0, c[xinit] == cinit,  c'[xinit] == c1,
         s[xinit] == sinit,  s'[xinit] == s2, {c, s}, {x, targetx, xinit}];
   cboundaryval0 = Evaluate[c[targetx] /. sol0];
   cboundaryval1 = Evaluate[c[targetx] /. sol1];
   sboundaryval0 = Evaluate[s'[targetx] /. sol0];
   sboundaryval1 = Evaluate[s'[targetx] /. sol1];
   cerror0 = N[targetc - cboundaryval0];
   cerror1 = N[targetc - cboundaryval1];
   serror0 = N[targets - sboundaryval0];
   serror1 = N[targets - sboundaryval1];

   c2  =  First[c1 - (c1 - c0)/(cerror1 - cerror0) * error1];

   sol2 = NDSolve[{f[c, s, x] == 0, g[c, s, x] == 0, c[xinit] == cinit,  c'[xinit] == c2,
      s[xinit] == sinit,  s'[xinit] == s2},  {c, s}, {x, targetx,  xinit}];
   cboundaryval2 = Evaluate[c[targetx] /. sol2];
   sboundaryval2 = Evaluate[s'[targetx] /. sol2];
   cerror = N[targetc - cboundaryval2];
   serror = N[targets - sboundaryval2];
   Print[k, "  c:    " , c2, cboundaryval2, cerror];
   Print[k, "  s:    ", s2, sboundaryval2,  serror];
   k = k + 1;
   ];
cerror  =. ;
s0  =  s1;
s1 = s2;
sol0 = NDSolve[{f[c, s, x] == 0, g[c, s, x] == 0,  c[xinit] == cinit,  c'[xinit] == c2,
  s[xinit] == sinit,  s'[xinit] == s0},  {c, s}, {x, targetx, xinit}];
sol1 = NDSolve[{f[c, s, x] == 0, g[c, s,  x] == 0,  c[xinit] == cinit,  c'[xinit] == c2,
  s[xinit] == sinit,  s'[xinit] == s1},  {c, s}, {x, targetx,  xinit}];
cboundaryval0 = Evaluate[c[targetx] /. sol0];
cboundaryval1 = Evaluate[c[targetx] /. sol1];
sboundaryval0 = Evaluate[s'[targetx] /. sol0];
sboundaryval1 = Evaluate[s'[targetx] /. sol1];
cerror0 = N[targetc - cboundaryval0];
cerror1 = N[targetc - cboundaryval1];
serror0 = N[targets - sboundaryval0];
serror1 = N[targets - sboundaryval1];
s2  =  First[s1 - (s1 - s0)/(serror1 - serror0) * serror1];
sol2 = NDSolve[{f[c, s, x] == 0, g[c, s, x] == 0,  c[xinit] == cinit,  c'[xinit] == c2,
  s[xinit] == sinit,  s'[xinit] == s2},  {c, s}, {x, targetx,  xinit}];
cboundaryval2 = Evaluate[c[targetx] /. sol2];
sboundaryval2 = Evaluate[s'[targetx] /. sol2];
cerror = N[targetc - cboundaryval2];
serror = N[targets - sboundaryval2];
Print["j = ",  j, "k = " , k - 1];
Print[k - 1, "c:    " , c2, cboundaryval2,  cerror];
```

```
    Print[k - 1, "  s:    ", s2,  sboundaryval2,  serror];
    j = j + 1;
    Print ["j+1 = ", j];]
  (* Again,  the order in the curly brackets depends on whether xinit > targetx or not *)[
  Print[" "];
  Print[" "];
  Print[" "];
  Print[" "];
  Print[" "];
  Print[" "];
  Print["Da = ",  Da,  "     β = ", β];
  Print["Plot of O3 conc. vs. depth"];
  Plot[Evaluate[c[x]] /. sol2, {x, targetx, xinit}];
  Print[" "];
  Print[" "];
  Print["Plot of substrate conc. vs. depth"];
  Plot[Evaluate[s[x]] /. sol2, {x, targetx,  xinit}];
  Print["The flux of O3 into mucus is  ", First[Evaluate[c'[0] /. sol2]]];
  Print["The flux of O3 into tissue is  ",  First[Evaluate[c'[1] /. sol2]]];]


n  =  50;
ShootingMeth2[-0.5, -0.6, 0, 1,  10^-8, 15];

myfile  =  OpenWrite["2nd order for comparison - Da = 1000"];
Write[myfile, "Da ", s,  Da];
Write[myfile, "b ", s,  β];
Write[myfile,  "g ", s,  γ];
Write[myfile,  "ELF Flux", s,   First[Evaluate[-c'[0] /. sol2]]];
Write[myfile,  "Tissue Flux", s,  First[Evaluate[-c'[1] /. sol2]]];

Write[myfile,  "z",  s,  "Co3",  s,  "Cs"];
Do[o3[i] = Evaluate[c[i/n] /. sol2]; sub[i] = Evaluate[s[i/n] /. sol2];  Print[N[i/n],  "   ",
  First[o3[i]],  "   ",  First[ sub[i] ]]; Write[myfile, N[i/n], s, First[  o3[i] ], s,  First[ sub[i]
  ] ], {i, 0,  n}];
Close[myfile]
```

D.2 SOLUTION OF GOVERNING EQUATIONS USING ASYMPTOTIC EXPANSIONS

The species conservation equations and boundary conditions for O_3 and substrate in the RTLF are:

$$\frac{\partial^2 c_l}{\partial y^2} = Da_2 c_l c_S; \qquad c_l(y=0)=1,\ c_l(y=1)=0\,, \tag{D.1}$$

$$\frac{\partial^2 c_S}{\partial y^2} = \beta Da_2 c_l c_S; \qquad \left.\frac{\partial c_S}{\partial y}\right|_{y=0} = 0,\ c_S(y=1)=1\,. \tag{D.2}$$

In the limit of small Da_2, and assuming the constant β is $O(1)$, c_l and c_S can be written as power series in Da_2:

$$c_l(y;\,Da_2) = c_{l0}(y) + Da_2 c_{l1}(y) + O(Da_2^2) \tag{D.3}$$

$$c_S(y;\,Da_2) = c_{S0}(y) + Da_2 c_{S1}(y) + O(Da_2^2) \tag{D.4}$$

Therefore, the species conservation equations and boundary conditions can be written as

$$\frac{\partial^2}{\partial y^2}\left(c_{l0} + Da_2 c_{l1} + \ldots\right) = Da_2\left(c_{l0} + Da_2 c_{l1} + \ldots\right)\left(c_{S0} + Da_2 c_{S1} + \ldots\right) \tag{D.5}$$

$$\left(c_{l0} + Da_2 c_{l1} + \ldots\right)_{y=0} = 1; \quad \left(c_{l0} + Da_2 c_{l1} + \ldots\right)_{y=1} = 0 \tag{D.6}$$

and

$$\frac{\partial^2}{\partial y^2}\left(c_{S0} + Da_2 c_{S1} + \ldots\right) = Da_2\beta\left(c_{l0} + Da_2 c_{l1} + \ldots\right)\left(c_{S0} + Da_2 c_{S1} + \ldots\right) \tag{D.7}$$

$$\frac{\partial}{\partial y}\left(c_{S0} + Da_2 c_{S1} + \ldots\right)_{y=0} = 0; \quad \left(c_{S0} + Da_2 c_{S1} + \ldots\right)_{y=1} = 0 \tag{D.8}$$

Solutions for the $O(1)$ and $O(Da_2)$ terms can now be obtained.

$O(1)$ equations and solutions:

Ozone concentration:

$$\frac{\partial^2 c_{l0}}{\partial y^2} = 0; \qquad c_{l0}(y=0) = 1, \quad c_{l0}(y=1) = 0 \tag{D.9}$$

$$\boxed{c_{l0} = 1 - y} \tag{D.10}$$

Susbtrate concentration:

$$\frac{\partial^2 c_{S0}}{\partial y^2} = 0; \qquad \left.\frac{\partial c_{S0}}{\partial y}\right|_{y=0} = 0, \quad c_{S0}(y=1) = 1 \tag{D.11}$$

$$\boxed{c_{S0} = 1} \tag{D.12}$$

$O(Da_2)$ solutions:

Ozone concentration:

$$\frac{\partial^2 c_{l1}}{\partial y^2} = c_{l0} c_{S0} = 1 - y; \qquad c_{l1}(y=0) = c_{l1}(y=1) = 0 \tag{D.13}$$

$$\boxed{c_{l1} = -\tfrac{1}{6}\left(2y - 3y^2 + y^3\right)} \tag{D.14}$$

Substrate concentration:

$$\frac{\partial^2 c_{S1}}{\partial y^2} = \beta\, c_{l0} c_{S0} = \beta(1 - y); \qquad \left.\frac{\partial c_{S1}}{\partial y}\right|_{y=0} = c_{S1}(y=1) = 0 \tag{D.15}$$

$$\boxed{c_{S1} = -\tfrac{1}{6}\beta\left(2 - 3y^2 + y^3\right)} \tag{D.16}$$

Therefore, the solutions of the governing equations are:

$$c_l\left(y; Da_2\right) = \left(1 - y\right) - \tfrac{1}{6} Da_2 \left(2y - 3y^2 + y^3\right) + \mathrm{O}\left(Da_2^2\right) \tag{D.17}$$

$$c_S\left(y; Da_2\right) = 1 - \tfrac{1}{6}\beta\, Da_2 \left(2 - 3y^2 + y^3\right) + \mathrm{O}\left(Da_2^2\right) \tag{D.18}$$

Appendix E

GRID CONVERGENCE RESULTS FOR Re 1000

GRID DESCRIPTIONS (HEXAHEDRAL ELEMENTS)

	Number of cells	Smallest cell size (parent)	Smallest cell size (daughter)	Largest cell size
Grid 1	1,093,668	0.02	0.02	0.04
Grid 2	1,051,248	0.01	0.007	0.04
Grid 3	1,197,680	0.005	0.0035	0.04

DESCRIPTIONS OF BOUNDARY LAYERS ATTACHED IN GAMBIT

	PARENT BRANCH			DAUGHTER BRANCH		
	Start Size	Growth rate	Number of boundary layers	Start Size	Growth rate	Number of boundary layers
Grid 1	N/A	N/A	N/A	N/A	N/A	N/A
Grid 2	0.01	1.2	6	0.007	1.2	6
Grid 3	0.005	1.25	10	0.0035	1.25	10

Grid 1 was the grid used for the reported simulations. One curvature-based adaption was performed in FLUENT on a uniform grid with elements of size 0.04 (see Section **4.1.1**).

In Grids 2 and 3, boundary layers were attached to the walls of the geometry in GAMBIT and the rest of the geometry was meshed with size 0.04 elements.

COMPARISON OF MACROSCOPIC QUANTITIES FOR THE DIFFERENT MESHES ($Da = 10^6$)

Dimensionless Mass Flow Rate

				Percent Changes	
	Grid 1	Grid 2	Grid 3	Grid 1 → 2	Grid 2 → 3
Inflow boundary	3.14	3.14	3.14	0.00 %	0.00 %
Outflow boundary 1	1.57	1.57	1.57	0.00 %	0.00 %
Outflow boundary 2	1.57	1.57	1.57	0.00 %	0.00 %
Mass Imbalance	1×10^{-7}	1×10^{-7}	1×10^{-7}	0.00 %	0.00 %

Average Dimensionless Velocity

				Percent Changes	
	Grid 1	Grid 2	Grid 3	Grid 1 → 2	Grid 2 → 3
Inflow boundary	0.981	0.990	0.995	0.97 %	0.50 %
Outflow boundary 1	1.019	1.021	1.021	0.20 %	0.04 %
Outflow boundary 2	1.019	1.021	1.021	0.20 %	0.05 %

Average Dimensionless Concentration

				Percent Changes	
	Grid 1	Grid 2	Grid 3	Grid 1 → 2	Grid 2 → 3
Inflow boundary	0.9996	0.9998	0.9999	0.02 %	0.01 %
Outflow boundary 1	0.8795	0.8796	0.8796	0.02 %	0.00 %
Outflow boundary 2	0.8795	0.8796	0.8796	0.02 %	0.00 %

Dimensionless Flow Rate of Ozone

	Grid 1	Grid 2	Grid 3	Percent Changes Grid 1 →2	 Grid 2 →3
Inflow boundary	3.139	3.140	3.141	0.03 %	0.01 %
Outflow boundary 1	1.444	1.445	1.446	0.10 %	0.01 %
Outflow boundary 2	1.444	1.445	1.446	0.10 %	0.01 %

Dimensionless Uptake Rate (Integral of dimensionless flux through walls)

	Grid 1	Grid 2	Grid 3	Percent Changes Grid 1 →2	 Grid 2 →3
Total Uptake Rate	210.2	209.3	209.2	-0.43 %	-0.03 %

VITA

Adekemi B. Taylor

EDUCATION

The Pennsylvania State University, University Park, PA
PhD in Chemical Engineering October 2006

Howard University, Washington DC
Bachelor of Science in Chemical Engineering May 2001

PUBLICATIONS

Reeser, W.H., G.M. Lee, **A. Taylor**, L. Wang, S.F. Arnold, J.S. Ultman, and A. Ben-Jebria. Uptake of ozone in human lungs and its relationship to local physiological response. *Inhal. Toxicol.* 17:699-707, 2005.

Taylor, A.B., G.M. Lee, K. Nellore, A. Ben-Jebria, and J.S. Ultman. Changes in the carbon dioxide expirogram in response to ozone exposure. *Toxicol. Appl. Pharmacol.* 213:1-9, 2006.

Taylor, A.B., A. Borhan, J.S. Ultman. Three-dimensional simulations of gas uptake in single airway bifurcations. *Ann. Biomed. Eng.* in press, 2006.